Numerical Modelling of the Time-Dependent Behaviour of Tunnels in Squeezing Ground

Eugie KABWE

BSc (MinSc). Mining Engineering, University of Zambia, Lusaka, Zambia

MEng. Mining Engineering, University of Science and Technology Beijing, Beijing, China

A thesis submitted in fulfillment of the requirements for the degree of Doctor of Philosophy in the

Faculty of Engineering, Computer and Mathematical Sciences

School of Civil, Environmental and Mining Engineering

The University of Adelaide

- October 2020-

Declaration of Authorship

I, Eugie KABWE, certify that this work contains no material which has been accepted for the award of any other degree or diploma in my name, in any university or other tertiary institution and, to the best of my knowledge and belief, contains no material previously published or written by another person, except where due reference has been made in the text. Also, I certify that no part of this work will, in the future, be used in a submission in my name, for any other degree or diploma in any university or other tertiary institution without the prior approval of the University of Adelaide and where applicable, any partner institution responsible for the joint-award of this degree.

I acknowledge that the copyright of published works contained within this thesis resides with the copyright holder(s) of those works.

I also permit the digital version of my thesis to be made available on the web, via the University's digital research repository, the Library Search, and also through web search engines, unless permission has been granted by the University to restrict access for some time.

I acknowledge the support I have received for my research through the provision of the Adelaide Scholarship International and partially from the Australian Government funding through an RTP funded scholarship fee-offset.

Signed:

Date: 04/02/2021

UNIVERSITY OF ADELAIDE

Abstract

Faculty of Engineering, Computer and Mathematical Sciences

School of Civil, Environmental and Mining Engineering

Doctor of Philosophy

Numerical Modelling of the Time-Dependent Behaviour of Tunnels in Squeezing Ground

by Eugie KABWE

During tunnel excavation in high stressed and weak rock masses, excessive deformation is often encountered characterized by squeezing. The squeezing phenomenon is referred to as the large time-dependent convergence which occurs during excavation and continues over time, essentially associated with the creep mechanism. This time-dependent behavior is usually not identified at the feasibility stage of tunnel development. Consequently, leads to high cost in rock reinforcement and support installation as well as time-consuming and unsafe rehabilitation to keep tunnels in operation. Prediction of the time-dependent deformation associated with squeezing at an early stage is of great significance for stable tunnel excavation and design. The depiction of this tunnel response requires analytical and numerical techniques, in numerical techniques, it is made possible by employing constitutive models. However, literature outlines the limitations of these conventional constitutive models in estimating time-dependent deformation in squeezing ground. Hence, this study makes three major contributions to the understanding of the 3-phase creep mechanism and presentation of efficient tools for its description.

The first major contribution is the derivation and presentation of the closed-form analytical solutions which can estimate the confining stress-dependent and time-dependent response of tunnels excavated in

squeezing ground. These solutions address the deficiencies encountered when employing the conventional analytical solution in the realistic estimation of the ground reaction attributed to squeezing.

The second major contribution is the presentation of a fractional-order derivative viscoelastic viscoplastic (FDVP) constitutive model capable of estimating delayed deformations characterized by squeezing. Its equations are derived as an extension to the Burgers model and adjusted Perzyna overstress function with an associated viscoplastic flow rule. It addresses the deficiencies experienced by the conventional integer-order derivative constitutive models in describing the power-law mechanism of materials. The model is calibrated using experimental data obtained from literature and verified by monitored tunnel convergence data. Thereafter, implemented in a finite volume numerical code to simulate the time-dependent tunnel response.

The third major contribution is the presentation of an elasto-viscoplastic with isotropic damage (EVPD) constitutive model that explicitly describes the 3-phase creep mechanism. This model is an enhancement of the FDVP constitutive equations considering the isotropic damage effect characterized by the accelerated creep phase. Its derived constitutive equations are based on fractal-order derivatives obtained by applying scaling transformations on integer-order derivatives. These derived constitutive equations are also calibrated using literature attained experimental data and numerically implemented in a finite volume code to simulate the time-dependent response of a tunnel excavated in squeezing ground.

In this study, these major contributions are presented and elaborated; includes the limitation that they address, their derivation, and applicability in the estimation of time-dependent tunnel deformations.

Acknowledgments

I would like to express my sincere gratitude to my principal supervisor Associate Professor Murat Karakus, for continuous support and encouragement, this thesis would not have been possible to complete as well as Professor Emmanuel Knox Chanda. Thank you all for the encouragement and support in the last 3 years of research, your love for research and expertise has been invaluable.

The financial support from the Adelaide Scholarship International is highly acknowledged. I also appreciated the help provided by the ECMS administrators, IT support officers, academics, Ph.D. students, and many others for their quick response and suggestions.

I would also like to express my greatest gratitude to those who helped in completing my Ph.D. thesis, I say thank you all.

I am very much indebted to the late Emmanuel Chilambwe Kabwe who allowed me to believe in myself. Also, to the late Eutone Makasa Kabwe who saw the potential in me and enhanced it, I am forever grateful. My exceptional gratitude also goes to Associate Professor Nicholas Chileshe of the University of South Australia whose advice and encouragement got me through this journey.

Finally, appreciation goes out to my family (mum, sisters, and brothers) for their support, tolerance, and patience. Special thanks go out to my fiancée for the encouragement and insight it would not have been possible without her support.

Table of Contents

List of Figures

List of Tables

Research Output

Kabwe, E., Karakus, M., & Chanda, E. (2019).
Numerical implementation of a time-based fractal derivative constitutive model for squeezing ground.
In Eurasian Conference on Civil and Environmental Engineering. Istanbul, Turkey.

Kabwe, E., & Karakus, M. (2019).
Estimation of a Tunnel's Long-Term Longitudinal Displacement Profile in Squeezing Ground.
In Advances in Science, Technology, and Innovation. Sousse, Tunisia.

Kabwe, E., Karakus, M., & Chanda, E. (2019).
Intermediate Principal Stress Influence on Tunnel Convergence Considering the Stress Lode Parameter.
In the 2nd Zambian National Conference on Geology, Mining, Metallurgy and Groundwater Resources. Kitwe, Zambia.

Kabwe, E., Karakus, M., & Chanda, E. (2018).
Fractional Order Derivative Solution for Prediction of Creep Deformation in Unlined Tunnels.
In the 1st Zambian National Conference on Geology, Mining, Metallurgy and Groundwater Resources. Lusaka.

Kabwe, E., Karakus, M., & Chanda, E. (2018).
Assessment of Analytical Solutions for Time-Dependent behavior of Unlined Tunnels.
In proceedings of the 4th International Symposium on Underground Excavation (pp. 1-9). Istanbul, Turkey.

Kabwe, E., Karakus, M., Chanda, E., & Akdag, S. (2018).
Investigating the Tunnel Closure using Convergence Confinement Method and 2D Plane Strain Finite Difference Analysis.
In the 4th Australasian Ground Control in Mining Conference.

Eugie Kabwe, Murat Karakus, Emmanuel K. Chanda,
Proposed solution for the ground reaction of non-circular tunnels in an elastic-perfectly plastic rock mass.
Computers and Geotechnics, Volume 119,2020,103354,
https://doi.org/10.1016/j.compgeo.2019.103354.

Eugie Kabwe, Murat Karakus, Emmanuel K. Chanda,
Time-dependent solution for non-circular tunnels considering the elasto-viscoplastic rockmass.
International Journal of Rock Mechanics and Mining Sciences, Volume 133,2020,104395.
https://doi.org/10.1016/j.ijrmms.2020.104395.

Eugie Kabwe, Murat Karakus, Emmanuel K. Chanda,
Creep constitutive model considering the overstress theory with an associative viscoplastic flow rule. Computers and Geotechnics, Volume 124,2020,103629,
https://doi.org/10.1016/j.compgeo.2020.103629.

Eugie Kabwe, Murat Karakus, Emmanuel K. Chanda,
Isotropic Damage Constitutive Model for Time-Dependent Behaviour of Tunnels in Squeezing Ground. Computers and Geotechnics, Volume 120, 2020.103738.
https://doi.org/10.1016/j.compgeo.2020.103738.

Eugie Kabwe, Murat Karakus, Emmanuel K. Chanda,
Identifying the Minimum Support Requirements for a Tunnel in Squeezing Ground of an Underground Mine: A Case Study. Mining, Metallurgy and Exploration. (**Under review**)

Chapter 1. Introduction

1.1 Research Background

In this study, an analytical solution and a constitutive model that will consider the time-dependent response of tunnels excavated in squeezing ground are presented. The functionality of these tools is to reliably estimate the tunnel convergence associated with squeezing. Intended as preliminary indicators of the squeezing potential which can be used for tunnel design and support element strategies. The analytical solution will improve the reliable estimation of time-dependent convergence that will aid practitioners (engineers) in determining the appropriate tunnel support in squeezing ground. Whereas the constitutive model is proposed with the intent of describing the 3-phase creep mechanism associated with squeezing and introduce constitutive laws to reproduce this mechanism explicitly, applicable for research and practice. Furthermore, reduce the significant extra support investment and the time-consuming rehabilitation to maintain tunnel serviceability in squeezing ground. Consequently, this will lead to an in-depth understanding of the nature and extent of squeezing at the feasibility stage.

1.2 Research Gaps

The mechanical behavior or ground reaction of tunnels excavated in squeezing ground is represented by constitutive equations which provide the ground stress-strain response. Even though the squeezing mechanism is complex, most of the conducted research and engineering design practice considers the ground reaction as a linear elastic or perfectly plastic material governed by the Mohr-Coulomb (MC) yield criterion. However, estimation of squeezing related deformations using the MC yield criterion is characterized by rock mass strength and volumetric behavior after failure. Additionally, the MC yield criterion neglects the rock mass stiffness on the confining stress (Intermediate principal stress) dependency as such leads to inaccurate tunnel convergence estimations unsafe for tunnel design. Hence, the widely employed MC yield criterion governed analytical solutions lead to uncertainties in estimating actual tunnel convergence. These uncertainties are related to the correlation between the

pressure which acts on the internal tunnel boundary and the convergence. In that the lower the pressure the larger the tunnel convergence, an important aspect to consider during excavation and support design. On the other hand, the conventional empirical and analytical tools employed to quantify this tunnel convergence are based on circular tunnels in a homogeneous isotropic rock mass condition. They neglect the influence of non-circular tunnel geometries, non-hydrostatic stress field, and sequential excavation process in a discontinuous, anisotropic, non-linear rock mass condition as well as the time-dependent mechanism characterized by squeezing.

This time-dependent behavior also referred to as squeezing can be described by theoretical and numerically implemented constitutive models that are subdivided into phenomenological and micromechanics-based. It is fundamentally clear that most researchers have concentrated on the phenomenological approach and non-linear stress-strain relationship. Models established on this approach neglect the intricate microstructural processes and are a combination of rheological models and empirical variables [1]. Lu *et al*. [2] argued that this time-dependent behavior associated with the creep mechanism of a rock mass cannot be explicitly captured by these phenomenological models. Even though studies were conducted on this phenomenon on a microscopic scale through laboratory creep tests. Most of these studies relied on empirical data and rock testing that does not clearly explain the actual rock mass behaviour undergoing the squeezing mechanism.

Furthermore, the numerical simulation conducted to describe this time-dependent behaviour in weak and/or soft rock formations mostly aims at describing it in the short-term. However, tunnels excavated in these rock formations experience large deformations over time which leads to critical tunnel instability. Thus, time-dependent analysis with the realistic representation of the creep phenomenon in numerical models is required for a better understanding of tunnel response in squeezing ground. Also, the time-dependent strength degradation of the rock mass and the accelerated creep phase initiation associated with creep damage should be considered in numerical simulations. The efficient process of these simulations requires equations and algorithms provided by constitutive models. However, the

conventional constitutive models developed and employed in earlier studies for creep simulation face limitations such as the explicit accelerated creep description. Hence, adequate knowledge of the time-dependent tunnel response in squeezing ground has not been fully explained.

Therefore, analysis of the time-dependent rock mass behaviour on an infinitesimal scale must be conducted to fully understand the squeezing mechanism and this can be achieved by employing viscoelasticity-viscoplasticity theory and creep damage mechanics. In this study, we will focus more on addressing the limitations associated with the analytical and numerical approach in estimating the tunnel time-dependent behavior characterized by creep.

1.2.1 Analytical approach

As mentioned earlier, the analytical formulations to date focus more on the phenomenological mechanism in circular tunnels and neglect other influencing factors. They are based on assumptions that neglect the influence of non-circular tunnel geometries, non-hydrostatic stress field in a rock mass that exhibits delayed viscoplastic shear failure responsible for squeezing. The tunnel ground response is dependent on the rock mass behaviour, linear for instantaneous reversible elastic behaviour and non-linear for irreversible behaviour characterized by elastoplasticity [3–7]. However, the irreversible time-dependent behaviour characterized by elasto viscoplasticity is not well-thought-out when employing these analytical solutions in squeezing tunnel stability analysis. Hence, they are not tailored for the tunnel ground reactions estimation associated with squeezing and its time-dependency. As such they cannot realistically predict irreversible viscoplastic strains characterized by delayed deformations responsible for the long-term response in squeezing ground. Therefore, an analytical solution able to estimate the time-dependent ground reaction in squeezing ground will be presented.

1.2.2 Numerical approach

The conventional constitutive models implemented in numerical simulation of squeezing ground assume isotropic deformation in a homogeneous rock material and fail to predict the initiation time of the accelerated creep. Furthermore, they are based on the integer-order derivative constitutive equations which neglect the power-law mechanism experienced by rock and rock masses when subjected to stress. As such they are incapable of the explicit accelerated creep description responsible for squeezing. Besides, squeezing is characterized by the rock mass discontinuities viscoplastic behaviour which they also neglect. Henceforth, understanding of the time-dependent tunnel response in weak heterogeneous rock formations with respect to the squeezing mechanism requires further improvement. Therefore, in this study viscoplasticity theory based on Perzyn's overstress function, fractional-order derivatives, fractal-order derivatives, and creep damage is applied to develop a time-based constitutive model. The model can explicitly capture the accelerated creep phase responsible for the time-dependent behavior associated with squeezing. The validation and calibration of this presented constitutive model are based on published creep test results.

In summary, the presented thesis improves the understanding of the appropriate tool employment for squeezing assessment and provide solutions that better represent the actual tunnel convergence in squeezing ground. This contribution to the understanding and realistic estimation of the squeezing mechanism will require addressing specific limitations of the conventional analytical and numerical tools:

- failure of the analytical solutions to estimate the time-dependent response of tunnels excavated in squeezing ground.
- failure of the constitutive models to explicitly estimate the accelerated creep phase and account for irrecoverable viscoplastic strains responsible for delayed deformations in squeezing ground.

Hence, in this thesis, the above limitations will be addressed by satisfying the aims listed in the proceeding section.

1.3 Research Aims and Objectives

The overall aim of this research is to develop an improved analytical solution and a constitutive model that will consider the time-dependent response of tunnels excavated in squeezing ground. In order to fulfill this, two research aims have been developed and listed below:

Aim 1: Improve the conventional analytical tools by presenting a closed-form analytical solution that will estimate delayed (time-dependent) convergence within non-circular tunnels excavated in squeezing ground. The following are the steps to achieve this first aim:

(1) To conduct a comparative analysis and identify the limitations of conventional analytical solutions.
(2) To formulate a closed-form analytical solution that will account for the confining stress effect and non-circular tunnel geometries on ground reaction.
(3) To formulate a closed-form analytical solution based on fractional-order derivatives that will consider the time-dependent ground reaction.
(4) To verify and implement the derived closed-form analytical solutions, estimate the tunnel ground reaction and appropriate support capacity in squeezing ground.

Aim 2: Derive and implement a time-dependent constitutive model for the explicit description of delayed deformations responsible for squeezing. The following are the steps to achieve this second aim:

(1) To derive constitutive equations to describe the power-law mechanism experienced by rocks and rock masses subjected to stress.
(2) To build a constitutive model based on the fractional-order and fractal-order derived constitutive equations.
(3) To calibrate and verify the derived constitutive equations using attained experimental data from literature and monitored tunnel convergence data.

(4) To implement the constitutive model in a finite volume numerical code, analyse a large scale tunnel layout and propose support structures required in squeezing ground.

1.4 Thesis outline

This thesis is organized into four (4) parts which consist of 7 chapters to achieve the aims stated above, this outline includes:

Part 1 of this study (Chapter 2), is an introduction that consists of a description of squeezing related deformations and their association with creep as well as limitations of the conventional techniques.

- The first section of Chapter 2 describes the time-dependent behaviour characterized by squeezing and its association with the 3-phase creep mechanism. It also outlines the major failure modes attributed to the time-dependent tunnel response experienced in squeezing ground.

- The second section of Chapter 2 discusses a comprehensive review centered on the analysis of the large deformation phenomenon observed in tunnels excavated in squeezing ground conditions. Evaluation of the conventional closed-form analytical solutions employed in the quantification of tunnel convergence associated with squeezing. It further evaluates these analytical tool's efficiency in ground response estimation and ground response-support interaction. Including their limitation when employed to estimate this time-dependent tunnel response.

- The third section of Chapter 2 is composed of a detailed review of the creep constitutive models proposed in the last 20 years and their theoretical framework. It also emphasizes the main assumption, limitations, and improvements that have been introduced for the time-dependent description of geomaterials. Most importantly focus on the creep constitutive models that have been employed successfully to simulate tunnels excavated in severe squeezing ground i.e. CVISC, SHELVIP, VIPLA, and Burgers constitutive models. Additionally, it acknowledges the use and limitation of this range of creep constitutive models. Further on, sums up a detailed review of viscoelastic viscoplastic theory, creep damage, and numerical modelling.

Part 2 studies the closed-form analytical solution derivation and implementation to estimate the ground reaction of tunnels excavated in squeezing ground. This part consists of Chapters 3 & 4 which outlines the derivation and verification of elastoplastic and elasto-viscoplastic closed-form solutions.

- Chapter 3 firstly details a conducted comparative investigation between the conventional analytical solutions developed for elastic and elasto-plastic ground reaction with the numerical solution. It relates the performance of employing analytical solutions with the numerical models for a chosen rock mass condition. Furthermore, verification of these analytical solutions is undertaken, and limitations are identified. Then a closed-form analytical solution for the elasto plastic ground reaction estimation is derived and proposed which addresses some of these limitations.

- Chapter 4 presents an improvement in the analytical solution's estimation of the time-dependent ground reaction characterized by the 3-phase creep mechanism. This enhancement is achieved by integrating the viscoplastic constitutive equation in a closed-form analytical solution. This solution based on fractional-order derivatives is further implemented in the convergence confinement methods (CCMs) and employed to estimate the time-dependent deformations. Hence, addresses the limitation of the CCMs in estimating delayed deformation characterized by the accelerated creep responsible for squeezing. It is further employed to quantify convergence and determine the appropriate support stiffness required for tunnel stability in squeezing ground.

Part 3, of this study, comprises Chapters 5 and 6, which involves the development of the creep constitutive models that consider the time-dependent behavior of geomaterials. This is achieved by employing the Perzyna viscoplastic theory, fractional-order derivative theory, fractal-order derivative theory and creep damage mechanics.

- Chapter 5 contains the development of the fractional-order derivative elastic-viscoplastic constitutive model neglecting damage as such does not explicitly capture the accelerated creep stage. Further on, it discusses the model validation with existing experimental data and verification using robust fitting of the monitored tunnel convergence data. The developed constitutive model is further implemented in a finite volume numerical code for potential tunnel squeezing mechanism simulation.

- Chapter 6 includes the development of an elastic-viscoplastic viscodamage constitutive model that considers isotropic damage for the explicit description of the accelerated creep phase. Validation, verification, and applicability of the constitutive model involve the creep parameter calibration with published experimental data and its numerical implementation through a user-defined subroutine written in object-oriented C++.

Part 4 consists of Chapter 7; it discusses the applicability of the proposed analytical solution in the estimation of the Nchanga Underground (NUG) tunnel convergence.

- Chapter 7 describes the tunnel convergence and support estimation in the NUG squeezing ground using the proposed analytical solution. This chapter further elaborates on the support design concept approved to accommodate large deformations that are expected to occur in squeezing ground. Additionally, the solution estimates ground support and reinforcement capacity, in terms of stiffness to restraining squeezing (resistance principle) or accepting a certain amount of deformation to avert the development of excessive squeezing (yielding principle).

Finally, the Conclusion (Chapter 8) summarizes the major findings, contributions, and limitations of the study as well as suggestions for further research.

Chapter 2. Literature review on squeezing mechanism and its estimation

Tunnel deformations due to squeezing ground conditions usually pose a significant challenge in the support structure set up, maintenance, and safety. Squeezing is generally described as a time-dependent cross-section area reduction of a tunnel as a result of induced stress and relatively weak surrounding rock mass parameters [8]. Squeezing can lead to large displacements such as floor heave and wall extrusion around tunnels essentially associated with the rock mass creep behavior [9], illustrated in Figure 2-1.

Figure 2-1. Squeezing in a tunnel at the NUG: (a) Crown sagging and (b) Floor heaving (Photos taken by the author).

Squeezing ground conditions has been a major challenge in tunnelling for civil and mining in weak rock mass relative to the induced stress field. It is usually not identified and predicted with the element of time at an early stage of tunnel operation [10]. Tunnelling under severe squeezing ground conditions is frequently associated with excessive rehabilitation, rock reinforcement, and support element failure (Figure 2-1a). Depending on the severity of the squeezing mechanism, significant investment in extra rock reinforcement and support installation and time-consuming rehabilitation is required to maintain the serviceability of tunnels [8,11,12]. When a tunnel is excavated in a high stressed rock mass a new stress redistribution occurs around the tunnel. The stress redistribution around the tunnel can lead to an increase in the magnitude of the deviatoric stresses, the increase of these deviatoric stresses induces

squeezing. Therefore, the study of this stress redistribution phenomenon is essential in the understanding of tunnel stability in squeezing ground.

The majority of case studies in squeezing ground conditions to date are based on circular tunnels in the weak rock, for instance, [13–20]. These researchers analyzed the squeezing mechanism in several tunnels and concluded that squeezing is the visco-plastic behaviour of rocks that can be predicted based on constitutive modelling and numerical analyses. According to their findings, the prediction of squeezing ground behaviour is based on rock mass strength and in situ state of stress. In deep underground tunnels, a few squeezing occurrences have been recorded as the mines continue to dig deeper. An example is the Blackwater mine of New Zealand which experienced severe squeezing behaviour in the 1940s [21]. In Australia, the Henty mine reported by [12], the Wattle Dam Gold Mine reported by Marlow and Mikula [22], the Perseverance mine in Kalgoorlie reported by Struthers *et al*. [23], and Rio Tinto's Argyle Diamond mine reported by Fernandez *et al.* [24] among others, report various cases of severe squeezing ground conditions. The Canadian Lapa and La Rhonde mines' squeezing ground conditions have been discussed by Mercier-Langevin and Hadjigeorgiou [25], Mercier-Langevin and Wilson [26], Karampinos, and Hadjigeorgiou [11] and Hadjigeorgiou [29]. The South African experience with squeezing is also described by Malan [30,31]. A further report was done in Zambia by Kabwe [33]. In this case, the Nchanga mine experienced severe squeezing conditions which led to the collapse and closure of most tunnels. The majority of tools used for the estimation of tunnel convergence due to squeezing are based on empirical and analytical formulations for circular tunnels in weak rocks [34]. This assumes that the rock mass behaves in a nearly isotropic manner, with this in mind the aim of this study is to develop a model capable of predicting squeezing potential before tunnelling. The model will take into account the time-dependent and anisotropic response of the heterogeneous rock mass as well as the influence of rheological properties of discontinuities and tunnel geometry in squeezing ground. The model is intended as an initial indicator of the squeezing potential and will potentially be used for the development and design of different support element strategies for tunnels. In this section, the description of squeezing as

a time-dependent mechanism associated with creep, conventional tools (empirical, analytical, and constitutive models) employed for tunnel convergence quantification in squeezing ground are discussed and their limitations outlined.

2.1 Squeezing mechanism

Tunnelling in the weak rock mass is often associated with swelling and/or squeezing which are time-dependent rock behaviours. These time-dependent rock mass responses are completely different but display the same large time-dependent tunnel convergence during and after excavation. The only difference between them is the aspect of material ground volume increment due to the other physical-chemical mechanism and most importantly water absorption. Squeezing is a time-dependent mechanism with the plastic flow (creep) of rock masses subjected to stress exceeding the shear stress limit. In actuality the definition of squeezing is associated with: non-linear time-dependent behavior, large support load, and or tunnel convergence and damage due to high-stress concentrations [9,35]. The definition of squeezing however has different versions in literature: for instance, Terzaghi [36] suggests that "squeezing is an advancement of the rock mass into the tunnel without a substantial volume increment before this is a high fraction of infinitesimal and sub infinitesimal particles of mica". A more general description of the phenomenological and mechanical aspects of both swelling and squeezing is provided by Gioda and Cividini [17]. They state that swelling is the time-dependent deformation with an increment in volume change due to an increase in water content and a reduction in volumetric effective stress whereas squeezing is an inward movement of the tunnel perimeter initiated by shear stress. Therefore, it can be generally accepted that squeezing is influenced by shear stress acting on the rock mass. A better definition of squeezing is to relate creep initiated by exceeding the shear stress limit and the deformation. This is clarified by Barla [9], defining squeezing as the time-dependent deformation around the tunnel boundary related to creep initiated by exceeding certain shear stress. The concentration of these shear stresses in the locality of the tunnel is usually characterized by limited volume changes [17].

Hence, Gioda and Cividini [17] define the squeezing phenomenon as the slow ground advancement to a tunnel's opening driven in soft squeezing rock without detectable fracturing or volume change. They further describe squeezing behaviour to be more prominent in tunnels driven in soft clay material at shallow depth. While in tunnels excavated in stiff clay and soft rock at greater depths, squeezing is displayed with a combination of raveling which is the constant inward deformation of the rock coupled with the separation of blocks from the tunnel roof and walls. Sterpi and Gioda [37] claim that the stress redistribution induced during tunnelling leads to the increase of deviatoric stresses around tunnels which further initiate squeezing an almost verbatim recapitulation of Barla's [9] definition of squeezing and this claim is further clarified by Malan [31]. Additionally, Malan [31] states that the occurrence of these stresses leads to non-revisable deviatoric creep strains which develop over time either at a constant or an increased rate referred to as the three creep stages and this constitutes the squeezing mechanism (Figure 2-2). The real particularity of squeezing phenomena is the time-dependent aspect of the rock mass behaviour. As such the process considers this aspect and is associated with creep the prime driver of this mechanism. The rock mass under these creep conditions undergoes a time-dependent deformation which is critical in the assessment of the long-term stability of tunnels and directly related to the stand-up time of unsupported tunnels [38–41].

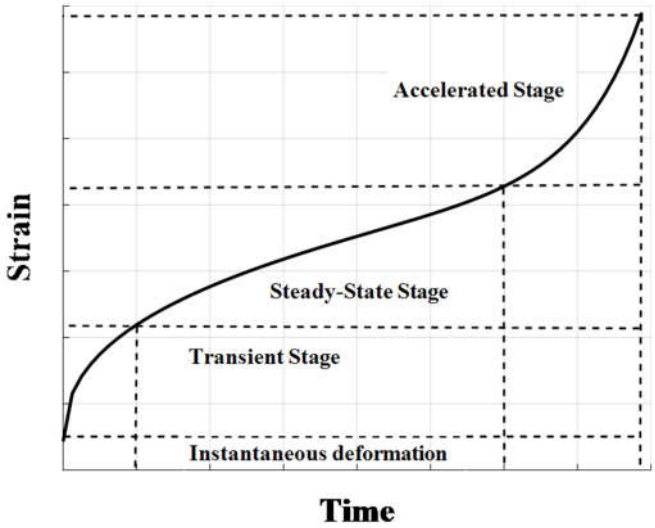

Figure 2-2. The characteristic curve of creep behaviour

The definition of the squeezing mechanism adopted within this study is one asserted by Barla [9] and Jimenez et al [35]. Identifying the driving mechanism associated with squeezing is important in determining the squeezing potential of underground tunnels. The general description of the three (3) major driving mechanism or failure modes associated with squeezing has been presented in the literature. These modes are a complete shearing failure that occurs within continuous ductile rock mass with widely spaced discontinuities, buckling failure occurs in thinly layered (thinly bedded sedimentary) rock masses and shearing and sliding occurs within thickly bedded sedimentary rock masses associated with sliding along bedding planes and intact rock shearing [13]. Figure 2-3 illustrates a schematic representation of the complete shear and buckling failure mechanisms.

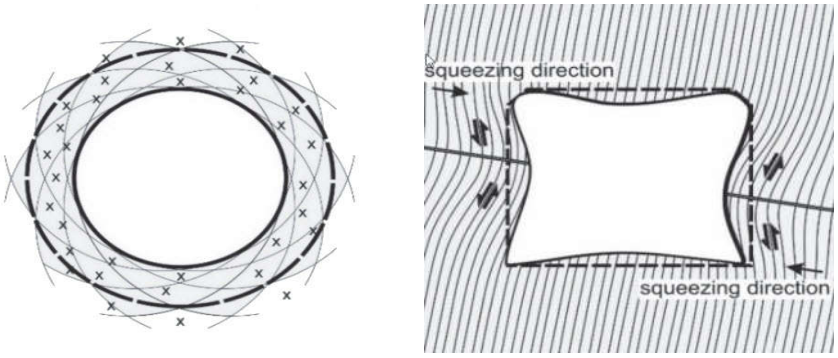

Figure 2-3. Squeezing failure: (a) Isotropic squeezing and (b) Anistropic squeezing

The squeezing mechanism depending on the above-mentioned modes can be either isotropic or anisotropic and we focus on shearing failure mode which is an isotropic squeezing mechanism.

2.2 Empirical, Analytical and Numerical techniques for squeezing prediction

2.2.1 Empirical methods

The main method used in the evaluation of tunnel vulnerability to the squeezing mechanism is an empirical analysis of circular tunnelling in weak rock and classification [13,19]. For instance, Jethwa *et al* [42] looked at squeezing quantification in terms of competency factor in their empirical approach which they defined as the ratio of the uniaxial compressive strength σ_{cr} of the rock mass to the overburden stress (Equation (2-1)).

$$N_c = \frac{\sigma_{cr}}{\gamma h} \tag{2-1}$$

Where: N_c is the competency factor, σ_{cr} is the uniaxial compressive strength (MPa), γ is the unit weight of the rock mass (kN/m^3) and h is the overburden height or depth (m). It was concluded that if N_c> 2.0 then squeezing will not occur. However, considering the effects of joints and fractures the relation was not accurate and thus it was redefined by incorporating the RMi proposed by Palmström [43];

$$N_c = \frac{\sigma_{cr} 0.2\sqrt{jC}\, Vb^D}{\sigma_\theta} \qquad D = 0.37 jC^{-0.2} \tag{2-2}$$

Where: N_c is the competency factor, jC is the joint condition factor, a combined measure for the joint size, joint roughness and joint alteration, Vb is the block volume (m^3) and σ_θ is the tangential stress (MPa). It can be deduced from the above formulation that the identification of potential squeezing occurrences is greatly influenced by the presence of rock structural features that most empirical formulations fail to consider. Aydan *et al.* [13] transformed Jethwa *et al* [42] competency factor idea into a concept based on the stress-strain relationship. The proposed levels to quantify squeezing are based on the tangential strain and elastic strain illustrated in Table 2-1. Their approach assumes hydrostatic

stress acting uniformly on the perimeter of a circular tunnel and only considers instantaneous squeezing. In addition to the competency factor idea, Singh *et al* [44] suggests that squeezing potential can be determined from the magnitude of the maximum tangential stress σ_θ acting on the boundary of a circular tunnel through their empirical analysis (Equation (2-3)). Further deduced that at failure the maximum σ_θ is related to the uniaxial compressive strength σ_{cr} of the rock mass and the depth of the excavation. They formulated the relation between the uniaxial compressive strength of a rock mass and the Tunnelling Index (Q) proposed by Barton *et al*. [45] (Equation (2-4)) and they suggest that the depth to anticipate squeezing conditions is greater than H (Equation (2-5)).

$$\sigma_\theta = 2\gamma H \tag{2-3}$$

$$\sigma_{cr} = 0.7\gamma Q^{1/3} \tag{2-4}$$

$$H = 350\, Q^{1/3} \tag{2-5}$$

Where: γ is the unit weight of the rock mass (kN/m^3). The relation is biased to circular tunnels as the magnitude of the tangential stress acting on a circular tunnel is different from that acting on a non-circular shaped tunnel. In a non-circular shaped tunnel, σ_θ acting on the boundary of the roof and walls is given by;

$$\sigma_\theta = (Ak - 1)P_v \text{ (roof)} \tag{2-6}$$

$$\sigma_\theta = (B - k)P_v \quad \text{(wall)} \tag{2-7}$$

$$k = {}^{P_h}/_{P_v} \tag{2-8}$$

Where: *A* and *B* are factors of the excavation geometry [46], *k* is the stress ratio, P_h is the horizontal stress (MPa) and P_v is the vertical stress *(*MPa*)*. It can be deduced from Hoek & Brown, [46] that the magnitude of the σ_θ acting on the roof will be higher than on the walls in a non-circular shaped tunnel. Hence, Singh *et al* [44] empirical formulation cannot determine the squeezing potential in non-circular

shaped tunnels accurately. It shows from Singh *et al* [44] interpretation of the influence of σ_θ on squeezing and Hoek and Brown [46] shape factor function, that geometry affects the tunnel convergence due to squeezing which most researchers neglect. The equation (2-5) for the prediction of squeezing potential is based on the Q-value, given the difficulties in estimating the Stress Reduction Factor (SRF), the empirical relation does not consider the actual geometrical features of discontinuities essential in squeezing prediction. Goel *et al*. [47] improved on this by eliminating the influence of SRF on Q and defined the rock mass number (N) defined as stress-free Q (SRF = 1) in the relation given by;

$$N = \frac{RQD\ J_r J_w}{J_n J_a} \tag{2-9}$$

$$H = (275\ N^{0.33}) B^{-1} \tag{2-10}$$

Where; RQD is the rock quality designation, J_n is the joint set number, J_r is the joint roughness number, J_a is the joint alteration number, J_w is the joint water reduction factor, H is the depth at which squeezing takes place (m) and B is the circular tunnel diameter (m). The approach seems to be a suitable empirical tool to address the stress situation by incorporating the overburden depth and tunnel dimension. However, the limitation of this approach is that it does not consider the influence of tunnel geometry. A recap on Jethwa *et al.* [42] competency factor idea, Hoek [19] used tunnel strain to define squeezing as suggested by Aydan *et al*. [13] and presents several levels of squeezing quantification based on strain induced by an unsupported tunnel in a rock mass with different values of the rock mass strength to hydrostatic pressure (Table 2-1). Their approach is also based on circular tunnels in an isotropic rock mass with a hydrostatic stress field seldom as simple as assumed. Quantification of squeezing potential suggested by Jethwa *et al*. [42] and Singh *et al* [44] was based on the comparison of the rock mass strength and induced stress. A slightly modified concept suggested by Aydan *et al*. [13] and Hoek [19] presented a comparison between the axial stress-strain response of laboratory rock samples and the tangential stress-strain response of rock around tunnels. Aydan *et al*. [13] and Hoek [19] modified the concept and made it easy to quantify the deformations due to squeezing because it relied directly on

strain increment. The quantification based on Hoek [19] defines a critical strain limit taken as 1%, above which support problems are most likely to occur due to squeezing. However, Singh *et al*. [20] observed that some tunnels which experienced strains as high as 4% did not display stability problems. They suggest critical strain not to be taken as 1% as it is entirely dependent on the intact rock material and joint rock mass properties and derived a correlation for critical strain in terms of the intact rock properties and modulus of deformation, represented as the squeezing index (*SI*) (Equation (2-11)).

$$SI = \frac{u_r}{a\varepsilon_{cr}} \tag{2-11}$$

Where: u_r is the radial closure (m), a is the tunnel opening radius (m) and ε_{cr} is the critical strain. The critical strain in Equation (2-11) is defined as a measure of tangential strain at the boundary of the tunnel. According to Hoek and Brown [46], the tangential strain will be different at diverse points on the tunnel boundary. Hence, tunnel geometry affects the measure of the tangential strain. However, Singh *et al*. [20] neglected this and assumed the tunnel to be circular with radius (a). The squeezing quantification levels based on many empirical approaches [13,19,20] are illustrated in Table 2-1 with the first three representing civil tunnels and the other mine tunnels.

Table 2-1. Classification for squeezing potential in tunnels [8].

	Aydan *et al.*, [13]		Hoek [19]		Singh *et al.*, [20]		Roache [12]	
	Squeezing level	Tunnel strain	Squeezing level	*SI*	Squeezing level	Tunnel strain	Squeezing level	Tunnel strain
1	Few support problems	$\varepsilon_t < 1\%$	No squeezing	$SI < 1.0$	No squeezing	$\varepsilon_\theta^a/\varepsilon_\theta^e \leq 1.0$	Few support problems	$\varepsilon_t < 2\%$
2	Minor squeezing problems	$1\% < \varepsilon_t < 2.5\%$	Light squeezing	$1.0 < SI \leq 2.0$	Light squeezing	$1.0\ \varepsilon_\theta^a/\varepsilon_\theta^e \leq 2.0$	Light squeezing	$2\% < \varepsilon_t < 5\%$
3	Severe squeezing problems	$2.5\% < \varepsilon_t < 5\%$	Fair squeezing	$2.0 < SI \leq 3.0$	Fair squeezing	$2.0 < \varepsilon_\theta^a/\varepsilon_\theta^e \leq 3.0$	Fair squeezing	$5\% < \varepsilon_t < 10\%$
4	Very severe squeezing problems	$5\% < \varepsilon_t < 10\%$	Heavy squeezing	$3.0 < SI \leq 5.0$	Heavy squeezing	$3.0 < \varepsilon_\theta^a/\varepsilon_\theta^e \leq 5.0$	Stripping zone	$10\% < \varepsilon_t < 20\%$
5	Extreme squeezing problems	ε_t >10%	Very heavy squeezing	$5.0 < SI$	Very heavy squeezing	$\varepsilon_\theta^a/\varepsilon_\theta^e > 5.0$	Post Striping Zone	$20\% < \varepsilon_t < 40\%$

2.2.2 Analytical methods

As mentioned earlier in Section 1.2, tunnel stability is dependent on the ability of the surrounding rock mass to undergo failure. Hence, this requires an adequate description of failure which is governed by failure criteria such as the simplest and widely employed MC yield criterion, among others. The MC yield criterion assumes the major principal stress (σ_1) as a linear function of only the minor principal stress (σ_3) neglecting the intermediate principal stress (σ_2) which is consistent with most triaxial tests ($\sigma_1 > \sigma_2 = \sigma_3$). However, the stress state ($\sigma_1 > \sigma_2 = \sigma_3$) does not depict the actual Earth's state of stress which is three-dimensional (3D) ($\sigma_1 \geq \sigma_2 \geq \sigma_3$). Even though, in excavation stability analysis, it is assumed that $\sigma_2 = \sigma_3$, the stress state close to tunnels and boreholes is usually in 3D [48]. Researchers [49–51] conducted true triaxial tests that represented the realistic 3D state of stress and concluded that σ_2 affects almost all aspects of rock failure. Hence, the employment of the MC, Hoek Brown (HB), and other two-dimensional (2D) failure criterion which neglects the effect of σ_2 are inappropriate for rock failure description in most cases. This brings back to the issue of employing analytical solutions that are governed by failure criteria that consider the effect of σ_2. However, conventional analytical solutions employed to quantify tunnel convergence due to squeezing are based on the CCM assumptions and most are governed by failure criteria that ignore the influence of σ_2. Their formulations are established on the initial hole-in-a-plate solution originally developed by Kirsch [52]. Since then several formulations have been modified and presented by Panet and Guenot [53], Duncan Fama [54] Carranza-Torres, and Fairhurst [4], Lee and Pietruszczak [55], Barbosa [57], and Vrakas and Anagnostou [7] among others. These solutions consider the ground reaction to the advancing tunnel face by a three-step analysis: (1) the Ground Reaction Curve (GRC) which relates in-situ stress to tunnel convergence; (2) the Support Reaction Curve (SRC) which relates deformation of the support pressure to the convergence; and (3) the Longitudinal Displacement Profile (LDP) which relates tunnel displacement to the position of the tunnel face.

To identify limitations in the use of these solutions, a preliminary comparative analysis is conducted between the solutions and numerical simulations on a circular tunnel. The numerical simulations employ elastic perfectly plastic constitutive models governed by different failure criteria (Drucker Prager (DP), MC, and HB) as well as a Softening Hardening Model (SHM). Figure 2-4 shows the results of this comparative analysis and it is drawn that numerical methods are more realistic with 30% more in tunnel convergence as compared to the CCM.

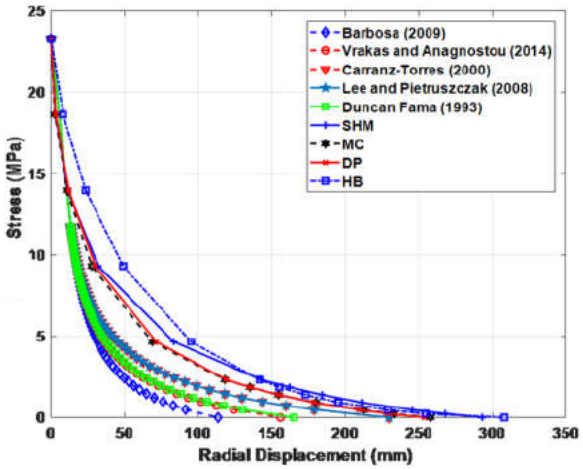

Figure 2-4. Comparison of the CCM and numerical ground reaction

Furthermore, a comparative numerical analysis conducted between a non-circular and a circular tunnel in an MC governed elastic-perfectly plastic model shows that a great deal of convergence occurs in a non-circular tunnel (Figure 2-5). It is drawn from the figure that the floor, crown, and walls convergence are 30%, 28% and 23% more compared to circular tunnel convergence.

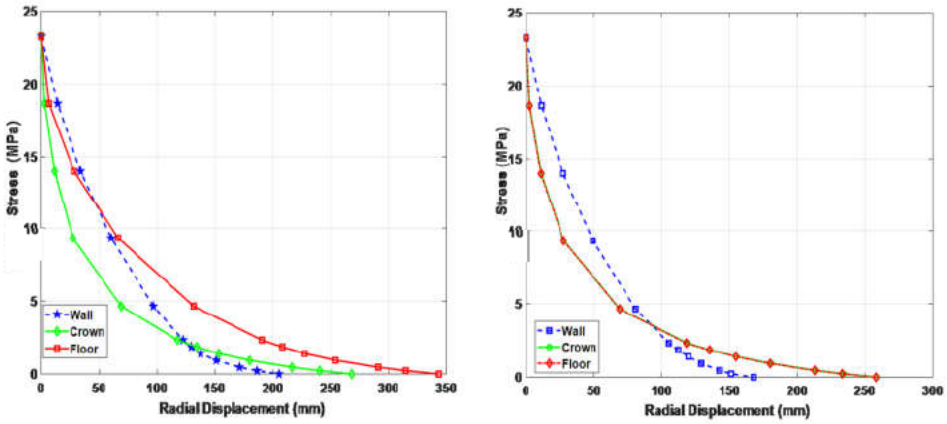

Figure 2-5. Boundary convergence: (a) horseshoe tunnel and (b) circular tunnel

Also, Bonini *et al* [58], Karampinos *et al* [28], Vlachopoulos and Diederichs [59] and others elaborate on the inaccuracies associated with the CCM approach, the commonly applied CCM does not estimate the time-dependent ground response associated with creep mechanism. The incapability of the CCM to deal with time-dependent ground reaction is explained by Paraskevopoulou & Diederichs [60] and Oke *et al*. [61]. As pointed out earlier, the analytical solutions discussed above are based on these assumptions as such cannot realistically quantify the squeezing potential in non-circular tunnels and its time-dependent behavior as well as account for the strengthening effect of σ_2.

2.2.3 Numerical methods

2.2.3.1 Rheological models

As pointed out in Section 2.1, when a rock mass is subjected to constant and sufficiently high stress over a long period it undergoes the 3-phase creep behaviour namely: transient, steady-state and accelerated creep which initiates squeezing [62]. Modelling of this mechanism is important in the assessment and prediction of the long-term stability of tunnels, a variety of theoretical and numerical approaches exist to represent this rock mass creep mechanism. They are divided into two categories: the phenomenological and micromechanics-based approaches. The phenomenological models are established on variables or a combination of elastic and viscous elements to form the Bingham, Burgers and Nishihara rheological models. Pan and Dong [63,64] conducted a study to model the rock mass time-dependent behaviour, they proposed a viscoelastic model which considered the rock mass as a homogenous and isotropic viscoelastic material. In their analysis they used a circular tunnel, they neglected the effects of normal stress on the axis of the tunnels and shear stress near the tunnel face. The model was incapable of handling non-circular tunnels in the heterogeneous and anisotropic material. Fakhimi and Fairhurst [65] further improved on this by presenting a continuum constitutive model capable of modelling a heterogeneous rock mass and predict the stand-up time. It is comprised of an MC non-associative elastoplastic model and traditional linear viscous substance illustrated in Figure 2-6. This rheological

model is characterized by the Kelvin shear modulus (G^K), the Kelvin viscosity (η^K) and governed by Equation (2-12).

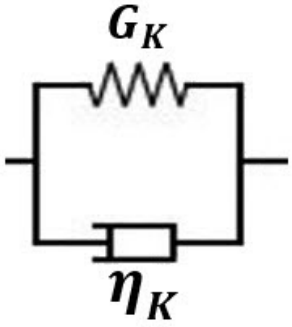

Figure 2-6. The viscous unit used in the visco-elastoplastic model [65].

$$\varepsilon_{ij} = \varepsilon_{ij}^{e} + \varepsilon_{ij}^{p} + \varepsilon_{ij}^{v} \tag{2-12}$$

Where ε_{ij} is the total strain, ε_{ij}^{e} is the elastic strain, ε_{ij}^{p} is the plastic strain and ε_{ij}^{v} is the vicious strain. In their analysis, the MC yield function and plastic potential were expressed as Equations (2-13) and (2-14) respectively.

$$f = 0.5(\sigma_1 - \sigma_3) + 0.5(\sigma_1 + \sigma_3)\sin\phi - c\cos\phi = 0 \tag{2-13}$$

$$g = 0.5(\sigma_1 - \sigma_3) + 0.5(\sigma_1 + \sigma_3)\sin\varphi \tag{2-14}$$

Where: σ_1 and σ_3 are the major and minor principal stresses while c , ϕ and φ are the cohesion, friction angle and dilation angle. However, Malan [31] argued that the Fakhimi and Fairhurst [65] model failed to determine the creep strain components in the accelerated creep phase. He pointed out that even though the model was successful in reproducing the stand-up time of the excavations its time-dependency was independent of the creep failure process. To overcome this limitation, he presented a viscoplastic model that assumed an intact rock behaving elastically, obeying the MC yield function to determine its failure strength represented by equation (2-15).

$$\varepsilon_{ij}^{vp} = \mu \langle f \rangle \frac{\partial g}{\partial \sigma_{ij}} \; for \; i = 1,2,3 \tag{2-15}$$

Where: μ is the fluidity parameter, σ_{ij} is the principal stress, g is the plastic potential function and f is the yield function. However, the presented model had its limitations such as failure to model the discontinuities in a rock mass leading to its strength reduction which was dependent on time and deformation. The strength reduction effect is usually observed in deep tunnels where the rock mass is more fractured and with time, leads to reduced cohesive strength in certain rock volumes [66]. Malan [66] assumed that the rate of cohesion reduction was proportional to the excessive stress above the residual limit.

$$C_c = k_c \langle f_{res} \rangle \tag{2-16}$$

In the equation (2-16) k_c is referred to as the cohesion decay factor and

$$f_{res} = \sigma_1 - \sigma_3 N_{\phi r} + 2C_r \sqrt{N_{\phi r}} \tag{2-17}$$

$$N_{\phi r} = \frac{1 + \sin \phi_r}{1 - \sin \phi_r} \tag{2-18}$$

Where: $N_{\phi r}$ is the residual target surface, C_r is the residual cohesion and ϕ_r is the residual friction angle. The model failed to perfectly capture the time-dependent behaviour of squeezing in deep tunnels mainly because of the influence of the rheological properties of discontinuities. Malan [31] further pointed out that in cases where discontinuities dominated, a different kind of modelling was more appropriate to simulate the rock mass behaviour. He later suggested a different approach to simulate the effect of these discontinuities and their associated creep and strongly advised the use of discontinuum viscoplastic models. Further interpretation of the influence of discontinuities on squeezing was conferred by Mercier-Langevin and Wilson [26] and Karampinos et al. [11,67]. Based on their experience at the LaRonde and Lapa mine. They observed and concluded that stress redistribution around the tunnel boundaries resulted

in the loading of the rock mass in a direction parallel to the foliation plane which leads to strength reduction by friction loss between the foliation planes. Also, Karampinos et al [11] pointed out that previous models faced limitations such as their inability to capture the buckling failure mechanism. In support of their claim, they used an approach suggested by Malan [31] to model a non-circular shaped tunnel in the LaRonde mine employed a perfectly plastic MC governed constitutive model to simulate the blocks and an elastic-plastic Coulomb slip failure to model the discontinuities. This discontinuum approach resulted in a better simulation of the role of fractures within the rock mass and the buckling mechanism. However, it faced considerable difficulties in obtaining an accurate numerical solution due to the MC failure surface's hexagonal shape on the π-plane convenient only when a selected side of the surface is used [68]. This deficiency can be eliminated by using a smoother Drucker-Prager failure criterion to approximate the numerical solution.

2.2.3.2 Time-dependent constitutive models

The conventional time-dependent constitutive models employed to capture squeezing are based on the general three-class type which includes:

- The burgers creep viscoplastic model [77–79] is based on the Kelvin and Maxwell component in the series. In this model, the Kelvin component is characterized by the shear modulus (G^K) and the viscosity coefficient (η^K) while the Maxwell component is characterised by the shear modulus (G^M) and the viscosity coefficient (η^M), illustrated in Figure 2-7. The Kelvin component in the model is responsible for the reversible transient creep and the Maxwell component for the irreversible viscoelastic strain in the steady-state creep phase [76].

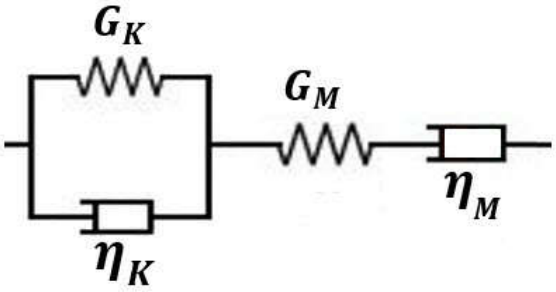

Figure 2-7. Schematic representation of the Burgers rheological model

- It can also be referred to as a time-dependent CVISC model when it couples a plastic flow rule based on the MC slider to consider rock failure. In the CVISC model, the Kelvin and the Maxwell components are characterized by G^K, η^K and G^M, η^M respectively while the MC slider is characterized by the cohesion (c), friction angle (ϕ), dilation angle (ψ) and tension cutoff (σ_t) illustrated in Figure 2-8;

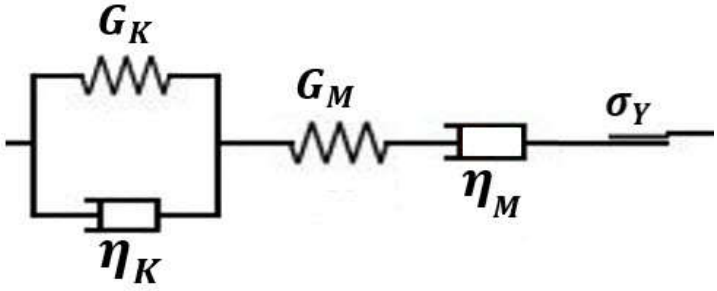

Figure 2-8. Schematic representation of the CVISC rheological model

- The VIPLA model is based on the viscoplastic flow rule and Perzyna [80] overstress theory to determine the viscoplastic strain rate. The viscoplastic strain is generated only when the magnitude of the deviatoric stress satisfies a yield criterion such as the DP [72,81]. The total strain constitutive formulation is given by:

$$\dot{\varepsilon}_{ij} = \dot{\varepsilon}^e_{ij} + \dot{\varepsilon}^{vp}_{ij} \tag{2-19}$$

Where: $\dot{\varepsilon}_{ij}$ is the total strain rate tensor, $\dot{\varepsilon}^e_{ij}$ is the elastic strain rate tensor and $\dot{\varepsilon}^{vp}_{ij}$ is the viscoplastic strain rate tensor which is determined by the flow rule:

$$\dot{\varepsilon}_{ij}^{vp} = \gamma\Phi(\langle F \rangle)\,\frac{\partial g}{\partial \sigma_{ij}} \tag{2-20}$$

Where: γ is the fluidity parameter, F is the overstress function, $\Phi(\langle F \rangle)$ is the viscous nucleus, σ_{ij} is the stress tensor and g is the plastic potential function.

- The SHELVIP (Stress Hardening Elastic Viscous Plastic) model is also derived from Perzyna's overstress theory, by adding a time-independent plastic component [82]. Splits the strain rate tensor into three components represented by:

$$\dot{\varepsilon}_{ij} = \dot{\varepsilon}_{ij}^{e} + \dot{\varepsilon}_{ij}^{p} + \dot{\varepsilon}_{ij}^{vp} \tag{2-21}$$

According to the conventional theory of elasto-plasticity, in this model the time-independent plastic strains ε_{ij}^{p} develop only when the stress point reaches the plastic yield surface $f_p = 0$, defined by the DP failure criterion given by:

$$f_p = (q - \alpha_p)(p - k_p) \tag{2-22}$$

The plastic strains ε_{ij}^{p} can be evaluated using the classical flow rule of elasto-plasticity given by:

$$\varepsilon_{ij}^{p} = \lambda\frac{\partial g}{\partial \sigma_{ij}} \tag{2-23}$$

Where λ is the plastic multiplier computed using the consistency condition.

Table 2-2 presents some creep constitutive models developed based on the three-class type and applied to analyze the time-dependent response of tunnels excavated in squeezing ground.

Table 2-2. The time-dependent constitutive models for squeezing tunnels.

Researcher	Constitutive model	Accelerated creep simulation	Structural features
Norton [83]	Two-Component Power Law	None	Neglected
Herrmann et al [84]	WIPP viscoelastic model	None	Neglected
Sjaardema & Kreig [85]	WIPP creep law model	None	Neglected
Callahan & DeVries [86]	Crushed Salt Model	None	Neglected
Lemaitre & Chaboche [87]	VIPLA	None	Neglected
Okubo & Fukui [88]	Okubo and Fukui model	Dependent on stress	Neglected
ITASCA [79]	CVISC model and Power Law VP model	Dependent on stress	Neglected
Sterpi & Gioda [37]	3-stage creep model	Dependent on stress	Neglected
Debernardi & Barla [89]	SHELVIP	None	Neglected
Weng et al [71]	Modified Burgers model	None	Neglected
Moghadam et al [72]	EVP model	None	Neglected
Tran et al [73]	Modified CVISC model	Dependent on stress	Considered
Causse et al [74]	Burger-creep VP model	None	Neglected
Fahimifar et al [75]	Modified 3-stage creep model	None	Neglected
Ofoegbu & Dasgupta [90]	FZK-INE creep model	Dependent on stress	Neglected
Sainoki et al [76]	Modified Okubo and Fukui model	Dependent on stress	Neglected
Zhang et al [91]	FVP model	Dependent on stress	Neglected

*Structural features: discontinuities, joints, and faults

The constitutive models outlined in Table 2-2 above can capture the transient and steady-state creep and to some extent the accelerated creep. However, the accelerated creep responsible for squeezing can be considered and captured by models that incorporate viscoplasticity and damage [76]. Most of these constitutive models assume isotropic deformation in homogeneous rock material and they cannot predict the time at the accelerated creep initiates.

It is also observed that the accelerated creep associated with rock failure responsible for squeezing can be characterized by the viscoplastic behaviour of structural features, which the conventional constitutive models neglect [73]. Tran *et al*. [73] suggested a model that included a single ubiquitous joint. However, it was based on the CVISC model which fails to explicitly capture the tertiary creep irrecoverable viscoplastic strains. Hence, failed to explicitly capture the time-dependent deformation in tunnels. Karampinos et al [11] confirmed this point in their study to capture buckling mechanisms using a numerical method. They concluded that the technique considers the influence of fractures contained by the rock mass. However, they used a perfectly plastic MC governed constitutive model which did not represent the actual viscoplastic behaviour of rocks subjected to squeezing.

2.3 Conclusion

This section aimed to provide a review of the existing tools to quantify squeezing and highlight their limitations. Tunnel design in squeezing ground requires the employment of a combined approach that considers analytical and numerical solutions. The analytical solutions proposed to estimate this ground deformation considers non-time dependent elastoplastic behaviour an exact opposite of the squeezing mechanism. However, engineers apply these tools with the above-stated limitation to quantify the squeezing mechanism. In line with this, an engineer should choose tools that replicate failure behaviour associated with the squeezing mechanism. From this review, it is possible to state that analytical and numerical solutions face limitations in quantifying deformation characterized by squeezing.

The squeezing mechanism considered in this study is associated with the isotropic shearing failure. Additionally, the time-dependent mechanism accounted for is that of an intact rock as opposed to rock mass with joints that play a major role in squeezing. Several time-dependent constitutive models and their numerical implements have been proposed. However, only those with a particular significance and specific assumption are mentioned in this section. It has also been clarified that most of these developed models neglect the power-law mechanism experienced by rock/rock masses.

References

[1] Challamel N, Lanos C, Casandjian C. Creep damage modelling for quasi-brittle materials. Eur J Mech A/Solids 2005;24:593–613.

[2] Lu Y, Elsworth D, Wang L. A dual-scale approach to model time-dependent deformation, creep and fracturing of brittle rocks. Comput Geotech 2014;60:61–76.

[3] E. Duncan Fama M. Numerical Modeling of Yield Zones in Weak Rock 1993:49–75.

[4] Carranza-Torres C, Fairhurst C. The elasto-plastic response of underground excavations in rock masses that satisfy the Hoek–Brown failure criterion. Int J Rock Mech Min Sci 1999;36:777–809.

[5] Alejano LR, Rodriguez-dono A, Alonso E, Fdez G. Ground reaction curves for tunnels excavated in different quality rock masses showing several types of post-failure behaviour. Tunn Undergr Sp Technol Inc Trenchless Technol Res 2009;24:689–705.

[6] González-Nicieza C, Álvarez-Vigil AE, Menéndez-Díaz A, González-Palacio C. Influence of the depth and shape of a tunnel in the application of the convergence–confinement method. Tunn Undergr Sp Technol 2008;23:25–37.

[7] Vrakas A, Anagnostou G. A finite strain closed-form solution for the elastoplastic ground response curve in tunnelling. International Journal for Numerical and Analytical Methods in Geomechanics. 2014;38(11):1131-48.

[8] Potvin, Y., & Hadjigeorgiou J. Ground support strategies to control large deformations in mining excavations. J South African Inst Min Metall 2008;108:397–404.

[9] Barla G. Squeezing rocks in tunnels. ISRM News J 1995;2:44–9.

[10] Varden RP, Woods MJ. Design approach for squeezing ground. Proc. Int. Semin. Des. Methods Undergr. Min., Australian Centre for Geomechanics; 2015, p. 489–504.

[11] Karampinos E, Hadjigeorgiou J, Hazzard J, Turcotte P. Discrete element modelling of the buckling phenomenon in deep hard rock mines. Int J Rock Mech Min Sci 2015;80:346–56.

[12] Roache B. Mining in extreme squeezing conditions at the Henty mine Mining in extreme squeezing conditions at the Henty mine 2016:0–13.

[13] Aydan O, Akagi T, Kawamoto T. The squeezing potential of rocks around tunnels; Theory and prediction. Rock Mech Rock Eng 1993;26:137–63.

[14] Cristescu N, Gioda G. Visco-plastic behaviour of geomaterials. Springer; 1994.

[15] Cristescu ND. Viscoplasticity of geomaterials. Visco-Plastic Behav. Geomaterials, Springer; 1994, p. 103–207.

[16] Ladanyi B. Time-dependent response of rock around tunnels. Anal. Des. Methods, Elsevier; 1995, p. 77–112.

[17] Gioda G, Cividini a. Numerical methods for the analysis of tunnel performance in squeezing rocks. Rock Mech Rock Eng 1996;29:171–93.

[18] Cristescu N, Hunsche U, Cristescu ND. Time effects in rock mechanics 1998.

[19] Hoek E. Big tunnels in bad rock - the 36 Karl Terzaghi Lecture. J Geotech Geoenvironmental Eng 2001;127:726–40.

[20] Singh M, Singh B, Choudhari J. Critical strain and squeezing of rock mass in tunnels. Tunn Undergr Sp Technol 2007;22:343–50.

[21] Pearson E. Thesis on the Blackwater Mine, Waiuta, New Zealand. University of Otago, Dunedin, 1946.

[22] Marlow P, and Mikula P. Shotcrete ribs and cemented rock fill ground control methods for stoping in weak squeezing rock at Wattle Dam Gold Mine 2013:133–48.

[23] Struthers MA, Turner MH, Mcnabb K, Jenkins PA. Rock Mechanics Design and Practice for Squeezing Ground and High Stress Conditions at Perseverance Mine. Proc Massmin 2000 2000;764:755–64.

[24] Fernandez F, Watt G, Ooi J. Strategic management for squeezing ground conditions at the Argyle Diamonds block cave project. Aust J Civ Eng 2012;10:193–206.

[25] Mercier-Langevin, F., & Hadjigeorgiou J. Towards a better understanding of squeezing potential in hard rock mines. Min Technol 2011;120:36–44.

[26] Mercier-Langevin, F., & Wilson D. Lapa mine-ground control practices in extreme squeezing ground. Proc. Seventh Int. Symp. Gr. Support, Mining and Underground Construction; 2013, p. 119–32.

[27] Karampinos, E., J. Hadjigeorgiou and PT. Management of squeezing ground conditions at LaRonde mine. 13th ISRM Int. Congr. Rock Mech., International Society for Rock Mechanics; 2015.

[28] Karampinos E, Hadjigeorgiou J, Turcotte P, Mercier-Langevin F. Large-scale deformation in underground hard-rock mines. J South African Inst Min Metall 2015;115:645–52.

[29] Hadjigeorgiou J, Karampinos E. Design tools for squeezing ground conditions in hard rock mines 2017:693–706.

[30] Malan DF. Time-dependent Behaviour of Deep Level Tabular Excavations in Hard Rock. Rock Mech Rock Eng 1999;32:123–55.

[31] Malan DF. Manuel Rocha medal recipient simulating the time-dependent behaviour of excavations in hard rock. Rock Mech Rock Eng 2002;35:225–54.

[32] AMC. Geological modelling and mineral resource evaluation, Nchanga underground Upper Orebody. Brisbane: 2007.

[33] Kabwe E. Mining Sequence Deformation and Failure Behaviour Analysis in the hangingwall and Orebody Rock Formations; A Continuum Approach. Geotech Geol Eng 2017;35.

[34] Gao F, Stead D, Kang H. Numerical simulation of squeezing failure in a coal mine roadway due to mining-induced stresses. Rock Mechanics and Rock Engineering. 2015;48(4):1635-45.

[35] Jimenez, R., and D. Recio. A linear classifier for probabilistic prediction of squeezing conditions in Himalayan tunnels. *Engineering geology* 121, 2011; 101-109.

[36] Terzaghi K. Introduction to tunnel geology. Rock Tunn with Steel Support 1946:17–99.

[37] Sterpi D, Gioda G. Visco-Plastic behaviour around advancing tunnels in squeezing rock. Rock Mech Rock Eng 2009;42:319–39.

[38] Gioda G. On the non-linear 'squeezing'effects around circular tunnels. Int J Numer Anal Methods Geomech 1982;6:21–46.

[39] Saari K. Analysis of plastic deformation (squeezing) of layers intersecting tunnels and shafts in rock. Doctoral dissertation, PhD Thesis. 1982.

[40] Akagi T, Ichikawa Y, Kuroda H, Kawamoto T. A non-linear rheological analysis of deeply located tunnels. Int J Numer Anal Methods Geomech 1984;8:457–71.

[41] Aydan Ö, Akagi T, Ito T, Ito J, Sato J. Prediction of deformation behaviour of a tunnel in squeezing rock with time-dependent characteristics. Proc Numer Model Geomech NUMOG V 1995:463–9.

[42] Jethwa JL, Singh B, Singh B. 28 Estimation of ultimate rock pressure for tunnel linings under squeezing rock conditions—a new approach. Des. Perform. Undergr. Excav. ISRM Symp. UK, 3–6 Sept. 1984, Thomas Telford Publishing; 1984, p. 231–8.

[43] Palmström A. Recent developments in rock support estimates by the RMi. Journal of Rock Mechanics and Tunnelling Technology. 2000;6(1):1-9.

[44] Singh B, Jethwa JL, Dube AK, Singh B. Correlation between observed support pressure and rock mass quality. Tunnelling and Underground Space Technology. 1992;7(1):59-74.

[45] Barton N, Lien R, Lunde J. Engineering Classification of Rock Masses for the Design of Tunnel Support 1974;6.

[46] Hoek E, Brown ET. Underground excavations in rock. 1980.

[47] Goel RK, Jethwa JL, Paithankar AG. Indian experiences with Q and RMR systems. Tunnelling and Underground Space Technology. 1995;10(1):97-109.

[48] Ma X, Rudnicki JW, Haimson BC. The application of a Matsuoka-Nakai-Lade-Duncan failure criterion to two porous sandstones. Int J Rock Mech Min Sci 2017;92:9–18.

[49] Haimson B. True triaxial stresses and the brittle fracture of rock. Pure Appl Geophys 2006;163:1101–30.

[50] Mogi K. Experimental rock mechanics. vol. 3. CRC Press; 2006.

[51] Ingraham MD, Issen KA, Holcomb DJ. Response of Castlegate sandstone to true triaxial states of stress. J Geophys Res Solid Earth 2013;118:536–52.

[52] Kirsch EG. The theory if elasticity and the need of the strength of materials (trans.). J Assoc Ger Eng 1898;42:797–807.

[53] Panet M, Guenot A. Analysis of convergence behind the face of a tunnel: Tunnelling 82, proceedings of the 3rd international symposium, Brighton, 7–11 June 1982, P197–204. Publ London: IMM, 1982. Int. J. Rock Mech. Min. Sci. Geomech. Abstr., vol. 20, Pergamon; 1983, p. A16.

[54] Duncan Fama ME. Numerical modelling of yield zones in rocks. Compr Rock Eng 1993;2:49–75.

[55] Lee YK, Pietruszczak S. A new numerical procedure for elasto-plastic analysis of a circular opening excavated in a strain-softening rock mass. Tunnelling and Underground Space Technology. 2008; 1;23(5):588-99.

[57] Barbosa RE. Analytical solution for a deep tunnel excavated in a porous elasto-plastic material considering the effects of seepage forces. In Proceedings of the 3rd CANUS rock mechanics symposium, Toronto 2009.

[58] Bonini M, Lancellotta G, Barla G. State of stress in tunnel lining in squeezing rock conditions. Rock Mech Rock Eng 2013;46:405–11.

[59] Vlachopoulos N, Diederichs MS. Appropriate uses and practical limitations of 2D numerical analysis of tunnels and tunnel support response. Geotechnical and Geological Engineering. 2014; 1;32(2):469-88.

[60] Paraskevopoulou C, Diederichs M. Analysis of time-dependent deformation in tunnels using the Convergence-Confinement Method. Tunn Undergr Sp Technol 2018;71:62–80.

[61] Oke J, Vlachopoulos N, Diederichs M. Improvement to the convergence-confinement method: inclusion of support installation proximity and stiffness. Rock mechanics and rock engineering. 2018; 1;51(5):1495-519.

[62] Takemura T, Oda M, Kirai H, Golshani A. Microstructural based time-dependent failure mechanism

and its relation to geological background. Int J Rock Mech Min Sci 2012;53:76–85.

[63] Pan YW, Dong JJ. Time-dependent tunnel convergence-I. Formulation of the model. Int J Rock Mech Min Sci 1991;28:469–75.

[64] Pan YW, Dong JJ. Time-dependent tunnel convergence-II. Advance rate and tunnel-support interaction. Int J Rock Mech Min Sci 1991;28:477–88.

[65] Fakhimi AA, Fairhurst C. A model for the time-dependent behavior of rock. Int J Rock Mech Min Sci 1994;31:117–26.

[66] Malan, D. Time-dependent Behaviour of Deep Level Tabular Excavations in Hard Rock . *Rock Mech Rock Engng* 1999; 32, 123–155.

[67] Karampinos E, Hadjigeorgiou J, Turcotte P. Discrete Element Modelling of the Influence of Reinforcement in Structurally Controlled Squeezing Mechanisms in a Hard Rock Mine. Rock Mech Rock Eng 2016;49:4869–92.

[68] Labuz JF, Zang A. Mohr-Coulomb failure criterion. Rock Mech Rock Eng 2012;45:975–9.

[69] Barla G, Bonini M, Debernardi D. Time Dependent Deformations in Squeezing Tunnels. 12th Int Conf Int Assoc Comput Methods Adv Geomech 2008:1–6.

[70] Pellet FL. Contact between a tunnel lining and a damage-susceptible viscoplastic medium. C - Comput Model Eng Sci 2009;52:279–95.

[71] Weng MC, Tsai LS, Liao CY, Jeng FS. Numerical modeling of tunnel excavation in weak sandstone using a time-dependent anisotropic degradation model. Tunn Undergr Sp Technol 2010;25:397–406.

[72] Nazary Moghadam S, Mirzabozorg H, Noorzad A. Modeling time-dependent behavior of gas caverns in rock salt considering creep, dilatancy and failure. Tunn Undergr Sp Technol 2013;33:171–85.

[73] Tran H, Jean M, Didier S, Billaux D, Abstr G, Mech IJR. Anisotropic Time-Dependent Modeling of Tunnel Excavation in Squeezing Ground. Rock Mech Rock Eng 2015:2301–17.

[74] Causse L, Cojean R, Fleurisson J-A. Interaction between tunnel and unstable slope – Influence of time-dependent behavior of a tunnel excavation in a deep-seated gravitational slope deformation. Tunn Undergr Sp Technol 2015;50:270–81.

[75] Fahimifar A, Karami M, Fahimifar A. Modifications to an elasto-visco-plastic constitutive model for prediction of creep deformation of rock samples. Soils Found 2015;55:1364–71.

[76] Sainoki A, Tabata S, Mitri HS, Fukuda D, Kodama J ichi. Time-dependent tunnel deformations in homogeneous and heterogeneous weak rock formations. Comput Geotech 2017;92:186–200.

[77] Pellet F, Roosefid M, Deleruyelle F. On the 3D numerical modelling of the time-dependent development of the damage zone around underground galleries during and after excavation. Tunn Undergr Sp Technol Inc Trenchless Technol Res 2009;24:665–74.

[78] S Sharifzadeh M, Tarifard A, Moridi MA. Time-dependent behavior of tunnel lining in weak rock mass based on displacement back analysis method. Tunnelling and Underground Space Technology. 2013; 1;38:348-56.

[79] Itasca Consulting Group Inc. Flac 5 Fast Lagrangian Analysis of Continua Manual 2005:3058.

[80] Perzyna P. Fundamental problems in viscoplasticity (in Polish). Mech Teor Stos 1963;1(2):3–30.

[81] Barla G, Debernardi D, Sterpi D. Time-dependent modeling of tunnels in squeezing conditions. Int J Geomech 2012;12:697–710.

[82] Debernardi D. Viscoplastic behaviour and design of tunnels. Turin Polytech Univ Turin 2008.

[83] Norton, Frederick Harwood. *The creep of steel at high temperatures*. No. 35. McGraw-Hill Book

Company, Incorporated, 1929.

[84] Herrmann W, Wawersik WR, Lauson HS. Analysis of steady state creep of southeastern New Mexico bedded salt. Sandia National Labs., Albuquerque, NM (USA); 1980.

[85] Sjaardema GD, Kreig RD. A constitutive model for the consolidation of WIPP [Waste Isolation Pilot Plant] crushed salt and its use in analyses of backfilled shaft and drift configurations. Sandia National Labs.; 1987.

[86] Callahan, G. D., and K. L. DeVries. *Analyses of backfilled transuranic wastes disposal rooms*. Sandia National Laboratories, 1991.

[87] Lemaitre, Jean, Jean-Louis Chaboche, Ahmed Benallal, and Rodrigue Desmorat. *Mécanique des matériaux solides-3e éd*. Dunod, 1996.

[88] Okubo S, Fukui K. An Analytical Investigation of a Variable- Compliance-type Constitutive Equation 2006;39:233–53.

[89] Debernardi D, Barla G. New viscoplastic model for design analysis of tunnels in squeezing conditions. Rock Mech Rock Eng 2009;42:259–88.

[90] Ofoegbu G, Dasgupta B. implementation of a creep model in FLAC to study the thermomechanical response of salt as a host repository medium—2nd progress report 2017.

[91] Zhang J-Z, Zhou X-P, Yin P. Visco-plastic deformation analysis of rock tunnels based on fractional derivatives. Tunn Undergr Sp Technol 2019;85:209–19.

Statement of Authorship

Title of Paper	Proposed solution for the ground reaction of non-circular tunnels in an elastic-perfectly plastic rock mass
Publication Status	☑ Published ☐ Accepted for Publication ☐ Submitted for Publication ☐ Unpublished and Unsubmitted work written in manuscript style
Publication Details	Eugie Kabwe, Murat Karakus, Emmanuel K. Chanda, Proposed solution for the ground reaction of non-circular tunnels in an elastic-perfectly plastic rock mass, Computers and Geotechnics, Volume 119,2020,103354, ISSN 0266-352X, https://doi.org/10.1016/j.compgeo.2019.103354.

Principal Author

Name of Principal Author (Candidate)	EUGIE KABWE		
Contribution to the Paper	Conceptualization, Formal analysis, Methodology, Investigation, Writing - original draft, Writing - review & editing and as the corresponding author		
Overall percentage (%)	80%		
Certification:	This paper reports on original research I conducted during the period of my Higher Degree by Research candidature and is not subject to any obligations or contractual agreements with a third party that would constrain its inclusion in this thesis. I am the primary author of this paper.		
Signature		Date	17/08/2020

Co-Author Contributions

By signing the Statement of Authorship, each author certifies that:

i. the candidate's stated contribution to the publication is accurate (as detailed above);

ii. permission is granted for the candidate in include the publication in the thesis; and

iii. the sum of all co-author contributions is equal to 100% less the candidate's stated contribution.

Name of Co-Author	MURAT KARAKUS		
Contribution to the Paper	Supervision of the work; Identification of the problem and methodology, reviewing & editing		
Signature		Date	18/08/2020

Name of Co-Author	EMMANUEL K. CHANDA		
Contribution to the Paper	Supervision, review & editing		
Signature		Date	18/08/2020

Chapter 3.

Proposed Solution for the Ground Reaction of Non-Circular Tunnels in an Elastic-Perfectly Plastic Rock Mass *(Paper 1)*

Eugie Kabwe, Murat Karakus, Emmanuel K Chanda

Published in Computer and Geotechnics

Abstract

The Convergence Confinement Method (CCM) is a solution typically employed for the preliminary evaluation of tunnel convergence and support suitability. The CCM represents stress relaxation on circular tunnel boundaries in the hydrostatic stress field and isotropic conditions. However, the CCMs employ yield criteria that neglect the intermediate principal stress as well as are not tailored for non-circular tunnels. This paper evaluates the CCMs for elastic-perfectly plastic (EPP) ground response in circular tunnels governed by the Mohr-Coulomb and Hoek-Brown criteria. Thereafter, presents an analytical solution that considers non-circular tunnels and the intermediate principal stress. This is achieved by the integration of an equivalent radius function and the circumscribed Drucker Prager yield criterion expressed by the stress Lode parameter. Furthermore, a numerical simulation is conducted in FLAC^{3D} to verify the presented solution with a native constitutive model for a chosen rock mass condition. The extent of the plastic zone and tunnel convergence predicted by the proposed solution is 10% and 4% more than the conventional solutions. Hence, the effect of the intermediate principal stress should be considered for accurate ground reaction estimation. The proposed solution can be used to predict tunnel convergence and design appropriate tunnel support structures.

Keywords: Analytical Solution; Drucker Prager; FLAC^{3D}; Stress Lode Parameter; Tunnel Convergence.

3.1 Introduction

There are issues related to the ground reaction response during tunnelling. One of these is the extent of tunnel convergence, which is essential for the design of the appropriate tunnel support system. The conventional and widely used methods to estimate tunnel convergence are the empirical, the analytical and the numerical methods. These methods are employed to predict and quantify the tunnel convergence and the pressure of the surrounding rock mass based on the in-situ state of stress [1]. The tunnel support system can be designed by using these approaches. The preliminary support design prefers using analytical and empirical methods and full analysis using numerical methods. Furthermore, analytical methods act as a quick verification tool for the numerical analysis and assessment of the ground-tunnel support interaction during tunnelling [2,3]. The CCM is one example of the existing analytical formulations used to quantify tunnel convergence. Several factors influence tunnel convergence including but not limited to (1) the initial state of stress, (2) rock mass mechanical properties, (3) method and tunnelling sequence, (4) tunnel support type and (5) tunnel cross-sectional area. The CCMs employed to estimate tunnel convergence have proved unreliable in obtaining accurate result of the interaction between tunnelling and ground reaction due to insufficient in-situ stress state information and the 3-dimensional (3D) nature of tunnels which require numerical analysis.

Tunnel convergence during tunnelling is a 3-dimensional (3D) procedure and the theory of the CCM takes the 3D aspect into account. However, modelling is done as an equivalent 2-dimensional (2D) process. The CCM reveals a correlation between the radial displacement and the natural support pressure acting on the tunnel boundary and analyses the ground interaction between this supporting pressure [4]. In the late 1930s, Fenner [5] presented a formulation to estimate the plastic zone extent around a circular tunnel in an EPP rock mass subjected to unvarying internal and far-field stress in-plane strain condition. The formulation did not consider cohesion in the elasto-plastic interface. Later on, Salencon [6] proposed an improved solution to the presented EPP analysis problem and it was further enhanced by Kastner [7]. In the past 30 years many researchers have made extensions and contribution to the work originally

presented by Fenner [5], Salencon [6] and Kastner [7], for example; [2,8–33]. However, the above-mentioned solutions are governed by the Hoek–Brown (HB), Mohr-Coulomb (MC) and Drucker Prager (DP) yield criteria that ignore the intermediate principal stress effect on the rock mass strength. The MC and HB yield criteria wholly ignore the intermediate principal stress effect. The DP, on the other hand, considers the intermediate principal stress influence but it is equated to the maximum and minimum principal stresses [11]. Shibata [34], Mogi [35] and Single et al [36] stated that the rock mass strength is wholly reliant on the intermediate principal stress which has the same effect as the confining stress and further suggested that the influence varies with the state of stress and material type. Additionally, all these studies except for Ng et al [20]are restricted to circular tunnels driven in an elastic brittle plastic, elasto-plastic with strain softening and hardening and EPP rock mass. Yu & He [37]proposed the Unified Strength Criterion (USC), a yield criterion that considers the maximum, intermediate and minimum principal stresses. Yu [38], Yu et al [39], Zhang et al [40], Xu & Yu [11,41], Zhang et al [42], Chen et al [43] and Ghorbani & Hasanzadehshooiili [44] later applied the criterion in their studies.

In this paper, the circumscribed DP yield criterion integrated with the stress Lode parameter is adopted to describe the ground response of a tunnel excavated in an EPP rock mass. The stress Lode parameter considers the influence of the intermediate principal stress on the rock mass yielding. Under plane strain conditions the analytical formulation is derived and presented to estimate the extent of the plastic radius, tunnel convergence and suitable tunnel support design in squeezing ground.

3.2 Convergence Confinement Method

The CCM considers ground reaction to the advancing tunnel face and is comprised of a three-step analysis: (1) the Support Characteristic Curve (SCC), (2) the Longitudinal Displacement Profile (LDP) and (3) the Ground Reaction Curve [9,24]. The CCM is based on a closed-form solution for a hole-in-a-plate [45]. The circular hole represents the tunnel subjected to uniform normal stresses σ_R and σ_0, acting on its internal and external walls. Plane strain conditions in an isotropic elastic-plastic rock mass are

normally assumed. Thus, a solution is computed in a rotationally symmetric procedure for the radial displacement (U_r) at the tunnel and plastic zone boundaries. The internal pressure (σ_R) as a function of U_r is referred to as the GRC. The SCC is attained in the same way as the GRC by plotting the internal pressure as a function of U_r.The intersection point of the GRC and the SCC describes the internal pressure and the U_r at equilibrium. The U_r at equilibrium, might exceed the elastic limit in that the rock mass undergoes plastic behaviour. Determination of the GRC using the CCMs requires the following assumptions:

- Homogenous material properties of the rock mass.
- Isotropic material law.
- Hydrostatic state of stress.
- Circular tunnel.
- Theory of 2D plane strain conditions.

However, the assumptions stated above are not realistic and a few analytical methods differ from these assumptions, such as the Feder and Arwanitakis [46] solution which employs oval cavity geometry for any state of stress in its computation. Additionally, the staged excavation process in discontinuous anisotropic non-linear rock mass conditions is usually ignored in the CCMs [2,47]. Bonini et al [48], Vlachopoulos and Diederichs [49], Rasouli et al [50] and Kabwe et al [51] further elaborate on the inaccuracies associated with the CCM approach.

3.2.1 Ground Reaction Curve

The CCM analysis approach is conducted by considering a section behind the tunnel face as an axisymmetric 2-dimensional plane strain problem. The tunnel face advance effect can be considered by applying a varying pseudo internal pressure (σ_R) on the tunnel boundary [19].

$$\sigma_R = (1 - \lambda)\sigma_0 \tag{3-1}$$

Where σ_0 is the in-situ stress and λ is the deconfinement ratio dependent on the distance from the tunnel face and λ varies between 0.0 and 1.0. Assume a cylindrical tunnel of the radius (R) excavated in a continuous, homogenous rock mass subjected to a hydrostatic stress field (σ_0). When the subjected σ_0 exceeds the surrounding rock mass strength, the plastic radius (R_P) develops and the surrounding rock mass is comprised of the elastic and plastic zone (Figure 3-1).

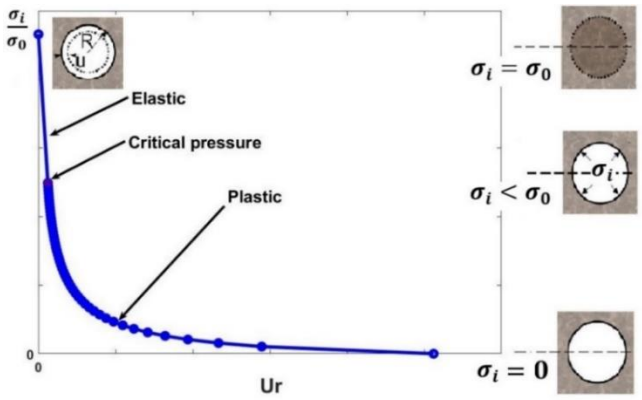

Figure 3-1. GRC of an elasto-plastic rock mass

When λ decreases in value the surrounding ground losses its confinement this leads to U_r convergence towards the centre of the tunnel. When σ_R decreases the surrounding rock mass behaves elastically up to a critical deconfinement ratio (λ_e) also referred to as the critical pressure (P_{cr}) in solutions by Duncan Fama [32], Carranza-Torres and Fairhurst [9] and Vrakas and Anagnostou [18]. Further σ_R reduction beyond λ_e, the rock mass yields plastically and the CCMs include the Duncan Fama [32] solution which considers an EPP material governed by the MC criterion. In the ground reaction analysis, the tunnel of radius R is subjected to σ_0 and σ_R. The surrounding rock mass undergoes plastic behaviour when the σ_R is less than the P_{cr} expressed as:

$$P_{cr} = \frac{2\sigma_0 - \sigma_{cm}}{1+k} \tag{3-2}$$

Where σ_{cm} is the uniaxial compressive strength of the rock mass and If σ_R is greater than P_{cr} the rock mass undergoes elastic behaviour and the inward radial elastic displacement U_e of the tunnel is given by:

$$U_e = \frac{R(1+v)}{E}(\sigma_0 - \sigma_R) \tag{3-3}$$

Where v is the Poisson ratio and E is the elastic modulus (MPa) and when σ_R is less than P_{cr} the plastic zone is formed around the tunnel with plastic radius (R_p) and the radial displacement U_p given by:

$$R_p = R\left[\frac{2(\sigma_0(k-1)+\sigma_{cm})}{(k+1)\big((k-1)\sigma_R+\sigma_{cm}\big)}\right]^{\frac{1}{(k-1)}} \tag{3-4}$$

$$U_p = \frac{R(1+v)}{E}\left[2(1-v)(\sigma_0 + P_{cr})\left(\frac{R_p}{R}\right)^2 - (1-2v)(\sigma_0 - \sigma_R)\right] \tag{3-5}$$

The Carranza-Torres and Fairhurst [9] solution employs the general form of the HB failure criterion on a tunnel of radius R exposed to the uniform far-field stress (σ_0) and σ_R. It is applicable to the EPP case and the σ_R and σ_0 can be scaled to give the scaled P_i and the far field stress S_0.

$$P_i = \frac{\sigma_R}{m_b\sigma_{cr}} + \frac{s}{m_b^2} \tag{3-6}$$

$$S_0 = \frac{\sigma_0}{m_b\sigma_{cr}} + \frac{s}{m_b^2} \tag{3-7}$$

where: s ,m_b are the rock mass parameters, the scaled critical internal pressure P_i^{cr} for which the elastic region is achieved and the actual p_i^{cr} are expressed by:

$$P_i^{cr} = \frac{1}{16}[1-(1+16S_0)^{0.5}]^2 \tag{3-8}$$

$$p_i^{cr} = \left[P_i^{cr} - \frac{s}{m_b^2}\right] m_b \sigma_{cr} \tag{3-9}$$

Provided that $\sigma_R \geq p_i^{cr}$ the relationship between the U_e and the P_i is given by:

$$U_e = R\frac{1+v}{E}(\sigma_0 - \sigma_R) \tag{3-10}$$

When the $\sigma_R < p_i^{cr}$ the R_p and the U_p is given by;

$$R_p = exp\left[2\left(P_i^{cr} - \sqrt{P_i}\right)^{0.5}\right] R \tag{3-11}$$

$$U_p = R\frac{1+v}{E_m}(\sigma_0 - p_i^{cr})\left[\frac{1-2v}{2}\frac{\sqrt{P_i^{cr}}}{S_0 - P_i^{cr}} + 1\right]\left(\frac{R_p}{R}\right)^2 + \frac{1-2v}{4(S_0 - P_i^{cr})}\left[ln\left(\frac{R_p}{R}\right)\right]^2 - \frac{1-2v}{2}\frac{\sqrt{P_i^{cr}}}{S_0 - P_i^{cr}}\left[2ln\left(\frac{R_p}{R}\right) + 1\right] \tag{3-12}$$

Vrakas and Anagnostou [18] proposed an explicit solution for the ground response that considers a linearly EPP behaviour obeying the MC yield criterion with a non-associated flow rule. If the $\sigma_R \geq P_{cr}$ the ground undergoes elastic behavior and elastoplastic if the $\sigma_R < P_{cr}$, the critical pressure at the onset of the elastic to plastic transition is given by.

$$P_{cr} = \frac{\zeta + 1}{(1 + \zeta\sigma_{cr})}\ \sigma_0 \tag{3-13}$$

where: ζ is the variable that is assumed to be unit for cylindrical openings, the expression for the elastic tunnel wall displacement is;

$$U_e = R\ \left[1 + \frac{\zeta E}{(1+v)(\sigma_0 - \sigma_R)}\right]^{-1} \tag{3-14}$$

The R_p is computed by considering the radial stress continuity condition at the elasto-plastic interface and the displacement are expressed by:

$$R_p = R\left(\frac{P_{cr}}{\sigma_R}\right)^{\left(\frac{1}{\zeta(\sigma_{cr}-1)}\right)} \tag{3-15}$$

$$U_p = \left[\frac{1+v}{\zeta}(\sigma_0 - P_{cr})\right]R_p \tag{3-16}$$

3.3 Evaluation of the performance and limitation of the CCM

In this section, an investigation on the performance of the CCMs developed for EPP ground behaviour is conducted. Furthermore, numerical analysis in FLAC^{3D} is presented to compare their performance for a chosen rock mass condition as well as using two different tunnel cross-sections in a hydrostatic stress field.

3.3.1 The ground reaction using analytical and numerical solutions

The analytical solutions are employed to estimate the tunnel face effect by analyzing the variation of the internal pressure acting on the tunnel peripheral with tunnel convergence, while pressure reduction method is used in the numerical analysis. To verify the analysis, the same rock mass parameters are adopted in all the solutions: [15,17,20,22,27]. It is observed from this analysis that the CCMs' and numerical GRC are not in close agreement (Figure 3-2 & Table 3-1). The analysis also draws that the CCMs only evaluates the EPP behaviour and underestimates tunnel convergence as compared to the numerical solution [51].

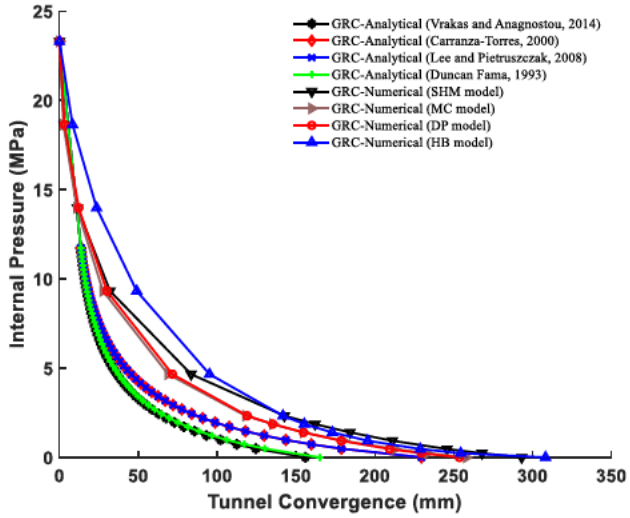

Figure 3-2. Ground reaction curves (analytical and numerical solutions)

Table 3-1. Results of the comparison between analytical and numerical solutions

Solution (Analytical/Numerical)	Plastic radius (m)	Convergence (m)
Analytical -Duncan Fama [32]	9.0	0.17
Analytical -Carranza-Torres [9]	10.5	0.23
Analytical -Lee and Pietruszczak [12]	10.5	0.23
Analytical -Vrakas and Anagnostou [18]	8.6	0.16
Numerical -MC model	10.0	0.26
Numerical -HB model	13.0	0.32
Numerical -DP model	12.0	0.25
Numerical -Soft-Hardening model (SHM)	12.5	0.28

Note: Circular tunnel radius = 5 m, σ_0 = 23 MPa

In unsupported tunnels, the CCM describes the reduction of internal pressure which results in convergence increment and plastic yield extension around an excavation. When supports are installed the support pressure is restrained until equilibrium is reached with the converging rock mass. Determination of the appropriate time for support installation requires the LDP developed for unsupported tunnels. Although convergence is restrained by support installed closer to the face, it may lead to support overload. On the contrary, when supports are installed further behind the advancing face. It results in a lower support pressure and substantial convergence occurrence leading to complete tunnel closure. Hence, a balance between early and late support installation is cardinal for the appropriate tunnel support design [53]. Figure 3-3 shows a comparison between the support load (p_{se}) at equilibrium estimated using the CCMs and numerical methods. It is observed that the support element installed closer to the face using numerical methods is subjected to higher p_{se} at equilibrium than when installed using the CCM's. This implies that the CCM underestimates p_{se} at equilibrium and estimation using the numerical solution shows that support system overload is imminent. Hence, the CCMs unrealistically estimate the required support capacity and location behind the tunnel face.

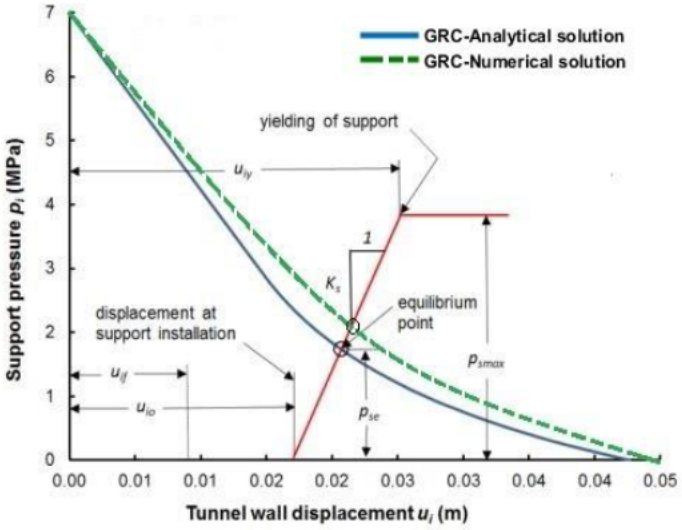

Figure 3-3. The GRC and SRC relationship between numerical and analytical solutions (modified after Duncan Fama [32])

As mentioned earlier the CCMs can only estimate the GRC for EPP rock mass and employ yield criteria that neglect the intermediate principal stress and can inaccurately determine the appropriate support capacity.

3.3.2 The ground reaction curves in the horseshoe and circular tunnels

In this section, an investigation of the tunnel cross-section effect on the ground response is conducted. In the evaluation, the estimated tunnel convergence within different cross-sections using an EPP constitutive model is compared.

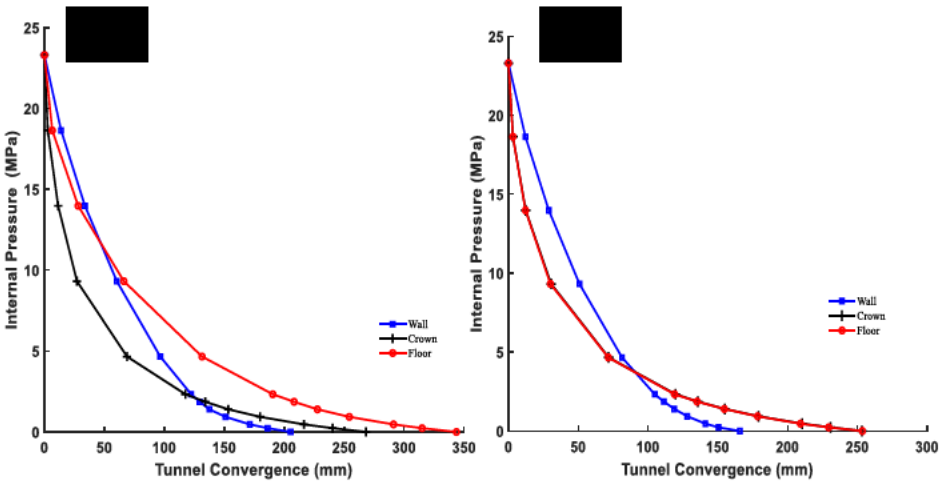

Figure 3-4. Ground reaction curves obtained from: (a) horseshoe and (b) circular tunnels

It is observed from Figure 3-4 that the overall convergence is greater in the horseshoe-shaped tunnel than the circular tunnel (Table 3-2). This Implies that the application of the CCM's tailored for circular tunnels would lead to inaccurate estimation of convergence within the horseshoe-shaped tunnel.

Table 3-2. The GRC results in the horseshoe and circular tunnel (MC numerical model).

Tunnel Geometry	**Average convergence**			**Maximum plastic radius (m)**	**Maximum convergence (m)**
	Roof (m)	**Wall (m)**	**Floor (m)**		
Circular	0.26	0.17	0.27	10.0	0.26
Horseshoe	0.28	0.21	0.34	12.4	0.34

As a result of these analyses, it is observed that the CCMs oversimplify ground conditions, stress-strain behaviour of the rock mass, excavation process and tunnel geometry. Therefore, in the proceeding section, an analytical solution for the ground response around tunnels is presented. The solution is derived in a hydrostatic stress state, isotropic and linearly EPP rock mass obeying the circumscribed DP yield criterion which integrates the stress Lode parameter.

3.4 Derivation of the solution governed by the Drucker Prager yield criterion

In this section, a solution for the estimation of tunnel convergence in an EPP rock mass is derived by incorporating the circumscribed DP yield criterion. As mentioned earlier the conventional solutions for convergence estimation are based on the MC and HB yield criteria which neglect the strengthening effect of the intermediate principal stress. Therefore, the stress Lode parameter [54] is integrated into the circumscribed DP yield criterion to account for the intermediate principal stress.

3.4.1 Strain condition and assumptions

We assume a cylindrical tunnel of R mined in a continuous, homogenous rock mass subjected to a hydrostatic stress field (σ_0). The stress equilibrium equation irrespective of body forces and under plane strain condition is expressed in polar coordinates by;

$$\frac{\partial \sigma_r}{\partial_r} + \frac{\sigma_\theta - \sigma_r}{r} = 0 \tag{3-17}$$

The relation between the radial (ε_r) and hoop (ε_θ) strains with u_r are expressed by

$$\varepsilon_r = \frac{\partial \Delta u_r}{\partial r} \tag{3-18}$$

$$\varepsilon_\theta = \frac{\Delta u_r}{r} \tag{3-19}$$

The total radial and hoop strains can be expressed as a sum of individual elastic and plastic components:

$$\varepsilon_r = \varepsilon_{re} + \varepsilon_{rp} \tag{3-20}$$

$$\varepsilon_\theta = \varepsilon_{\theta e} + \varepsilon_{\theta p} \tag{3-21}$$

In the elastic zone for $R > R_P$ the generalized Hooke's law is valid and the relationship between E, v, ε_r, ε_θ in plane strain conditions is given by;

$$\varepsilon_r = \frac{1+v}{E}[(1-v)\sigma_r - v\sigma_\theta] \tag{3-22}$$

$$\varepsilon_\theta = \frac{1+v}{E}[(1-v)\sigma_\theta - v\sigma_r] \tag{3-23}$$

3.4.2 Yield criterion and the Lode stress parameter

The MC yield criterion underrates the strength of the rock with increasing intermediate principal stress [55]. In this case, applying the circumscribed DP yield criterion will address this limitation expressed by:

$$f = \alpha I_1 + \sqrt{J_2} - k \tag{3-24}$$

Where

$$I_1 = \sigma_1 + \sigma_2 + \sigma_3 \tag{3-25}$$

$$J_2 = \frac{1}{6}[(\sigma_1 - \sigma_2)^2 + (\sigma_2 - \sigma_3)^2 + (\sigma_1 - \sigma_3)^2] \tag{3-26}$$

$$\alpha = \frac{2\,sin\,\phi}{\sqrt{3}(3 - sin\,\phi)} \tag{3-27}$$

$$k = \frac{6\,ccos\,\phi}{\sqrt{3}(3 - sin\,\phi)} \tag{3-28}$$

Where σ_1 , σ_2 and σ_3 are the major, intermediate and minor principal stresses respectively, c is the cohesion and ϕ is the internal frictional angle. Where I_1 is the principal stress invariant and J_2 is the second deviatoric stress invariant. The stress Lode parameter is then introduced to account for the intermediate principal stress influence [54];

$$\tau = \frac{2\sigma_2 - \sigma_1 - \sigma_3}{\sigma_1 - \sigma_3} \tag{3-29}$$

The σ_2, I_1 and J_2 are expressed in terms of the stress Lode parameter as:

$$\sigma_2 = \frac{1}{2}[\sigma_1(1+\tau) + \sigma_3(1+\tau)] \tag{3-30}$$

$$I_1 = \frac{1}{2}[\sigma_1(3+\tau) + \sigma_3(3-\tau)] \tag{3-31}$$

$$J_2 = \left[\frac{(\sigma_1 - \sigma_3)^2}{4}\left(1 + \frac{\tau^2}{3}\right)\right] \tag{3-32}$$

We can express the DP yield criterion in terms of the stress Lode parameter in polar coordinates by substituting Eqs (3-31) and (3-32) into Eq (3-24) to give;

$$\frac{(\sigma_r + \sigma_\theta)}{2}\left[\left(1 + \frac{\tau^2}{3}\right)^{0.5} - \frac{\alpha\tau}{2}\right] - \frac{3\alpha(\sigma_r + \sigma_\theta)}{2} - k = 0 \tag{3-33}$$

3.5 Analytical solution in an elastic-perfectly plastic medium

During the GRC and SCC interaction, the surrounding rock mass deforms elastically this completely mobilizes the rock mass self-bearing capacity. The process limits the development of excessive load on supports (yielding principle). When the tunnel converges its radius decreases towards the center, further convergence the surrounding rock mass satisfies the yield criterion and the plastic zone with R_p develops. R_p lies in the surrounding rock mass and beyond is the elastic zone.

3.5.1 Solutions in the Elastic Zone

The surrounding elastic zone has boundary conditions $(\mathrm{r} = R_P, \sigma_r = \sigma_R)$. Substitution of $\varepsilon_r = \varepsilon_{re}$, $\varepsilon_\theta = \varepsilon_{\theta e}$ from Eqs. (3-18) and (3-19) into Hooke's law Eqs. (3-22) and (3-23). Eliminating u_r from the equilibrium condition Eq (3-17) under the axisymmetrical condition and stresses can be expressed by;

$$\sigma_{re} = \left[1 - \left(\frac{R_P}{r}\right)^2\right]\sigma_0 + \sigma_R\left(\frac{R_P}{r}\right)^2 \qquad (\mathrm{r} \geq R_P) \tag{3-34}$$

$$\sigma_{\theta e} = \left[1 + \left(\frac{R_P}{r}\right)^2\right]\sigma_0 - \sigma_R\left(\frac{R_P}{r}\right)^2 \qquad (\mathrm{r} \geq R_P) \tag{3-35}$$

Hence, the radial deformation component of the elastic zone is expressed by;

$$u_e = \frac{1+v}{E}\left(\frac{{R_P}^2}{r}\right)(\sigma_0 - \sigma_R) \tag{3-36}$$

Where $\sigma_{re}, \sigma_{\theta e}, u_e$ are the radial stress, hoop stress and tunnel convergence in the elastic zone, respectively.

3.5.2 Solutions in the Plastic Zone

The circumscribed DP failure function expressed in polar coordinates (Eq (3-33)) is used to examine the plastic zone stress state. When the inner radius of the tunnel reduces the hoop and radial stress component are obtained by using the stress equilibrium equation (Eq (3-17)) and Eq (3-33) to get;

$$\sigma_{rp} = \left(\frac{r}{R}\right)^{\beta}\left(\sigma_R + \frac{\rho}{\beta}\right) - \left(\frac{\rho}{\beta}\right) \tag{3-37}$$

$$\sigma_{\theta p} = \left(\frac{r}{R}\right)^{\beta}\left[(\beta+1)\sigma_R + \frac{(\beta+1)\rho}{\beta}\right] - \left(\frac{\rho}{\beta}\right) \tag{3-38}$$

Where;

$$\beta = \frac{6\alpha - \left(1 + \frac{\tau^2}{3}\right)^{0.5}}{\left(1 + \frac{\tau^2}{3}\right)^{0.5} - \frac{\alpha\tau}{2} - 3\alpha} \tag{3-39}$$

$$\rho = \frac{2k}{\left(1+\frac{\tau^2}{3}\right)^{0.5} - \frac{\alpha\tau}{2} - 3\alpha} \tag{3-40}$$

Where σ_{rp}, $\sigma_{\theta p}$ are the radial stress and hoop stress in the plastic zone respectively. R_p is obtained from the stress acting on the elastic and plastic interface which satisfies the elastic and plastic zones stress condition. In the elastic zone, Eqs (3-34) and (3-35) are satisfied and we obtain:

$$\sigma_{re} + \sigma_{\theta e} = 2\sigma_0 \tag{3-41}$$

The stress magnitude also lies in the plastic zone and the DP yield criterion is also satisfied to give;

$$\frac{\left(\sigma_{rp}+\sigma_{\theta p}\right)}{2}\left[\left(1+\frac{\tau^2}{3}\right)^{0.5} - \frac{\alpha\tau}{2}\right] - \frac{3\alpha\left(\sigma_{rp}+\sigma_{\theta p}\right)}{2} - k = 0 \tag{3-42}$$

Equating the hoop stresses using Eqs (3-35) and (3-38), and the radial stresses using Eqs (3-34) and (3-37) $\left(\sigma_{re} = \sigma_{rp}, \sigma_{\theta e} = \sigma_{\theta p}\right)$. Thereafter, combining Eqs (3-41) and (3-42) one obtains the relation for the stress at the elastic-plastic interface by:

$$\sigma_{RP} = \sigma_0 - \frac{3\alpha\sigma_0 + k}{\left(1+\frac{\tau^2}{3}\right)^{0.5} - \frac{\alpha\tau}{2}} \tag{3-43}$$

This further calculates R_P in Eq (3-44) and radial stress σ_{RP} at the interface. R_p is obtained by adhering to the conditions $\left(R_p = R, \sigma_R = \sigma_{RP} = \sigma_{re}\right)$. Hence, using Eqs. (3-37), (3-38) and (3-43) we obtain the relation;

$$R_p = R\left(\frac{\sigma_{RP} + \left(\frac{\rho}{\beta}\right)}{\sigma_R + \left(\frac{\rho}{\beta}\right)}\right)^{\frac{1}{\beta}} \tag{3-44}$$

At the elastic and plastic interface, they tend to occur a displacement when $R_p = R$ estimated by the following relation;

$$u_r = \frac{1+v}{E} R_p \frac{3\alpha\sigma_0 + k}{\left(1 + \frac{\tau^2}{3}\right)^{0.5} - \frac{\alpha\tau}{2}} \tag{3-45}$$

When $R_p = R$ the tunnel boundary displaces plastically, the relation to estimating this displacement is obtained by an integration determined by the boundary conditions given by;

$$u_P = \frac{1+v}{E} \left(\frac{R_p^2}{R}\right) \frac{3\alpha\sigma_0 + k}{\left(1 + \frac{\tau^2}{3}\right)^{0.5} - \frac{\alpha\tau}{2}} \tag{3-46}$$

3.5.3 Determination of the Longitudinal Displacement Profile

There are several proposed empirical techniques to estimate the LDP. In this section, the LDP analysis is based on Vlachopoulos and Diederichs [56] solution in an EPP medium which considers the influence of the maximum plastic radius (R_m). The displacement at the tunnel face (U_{rf}) is expressed as:

$$U_{rf} = \left(\frac{U_{rm}}{3}\right) e^{-0.15\left(\frac{R_m}{R}\right)} \tag{3-47}$$

Where U_{rm} is the maximum tunnel displacement at R_m obtained from Eq. (3-46) by substituting R_P with R_m . R_m on the hand is obtained from Eq. (3-44) by equating $\sigma_R = 0$. The tunnel wall displacement ahead of the face $(X < 0)$ and behind the face $(X > 0)$ are computed by Eqs. (3-48) and (3-49) respectively:

$$U_{rX} = \left(\frac{U_{if}}{U_{rm}}\right) e^{\left(\frac{X}{R}\right)} \tag{3-48}$$

$$U_{rX} = 1 - \left(1 - \frac{U_{if}}{U_{rm}}\right) e^{\left(\frac{-3X}{R} \Big/ \frac{2R_m}{R}\right)} \tag{3-49}$$

Where U_{rX} is the tunnel wall displacement at distance (X) from the tunnel face.

3.5.4 Determination of the Support Characteristic Curves

The extent of the plastic zone and tunnel convergence can be controlled by the addition of an internal support pressure provided by a combination of Cable bolts, Steel sets and Shotcrete linings. If we assume that support elements are installed at a given distance behind the tunnel face, the tunnel convergence (U_{io}) at this point is obtained using the LDP. The tunnel support interaction with the tunnel inward convergence is partially dependent on the support element stiffness (K_s). The support element tends to yield at a given phase of tunnel convergence (U_{iy}) expressed by:

$$U_{iy} = U_{io} + U_{im} = U_{io} + \frac{p_{smax}}{K_s} \tag{3-50}$$

Where p_{smax} is the support element capacity and U_{im} is the maximum elastic deformation of the support element. Provided that the installed support element can hold the rock mass, its SCC will meet at an equilibrium point where the tunnel convergence is equal to the support yield. This defines the safety coefficient (FS) of the installed support expressed as:

$$FS = \frac{p_{smax}}{p_{se}} \tag{3-51}$$

The support element can be considered suitable for a tunnel if its safety coefficient is greater than the allowable limit: $FS \geq F_{s\,min}$. This entirely depends on the tunnel construction type i.e. mining or civil tunnels and permanent or temporal tunnels.

3.6 Verification and comparison of the proposed solution

The proposed solution verification is conducted using the conventional CCMs and numerical simulation within FLAC^{3D} [57] governed by the MC and DP yield criteria. The horseshoe-shaped tunnel excavated in isotropic, continuous and homogeneous material is considered for verification (Appendix 1 & 2). The numerical simulation is demonstrated using this excavation in the Upper Banded Shale (UBS) rock formation of the Nchanga Underground Mine (NUG) at a depth of 700 m with initial stress $\sigma_0 = 23\ \mathrm{MPa}$ [58,59]. The influence of the rock mass weight on the plastic zone and tunnel convergence is neglected and parameters used in the simulation are presented in Table 3-3. The assumptions, boundary and compatibility conditions of the numerical simulation are similar to the proposed solution.

Table 3-3. Nchanga UBS rock mass and geometrical parameters [51]

Geometrical parameters		**Mohr-coulomb**	
Specific weight (MN/m^3)	0.027	Cohesion (MPa)	1.28
Tunnel depth (m)	700	Friction angle (°)	26.6
Diameter (m)	10.0	Uniaxial compressive strength (MPa)	1.15
Rock Mass Parameters		**Drucker-Prager**	
Tensile strength (MPa)	0.05	Tensile Strength (MPa):	0.05
Global strength (MPa)	4.38	α parameter	0.4478
Modulus of deformation (MPa)	3193	k parameter	1.5534
v	0.20	Dilation parameter	0
G (MPa)	1330		
K (MPa)	1774		

3.6.1 Numerical verification

The proposed analytical solution is verified numerically using EPP constitutive models which employ the MC and DP yield criteria. Figure 3-5 draws a comparison of the proposed solution and the numerical ground response results. The agreement between the presented solution and the numerical GRC interpreted by the pressure stepwise reduction procedure is observed to be excellent.

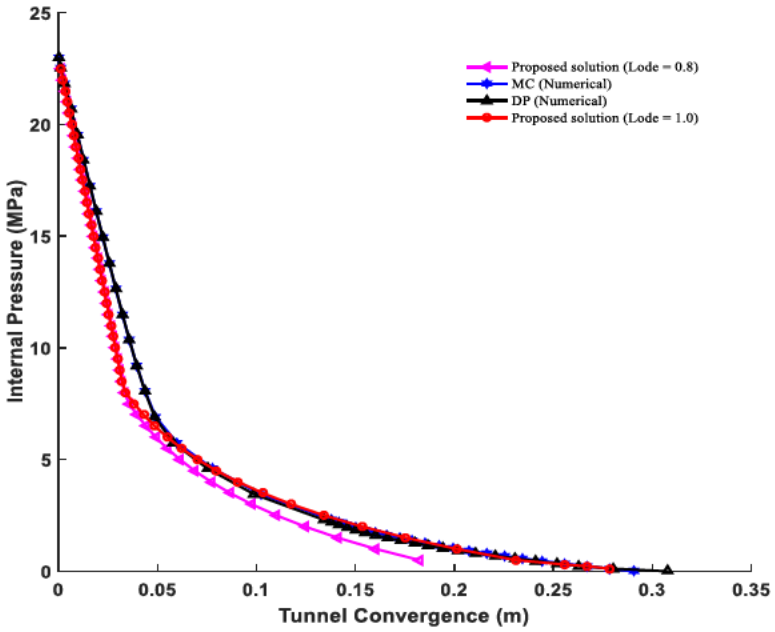

Figure 3-5. Ground response curves of the proposed and numerical solutions

The circumscribed DP yield criterion is adopted in the solution because it tends to overrate the rock mass strength due to the strengthening effect of the intermediate principal stress. It can estimate the rock mass strength more than other yield criteria using the same strength parameters $(\emptyset, c)$ [60] The results from this numerical verification indicate that considering the circumscribed DP criterion coupled with the stress Lode parameter as an appropriate criterion could lead to accurate tunnel convergence estimation.

3.6.2 Analytical verification

The preceding section (Section 3.6.1) verified the proposed solution with the numerical GRC. In this section, the solution is further compared with the MC and HB yield criteria governed CCMs.

3.6.2.1 Plastic zone and tunnel convergence

The Duncan-Fama [32], Fritz [28] and Carranza-Torres [61] analytical solutions are employed to verify the accuracy of the proposed solution. Figure 3-6 (a) illustrates the estimated plastic zone using the proposed solution ($\tau = 1.0$) and the conventional CCMs. The plastic zone extension is greater when estimated by the proposed solution as compared to other solutions and evolves with an increase in stress Lode parameter values (Table 3-4). The influence of τ values on tunnel convergence is also illustrated in Figure 3-6 (b) where tunnel convergence is represented by the abscissa and internal pressure by the ordinate.

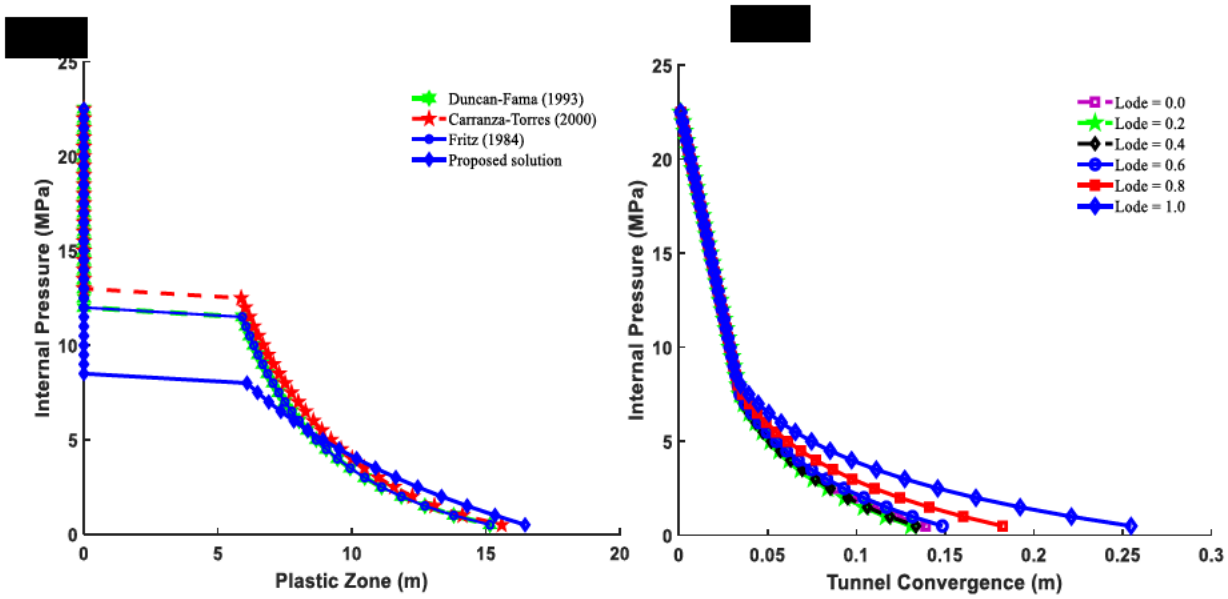

Figure 3-6. (a) Extent of the plastic zone and (b) ground reaction curves for different τ values

Table 3-4. Plastic zone radius and tunnel convergence: proposed (τ = 0.0 - 1.0) and numerical solutions

	Lode parameter (τ)						Numerical solution	
	0.0	0.2	0.4	0.6	0.8	1.0	MC	DP
Plastic radius (m)	11.85	11.41	11.53	12.23	13.71	16.46	16.56	16.60
Convergence (m)	0.14	0.13	0.13	0.15	0.18	0.27	0.28	0.31

The plastic zone extent predicted by the MC and HB yield criteria governed solutions and the proposed solution yield different results. Figure 3-6 (a) shows that the proposed solution's plastic zone extent is the largest since the circumscribed DP yield criterion overrates the magnitude of the hoop stress at failure hence leads to an extended plastic zone. Furthermore, Figure 3-7 draws a comparison of the tunnel convergence obtained by analytical and the proposed solution ($\tau = 1.0$).

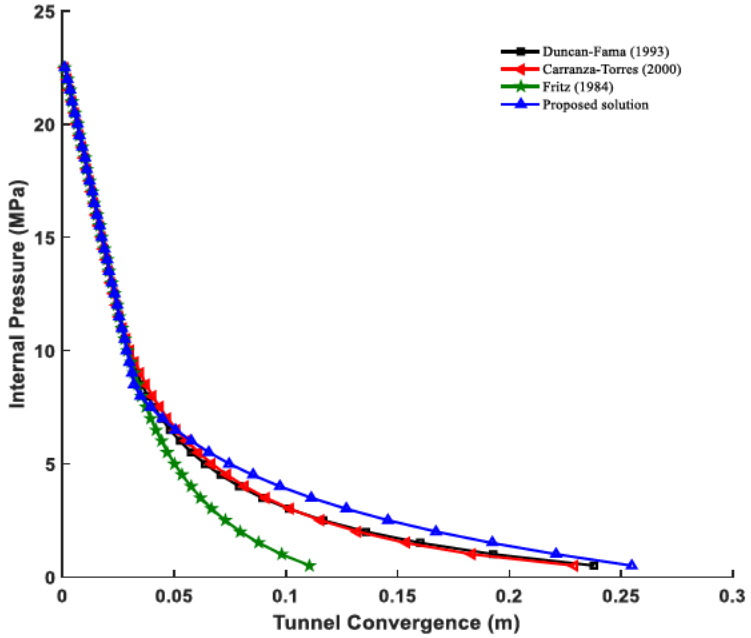

Figure 3-7. Comparison of the GRC from the proposed and analytical solutions

Figure 3-7 illustrates that the GRC attained from the conventional analytical and proposed solutions are not that close in agreement. It further shows that the proposed and Fritz [28] analytical solutions estimate the highest and lowest tunnel convergence respectively (Table 3-5).

Table 3-5. Estimation of the plastic zone radius and tunnel convergence

	Fritz [28]	**Duncan-Fama [32]**	**Carranza-Torres [9]**	**Proposed solution (τ = 1.0)**
Plastic radius (m)	15.00	15.15	15.60	16.46
Convergence (m)	0.11	0.24	0.23	0.27

Note: R_q = 5.8

3.6.2.2 Longitudinal Displacement Profile

Application of the CCMs in the design of an appropriate tunnel system requires the use of equations for the construction of the GRC, SCC and LDP. Eqs. (3-48) & (3-49) are used to construct the unsupported tunnel LDP for the proposed and conventional solutions (Figure 3-8). The attained curves from the analysis indicate that the maximum tunnel convergence occurs approximately 60 m behind the tunnel face and is zero at 20 m ahead of the face. Tunnel convergence at the face using the curves defined by the proposed and analytical solutions shows a range of 21% - 24% of the U_{rm} (Table 3-6 & Table 3-7). Figure 3-8 also shows that estimates determined by the proposed solution underrate the extent of tunnel convergence this results in an overestimation of the installed support load.

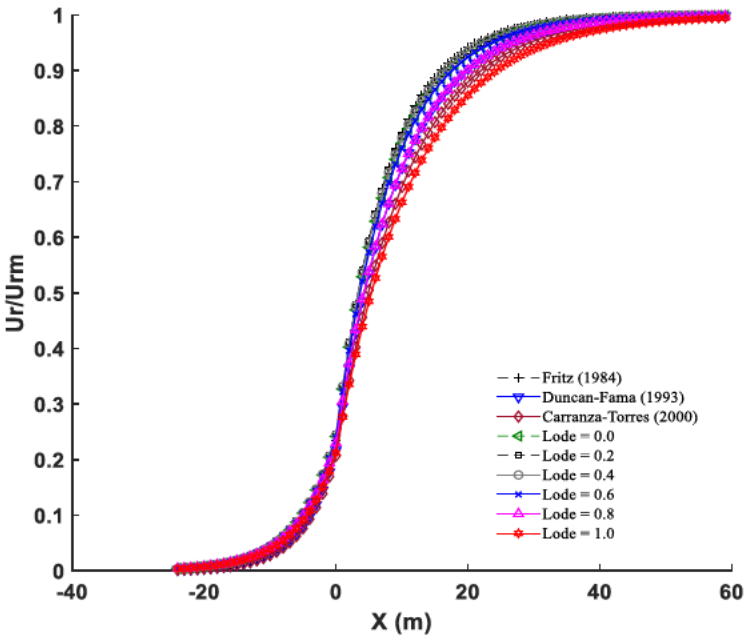

Figure 3-8. Comparison of the LDP from proposed and analytical solutions

Table 3-6. Scaled convergence at a normalized distance behind the tunnel face for different solutions

	Fritz [28]	Duncan-Fama [32]	Carranza-Torres [9]	Proposed solution (τ = 1.0)
X (m)	U_r/U_{rm}			
0	0.24	0.22	0.21	0.21
1	0.33	0.30	0.28	0.28
2	0.41	0.37	0.34	0.34
3	0.48	0.43	0.40	0.40
4	0.54	0.49	0.46	0.44
5	0.60	0.54	0.51	0.49

Table 3-7. Maximum plastic radius, tunnel and face displacement for different solutions

	Fritz [28]	Duncan-Fama [32]	Carranza-Torres [9]	Proposed solution (τ = 1.0)
R_m (m)	11.70	14.30	15.92	17.68
U_{rm} (m)	0.08	0.26	0.29	0.29
U_{if} (m)	0.02	0.06	0.06	0.06

3.6.2.3 Support Interaction Curves

The GRC and SRC interaction concept is used to determine and optimize the appropriate tunnel support system by considering the load imposed on the supports and tunnel convergence. The tunnel support system may be composed of one or more than one support element, depending on the extent of the plastic zone (failure zone) around the tunnel. In poor rock masses where the failure zone is extensive such that rock bolts cannot reach the stable zone a combination of support elements is needed to build up a support structure [62]. When the plastic zone extends beyond the depth of the rock bolts, they are used in a tightly spaced pattern to build up an artificial arch in the plastic zone. They are further coupled with cable bolts able to anchor into the stable rock mass beyond the plastic zone (**Figure 3-9**). In extremely poor rock masses, when the plastic zone is so extensive that cable bolts cannot reach the competent strata beyond the plastic zone and in time-dependent squeezing rock mass when it takes a long time for the plastic zone extension to stop. The employment of stiff external support coupled with cable bolts is more effective to restrict rock dilation in the plastic zone. Hence, in this section, a combination of steel sets, shotcrete lining and cable bolting is adopted to estimate the suitable support structure capacity for tunnels in squeezing ground.

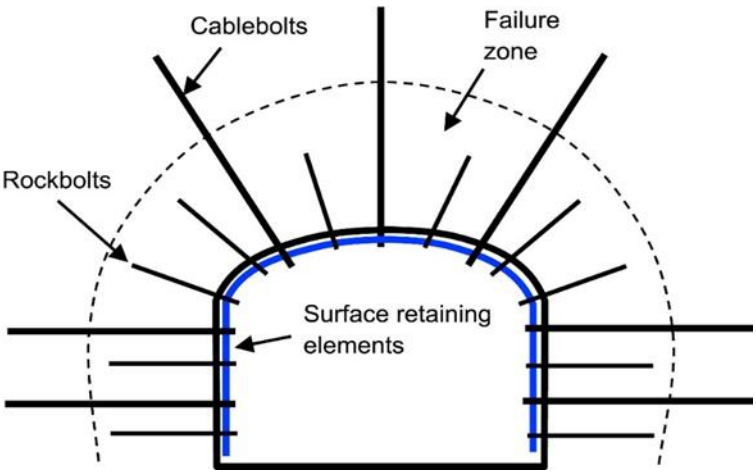

Figure 3-9. Principles of supporting tunnels in a weak rock mass (After [62])

In sections 3.6.2.3.1 & 3.6.2.3.2, estimation of the support capacity will first be assumed to act independently so that each support element-rock interaction is analyzed. Thereafter, a composite support structure GRC interaction is analyzed. The support elements, composite support structures and their capacity computations for the analysis are presented in Appendix 3.

3.6.2.3.1 Reaction of individual support elements

Steel sets, cable bolts and shotcrete linings are the primary support elements commonly used in tunnel design. The mechanical behaviour of these support elements is complex in that it considers the support element-rock mass interaction. The support element-rock mass interaction in tunnels is fully understood by applying the CCMs and equations that characterize the support elements together with their rock mass interaction concept. When these primary support elements are used, their stiffness, maximum acceptable pressure, maximum elastic displacement and maximum allowable failure displacement are computed by Eqs A56 – A61 (Appendix 3). In this section the GRC and the SCC are constructed based on the proposed and conventional solutions, the ground pressure expected to act on the support elements is determined as the intersection of both curves. The results of each expected pressure are then compared between solutions for instance Figure 3-10a shows support defined by the other solutions can be subjected to failure when applied using the GRC constructed by the proposed solution. This indicates that employing

solutions governed by yield criteria that ignore the intermediate principal stress in their formulation can unrealistically estimate the appropriate support capacity to restrain squeezing in tunnels. The conventional solutions underestimate the support load (p_{se}) at equilibrium and it is observed that 0. 3 m shotcrete thickness (t = 0.3 m) is inappropriate. While using the conventional solutions an estimated safety coefficient of 1.0 is observed. However, the steel sets and shotcrete (t = 0.5 m) are probably the most suitable with a safety coefficient of 1.6 and 1.2 respectively (Figure 3-10b & c).

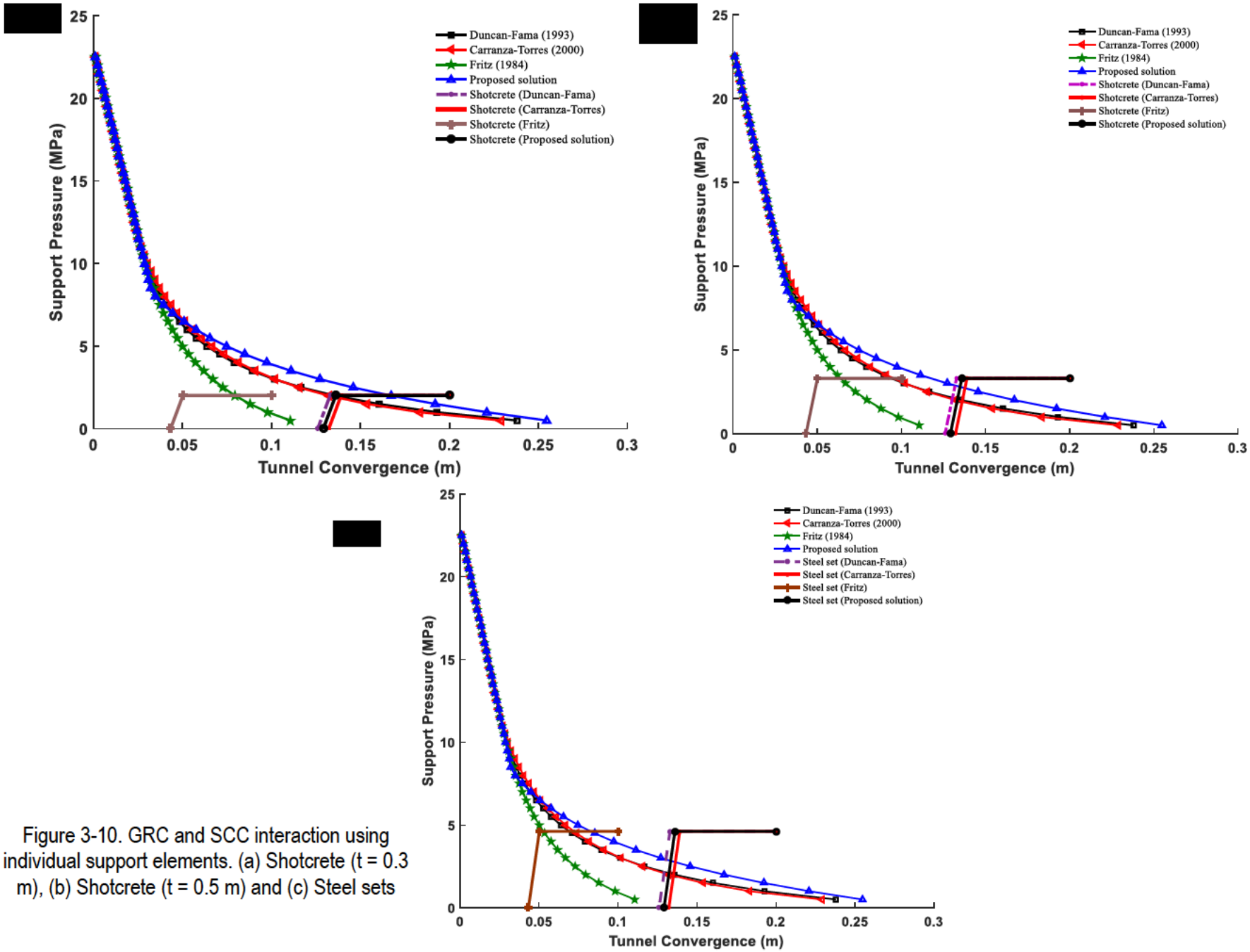

Figure 3-10. GRC and SCC interaction using individual support elements. (a) Shotcrete (t = 0.3 m), (b) Shotcrete (t = 0.5 m) and (c) Steel sets

3.6.2.3.2 Reaction of composite support structures

When more than one support elements are installed at the same distance behind the tunnel face, their accumulative effect is obtained by the addition of their stiffnesses for each support element. When steel sets and cable bolts are combined in a single application, it is assumed that the stiffness of their elements is:

$$K_{st} = K_{ss} + K_{sb} \tag{3-52}$$

Where K_{st} is the total support stiffness, K_{ss} and K_{sb} are the steel set and cable bolt stiffnesses respectively. The individual support element with low U_{im} is used to determine p_{smax} of the composite support structure:

$$U_{im} = \frac{p_{smax}}{K_{st}} \tag{3-53}$$

The composite support structures applied with their p_{smax} and K_{st} are presented in (Appendix 3). Figure 3-11 below shows the SCC effect of composite support structures SCCB (shotcrete + cable bolts), STSCCB (steel sets + shotcrete + cable bolts) and STCB (steel sets + cable bolts). The composite support structure considers shotcrete (t = 0.3 m), Steel sets and Cable bolts as the support alternatives for the tunnel problem. In Figure 3-11a the SCC of the SCCB support system indicates that it is subjected to failure when analyzed using the proposed solution. This implies that the use of this support combination is ineffective to restrict tunnel convergence. While for the same support structure the conventional solutions estimate a safety coefficient of 1.0. Further, an average safety coefficient of 1.63 is estimated on the STCB support system using the proposed solution (Figure 3-11b). The STCB support system is effective in restricting tunnel convergence but an increment of the safety coefficient will be more effective. Hence, the STSCCB support system is more appropriate and tunnel convergence is restricted by the

stiffer support elements in this system. The safety coefficient of the support elements and composite support structures estimated by the proposed and conventional GRC are presented in Table 3-8 & Table 3-9. There is an improvement in the safety coefficient after installing the composite support structures. The type of tunnel support structure setup is dependent on the allowable tunnel closure. To this regard, the STSCCB composite structure is recommended for permanent tunnels and the STCB is suitable for temporal tunnels. In this study, the STSCCB support structure is required.

Table 3-8. Safety coefficient of the conventional solution defined support structures

Solution	**Cable bolt**	**Shotcrete**	**Steel sets**
		Safety coefficient (*FS*)	
Duncan-Fama [32]	F	0.8	2.16
Carranza-Torres [9]	F	0.9	2.37
Proposed solution	F	F	1.61

Note: F = Support failure

Table 3-9. Safety coefficient of the proposed solution defined support structures

Solution	**Cable bolt**	**Shotcrete**	**Steel sets**	**SCCB**	**STCB**	**STSCCB**
			Safety coefficient (*FS*)			
Duncan-Fama [32]	F	1.0	2.16	1.1	2.2	3.0
Carranza-Torres [9]	F	1.0	2.37	1.1	2.4	3.4
Proposed solution	F	F	1.61	F	1.63	2.3

Note: F = Support failure

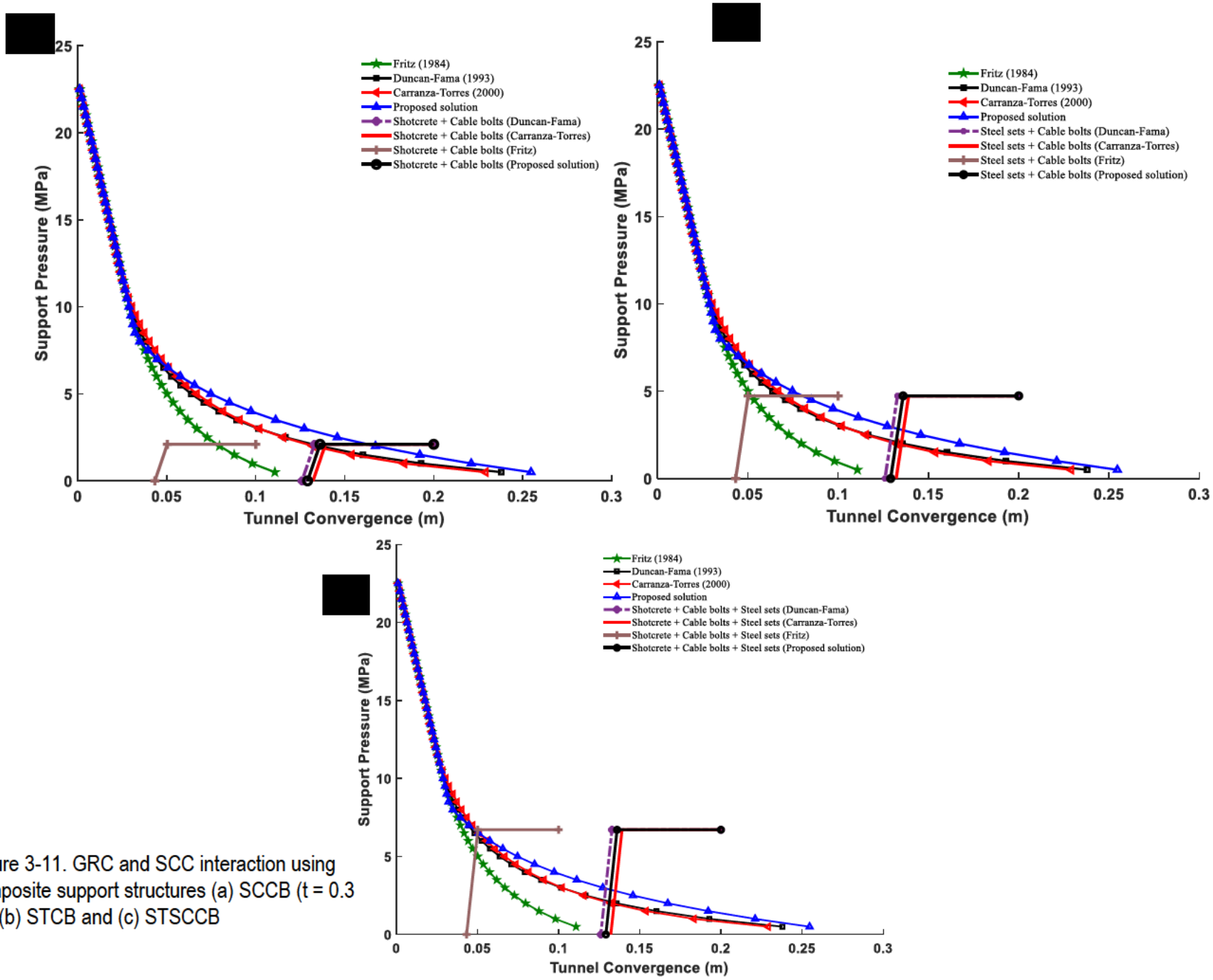

Figure 3-11. GRC and SCC interaction using composite support structures (a) SCCB (t = 0.3 m), (b) STCB and (c) STSCCB

3.7 Discussion

The accurate estimation of tunnel convergence and the ability to consider the intermediate principal stress effect on the rock mass strength are required for the suitable design of tunnels. Therefore, stability analyses using a more reliable and accurate analytical solution is essential. The CCM, as mentioned earlier in the introduction section is based on specific assumptions. Exploring one of these assumptions realistically creates a limitation in non-circular tunnel stability analysis. Hence, the paper addressed limitations pertaining to the CCMs by the inclusion of an equivalent radius function (Appendix 1).

The criteria used in these CCMs generally neglected the influence of the intermediate principal stress. However, it has been established through experimental tests that the rock and rock mass strength is dependent on the intermediate principal stress effect. Therefore, the real definition of the analytical solutions' strength parameters requires the consideration of the intermediate principal stress. This was addressed by the inclusion of the stress Lode parameter in the circumscribed DP yield criterion. Figure 3-6a & b further illustrates the significant effect of the intermediate principal stress on tunnel convergence. The plastic zone extension, tunnel convergence and support pressure all decrease with a decrease in the presented solution's stress Lode parameter. The significant variation in the results attained by employing different stress Lode parameter values indicates the importance of considering the intermediate principal stress effect in the CCM formulations.

Tunnel excavation effect simulation in the numerical code FLAC^{3D} is conducted by a pressure relaxation procedure to determine the confinement loss around the tunnel. The procedure is a stepwise reduction of tunnel internal pressure computing each step's ground response and drawing the displacement and plastic yield on the tunnel cross-section. This is attained by the FISH command "RELAX" within FLAC^{3D} which provides control over the unloading rate of the tunnel boundary. The internal pressure is relaxed in 40 relaxation steps to an end factor of 0.001 signifying 97.7% relaxation. Tunnel closure is then monitored by recording displacement histories at selected grid points around the tunnel boundary. In turn,

the recorded displacement histories are used to construct numerical GRC. Figure 3-5 illustrates the agreement between the presented solution GRC and the numerical GRC interpreted by the pressure stepwise reduction procedure to be excellent. Figure 3-6a and Figure A1 3a show that plastic yielding of the rock mass around the tunnel is influenced by its strength parameters, the initial state of stress as well as the confinement loss. Hence, an increase in the confinement loss necessitates plastic yield evolution which leads to an extension of the plastic radius.

Determination of the installed support structure located along a tunnel with respect to the GRC is a cumbersome process that requires the computation of the LDP. The significant aspect of support analysis is that the structures should be installed late enough to avoid support overload and early enough to restrain rock mass plastic yielding. Figure 3-10 & Figure 3-11 illustrate early support element installation at the face determined by the conventional CCMs is subjected to significantly higher load at equilibrium than delayed support installation. Consequently, leads to overloading and in some cases failure of the support elements (Table 3-8 & Table 3-9). It must be emphasized that delayed installation indicates equilibrium before the supports are overloaded. It is observed that the presented solution herein considers delayed support installation as compared to conventional CCMs.

It must be emphasized that the analysis conducted in section 3.6.2.3, is not focused on the yielding and/or resistance principles of the support elements but their installation timing and location. This is determined by the extent of tunnel convergence at which they are required to be installed. Hence, the comparison and analysis are based on the support structures with identical mechanical and physical properties. In conclusion, employing the same support structures at a different location along the tunnel in time determines their efficacy. This is quantified by their rock mass load-carrying capacity to restrain deformation within squeezing tunnels.

The presented solution offers a more realistic approach to estimate the installation timing and location of the support structures along a tunnel. Application of the conventional CCMs determined support

structures, installed along tunnels excavated in the Nchanga rock mass may be subjected to overloading and consequently support failure. The presented solution is a practical technique to adjust the support structure installation at a distance from the tunnel face in squeezing ground of the NUG.

3.8 Conclusions

The closed-form solution is presented for tunnel convergence and plastic zone estimation within an EPP rock mass. The solution is governed by the circumscribed DP yield criterion incorporating the stress Lode parameter. Accuracy verification of the presented solution was conducted using conventional CCMs and numerical simulation. The GRC attained from the presented solution was verified with the numerical simulation within FLAC^{3D} using the DP and MC yield criteria governed EPP models.

The verification shows that the presented solution agrees well with the numerical solution, signifying that it is fundamentally sound. The extent of the plastic zone and tunnel convergence predicted by the proposed solution is 10% and 4% more than predicted by the conventional analytical solutions respectively. The numerical verification indicates that considering the circumscribed DP yield criterion coupled with the stress Lode parameter as an appropriate criterion could lead to accurate tunnel convergence estimation in squeezing ground.

Tunnel support structure design based on the GRC and SCC equilibrium approach in squeezing ground is not a trivial task. However, optimizing this GRC and SCC equilibrium approach an appropriate tunnel support structure can be achieved. Results from the proposed GRC and SCC interaction shows that the STSCCB composite support structure (FS = 2.3) is more appropriate. The proposed GRC defined support structures can also lead to an increased safety coefficient if applied using conventional CCMs.

The advantages of the presented solution as compared to the others governed by the USC yield criteria is that it is applicable when computing convergence of a simple tunnel case, requires few parameters and variables. The USC governed solutions, on the other hand, require a long computational time, employ parameters and variables obtained from experimental tests.

This study indicates that the conventional CCMs which employ the yield criteria that neglect the intermediate principal stress unrealistically estimates the strength of the rock mass. Hence, yield criteria that consider the intermediate principal stress effect should be employed in analytical solutions for accurate ground reaction estimation. The proposed solution can be used to predict tunnel convergence and design appropriate tunnel support structures.

Appendix 1: Inclusion of the equivalent radius

The horseshoe cross-section tunnel with the dimension illustrated in Figure A1 1 is equivalent to the circular tunnel with radius R_q (equivalent radius), the radius is computed using the equal area method [63];

$$R_q = \sqrt{\frac{A}{\pi}} \tag{A54}$$

$$A = \frac{1}{2}\pi R^2 + LR \tag{A55}$$

Where A is the cross-section area, L is the height of the tunnel wall, π is the constant and the equivalent radius for the cross-section is 5.8 m, equivalent to a circular tunnel of radius 5.8 m.

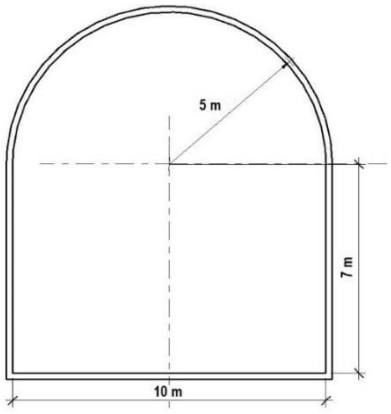

Figure A1 1. Layout of horseshoe cross section tunnel

Appendix 2: Numerical simulation

The functionality and accuracy of the proposed solution were verified in Section 3.6. The solution and numerical simulation employed in the verification both exhibit the same boundary and compatibility conditions. Figure A1 2 illustrates the 50 x 5 x 80 m symmetrical model constructed in FLAC^{3D} and it is designed to reduce the numerical simulation's computation time. The boundary and initial conditions of the model are set as; zero normal displacements at the bottom left and back boundaries respectively as well as the initial stress set at 23 MPa. It is constructed in 3D to consider the σ_2 assumed to act along the tunnel axis. σ_2 in the analysis is assumed to be equal to the mean tangential and radial stress.

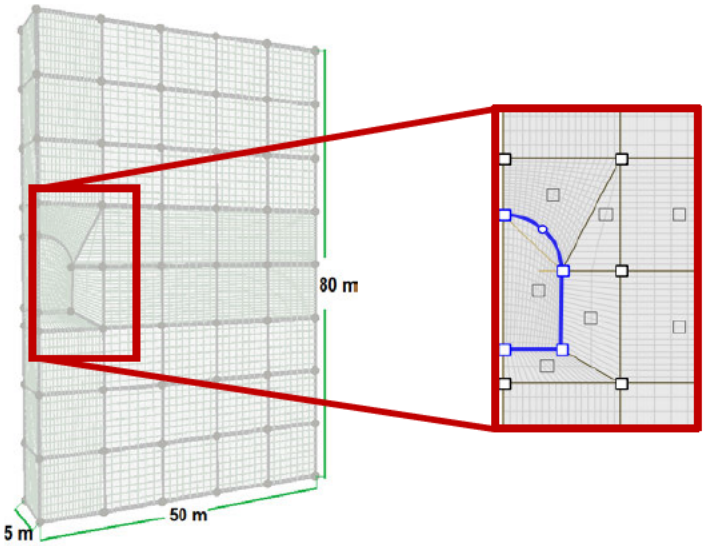

Figure A1 2. Layout of the FLAC^{3D} model

The material properties employed in the simulation are given in Table 3-2 with the circumscribed DP non-associated flow strength parameters given by Eqs (3-27) and (3-28). Figure A1 3 illustrates the results of the plastic zone extension and total tunnel convergence employing the EPP constitutive model governed by the MC yield criterion.

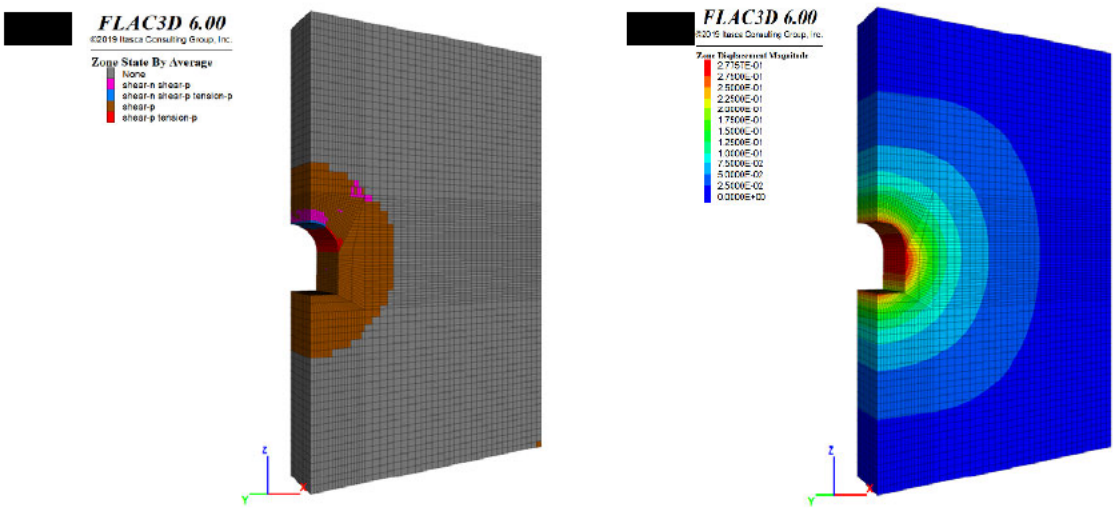

Figure A1 3. Tunnel estimation: (a) plastic zone extension and (b) total displacement

Appendix 3: Support capacity estimation

Estimation of the support capacity in tunnels subjected to a hydrostatic stress field, Brady and Brown [64] formulations for steel sets, cable bolts and shotcrete lining in tunnels are approved which are expressed by:

$$p_{ssmax} = \frac{A\sigma_{ys}}{\omega R} \tag{A56}$$

$$K_{ss} = \frac{E_s A}{\omega R^2} \tag{A57}$$

$$p_{scmax} = \frac{\sigma_{cc}}{2}\left[1 - \frac{(R-t)^2}{R^2}\right] \tag{A58}$$

$$K_{sc} = \frac{E_c(R^2 - (R-t)^2)}{2(1-v^2)(R-t)R^2} \tag{A59}$$

$$p_{sbmax} = \frac{T}{\omega_l R_c} \tag{A60}$$

$$K_{sb} = \frac{E_b \pi D^2}{4l\omega_l R_c} \tag{A61}$$

Where p_{ssmax} is the maximum steel set support pressure, A is the cross-section area, σ_{ys} is the yield strength of steel, ω is the set spacing along the tunnel, K_{ss} is the stiffness of the steel sets, E_s is the young modulus of the steel, p_{scmax} is the maximum shotcrete support pressure, σ_{cc} is the uniaxial compressive strength of the shotcrete, t is the thickness of the shotcrete, K_{sc} is the stiffness of the

shotcrete, p_{sbmax} is the maximum cable bolt pressure, T is the ultimate cable load, ω_l is the longitudinal cable bolt spacing, R_c is the circumferential cable bolt spacing, K_{sb} is the cable bolts elastic stiffness, E_b is the cable bolt young modulus, D^2 is the cable diameter and l is the free length of the cable bolt. In the formulations the following assumptions are considered; σ_{ys} = 245 MPa, ω = 1 m, σ_{cc} = 40 MPa and the supports are installed X = 4 m behind the face. Table A1 presents the support properties and computation of the support interaction curves one applies Eq. (3-50), where values of p_{ssmax} , K_{ss} and U_{io} are obtained from Table A1 1 and Table A1 2 and the results are presented in Table A1 3 and Table A1 4.

Table A1 1. Mechanical and geometrical characteristic of support elements

Steel sets (without wood blocks)				**Shotcrete**			
A	109.27 m²	p_{ssmax}	4.61 MPa	A	109.27 m²	p_{scmax}	2.02 MPa
E_s	207000 MPa	K_{ss}	672.38 MPa/m	E_c	30000 MPa	K_{sc}	286.29 MPa/m
σ_{ys}	245 MPa	p_{smax}/K_{ss}	0.0069 m	σ_{cc}	40 MPa	p_{scmax}/K_{s}	0.0070 m
R	5.8 m			R	5.8 m	v	0.2
ω	1 m			t	0.3 m		
Shotcrete							
A	109.27 m²	p_{scmax}	3.30 MPa	A	109.27 m²	p_{scmax}	6.30 MPa
E_c	30000 MPa	K_{sc}	486.39 MPa/m	E_c	30000 MPa	K_{sc}	1025.72 MPa/m
σ_{cc}	40 MPa	p_{scmax}/K_{sc}	0.00679 m	σ_{cc}	40 MPa	p_{scmax}/K_{s}	0.00614 m
R	5.8 m	v	0.2	R	5.8 m	v	0.2
t	0.5 m			t	1.0 m		
Cable bolts							

T	0.354 MN	l	14 m		
ω_l	1.0 m	R	5.8 m		
R_c	1.0 m	p_{sbmax}	0.354 MPa		
E_b	207000 MPa	K_{sb}	13.424 MPa/m		
D	0.034 m	p_{scmax}/K_{sb}	0.02637		

Table A1 2. Tunnel convergence at a distance behind the tunnel face for different solutions

	Fritz [28]	**Duncan-Fama [32]**	**Carranza-Torres [9]**	**Proposed solution (τ = 1.0)**
X (m)		U_{io}		
1	0.026	0.077	0.081	0.081
2	0.033	0.095	0.0995	0.0986
3	0.038	0.111	0.117	0.116
4	0.043	0.126	0.132	0.129
5	0.048	0.139	0.146	0.143

Table A1 3. Support characteristic curve computations

	Steel sets		**Shotcrete**					
			0.3 m		**0.5 m**		**1.0 m**	
	MPa	m	MPa	m	MPa	m	MPa	m
Duncan-Fama [32]	4.61	0.2	2.02	0.2	3.3	0.2	6.3	0.2
	4.61	0.133	2.02	0.133	3.3	0.133	6.3	0.132
	0	0.126	0	0.126	0	0.126	0	0.126
Fritz [28]	4.61	0.1	2.02	0.1	3.3	0.1	6.3	0.1

	4.61	0.050	2.02	0.050	3.3	0.050	6.3	0.050
	0	0.043	0	0.043	0	0.043	0	0.043
Carranza-Torres [9]	4.61	0.2	2.02	0.2	3.3	0.2	6.3	0.2
	4.61	0.139	2.02	0.139	3.3	0.139	6.3	0.138
	0	0.132	0	0.132	0	0.132	0	0.132
Proposed solution	4.61	0.2	2.02	0.2	3.3	0.2	6.3	0.2
	4.61	0.136	2.02	0.136	3.3	0.136	6.3	0.135
	0	0.129	0	0.129	0	0.129	0	0.129

Table A1 4. SCC parameters for Individual support elements

Support	p_{smax} **(MPa)**	K_s **(MPa/m)**	U_{im}**(m)**
Shotcrete (t = 0.3 m)	2.02	286.29	0.0070
Shotcrete (t = 0.5 m)	3.30	486.39	0.00679
Steel set	4.61	672.38	0.0069
Cable bolt	0.35	13.42	0.02637

Table A1 5. SCC parameters for composite support structure

Support	p_{smax} **(MPa)**	K_{st} **(MPa/m)**	U_{im}**(m)**
Shotcrete (t = 0.3 m) + Cable bolt	2.10	299.714	0.0070
Shotcrete (t = 0.5 m) + Cable bolt	3.39	499.814	0.0068
Steel set + Cable bolt	4.73	685.804	0.0069
Shotcrete (t = 0.3 m) + Cable bolt + Steel set	6.71	972.094	0.0069

Table A1 6. Displacement results at support-GRC equilibrium points for Individual support elements

			Fritz [28]	Duncan-Fama [32]	Carranza-Torres [9]	Proposed solution (τ = 1.0)
	U_{io}		0.043	0.126	0.132	0.129
Shotcrete	U_{iy}	0.3 m	0.050	0.133	0.139	0.136
		0.5 m	0.050	0.133	0.140	0.136
		1.0 m	0.050	0.132	0.138	0.135
Cable Bolt	U_{iy}		0.070	0.152	0.159	0.156
Steel sets	U_{iy}		0.050	0.133	0.139	0.136

Table A1 7. Displacement results at GRC-SCC equilibrium points for composite support structure

		Fritz [28]	Duncan-Fama [32]	Carranza-Torres [9]	Proposed solution (τ = 1.0)
	U_{io}	0.04	0.13	0.13	0.13
Shotcrete (t = 0.5 m) + Cable bolt	U_{iy}	0.05	0.13	0.14	0.14
Shotcrete (t = 0.3 m) + Cable bolt	U_{iy}	0.05	0.13	0.14	0.14
Steel set + Cable Bolt	U_{iy}	0.05	0.13	0.14	0.14
Shotcrete (t = 0.3 m) + Cable bolt + Steel set	U_{iy}	0.05	0.13	0.14	0.14

3.9 References

[1] Pan, Y. W., & Dong, J. J. (1991). Time-dependent tunnel convergence-I. Formulation of the model. *International Journal of Rock Mechanics and Mining Sciences And*, *28*(6), 469–475.

[2] Gschwandtner, G. G., & Galler, R. (2012). Input to the application of the convergence confinement method with time-dependent material behaviour of the support. *Tunnelling and Underground Space Technology Incorporating Trenchless Technology Research*, *27*(1), 13–22.

[3] Karakus, M. (2007). Appraising the methods accounting for 3D tunnelling effects in 2D plane strain FE analysis. *Tunnelling and Underground Space Technology*, *22*(1), 47-56.

[4] González-Nicieza, C., Álvarez-Vigil, A. E., Menéndez-Díaz, A., & González-Palacio, C. (2008). Influence of the depth and shape of a tunnel in the application of the convergence–confinement method. *Tunnelling and Underground Space Technology*, *23*(1), 25–37.

[5] Fenner, R. (1938). *Untersuchungen zur erkenntnis des gebirgsdrucks*. Glückauf

[6] Salencon, J. (1969). Contraction quasi-statique d'une cavite a symetrie spherique ou cylindrique dans un milieu elastoplastique. In *Annales des ponts et chaussées* (Vol. 4, pp. 231–236).

[7] Kastner, H. (1971). Statik des Tunnel-und Stollenbaus auf der Grundlage geomechanischer Erkenntnisse. *Zweite Neubearbeitete Auflage*.

[8] Kennedy, T. C., & Lindberg, H. E. (1978). Tunnel closure for nonlinear Mohr-Coulomb functions. *Journal of the Engineering Mechanics Division*, *104*(6), 1313–1326.

[9] Carranza-Torres, C., & Fairhurst, C. (1999). The elasto-plastic response of underground excavations in rock masses that satisfy the Hoek–Brown failure criterion. *International Journal of Rock Mechanics and Mining Sciences*, *36*(6), 777–809.

[10] Carranza-Torres, C. (2003). Dimensionless graphical representation of the exact elasto-plastic solution of a circular tunnel in a Mohr-Coulomb material subject to uniform far-field stresses. *Rock Mechanics and Rock Engineering*, *36*(3), 237-253.

[11] Xu, S.-Q., & Yu, M.-H. (2006). The effect of the intermediate principal stress on the ground response of circular openings in rock mass. *Rock Mechanics and Rock Engineering*, *39*(2), 169–181.

[12] Lee, Y. K., & Pietruszczak, S. (2008). A new numerical procedure for elasto-plastic analysis of a circular opening excavated in a strain-softening rock mass. *Tunnelling and Underground Space Technology*, *23*(5), 588-599.

[13] Alejano, L. R., Rodriguez-dono, A., Alonso, E., & Fdez, G. (2009). Ground reaction curves for tunnels excavated in different quality rock masses showing several types of post-failure behaviour. *Tunnelling and Underground Space Technology Incorporating Trenchless Technology Research*, *24*(6), 689–705.

[14] Barbosa, R. E. (2009). Analytical solution for a deep tunnel excavated in a porous elasto-plastic material considering the effects of seepage forces. In *Proceedings of the 3rd CANUS rock mechanics symposium, Toronto*.

[15] Fahimifar, A., Tehrani, F. M., Hedayat, A., & Vakilzadeh, A. (2010). Analytical solution for the excavation of circular tunnels in a visco-elastic Burger's material under hydrostatic stress field. *Tunnelling and Underground Space Technology*, *25*(4), 297–304.

[16] Wang, S., & Yin, S. (2011). A closed-form solution for a spherical cavity in the elastic–brittle–plastic medium. *Tunnelling and Underground Space Technology*, *26*(1), 236-241.

[17] González-Cao, J., Varas, F., Bastante, F. G., & Alejano, L. R. (2013). Ground reaction curves for circular excavations in non-homogeneous, axisymmetric strain-softening rock masses. *Journal of Rock Mechanics and Geotechnical Engineering*, *5*(6), 431-442.

[18] Vrakas, A., & Anagnostou, G. (2014). A finite strain closed-form solution for the elastoplastic ground response curve in tunnelling. *International Journal for Numerical and Analytical Methods in Geomechanics*, *38*(11), 1131-1148.

[19] Panet, M., & Guenot, A. (1983). Analysis of convergence behind the face of a tunnel: Tunnelling 82, proceedings of the 3rd international symposium, Brighton, 7–11 June 1982, P197–204. Publ London: IMM, 1982. In *International Journal of Rock Mechanics and Mining Sciences & Geomechanics Abstracts* (Vol. 20, p. A16). Pergamon.

[20] Ng, C. W. W., Wang, R., & Boonyarak, T. (2016). A comparative study of the different responses of circular and horseshoe-shaped tunnels to an advancing tunnel underneath. *Géotechnique Letters*, *6*(2), 168-175.

[21] Zou, J., Zuo, S., & Xu, Y. (2016). Solution of Strain-Softening Surrounding Rock in Deep Tunnel Incorporating 3D Hoek-Brown Failure Criterion and Flow Rule. Mathematical Problems in Engineering, 2016.

[22] Zou, J., Li, C., & Wang, F. (2017). A new procedure for ground response curve (GRC) in strain-softening surrounding rock. Computers and Geotechnics, 89, 81–91.

[23] Lu, A., Wang, S., Zhang, X., & Zhang, N. (2018). Solution of the elasto-plastic interface of circular tunnels in Hoek–Brown media subjected to non-hydrostatic stress. *International Journal of Rock Mechanics and Mining Sciences*, *106*, 124-132.

[24] Oke, J., Vlachopoulos, N., & Diederichs, M. (2018). Improvement to the Convergence-Confinement Method: Inclusion of Support Installation Proximity and Stiffness. *Rock Mechanics and Rock Engineering*, *51*(5), 1495-1519.

[25] Yan, Q., Li, S. C., Xie, C., & Li, Y. (2018). Analytical Solution for Bolted Tunnels in Expansive Loess Using the Convergence-Confinement Method. *International Journal of Geomechanics*, *18*(1), 04017124.

[26] Lv, A., Masoumi, H., Walsh, S. D., & Roshan, H. (2019). Elastic-Softening-Plasticity Around a Borehole: An Analytical and Experimental Study. *Rock Mechanics and Rock Engineering*, *52*(4), 1149-1164.

[27] Brown, E. T., Bray, J. W., Ladanyi, B., & Hoek, E. (1983). Ground response curves for rock tunnels. J Geotech Eng;109:15–39.

[28] Fritz, P. (1984). An analytical solution for axisymmetric tunnel problems in elasto-viscoplastic media. *International journal for numerical and analytical methods in geomechanics*, *8*(4), 325-342.

[29] Detournay, E. (1986). Elastoplastic model of a deep tunnel for a rock with variable dilatancy. *Rock Mechanics and Rock Engineering*, *19*(2), 99–108.

[30] Reed, M. B. (1986). Stresses and displacements around a cylindrical cavity in soft rock. *IMA Journal of Applied Mathematics*, *36*(3), 223–245.

[31] Sulem J, Panet M, Guenot A. An analytical solution for time-dependent displacements in a circular tunnel. Int. J. rock Mech. Min. Sci. Geomech. Abstr., vol. 24, Elsevier; 1987, p. 155–64.

[32] Duncan Fama, M. E. (1993). Numerical modelling of yield zones in rocks. *Comprehensive Rock Engineering*, *2*, 49–75.

[33] Wang, Y. (1996). Ground response of circular tunnel in poorly consolidated rock. *Journal of Geotechnical Engineering*, *122*(9), 703-708.

[34] Shibata, T. (1965). Influence of the variation of the intermediate principal stress on the mechanical properties of normally consolidated clays. In *Proc. 6th Int. Conf. SMFE,* Vol. 1, pp. 361–367.

[35] Mogi, K. (1967). Effect of the intermediate principal stress on rock failure. *Journal of Geophysical Research*, *72*(20), 5117–5131.

[36] Single, B., Goel, R. K., Mehrotra, V. K., Garg, S. K., & Allu, M. R. (1998). Effect of intermediate principal stress on strength of anisotropic rock mass. *Tunnelling and Underground Space Technology*, *13*(1), 71–79.

[37] Yu, M. H., & He, L. N. (1992). A new model and theory on yield and failure of materials under the complex stress state. In *Mechanical Behaviour of Materials VI* (pp. 841–846). Elsevier.

[38] Yu, M. (2002). Advances in strength theories for materials under complex stress state in the 20th century. *Applied Mechanics Reviews*, *55*(3), 169–218.

[39] Yu, M.-H., Yu, M., & Yu, M.-H. (2004). Unified strength theory and its applications.

[40] Zhang, Y.-Q., Hao, H., & Yu, M.-H. (2003). A unified characteristic theory for plastic plane stress and strain problems. *Journal of Applied Mechanics*, *70*(5), 649–654.

[41] Xu, S. Q., & Yu, M. H. (2005). Shakedown analysis of thick-walled cylinders subjected to internal pressure with the unified strength criterion. *International journal of pressure vessels and piping*, *82*(9), 706-712.

[42] Zhang, C., Zhao, J., Zhang, Q., & Hu, X. (2012). A new closed-form solution for circular openings modeled by the Unified Strength Theory and radius-dependent Young's modulus. *Computers and*

Geotechnics, *42*, 118-128.

[43] Wang, H. N., Chen, X. P., Jiang, M. J., Song, F., & Wu, L. (2018). The analytical predictions on displacement and stress around shallow tunnels subjected to surcharge loadings. *Tunnelling and Underground Space Technology*, *71*, 403-427.

[44] Ghorbani, A., & Hasanzadehshooiili, H. (2019). A comprehensive solution for the calculation of ground reaction curve in the crown and sidewalls of circular tunnels in the elastic-plastic-EDZ rock mass considering strain softening. *Tunnelling and Underground Space Technology*, *84*, 413-431.

[45] Kirsch, E. G. (1898). The theory if elasticity and the need of the strength of materials (trans.). *Journal of the Association of German Engineers*, *42*, 797–807.

[46] Feder, G., & Arwanitakis, M. (1977). Zur Gebirgsmechanik ausbruchsnaher Bereiche tiefliegender Hohlraumbauten. *Berg-u. Huettenmaennische Monatshefte*, *122*(4).

[47] Zhao, C., Alimardani, A., Barciaga, T., Kämper, C., Mark, P., & Schanz, T. (2017). Prediction of tunnel lining forces and deformations using analytical and numerical solutions. *Tunnelling and Underground Space Technology Incorporating Trenchless Technology Research*, *64*, 164–176.

[48] onini, M., Lancellotta, G., & Barla, G. (2013). State of stress in tunnel lining in squeezing rock conditions. *Rock Mechanics and Rock Engineering*, *46*(2), 405–411

[49] Vlachopoulos, N., & Diederichs, M. S. (2014). Appropriate uses and practical limitations of 2D numerical analysis of tunnels and tunnel support response. *Geotechnical and Geological Engineering*, *32*(2), 469-488.

[50] Rasouli Maleki, M., & Narimani Dehnavi, R. (2018). Influence of Discontinuities on the Squeezing Intensity in High In Situ Stresses (a Tunnelling Case Study; Actual Evidences and TBM Release

Techniques). *Rock Mechanics and Rock Engineering*, *51*, 2911-2933.

[51] Kabwe E., Karakus M., & Chanda E. (2018b). Investigating the Tunnel Closure using Convergence Confinement Method and 2D Plane Strain Finite Difference Analysis. In *Proceedings of The fourth Australasian Ground Control in Mining Conference.* Carlton Victoria: Australian Mining and Mettalurgy.

[52] Barbosa, R. E. (2009). Analytical solution for a deep tunnel excavated in a porous elasto-plastic material considering the effects of seepage forces. In *Proceedings of the 3rd CANUS rock mechanics symposium, Toronto*.

[53] Cui, L., Zheng, J.-J., Zhang, R.-J., & Lai, H.-J. (2015). A numerical procedure for the fictitious support pressure in the application of the convergence–confinement method for circular tunnel design. *International Journal of Rock Mechanics and Mining Sciences*, *78*, 336–349.

[54] Lode, W. (1926). Versuche über den Einfluß der mittleren Hauptspannung auf das Fließen der Metalle Eisen, Kupfer und Nickel. *Zeitschrift Für Physik*, *36*(11–12), 913–939

[55] Alejano, L. R., & Bobet, A. (2012). Drucker–Prager Criterion. In *The ISRM Suggested Methods for Rock Characterization, Testing and Monitoring: 2007-2014* (pp. 247-252). Springer, Cham.

[56] Vlachopoulos, N., & Diederichs, M. S. (2009). Improved longitudinal displacement profiles for convergence confinement analysis of deep tunnels. *Rock mechanics and rock engineering*, *42*(2), 131-146.

[57] Itasca Consulting Group, Inc. (2017). FLAC^{3D} Version 6.0. User manual. Consulting Group, Inc., Minneapolis.

[58] Kabwe, E. (2017b). Mining Sequence Deformation and Failure Behavior Analysis in the hanging

wall and Orebody Rock Formations; A Continuum Approach. *Geotechnical and Geological Engineering*, 35(4), 1453-1473.

[59] Kabwe E. (2017) Optimal mining method selection for Nchanga's Upper Orebody using analytic hierarchy process and Yager's method, Mining Technology, 126:3, 151-162.

[60] Wojciechowski, M. (2018). A note on the differences between Drucker-Prager and Mohr-Coulomb shear strength criteria. *Studia Geotechnica et Mechanica*.

[61] Carranza-Torres C, Fairhurst C. (2000). Application of the Convergence-Confinement method of tunnel design to rock masses that satisfy the Hoek-Brown failure criterion. Tunn Undergr Sp Technol; 15:187–213. https://doi.org/https://doi.org/10.1016/S0886-7798(00)00046-8.

[62] Li, C. C. (2017). Principles of rockbolting design. *Journal of Rock Mechanics and Geotechnical Engineering*, *9*(3), 396-414.

[63] Zhang, J. Z., Zhou, X. P., & Yin, P. (2019). Visco-plastic deformation analysis of rock tunnels based on fractional derivatives. *Tunnelling and Underground Space Technology*, *85*, 209-219.

[64] Brady, B. H., & Brown, E. T. (2013). *Rock mechanics: for underground mining*. Springer science & business media.

Statement of Authorship

Title of Paper	Time-dependent solution for non-circular tunnels considering the elasto-viscoplastic rockmass
Publication Status	☑ Published ☐ Accepted for Publication ☐ Submitted for Publication ☐ Unpublished and Unsubmitted w ork w ritten in manuscript style
Publication Details	Eugie Kabwe, Murat Karakus, Emmanuel K. Chanda, Time-dependent solution for non-circular tunnels considering the elasto-viscoplastic rockmass, International Journal of Rock Mechanics and Mining Sciences, Volume 133,2020,104395, ISSN 1365-1609, https://doi.org/10.1016/j.ijrmms.2020.104395.

Principal Author

Name of Principal Author (Candidate)	EUGIE KABWE		
Contribution to the Paper	Conceptualization, Formal analysis, Methodology, Investigation, Writing - original draft, Writing - review & editing and as the corresponding author		
Overall percentage (%)	80%		
Certification:	This paper reports on original research I conducted during the period of my Higher Degree by Research candidature and is not subject to any obligations or contractual agreements with a third party that would constrain its inclusion in this thesis. I am the primary author of this paper.		
Signature		Date	17/08/2020

Co-Author Contributions

By signing the Statement of Authorship, each author certifies that:

i. the candidate's stated contribution to the publication is accurate (as detailed above);

ii. permission is granted for the candidate in include the publication in the thesis; and

iii. the sum of all co-author contr butions is equal to 100% less the candidate's stated contribution.

Name of Co-Author	MURAT KARAKUS		
Contribution to the Paper	Supervision of the work; Identification of the problem and methodology, reviewing & editing		
Signature		Date	18/08/2020

Name of Co-Author	EMMANUEL K. CHANDA		
Contribution to the Paper	Supervision, review & editing		
Signature		Date	18/08/2020

Chapter 4

Time-Dependent Solution for Non-Circular Tunnels Considering the Elasto-viscoplastic Rockmass *(Paper 2)*

Eugie Kabwe, Murat Karakus, Emmanuel K Chanda

Published in the International Journal of Rock Mechanics and Mining Sciences

Abstract

The time-dependent ground response of tunnels in squeezing ground requires a thorough understanding of the creep mechanism. Several studies conducted assume that this ground response can be characterized by elastoplastic and viscoelastic behaviour. However, the elasto-viscoplastic behaviour associated with the creep mechanism can predict this ground response realistically. Thus, this paper, presents a solution considering the elasto-viscoplastic behaviour for the ground response estimation of a non-circular tunnel under hydrostatic stress field in an isotropic and homogenous rock mass. The proposed method is an extended form of the closed-form solution based on the fractional-order derivative viscoplastic constitutive law. Thereafter, the proposed method is applied to the horseshoe tunnel ground response and support structure capacity estimation in squeezing ground. It is ascertained that delayed behaviour responsible for squeezing can be estimated realistically about 14% convergence and 24 m yield extension. Whereas the conventional solutions underestimate the convergence range between 2.5% - 5% and the yield zone extension between 12 m - 16 m. In comparison to these conventional solutions, it accounts for 10% tunnel convergence and 50% extension of the yield zone in the long-term. Additionally, the solution determines the suitable long-term safety coefficient for support structure installed at the right time and location behind the tunnel face in squeezing ground.

Keywords: Creep; Ground reaction; Squeezing; Time-dependent behaviour; Elasto-viscoplastic behaviour

4.1 Introduction

A prior assessment of tunnel convergence and support capacity is cardinal for a reliable design of excavations and appropriate support structures. During the excavation process, the ground pressure acting on the tunnel boundary increases with time, as a result, the tunnel convergence extends. This convergence is referred to the time-dependent response of the surrounding rock mass and tunnel advancement essentially associated with creep responsible for squeezing[1],[2]. Generally, the methods employed to describe this tunnel advancement and ground reaction are empirical[1,3,4], analytical [5,6] and numerical methods. Most of these methods rely on the elastic and elastoplastic (EP) constitutive equations to determine the stresses and strains in the surrounding rock mass as well as design tunnel support structure. However, these constitutive equations neglect the time factor which in some cases contributes a proportion of over 70% in overall tunnel convergence [3]. In analytical methods, the face advancement and ground reaction are analyzed and modelled by the employment of EP stress-strain solutions coupled with the convergence confinement concept. Among these include Duncan-Fama [7] presented a solution for stress and strain analysis around a circular tunnel in a Mohr-Coulomb (MC) yield criterion governed EP rock mass. Further on, Brown et al [8] presented an EP solution which considered the Hoek-Brown (HB) yield criterion for a circular tunnel, Carranza Torres and Fairhurst [9] proposed a solution for a circular tunnel excavated in an EP rock mass which obeyed the Hoek Brown yield criterion and most recently Kabwe et al [10] proposed a solution for a non-circular tunnel in an EP rock mass governed by the Lode angle-dependent Drucker-Prager yield criterion.

These solutions are based on the Convergence Confinement Method (CCM), a two-dimensional (2D) approach that can be employed to simulate a three-dimensional (3D) problem in tunnels. However, the CCM is associated with the EP behaviour of the rock mass which is characterized by the time-independent permanent deformations. Hence, the elasto-viscoplastic (EVP) rock mass behaviour responsible for delayed deformations in squeezing ground cannot be estimated by this approach [11]. As such cannot be employed

in the realistic estimation of the time-dependent deformations related to creep. In addition to the above-mentioned limitation of the CCM employment in tunnels excavated in squeezing ground other solutions considered this rock mass time-dependent response. For instance, Gnirk & Johnson [5] analytically determined the boundary convergence of a circular shaft with and without tunnel support. The solution considered the time-dependent deformation characterised by the viscoelastic behaviour. Sulem et al [3] developed a time-dependent closed-form solution which considered a face advance effect in a homogeneous and isotropic rock mass. Ladanyi & Gill [6] evaluated the time-dependent rock mass deformation and proposed a solution which considered the linear and non-linear viscoelastic behaviour of a rock mass. Pan & dong [12] presented a time-dependent solution for a circular tunnel advancement and convergence with supports in a viscoelastic rock mass.

Furthermore, researchers proposed closed-form solutions for the time-dependent response in tunnels by employing viscoelastic constitutive equations. These include: Nomikos et al [13] derived closed-form solution for the mechanical behaviour of a linear viscoelastic Burgers rock mass around an axisymmetric tunnel. Birchall and Osman[14] presented a solution for estimation of the time-dependent deformation by employing the Burgers viscoelastic constitutive equation. Fahimifar et al[15] suggested a closed-form solution for the time-dependent response of the visco-elastic rock mass. Gschwandtner & Galler [16] further proposed a novel method employing the CCM while considering the time-dependent behaviour in tunnels. Wang et al [17] introduced a closed-form solution using a viscoelastic relationship applicable for sequential non-circular excavation. Even though these closed-form solutions account for the time-dependent behaviour, they neglect the viscoplastic permanent deformations associated with squeezing. Moreover, they employ integer-order derivatives constitutive equations which can not describe the power-law characteristic of geomaterials (rocks and soils) associated with creep behaviour. Which is responsible for squeezing mechanism a challenge in tunnel operation frequently linked with post tunnel rehabilitation and support element failure. Depending on

the severity of the mechanism, significant investment in support installation and time-consuming rehabilitation is required to sustain the serviceability of tunnels[18–23]. Therefore, this paper presents a solution for the time-dependent ground response and support structure capacity estimation for a non-circular tunnel excavated in squeezing ground. It is achieved by the derivation of a time-dependent closed-form solution based on the newly developed fractional-order derivative viscoplastic (FDVP) constitutive model [24]. Thereafter, extended to the time-dependent solution for the ground response of horseshoe tunnels in squeezing ground.

4.2 Limitation of the ground response solutions

The CCM considers ground response to the tunnel face advance and comprised of a three-step analysis: (1) the Support Characteristic Curve (SCC) relates deformation of the support pressure to the convergence, (2) the Longitudinal Displacement Profile (LDP) relates tunnel displacement to the position of the tunnel face and (3) the Ground Reaction Curve (GRC) relates in-situ stress to tunnel convergence [25–28]. The GRC, on the other hand, is composed of two analysis sections which are; the elastic section based on initial hole-in-a-plate solution attributed to Kirsch [29] and the plastic section based on a solution by Fenner [30]. The ground response is dependent on the rock mass behaviour, linear for instantaneous reversible elastic ground behaviour and non-linear for irreversible convergence characterized by the EP ground behavior [7,9,31–33]. Hence, the irreversible time-dependent convergence characterized by the EVP rock mass behaviour is not well-thought-out in this analysis (Figure 4-1).

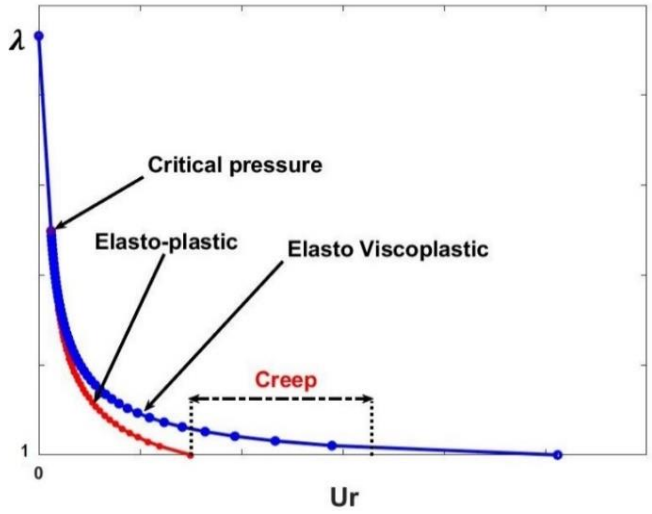

Figure 4-1. Ground response of an elastoplastic and elasto-viscoplastic rock mass.

The conventional CCMs [7,9,33–35] are employed for tunnel face effect evaluation by the internal pressure variation acting on the tunnel boundary with convergence. However, face limitations in that they neglect the time-dependent rock mass behaviour associated with creep mechanism [27]. Figure 4-2 illustrates the results of a comparison between the CCMs generated GRC and a numerical time-dependent GRC attained by a stepwise pressure reduction on the tunnel boundary. It is drawn from the illustration that the CCMs underrate the ground response of tunnels as compared to the numerical solution. The support structure installed at the CCM predicted location behind the tunnel face is subjected to a low support load (p_s) at equilibrium.

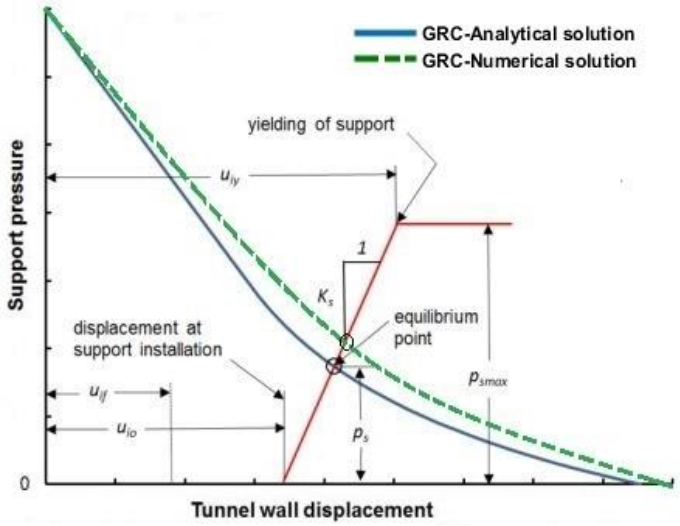

Figure 4-2. Comparison of the time-dependent numerical and convergence confinement solutions

Hence, the installed support structure safety coefficient is unrealistically higher compared to the numerically predicted. As such the CCMs unrealistically estimate the appropriate stiffness, location and capacity of the installed tunnel support structure in squeezing ground. It is cardinal that this support structure should be installed before rock mass loosening but late enough to avoid support overload. Hence, the time of support structure installation and location is very important for the effectiveness of tunnel stability in squeezing ground [27]. As a result, the CCMs face limitation in the stability analysis of tunnels excavated in squeezing ground because they are:

- based on the rock mass that exhibits EP shear failure.
- neglect the delayed viscoplastic strains responsible for squeezing.
- are based on the EP assumption which underestimates the appropriate tunnel support structure capacity.

Hence, in section 4.3, a time-dependent closed-form solution for stress-strain estimation around a circular tunnel governed by the FDVP constitutive law is derived and verified.

4.3 Derivation of the time-dependent closed-form solution

The ability of rocks and rock masses to undergo time-dependent deformation upon being subjected to a constant state of stress is referred to as creep [36–38]. During excavation, this time-dependent behaviour can be an instantaneous or a steady increase of tunnel convergence. This instantaneous or steady increase of the tunnel convergence is due to the rock mass rheological properties, its ability to undergo creep [12]. Sulem et al [3] concluded that the time-dependent behaviour can account for about 70% of the total tunnel convergence. Hence, it is vital to take into consideration the aspect of the creep phenomenon during the design and excavation of tunnels. Panet [39], Sulem et al [3], Malan [36,40], Barla et al [37] and Debernardi & Barla [38] proposed solutions and constitutive laws to capture creep related time-dependent behaviour based on either the Kelvin and Maxwell rheological models or their combination (Figure 4-3).

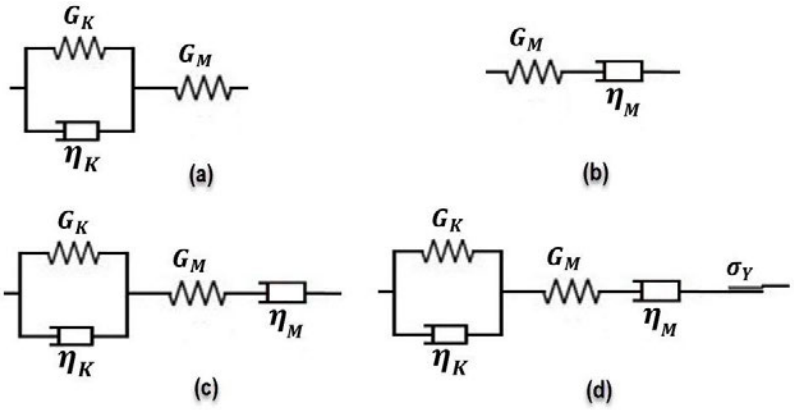

Figure 4-3. Schematic representation of rheological models: (a) Kelvin, (b) Maxwell, (c) Burgers and (d) CVISC models

However, these rheological models and their combination can only describe the viscoelastic deformations. On the other hand, the Burgers model and a plastic slider characterized by the MC failure criterion combination describes the EVP deformations. Nevertheless, the plastic slider is independent of time unless coupled with a viscous dashpot. Hence, viscoplastic deformation captured by this model is only dependent on stress. Additionally, Kabwe et al [42] concluded that it failed to simulate the time-dependent plastic shearing characterized by the irreversible viscoplastic deformation. Therefore, a closed-form solution capable of estimating the irreversible viscoplastic deformations characterised by squeezing is presented in this section. Firstly, it is derived based on the experimentally validated FDVP constitutive model governed by an associative viscoplastic flow rule. Thereafter, it is verified by comparing with conventional viscoelastic and viscoplastic models, respectively.

4.3.1 Derived fractional-order constitutive equations

In this section, a solution is derived based on the fractional-order derivative theory [43]. Employing the fractional-order derivatives will allow for the proposed solution to replicate and characterize all the creep stages. The fractional derivative theory employs the Riemann-Liouville fractional-order differential operator

which assumes that $f(t)$ is continuous in $(0, +\infty)$ and is integrated in any finite subdomain of $[0, +\infty)$ for $t > 0$ and $Re(\beta) > 0$ where β is the order integral of the function $f(t)$ [44]. The Riemann–Liouville fractional integral of the function $f(t)$ is expressed as [45].

$$\frac{d^{-\beta} f(t)}{dt^{-\beta}} = \frac{1}{\Gamma(\beta)} \int_{t_0}^{t} (t-\tau)^{\beta-1} f(t) d\tau \tag{4-1}$$

Where $\Gamma(\beta)$ is the gamma function given by:

$$\Gamma(\beta) = \int_0^{\infty} x^{\beta-1} e^{-x} dx\,, \qquad Re(\beta) > 0 \tag{4-2}$$

The fractional derivative $\frac{d^{\beta}}{dt^{\beta}}$ with the order $\beta \in (0,1)$ of the function $f(t)$ is defined by:

$$\frac{d^{\beta} f(t)}{dt^{\beta}} = \left(\frac{1}{\Gamma(1-\beta)} \int_{t_0}^{t} (t-\tau)^{1-\beta} f(t) d\tau \right) \frac{df(t)}{dt} \tag{4-3}$$

and the fractional-order derivative $\frac{d^{\beta}}{dt^{\beta}}$ with the order $\beta \in (n-1, n)$ of the function $f(t)$ is defined by:

$$\frac{d^{\beta} f(t)}{dt^{\beta}} = \left(\frac{1}{\Gamma(n-\beta)} \int_{t_0}^{t} (t-\tau)^{n-\beta} f(t) d\tau \right) \frac{d^n f(t)}{dt^n} \tag{4-4}$$

A typical application of the fractional-order derivative theory is the fractional derivative dashpot characterized by the constitutive relation:

$$\sigma(t) = \eta^{\beta} \frac{d^{\beta}[\varepsilon(t)]}{dt^{\beta}} \qquad (0 \le \beta \le 1) \tag{4-5}$$

Where η^{β} is the fractional-order derivative dashpot viscosity coefficient and β is the fractional-order coefficient. When β = 1.0 the fractional-order derivative dashpot represents the Newtonian dashpot and when β = 0.0 it represents a solid element [46–48]. Hence, the fractional-order derivative dashpot exhibits characteristic of an element amid an ideal Newtonian dashpot and an ideal spring this reduces the limitation of both elements [49,50]. An ideal schematic representation of the rheological model which integrates the fractional derivative dashpot is illustrated in Figure 4-4. The model is composed of the Kelvin, fractional-order Maxwell and fractional-order viscoplastic components all connected in series.

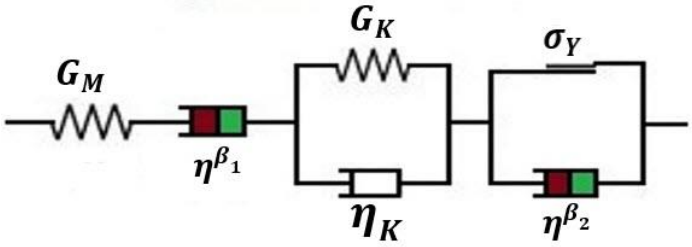

Figure 4-4. Schematic view of the FDVP consitutive model
(Kabwe et al [24])

The fractional-order Maxwell component is composed of a spring and fractional-order derivative dashpot coupled in series, and the fractional-order viscoplastic component is parallelly linked by a fractional-order derivative dashpot and a plastic slider. From Figure 4-4 expressions for the total strain and stress can be obtained by:

$$\sigma(t) = \sigma^K = \sigma^M = \sigma^{VP}; \qquad \varepsilon(t) = \varepsilon^K + \varepsilon^M + \varepsilon^{VP} \tag{4-6}$$

Where σ^K, σ^M and σ^{VP} are the stress acting in the Kelvin, fractional-order Maxwell and the fractional-order viscoplastic components respectively; ε^K, ε^M and ε^{VP} are the strain in the Kelvin, fractional-order Maxwell and the fractional-order viscoplastic components respectively. Based on the fractional-order derivative

dashpot the total stress is obtained by Eq. (4-5). Therefore, setting $\sigma(t) = \sigma$ (constant stress), employing the fractional-order calculus attributed to Reimann-Liouville [51] operation and applying Laplace transformation on either side of Eq. ((4-5)), the following expression can be obtained:

$$F_{\beta_{1,2}}(s) = \frac{\sigma}{\eta^{\beta_{1,2}}(s^{1+\beta_{1,2}})} \tag{4-7}$$

Conducting an inverse Laplace transformation on Eq. (4-7), the total strain represented by the fractional-order derivative dashpot is given by:

$$\varepsilon(t) = \frac{\sigma}{\eta^{\beta_{1,2}}} \frac{t^{\beta_{1,2}}}{\Gamma\left(1+\beta_{1,2}\right)} \qquad \left(0 \leq \beta_{1,2} \leq 1\right) \tag{4-8}$$

The total stress in the fractional-order viscoplastic component σ^{VP} is given as:

$$\sigma^{VP} = \sigma^{p} + \sigma^{v} \tag{4-9}$$

Where σ^{p} is the stress in the plastic slider and σ^{v} is the stress in the fractional-order derivative dashpot. The σ^{p} is expressed as:

$$\sigma^{p} = \begin{cases} \sigma_{0,} & \sigma_0 < \sigma_Y \\ \sigma_Y, & \sigma_0 \geq \sigma_Y \end{cases} \tag{4-10}$$

When $\sigma_0 < \sigma_Y$, combining Eq. (4-9) and Eq. (4-10), then $\sigma^{v} = 0$ and $\varepsilon^{VP} = 0$. When $\sigma_0 \geq \sigma_Y$, the total stress on the fractional-order viscoplastic unit is expressed as:

$$\sigma^{VP} = \eta^{\beta_2}\left(\frac{\sigma_0 - \sigma_Y}{\eta^{\beta_2}}\right) + \sigma_Y \tag{4-11}$$

Where η^{β_2} is the viscosity coefficient in the fractional-order viscoplastic component. Considering the fractional-order derivative relation Eq. (4-8) and setting initial condition as ε^{VP} = 0 and t = 0, expression for Eq. (4-11) is:

$$\varepsilon^{VP} = \frac{\sigma_0 - \sigma_Y}{\eta^{\beta_2}} \frac{t^{\beta_2}}{\Gamma(1+\beta_2)} \qquad \sigma_0 \geq \sigma_Y, (0 \leq \beta_2 \leq 1) \quad (4\text{-}12)$$

Therefore, from Eq. A7 (Appendix: A) and Eq. (4-12), the relationship between radial tunnel convergence and time befits:

$$u_r = \begin{cases} \frac{R}{2}\left\{\frac{\sigma_0}{G_M} + \frac{\sigma_0 t}{\eta_M} + \frac{\sigma_0}{G_K}\left[1 - exp\left(-\frac{t}{T_K}\right)\right]\right\}, & \sigma_0 < \sigma_Y \\ \frac{R}{2}\left\{\frac{\sigma_0}{G_M} + \frac{\sigma_0 t}{\eta_M} + \frac{\sigma_0}{G_K}\left[1 - exp\left(-\frac{t}{T_K}\right)\right] + \left(\frac{\sigma_0 - \sigma_Y}{\eta^{\beta_2}} \frac{t^{\beta_2}}{\Gamma(1+\beta_2)}\right)\right\}, & \sigma_0 \geq \sigma_Y \end{cases} \quad (4\text{-}13)$$

Where u_r is the tunnel convergence (u_r = $\varepsilon(t) = \varepsilon^K + \varepsilon^M + \varepsilon^{VP}$) and β_2 is the fractional-order coefficient (viscoplastic unit dashpot). Integrating the fractional-order derivative relation Eq. (4-8) in the Maxwell dashpot of Eq. (4-13), one gets the radial convergence relation in an EVP material expressed based on the FDVP constitutive model:

$$u_r = \frac{R}{2} \begin{cases} \left\{\frac{\sigma_0}{G_M} + \frac{\sigma_0 t^{\beta_1}}{\eta^{\beta_1}\Gamma(1+\beta_1)} + \frac{\sigma_0}{G_K}\left[1 - exp\left(-\frac{t}{T_K}\right)\right]\right\}, & \sigma_0 < \sigma_Y \\ \left\{\frac{\sigma_0}{G_M} + \frac{\sigma_0 t^{\beta_1}}{\eta^{\beta_1}\Gamma(1+\beta_1)} + \frac{\sigma_0}{G_K}\left[1 - exp\left(-\frac{t}{T_K}\right)\right] + \left(\frac{\sigma_0 - \sigma_Y}{\eta^{\beta_2}} \frac{t^{\beta_2}}{\Gamma(1+\beta_2)}\right)\right\}, & \sigma_0 \geq \sigma_Y \end{cases} \quad (4\text{-}14)$$

Where η^{β_1} is the viscosity coefficient of the Maxwell dashpot and the fractional-order derivatives can describe the rheological behaviour of geomaterials. The gamma function adopted in these derivatives describes the power-law characteristic observed in creep behaviour. Whereas the conventional integer-order solutions assume linearity in the rheological behaviour of geomaterials. Hence, the gamma function employment provides a realistic estimation of the delayed deformations responsible for squeezing. The closed-form solution (Eq. (4-14)) presented herein is derived from the constitutive equations based on the FDVP constitutive model [24] calibrated using experimental data attained from Zhou et al [52] and Chen et al [53] (Appendix B).

4.3.1.1 Verification of the proposed closed-form solution

In this section, verification is conducted in which the closed-form solution (Eq. (4-14)) is compared with the existing viscoelastic and viscoplastic solutions[53,54] (Figure 4-5). The solutions are employed to determine the time-dependent radial deformation of a circular tunnel excavated in a rock mass governed by the creep parameters presented in Table 4-1.

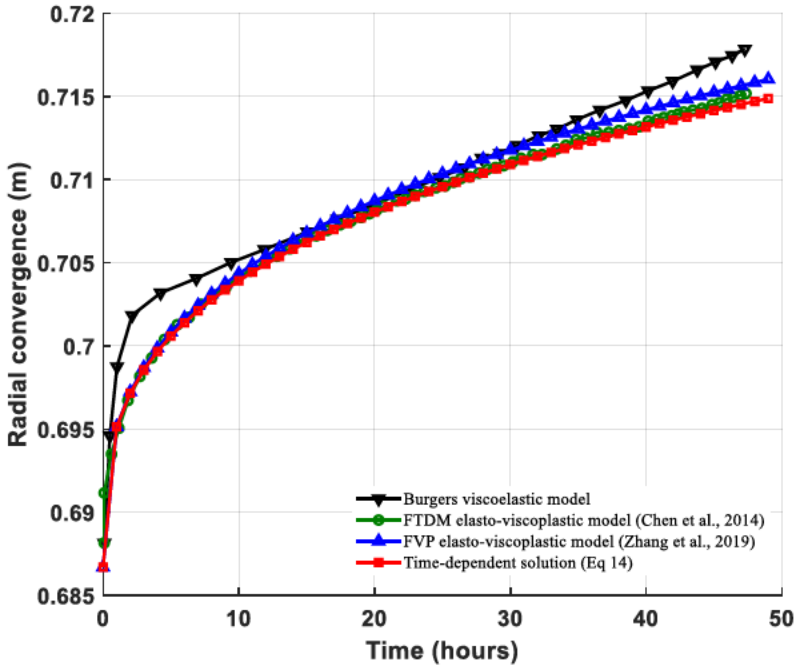

Figure 4-5. Comparison of the time-dependent solution (Eq.14) with the conventional time-dependent models

Table 4-1. Geometry and creep parameters employed in the FTDM, FVP and time-dependent solutions

η_M(GPa.h)	G_K(GPa)	η_K(GPa.h)	G_M(GPa)	η^{β_1}(GPa.h)	η^{β_2}(GPa.h)	$\beta_{1,2}$	$\Gamma(1+\beta_{1,2})$	R (m)	σ_0(MPa)
4650	2610	1961	53	4650	4959	0.31	0.895	5.8	23

Creep parameters of the Burgers model

η_K(GPa.h)	η_M(GPa.h)	G_K(GPa)	G_M(GPa)
1961	107300	2610	53

Note: GPa.h is Giga pascal per hour.

The FDVP constitutive law based closed-form solution derived and verified for time-dependent behaviour of circular tunnels in squeezing ground. In the preceding section, the solution (Eq. (4-14)) is extended to the time-dependent ground response solution. It is extended to account for the horseshoe tunnel time-dependent GRC and support structure capacity estimation. As such it addresses the limitation associated with the conventional CCMs in estimating non-circular tunnel convergence in squeezing ground.

4.3.2 Determination of the time-dependent ground reaction curve

4.3.2.1 General assumptions

In the evaluation of a circular tunnel in an EVP rock mass characterized by squeezing the following assumptions are considered:

1. Circular tunnel in a homogenous, isotropic rock mass which obeys an FDVP constitutive law.
2. The MC yield criterion governed FDVP constitutive model with an associated viscoplastic flow rule.
3. Circular tunnel in-plane strain conditions subjected to the hydrostatic stress field.

However, it must be mentioned that the preliminary derivation is based on a circular tunnel. Subsequently, the shape function which considers the non-circular tunnel shape is incorporated to estimate the EVP deformations characterized by squeezing in horseshoe tunnels. The proposed closed-form solution (Eq. 14) is implemented in the CCM to derive the ground response of a circular tunnel in an EVP rock mass. The ground response estimation using conventional CCMs considers EVP rock mass which employs time-independent material parameters. Therefore, in this section, the time-independent and creep parameters are integrated into the solution to realistically estimate the ground response of tunnels in an EVP rock mass associated with squeezing. The CCM approach is presented by considering a section behind the tunnel face as an axisymmetric 2D plane strain problem. The tunnel face advance effect is considered by employing a pseudo internal pressure σ_i alteration on the tunnel boundary [55]:

$$\sigma_i = (1 - \lambda)\sigma_0 \tag{4-15}$$

Where σ_0 is the in-situ stress and λ is the deconfinement ratio which lies between 0.0 and 1.0. During the excavation of a cylindrical tunnel (radius = R) in a continuous, homogenous rock mass subjected to a hydrostatic state of stress. When σ_0 exceeds the strength of the surrounding rock mass a viscoplastic zone

radius (R_P) develops. Figure 4-6 illustrates the viscoplastic, elastic and viscoelastic zones created as a result of σ_0 exceeding the strength of the surrounding rock mass. Moreover, the surrounding rock mass viscoplastic behaviour is represented by the fractional-order derivative formulation Eq. (4-14) characterised by the EVP constitutive laws.

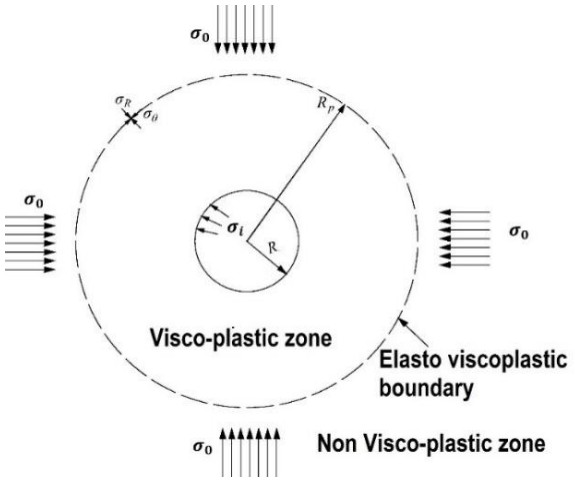

Figure 4-6. Viscoplastic zone surrounding a circular tunnel. Note: $\sigma_R = \sigma_r$ and Non visco-plastic zone refers to elastic and viscoelastic zones.

4.3.2.2 Failure surface definition

In axisymmetric conditions the MC yield criterion is expressed as:

$$F(\sigma_\theta, \sigma_r) = \sigma_\theta - \sigma_r N_\phi + \sigma_c = 0 \tag{4-16}$$

Where σ_θ and σ_r are the tangential and radial stress respectively. Where N_ϕ is expressed as $(1 + \sin\phi / 1 - \sin\phi)$ and σ_c is the unconfined compressive strength $\left(\sigma_c = 2c\sqrt{N_\phi}\right)$. During excavation, a tunnel loses its surrounding rock mass confinement when λ decreases as a result U_r converges towards its central axis. During this decrease, the surrounding rock mass undergoes elastic behaviour up to a critical deconfinement ratio (λ_e). Further reduction (< λ_e), the rock mass yields plastically, in this case, it

undergoes viscoplastic behaviour characterised by creep mechanism. The λ_e is governed and can be obtained from the MC yield criterion by substituting Eq. (4-15) for σ_θ and σ_r to obtain the relation:

$$F\big((1+\lambda_e)\sigma_0, (1-\lambda_e)\sigma_0\big) = 0$$

which is expanded to:

$$(1+\lambda_e)\sigma_0 - (1-\lambda_e)\sigma_0 N_\phi - \sigma_c = 0 \tag{4-17}$$

Solving for λ_e, Eq. (4-17) is simplified to [56]:

$$\lambda_e = \frac{1}{N_\phi + 1}\left(N_\phi - 1 + \frac{2c\sqrt{N_\phi}}{\sigma_0}\right) \tag{4-18}$$

4.3.2.3 Stresses and displacements in the viscoelastic and viscoplastic zones

The stress equilibrium equation assuming axisymmetric loading around the circular tunnel is expressed in cylindrical coordinates by:

$$\frac{\partial \sigma_r}{\partial_r} + \frac{\sigma_\theta - \sigma_r}{r} = 0 \tag{4-19}$$

Substitution of Eq (4-16) in Eq. (4-19), then conducting an integration one obtains the radial and tangential stress for the viscoplastic zone ($R \leq \mathrm{r} \leq R_P$) as:

$$\sigma_r = \frac{2c\sqrt{N_\phi}}{N_\phi - 1}\left[\left(\frac{r}{R}\right)^{N_\phi - 1} - 1\right] + (1-\lambda)\sigma_0\left(\frac{r}{R}\right)^{N_\phi - 1} \tag{4-20}$$

$$\sigma_\theta = \frac{2c\sqrt{N_\phi}}{N_\phi - 1}\left[N_\phi\left(\frac{r}{R}\right)^{N_\phi - 1} - 1\right] + N_\phi(1-\lambda)\sigma_0\left(\frac{r}{R}\right)^{N_\phi - 1} \quad (4\text{-}21)$$

Where R and R_P is the tunnel radius and viscoplastic zone radius respectively and the ratio of the viscoplastic radius to the tunnel radius is expressed by [57]:

$$\frac{R_P}{R} = \left[\left(\frac{2}{N_\phi + 1}\right)\frac{(N_\phi - 1)\sigma_0 + 2c\sqrt{N_\phi}}{(1-\lambda)(N_\phi - 1)\sigma_0 + 2c\sqrt{N_\phi}}\right]^{\frac{1}{N_\phi - 1}} \quad (4\text{-}22)$$

The radial (σ_r) and tangential (σ_θ) stress in the viscoelastic zone ($\mathrm{r} \geq R_P$) are given by [3]:

$$\sigma_r = \left[1 - \lambda_e\left(\frac{R_P}{r}\right)^2\right]\sigma_0 \quad (4\text{-}23)$$

$$\sigma_\theta = \left[1 + \lambda_e\left(\frac{R_P}{r}\right)^2\right]\sigma_0 \quad (4\text{-}24)$$

The analysis in this study accounts for stress and strain of near section of a tunnel and the effect of the tunnel face. Hence, the mean stress (σ_m) of the near section to be considered is given by [15]:

$$\sigma_m = \frac{\sigma_\theta + \sigma_z + \sigma_r}{3} = \sigma_0 \quad (4\text{-}25)$$

$$s_r = \sigma_r - \sigma_m = \sigma_0\left[1 - \lambda_e\left(\frac{R_P}{r}\right)^2\right] - \sigma_0 = -\lambda_e\sigma_0\left(\frac{R_P}{r}\right)^2 \quad (4\text{-}26)$$

$$s_\theta = \sigma_\theta - \sigma_m = \sigma_0 \left[1 + \lambda_e \left(\frac{R_P}{r}\right)^2\right] - \sigma_0 = \lambda_e \sigma_0 \left(\frac{R_P}{r}\right)^2 \quad (4\text{-}27)$$

Where σ_z is the longitudinal stress, s_r is the radial deviatoric stress and s_θ is the tangential deviatoric stress. Since the stress field acting around the tunnel boundary is obtained from Eq. (4-26) and Eq. (4-27). The total deviatoric strain (e_{ij}) in the viscoelastic zone ($\mathrm{r} \geq R_P$) is computed by deviatoric components of the strain tensor:

$$e_{ij} = e_{ij}^K + e_{ij}^M \quad (4\text{-}28)$$

Where e_{ij}^K and e_{ij}^M are the Kelvin and Maxwell material strain contribution respectively. The Kelvin strain and deviatoric stress tensors relation are expressed by:

$$s_{ij} = 2\eta_K \dot{e}_{ij}^K + 2G_K e_{ij}^K \quad (4\text{-}29)$$

and setting initial condition as e_θ^K = 0, the tangential strain $\left(e_\theta^K\right)$ of the Kelvin material is expressed by:

$$e_\theta^K = \frac{s_\theta}{2G_K}\left[1 - exp\left(-\frac{t}{T_K}\right)\right] \quad (4\text{-}30)$$

While the stress-strain relation of the fractional-order Maxwell material is expressed by:

$$\dot{e}_{ij}^M = \frac{s_{ij} t^{\beta_1}}{2\eta^{\beta_1}\Gamma(1+\beta_1)} + \frac{\dot{s}_{ij}}{2G_M} \quad (4\text{-}31)$$

Therefore, the tangential strain $\left(e_\theta^M\right)$ of the fractional-order Maxwell material is expressed as:

$$e_{\theta}^{M} = \frac{s_{\theta} t^{\beta_1}}{2\eta^{\beta_1}\Gamma(1+\beta_1)} + \frac{s_{\theta}}{2G_M} \tag{4-32}$$

Coupling the fractional-order Maxwell and Kelvin material in series (Eq. (4-16)) and substituting Eq. (4-27), one obtains tangential strain expression:

$$\varepsilon_{\theta}{}^{ve} = \lambda_e \left(\frac{R_P}{r}\right)^2 \sigma_0 \frac{1}{2}\left(\frac{1}{G_M} + \frac{t^{\beta_1}}{\eta^{\beta_1}\Gamma(1+\beta_1)} + \frac{1}{G_K}\left[1 - exp\left(-\frac{t}{T_K}\right)\right]\right) \tag{4-33}$$

and the viscoelastic zone deformation $\left(\frac{u_{ve}}{r}\right)$ from:

$$\frac{u_{ve}}{r} = \lambda_e \left(\frac{R_P}{r}\right)^2 \sigma_0 \frac{1}{2}\left(\frac{1}{G_M} + \frac{t^{\beta_1}}{\eta^{\beta_1}\Gamma(1+\beta_1)} + \frac{1}{G_K}\left[1 - exp\left(-\frac{t}{T_K}\right)\right]\right) \tag{4-34}$$

In the viscoplastic zone $(R \leq \mathrm{r} \leq R_P)$ the strains are typically expressed as a totality of the viscoelastic and viscoplastic strains expressed as:

$$\begin{gathered} e_{ij} = e_{ij}^{M} + e_{ij}^{K}\}e_{ij}^{ve} + e_{ij}^{vp} \\ \dot{e}_r = \dot{e}_r^{ve} + \dot{e}_r^{vp}; \quad \dot{e}_{\theta} = \dot{e}_{\theta}^{ve} + \dot{e}_{\theta}^{vp} \end{gathered} \tag{4-35}$$

When $\lambda > \lambda_e$ a viscoplastic zone develops around the tunnel periphery and the deformation in the zone is associated with dilation. Therefore, an associative flow rule is applied and the viscoplastic strains are derived from a plastic potential:

$$g(\sigma_{\theta}, \sigma_r) = \sigma_{\theta} - \sigma_r N_{\psi} \tag{4-36}$$

Where N_{ψ} is the dilatancy coefficient $\left(N_{\psi} = 1 + \sin\psi / 1 - \sin\psi\right)$. Therefore:

$$\dot{e}_r^{vp} = \Lambda \frac{\partial g}{\partial \sigma_r} = \Lambda N_\psi \tag{4-37}$$

$$\dot{e}_\theta^{vp} = \Lambda \frac{\partial g}{\partial \sigma_\theta} = \Lambda \tag{4-38}$$

Where Λ represents the viscoplastic multiplier and using the flow rule one can express:

$$\dot{e}_r^{vp} + N_\psi \dot{e}_\theta^{vp} = 0 \tag{4-39}$$

In axisymmetric conditions $\dot{e}_r^{vp}$ and $\dot{e}_\theta^{vp}$ are expressed as:

$$\dot{e}_r^{vp} = \frac{\partial \Delta \dot{u}_r^{vp}}{\partial r};\ \ \dot{e}_\theta^{vp} = \frac{\Delta \dot{u}_r^{vp}}{r} \tag{4-40}$$

Substituting Eq. (4-40) into Eq. (4-39) gives:

$$\frac{\partial \Delta \dot{u}_r^{vp}}{\partial r} + N_\psi \frac{\Delta \dot{u}_r^{vp}}{r} = 0 \tag{4-41}$$

Reference to Eq. (4-30) and Eq. (4-31) the tangential strain (e_θ^{ve}) of the viscoelastic material is expressed as:

$$e_\theta^{ve} = \frac{s_\theta}{2G_K}\left[1 - exp\left(-\frac{t}{T_K}\right)\right] + \frac{s_\theta}{2}\left(\frac{t^{\beta_1}}{\eta^{\beta_1}\Gamma(1+\beta_1)} + \frac{1}{G_M}\right) \tag{4-42}$$

and the stress-strain relation of the viscoplastic material is expressed by:

$$\dot{e}_{ij}^{vp} = \frac{s_{ij} - \sigma_Y}{2\eta^{\beta_2}} \frac{t^{\beta_2}}{\Gamma(1+\beta_2)} \tag{4-43}$$

Therefore, the tangential strain (e_θ^{vp}) is given by:

$$e_\theta^{vp} = \frac{s_\theta - \sigma_Y}{2\eta^{\beta_2}} \frac{t^{\beta_2}}{\Gamma(1+\beta_2)} \tag{4-44}$$

Substituting Eq. (4-29), Eq. (4-31) and Eq. (4-43) into Eq. (4-35) one gets an expression:

$$\begin{aligned} &{\varepsilon_\theta}^{vp} \\ &= \lambda_e \left(\frac{R_P}{r}\right)^2 \frac{1}{2}\left[\frac{\sigma_0}{G_M} + \frac{\sigma_0 t^{\beta_1}}{\eta^{\beta_1}\Gamma(1+\beta_1)} + \frac{\sigma_0}{G_K}\left[1 - exp\left(-\frac{t}{T_K}\right)\right] + \left(\frac{\sigma_0 - \sigma_Y}{\eta^{\beta_2}} \frac{t^{\beta_2}}{\Gamma(1+\beta_2)}\right)\right] \end{aligned} \tag{4-45}$$

Therefore.

$$\begin{aligned} &\frac{\partial \Delta\dot{u}_r^{vp}}{\partial r} + N_\psi \frac{\Delta\dot{u}_r^{vp}}{r} \\ &= F_1 \frac{1}{2}\left[\frac{1}{G_M} + \frac{t^{\beta_1}}{\eta^{\beta_1}\Gamma(1+\beta_1)} + \frac{1}{G_K}\left[1 - exp\left(-\frac{t}{T_K}\right)\right] + \left(\frac{\sigma_0 - \sigma_Y}{\eta^{\beta_2}} \frac{t^{\beta_2}}{\Gamma(1+\beta_2)}\right)\right] F_2 \end{aligned} \tag{4-46}$$

$$F_1 = \left[\left(1 - N_\psi\right)\left[\left(1 - N_\phi\right)(1-\lambda)\sigma_0 - 2c\sqrt{N_\phi}\right]\right] \tag{4-47}$$

$$F_2 = \left(\frac{r}{R}\right)^{N_\phi - 1} \tag{4-48}$$

With ($R \leq \mathrm{r} \leq R_P$) and computing the differential equation (Eq. (4-46)) gives the proposed solution of the radial deformation in the viscoplastic zone as:

$$\frac{u_{vp}}{r}$$

$$= \left[\frac{F_1 \frac{1}{2}\left[\frac{1}{G_M} + \frac{t^{\beta_1}}{\eta^{\beta_1}\Gamma(1+\beta_1)} + \frac{1}{G_K}\left[1 - exp\left(-\frac{t}{T_K}\right)\right] + \left(\frac{\sigma_0 - \sigma_Y}{\eta^{\beta_2}}\frac{t^{\beta_2}}{\Gamma(1+\beta_2)}\right)\right]}{N_\psi + N_\phi}\right] F_2 \quad (4\text{-}49)$$

$$+ \mathrm{G}\left(\frac{R_P}{r}\right)^{N_\psi + 1}$$

Where G is an integral constant computed by the application of the displacement continuity condition on the viscoelastic and viscoplastic interface, G is then expressed as:

$$\mathrm{G} = \left[\lambda_e \sigma_0 - \frac{F_1}{N_\psi + N_\phi}\left(\frac{R_P}{R}\right)^{N_\phi - 1}\right]\frac{1}{2}\left[\frac{1}{G_M} + \frac{t^{\beta_1}}{\eta^{\beta_1}\Gamma(1+\beta_1)} + \frac{1}{G_K}\left[1 - exp\left(-\frac{t}{T_K}\right)\right] + \left(\frac{\sigma_0 - \sigma_{Rp}}{\eta^{\beta_2}}\frac{t^{\beta_2}}{\Gamma(1+\beta_2}\right.\right. \quad (4\text{-}50)$$

Where σ_{Rp} in this case is the radial stress at the viscoelastic and viscoplastic interface which is expressed as [57]:

$$\sigma_{Rp} = \frac{2\sigma_0 - \sigma_c}{1 + N_\phi} \quad (4\text{-}51)$$

It must be emphasized that the presented ground response solution (Eq (4-49)) is consistent with the newly proposed by Nomikos et al [13] and Tran-Manh et al [56] solutions. However, these solutions are based on integer-order derivatives as opposed to Eq. (4-49) capable of the power-law realistic description of the creep mechanism of geomaterials.

4.3.2.4 Determination of the horseshoe tunnel ground response

The presented time-dependent ground response solution (Eq. (4-49)) constructs the time-dependent GRC for circular tunnels by the reduction of r to R. However, it must empathize that the solution in its present form is applicable for circular tunnels excavated in civil engineering operations. It neglects the non-circular (Horseshoe) tunnels excavated in underground mine operations. Hence, the solution (Eq. (4-49)) cannot realistically estimate the time-dependent ground response of tunnels in most underground mines. Therefore, in this section, the equivalent radius function is incorporated into Eq. (4-49), to enhance its functionality in estimating the time-dependent wall convergence within a horseshoe tunnel. The equivalent radius (R_q) function based on the equal area method is expressed by:

$$R_q = \sqrt{\frac{A}{\pi}} \tag{4-52}$$

$$A = \frac{1}{2}(\pi R^2) + LR \tag{4-53}$$

$$R_q = \sqrt{\left(\frac{\frac{1}{2}(\pi R^2) + LR}{\pi}\right)} \tag{4-54}$$

Where A is the tunnel cross-section area, π is the radial constant, R is the radius of the tunnel arc and L is the tunnel wall height. Therefore, to determine the time-dependent convergence within a horseshoe tunnel we substitute R with R_q in Eq. (4-49) herein and after. The time-dependent convergence of a horseshoe tunnel estimated using the solution is compared with the conventional CCMs [7,9,58] and the Burgers viscoelastic model. The tunnel considered for this estimation is illustrated in Figure 4-7. Horseshoe tunnel

geometry with R_q = 5.8 m and parameters presented in Table 4-2. Rock mass strength, creep and tunnel geometrical parameters.. The results attained from this comparative analysis shows that the presented time-dependent solution estimates the overall time-dependent horseshoe tunnel convergence in squeezing ground (Figure 4-8).

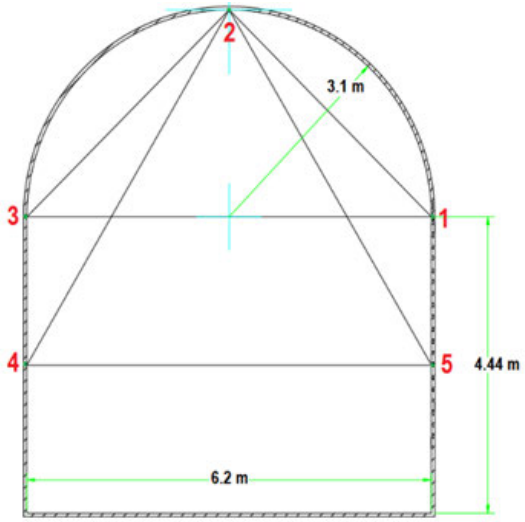

Figure 4-7. Horseshoe tunnel geometry and dimensions.

Table 4-2. Rock mass strength, creep and tunnel geometrical parameters.

ν	c (MPa)	ϕ(°)	σ_{cm}(MPa)	GSI	m_i	m_b	s	a	σ^t	ρ(kg/m³)	R_q(m)	σ_0(MPa)	E (MPa)
0.2	1.28	26	35	40	8	0.94	0.0013	0.5	0.05	2700	5.8	23	3193

η_K(GPa.d)	η_M(GPa.h)	G_K(GPa)	G_M(GPa)	K_H(GPa)	η_B(GPa.h)	η^{β_1}(GPa.h)	η^{β_2}(GPa.h)	$\beta_{1,2}$
49.5	478.97	23.39	2.714	5.88	4.8	4789.7	4.8	0.9

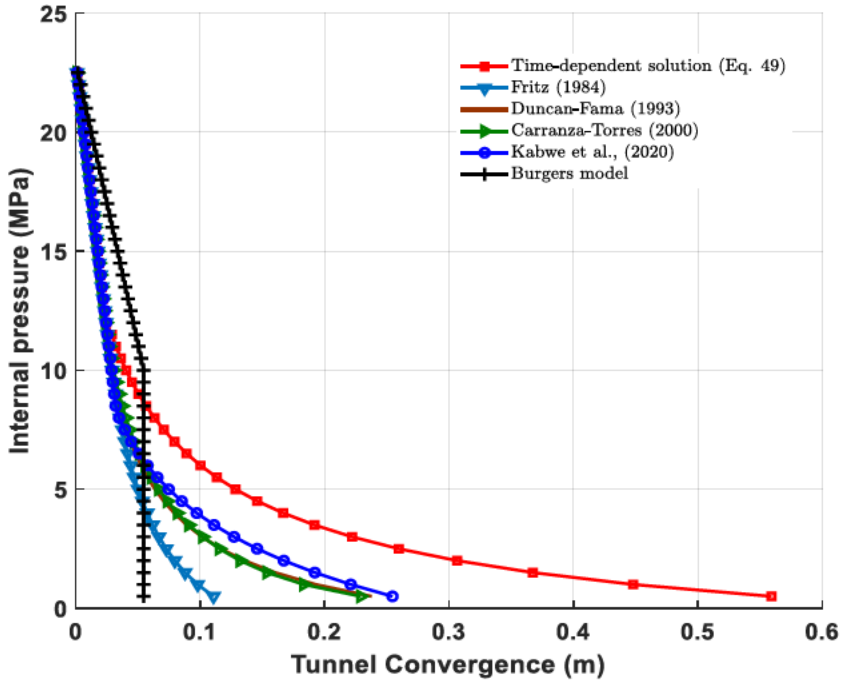

Figure 4-8. Ground response of the time-dependent and conventional solutions

As drawn in Figure 4-8, the time-dependent GRC can be obtained with a decrease in the internal pressure and wall convergence increment around a horseshoe tunnel. The illustration also draws that the time-dependent GRC shifts more to the right because the creep associated deformations change while the internal pressure stays the same. Additionally, for an effective horseshoe tunnel stability analysis, the support structure-squeezing ground interaction is another aspect that requires consideration.

4.4 Determination of the time-dependent convergence in supported tunnels

In unsupported tunnels the internal pressure reduction results in an increased tunnel convergence and extensive yield zone. However, in supported tunnels, the support structure pressure is activated until support -rock mass equilibrium is reached. The appropriate installation time and location of this support structure is

determined by the LDP of unsupported tunnels. Which utilizes the relation between support structure installation timing and nominal tunnel boundary convergence.

4.4.1 Determination of the longitudinal displacement profile

During tunnel stability analysis support elements need to be installed at the appropriate distance behind the face. In such a case the LDP is required to calibrate the tunnel model so that the internal pressure and convergence is correlated to the actual tunnel support setup behind the face. Hence, to determine the appropriate timing for support structure installation and optimization, the LDP is determined based on the Vlachopoulos and Diederichs [59] which considers the maximum plastic radius (R_m) influence. In the LDP analysis, the tunnel face displacement $\left(U_{rf}\right)$ is expressed as:

$$U_{rf} = \left(\frac{U_{rm}}{3}\right) e^{-0.15\left(\frac{R_m}{R_q}\right)} \tag{4-55}$$

Where U_{rm} is the maximum tunnel displacement at R_{max} obtained from Eq. (4-49) by substituting R_P with R_m and the value of R_m is attained from Eq. (4-22) by substituting $(1-\lambda)\sigma_0$ with 0.0. The tunnel wall displacement ahead of the face $(X < 0)$ and behind the face $(X > 0)$ are estimated by Eq. (4-53) and Eq. (4-54) respectively:

$$U_{rx} = \left(\frac{U_{rf}}{U_{rm}}\right) \exp^{\left(\frac{X}{R_q}\right)} \tag{4-56}$$

$$U_{rx} = 1 - \left(1 - \frac{U_{rf}}{U_{rm}}\right) \exp^{\left(\frac{\frac{-3X}{R_q}}{\frac{2R_m}{R_q}}\right)} \tag{4-57}$$

Where U_{rx} is the tunnel wall displacement at distance (X) from the tunnel face. It must be emphasized that the LDP [59] is tailored for EPP rock mass behaviour as such it is not 100% realistic because this study considers time-dependent rock mass behaviour. However, the analysis serves as a demonstration to justify the time-dependent effects on the LDP **and** it is drawn that tunnel convergence is underestimated when the time effect is neglected (Figure 4-9). The LDP curves show that when the time effect is considered delayed tunnel convergence are estimated 80 m behind the face. The relative convergence at 0 - 4 m behind the face using the conventional CCMs and the time-dependent solution are presented in Table 4-3 & A2 (Appendix C). It is also shown in Table 4-4 that the conventional CCMs underestimates U_{rm} and U_{rf} as compared to the time-dependent solution. Additionally, the time-dependent solution overestimates the R_m value responsible for delayed convergence associated with squeezing.

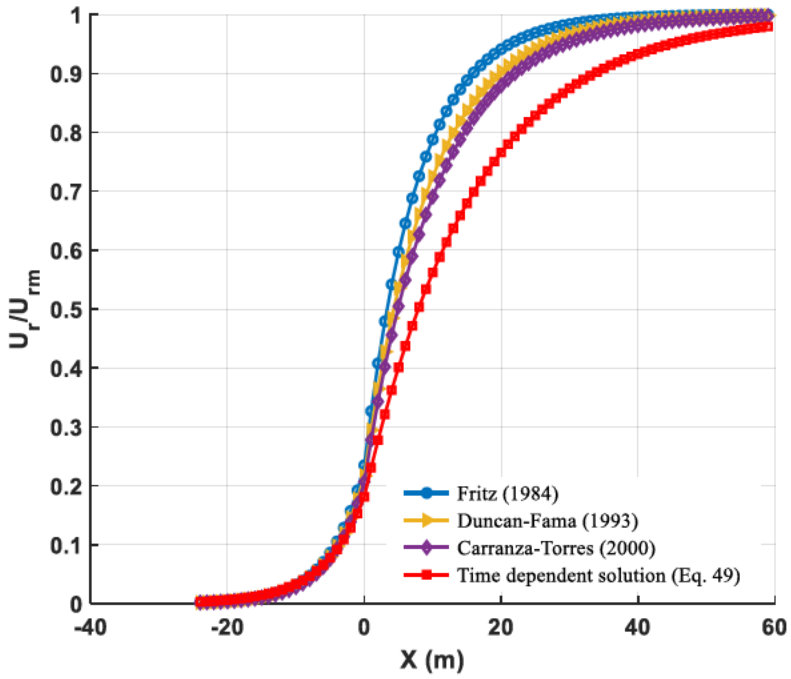

Figure 4-9. LDP estimation using the time-dependent and convergence confinement solutions

Table 4-3. Scaled convergence at a normalized distance behind the tunnel face for different solutions

X (m)	**Fritz**[58]	**Duncan-Fama**[7]	**Carranza-Torres**[9]	**Time-dependent solution (Eq. 49)**
	U_r/U_{rm}			
0	0.24	0.22	0.21	0.18
2	0.41	0.37	0.34	0.28
4	0.54	0.49	0.46	0.36

Table 4-4. Maximum plastic radius, tunnel and face displacement for different solutions

	Fritz[58]	**Duncan-Fama**[7]	**Carranza-Torres**[9]	**Time-dependent solution**
R_m	11.70	14.30	15.92	23.98
U_{rm}	0.08	0.26	0.29	0.48
U_{rf}	0.02	0.06	0.06	0.09

Installation of an appropriate support structure is important for the effective and efficient stability of tunnels in squeezing ground. This can be done by considering the capacity and safety coefficient of the installed support structures. The estimation of these parameters requires the employment of the SCC which describes the stress-strain relations of the support structure-rock mass interaction.

4.4.2 Tunnel support capacity estimation

Tunnel pre-deformation behind its advancing face is dependent on the installed support structure and tunnel construction process. The bearing capacity of support measure of this installed support structure can be determined by the SCC. Which defines the support pressure (p_i) at the predetermined tunnel convergence

by a mathematical formulation associated with its estimated parameters (support stiffness (K_s), support capacity (p_{smax}) and support structure yield at certain tunnel convergence (U_{iy})) (Figure 4-10). This mathematical formulation consists of three important components:

- convergence at the support structure installation point (U_{io}).
- support structure elastic deformation (U_{im}).
- support structure plastic deformation (U_{ip}).

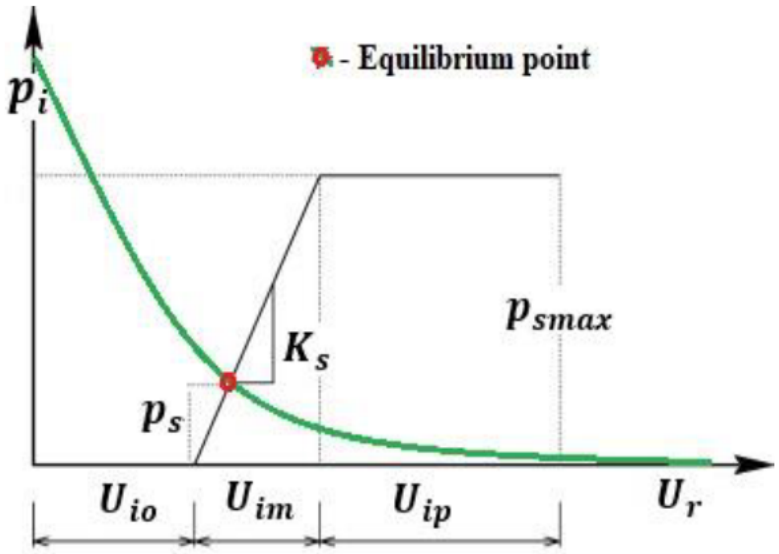

Figure 4-10. Schematic representation of the support and ground response interaction

The p_i provided by this installed support structure restrains the tunnel convergence and yield extension around the tunnel (Eq. (4-55)). If the support structure is installed at a given distance behind the tunnel face, the U_{io} at this estimated distance is attained using the LDP. The support structure installed at this location tends to undergo some form of yielding estimated by Eq (4-56).

$$p_i = K_s \frac{U_r}{R_q} \tag{4-58}$$

$$U_{iy} = U_{io} + U_{im} = U_{io} + \frac{p_{smax}}{K_s} \tag{4-59}$$

4.4.2.1 Support characteristic curve construction

In the supported tunnels, the support structure is installed after the occurrence of an instantaneous elastic deformation[15]. In this paper, the tunnel face effects, and rock mass-support interaction is considered. If t_0 is the elapsed time until support structures are installed before that time it was unsupported $(t \leq t_0)$. During excavation, it is assumed that the support structure is installed instantaneously at $t = t_0$ as such convergence at this time is neglected. When $t \leq t_0$ the tunnel convergence is calculated from Eq. (4-14) whereas when $t > t_0$ excavation is halted and the ground pressure on the support structure is related to the tunnel convergence by:

$$p_{smax} = K_s \left(\frac{U_r(t)}{R_q} - \frac{U_r(t_0)}{R_q} \right) \tag{4-60}$$

Where $U_r(t)$ and $U_r(t_0)$ are the tunnel convergence after and before support structure installation, respectively. The tunnel radial stress, in this case, will be the sum of p_{smax} and the pseudo internal pressure $((1-\lambda)\sigma_0)$ expressed by Eq. (4-61) and the radial deviatoric stress of the tunnel wall can be expressed by Eq. (4-62):

$$\sigma_r = p_{smax} + (1-\lambda)\sigma_0 \tag{4-61}$$

$$s_r = \sigma_r - \sigma_m = p_{smax} + (1-\lambda)\sigma_0 - \sigma_0 = p_{smax} - \lambda\sigma_0 \tag{4-62}$$

$$U_r(t) = R_q \frac{(p_{smax} - \lambda\sigma_0)}{2}\left[\frac{1}{G_M} + \frac{t^{\beta_1}}{\eta^{\beta_1}\Gamma(1+\beta_1)} + \frac{1}{G_K}\left[1 - exp\left(-\frac{t}{T_K}\right)\right] + \left(\frac{\sigma_0 - \sigma_Y}{\eta^{\beta_2}}\frac{t^{\beta_2}}{\Gamma(1+\beta} \right.\right. \quad \text{(4-63)}$$

Therefore, the substitution of Eq. (4-60) into Eq. (4-57) one gets the expression for p_{smax} as:

$$\begin{cases} p_{smax} = K_s\left(\dfrac{(p_{smax} - \lambda\sigma_0)}{2G(t)} - \dfrac{(\lambda\sigma_0)}{2G(t_0)}\right) \\ \dfrac{1}{G(t)} = \left[\dfrac{1}{G_M} + \dfrac{t^{\beta_1}}{\eta^{\beta_1}\Gamma(1+\beta_1)} + \dfrac{1}{G_K}\left[1 - exp\left(-\dfrac{t}{T_K}\right)\right] + \left(\dfrac{\sigma_0 - \sigma_Y}{\eta^{\beta_2}}\dfrac{t^{\beta_2}}{\Gamma(1+\beta_2)}\right)\right] \\ \dfrac{1}{G(t_0)} = \left[\dfrac{1}{G_M} + \dfrac{t_0^{\beta_1}}{\eta^{\beta_1}\Gamma(1+\beta_1)} + \dfrac{1}{G_K}\left[1 - exp\left(-\dfrac{t_0}{T_K}\right)\right] + \left(\dfrac{\sigma_0 - \sigma_Y}{\eta^{\beta_2}}\dfrac{t_0^{\beta_2}}{\Gamma(1+\beta_2)}\right)\right] \end{cases} \quad \text{(4-64)}$$

Provided that the installed support structure can hold the rock mass, its SCC intersects the tunnel GRC at an equilibrium point (Figure 4-10). At this point, the tunnel convergence is equal to the support yield this further allows the determination of the support structure safety coefficient (FS).

$$FS = \frac{p_{smax}}{p_s} \quad \text{(4-65)}$$

The installed support structure can be considered suitable within a tunnel if its safety coefficient is greater than the allowable limit ($FS \geq F_{s\,min}$). However, unsupported excavations in squeezing ground conditions experience severe strain (20%) which makes it extremely challenging. In such conditions, the support structure is installed early enough to maintain a safe working area behind the face and delayed enough to avert load build-up and consequent failure. Besides, early support structure installation results in a low short-term safety coefficient and an unsuitable long-term safety coefficient (< 1.0). However, the safety coefficient can be more appropriate by installing support structures at the right time (Figure 4-11).

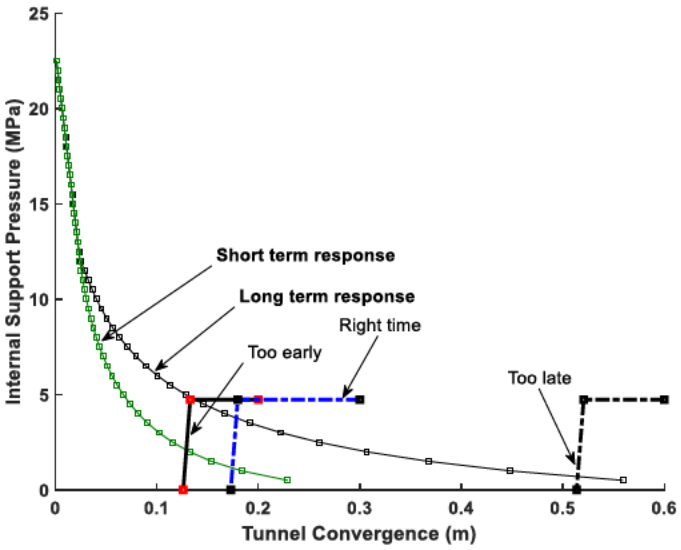

Figure 4-11. Ground reaction and support characteristic curves

4.4.2.2 Support characteristic curves of individual and composite support elements

The complexity of support structure mechanical behaviour considers the support-rock mass interaction entirely understood by employing the CCMs and equations that characterize this interaction. The effective application of the support structures requires the estimation of stiffness, maximum acceptable pressure, elastic displacement and allowable failure displacement[10] (Appendix C: Eqs. A8 – A13). Figure 4-12 shows the GRC and the SCC constructed based on the time-dependent solution and CCMs. The ground pressure expected to act on the support structure is determined at their GRC - SCC intersection. This pressure is compared between the time-dependent solution and CCMs and it is drawn that the CCM defined support structure overload under the time-dependent based GRC (long-term GRC). These results indicate that the CCMs unrealistically estimate the tunnel support structure capacity in squeezing ground. Figure 4-12a shows that employing shotcrete (t = 0.5) as a standalone support element is inappropriate for effective tunnel stability in squeezing ground. However, when installed by employing the CCM and Eq. (4-62) an estimated safety

coefficient of 1.6 and 1.7 above the allowable limit is attained. Figure 4-12b draws that the steel set support element installed early at a location estimated by the CCM is overloaded under the long-term GRC. Whereas if installed at a delayed location estimated by the time-dependent solution it is subjected to a lower load at equilibrium. As a result, the delayed support installation estimates a long-term safety coefficient of 1.2 this signifies the importance of installing support structures at the right time and location.

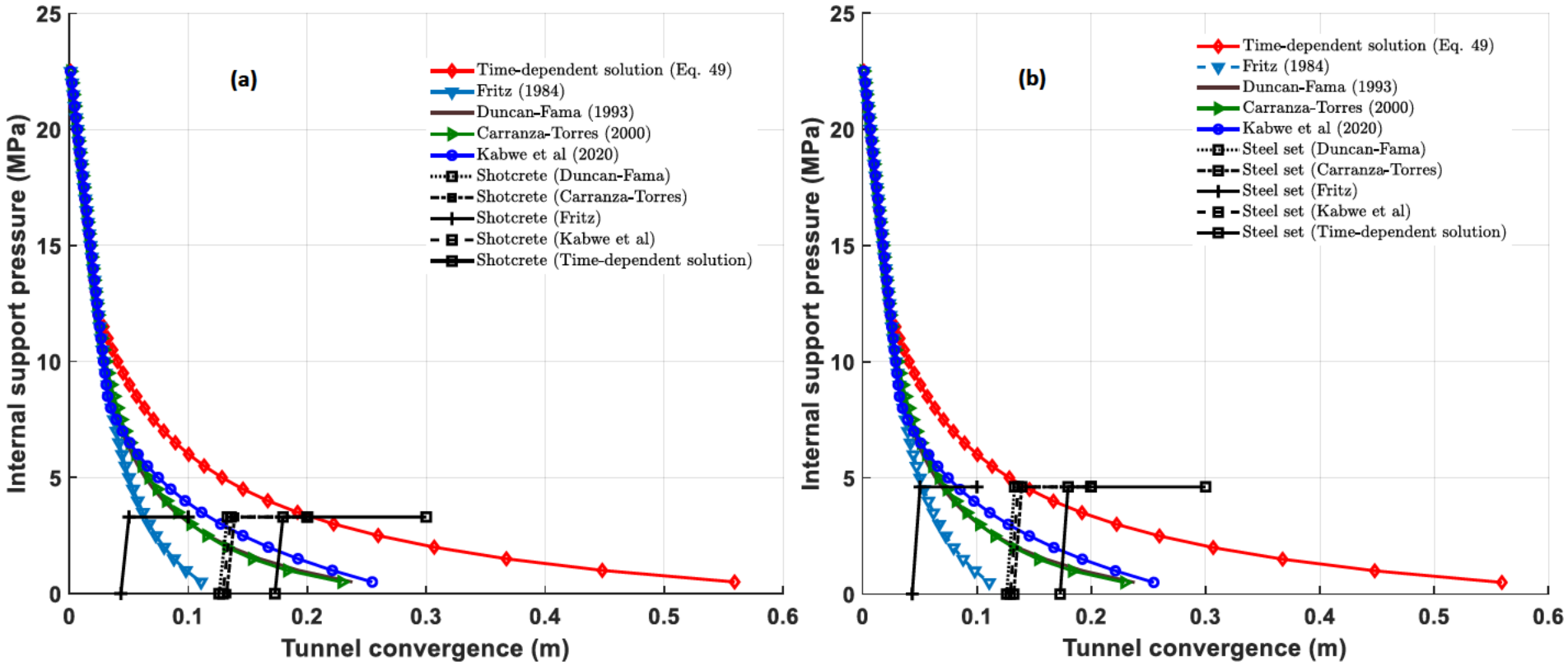

Figure 4-12. Ground response and individual support element interaction: (a) Shotcrete (t = 0.5) and (b) Steel sets.

Besides, the effect of two or more support elements installed at the same location behind the tunnel face can be determined by their accumulative stiffness. When steel set, shotcrete and cable bolts are merged in a single application the accumulative stiffness (K_{st}) of this composite structure is:

$$K_{st} = K_{ss} + K_{sb} + K_{sc} \tag{4-66}$$

The individual support element with low U_{im} is employed to ascertain p_{smax} of the composite support structure:

$$U_{im} = \frac{p_{smax}}{K_{st}} \tag{4-67}$$

The composite support structure considered in this analysis with their p_{smax} and K_{st} values are presented in Appendix C: Table C 5. It is composed of 0.3 m thick shotcrete, steel sets and cable bolts. Figure 4-13 illustrates the SCC effect of the SCCB (shotcrete + cable bolts) and STSCCB (steel sets + shotcrete + cable bolts) composite support structures. If the SCCB support structure is installed at the CCM defined location behind the face, the structure fails to restrain the long-term convergence associated with squeezing (Figure 4-13a). It is drawn that the SCCB support structure will be subjected to failure as compared to its short-term application with the safety coefficient between 1.0-1.1. As such application of the support structure at the time-dependent solution and CCM defined locations will be inappropriate to restrain tunnel convergence in squeezing ground. Besides, the installation location estimated in the long-term by the time-dependent solution raises the safety coefficient for the CCM defined support structure. Employing the STSCCB support structure at the CCM defined position estimates a low safety coefficient in the long-term as compared to the time-dependent solution defined location (Figure 4-13b). The support structure has a safety coefficient of 1.8 in the long-term when installed at the time-dependent solution defined location. Hence, the STSCCB support

structure is more appropriate to restrain tunnel convergence in squeezing ground when installed at a time-dependent solution determined location behind the advancing tunnel face.

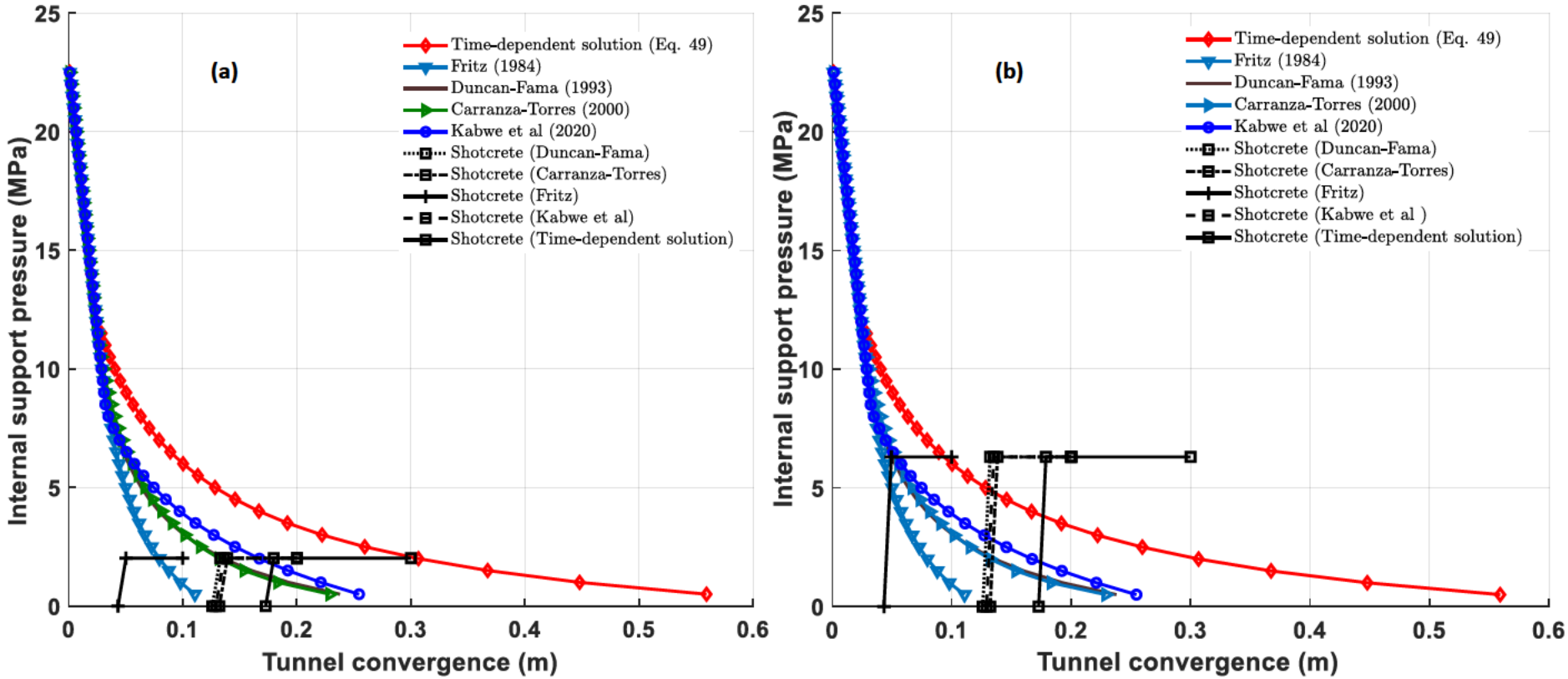

Figure 4-13. Ground response and composite support structure interaction: (a) SCCB (t = 0.3) and (b) STSCCB (t = 0.3).

4.5 Discussion

The study presented herein shows that during tunnel excavation, the convergence should be considered a function of tunnel advancement and the time-dependent behaviour of the rock mass. The traditional CCMs employed to estimate the LDP and GRC neglect this time-dependent behaviour as such fail to realistically estimate delayed deformations associated with squeezing. The analysis conducted to estimate the time-dependent tunnel convergence comprise of; 1) derivation of a time-dependent closed-form solution, 2) verification of the derived solution using creep models, 3) extension of the time-dependent closed-form solution to a ground reaction solution and estimation of the support structure capacity.

The closed-form solution based on the FDVP constitutive model employs constitutive equations which realistically describe the creep behaviour of rock mass. This makes it a better fit to describe the time-dependent ground response of tunnels in squeezing ground as compared to the integer-order derivative-based constitutive equations. The study is conducted to describe the time-dependent creep behaviour of tunnels in squeezing ground and the constitutive equations derived appear to be adequate for its description.

The derived closed-form solution is compared with existing viscoelastic and viscoplastic models and agrees very well with other time-dependent viscoplastic models. This signifies that the closed-form solution is robust for the accurate estimation of tunnel convergence. Its extension, the time-dependent ground response solution is further compared with the Burgers model and the conventional CCMs in a horseshoe tunnel. This extended solution estimates the delayed ground reaction experienced within tunnels excavated in adverse squeezing ground conditions. It estimates the delayed ground response as such addresses the limitation that the conventional CCMs face during tunnel stability analysis in squeezing ground.

The convergence estimation and support structure design of tunnels in EPP rock mass tend to be unrealistic because during excavation the assumption considered underestimate the stress relief. Additionally, the

estimation of tunnel support capacity by considering these assumptions proves to be inadequate in squeezing ground conditions. Also, an important factor to be considered in support design is the time and location of these support structure installation. Even though they must be installed immediately behind the face for a safe working environment their installed support capacity cannot be activated.

It is drawn from section 4 that the SCCB support structure installation is ineffective whereas the STSCCB support structure installation is more appropriate in squeezing ground. Moreover, the installation of the composite support structure increased the safety coefficient as compared to the individual support elements. Installation of the support structure can be more effective if we consider the life of the tunnel either temporal or permanent. However, in this study the allowable tunnel closure considered applies for a temporal tunnel as such the STSCCB support structure is installed at tunnel convergence (0.17 m). It has been drawn that the conventional CCMs employed for LDP and GRC estimation neglect the time-dependent convergence which occurs over time. The convergence considered in this study is characterized by creep which can be estimated by employing the presented solution.

4.6 Conclusion

A time-dependent ground reaction solution is presented for unsupported and supported non-circular tunnels in the rock mass which exhibit EVP behaviour. The solution is successfully derived as an extension of the closed-form solution based on the newly proposed FDVP constitutive equations. It is further tailored for estimation of the delayed ground reaction within horseshoe tunnels excavated in squeezing ground. It is drawn from the results that the solution estimates delayed deformations responsible for squeezing realistically with about 14% convergence and maximum yield extension of 23 m. whereas the CCMs unrealistically underestimates the convergence between 2.5% - 5% and the yield extension between 12 m - 16 m. On the other hand, the solution's estimation accounts for 10% and 50% more tunnel convergence and yield extension respectively.

Additionally, the solution determines the suitable long-term safety coefficient for support structure installed at the right time and location behind the tunnel face in squeezing ground. It is drawn that steel sets installed at 0.17 m tunnel convergence exhibited a safety coefficient of 1.2 in the long-term. This is further increased to 1.8 when the STSCCB support structure is installed at the same defined location. This shows that for this tunnel excavated in squeezing ground characterized by the FDVP constitutive law with a viscoplastic flow rule the STSCCB support structure is the most appropriate for convergence restraint. It is the most suitable based on the support structure capacity estimation, installation timing and location.

Ultimately, the presented solution addresses the limitation encountered during time-dependent convergence estimation in squeezing ground. It also shows that the time-dependent behaviour is a significant factor to be considered in ground reaction and stability assessment of tunnels in squeezing ground. Hence, the solution can be a useful tool for the optimum tunnel and support structure design based on the ground reaction-support structure interaction in squeezing ground

Appendix A. Derivation of the EVP constitutive equations

The following relation (A1) is employed to describe the EVP model by taking $\sigma(t) = \sigma$ (constant stress) given by:

$$\sigma^v = \eta \dot{\varepsilon}^p \tag{A1}$$

Where σ^v is the viscous stress, η is the viscosity coefficient and $\dot{\varepsilon}^p$ is the plastic strain rate. Given that the total stress σ_0 is the sum of viscous stress σ^v, the initial yield stress σ_Y and hardening stress $R(\varepsilon^p)$ as shown:

$$\sigma_0 = \sigma^v + \sigma_Y + R(\varepsilon^p) \tag{A2}$$

Substituting Eq. A1 into Eq. A2 and differentiating for $\dot{\varepsilon}^p$ gives:

$$\dot{\varepsilon}^p = \frac{\sigma_0 - \sigma_Y - R(\varepsilon^p)}{\eta} \tag{A3}$$

The total strain ε is the sum of the elastic strain and the plastic strain ε^p gives:

$$\varepsilon = \frac{\sigma_0}{E} + \varepsilon^p \tag{A4}$$

Where E is the stiffness matrix, assuming no isotropic hardening $R(\varepsilon^p) = 0$ then integration of Eq. A3 to time gives the total strain as:

$$\varepsilon(t) = \frac{\sigma_0}{E} + \frac{\sigma_0 - \sigma_Y}{\eta} t \tag{A5}$$

Viscoplastic model without hardening assumes that the material behaves elastically below the yield stress σ_Y level and undergoes viscoplastic behaviour above the σ_Y expressed by:

$$\varepsilon(t) = \begin{cases} \frac{\sigma_0}{E} & \sigma_0 < \sigma_Y \\ \frac{\sigma_0}{E} + \frac{\sigma_0 - \sigma_Y}{\eta} t & \sigma_0 \geq \sigma_Y \end{cases} \quad \text{(A6)}$$

Combining the Burgers viscoelastic material formulation [15] and Eq. A6, the relationship between strain and time is given by:

$$\varepsilon(t) = \begin{cases} \sigma_0 \left\{ \frac{1}{G_M} + \frac{t}{\eta_M} + \frac{1}{G_K} \left[1 - exp\left(-\frac{t}{T_K} \right) \right] \right\}, & \sigma_0 < \sigma_Y \\ \sigma_0 \left\{ \frac{1}{G_M} + \frac{t}{\eta_M} + \frac{1}{G_K} \left[1 - exp\left(-\frac{t}{T_K} \right) \right] + \left(\frac{\sigma_0 - \sigma_Y}{\eta_B} t \right) \right\}, & \sigma_0 \geq \sigma_Y \end{cases} \quad \text{(A7)}$$

Where η_B are the viscoplastic component viscosity coefficient and retardation time $T_k = \eta_K / G_K$. The theory of hardening can be a justification for the deferred plastic deformation developed during creeping at both low-stress levels ($< \sigma_Y$) and high-stress levels.

Appendix B: Constitutive model calibration

In this section, the FDVP constitutive model is calibrated based on experimental data achieved from salt rock[52] and Jinping marble[53] sample creep tests. The constitutive model parameters are calibrated by creep curves attained from the experimental data of salt rock over 1256 days. Neglecting damage and viscoplastic hardening subjected to the uniaxial stress load σ_0 = 14.1 MPa with σ_Y = 8.46 MPa (Figure A 1a). Additional creep curves attained from the experimental data of marble under uniaxial stress load σ_0 = 125.5 MPa with σ_Y = 130.1 MPa over 50 hours is used for further model calibration (Figure A 1b).

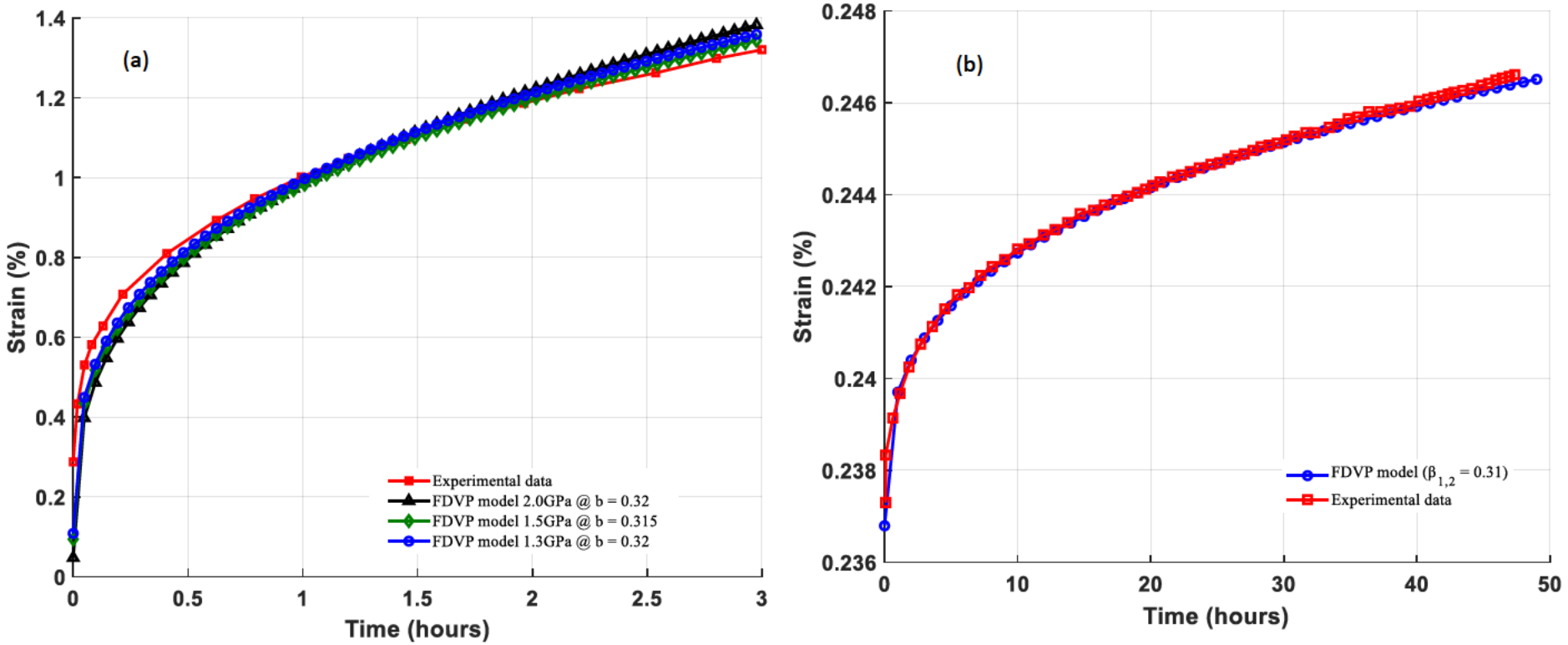

Figure A 1. Calibration of the FDVP model using experimental data: (a) salt rock[52] and (b) Jinping marble[53]

Figure A 2 illustrates the results attained from the evaluation of the critical parameters $\beta_{1,2}$ effect on the creep curves. Figure A 2a shows creep curves obtained from salt rock indicating that the higher the values of $\beta_{1,2}$ the greater the creep strain. Figure A 2b draws the creep curves attained from marble and it is shown that the rise in the $\beta_{1,2}$ values have an incremental effect on the creep strain rates. This indicates the importance of choosing an appropriate value of $\beta_{1,2}$ to realistically describe the viscoelastic and viscoplastic behaviour of rocks or rock masses. Hence, optimized $\beta_{1,2}$ values are required when the FDVP constitutive model is employed for time-dependent deformation estimation in squeezing ground and the values attained are between 0.2 - 0.32 with 0.315 as the most accurate.

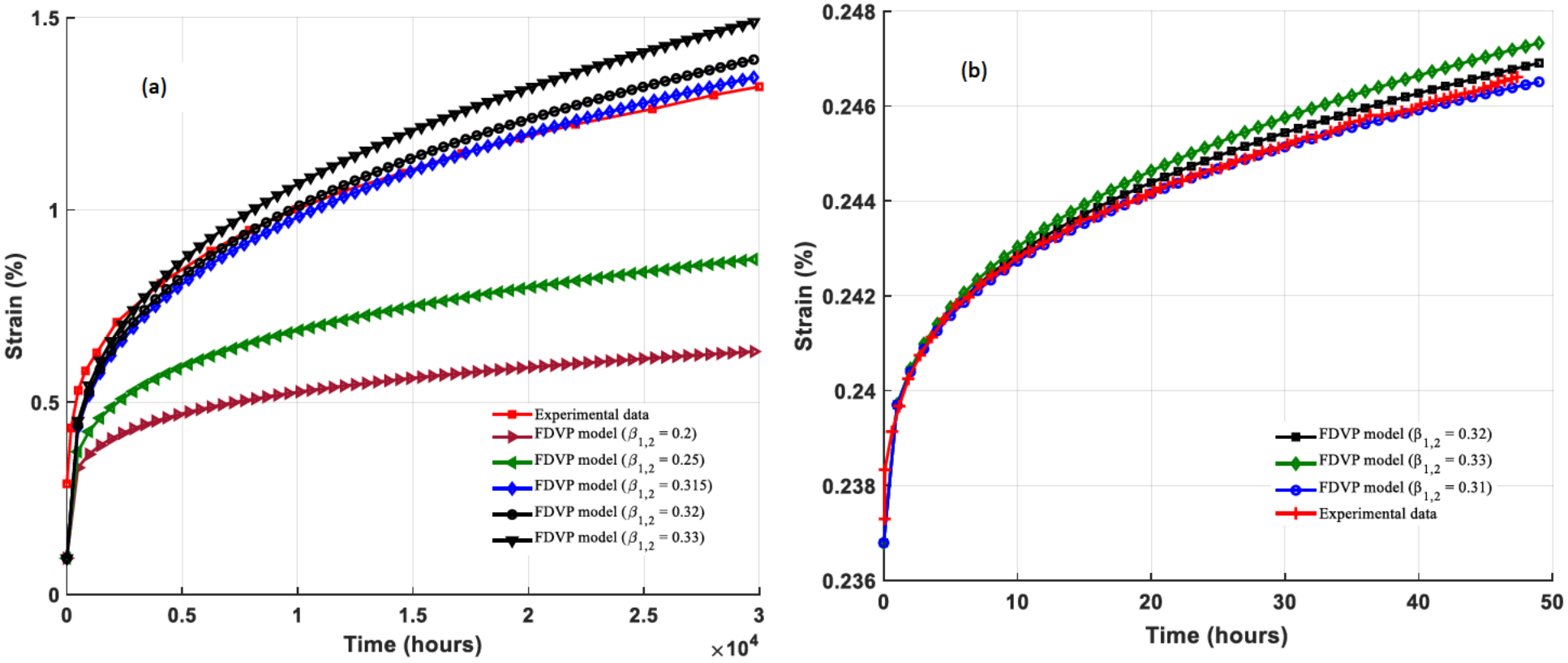

Figure A 2. Fractional-order coefficient effect on the FDVP model : (a) salt rock[52] and (b) Jinping marble[53]

The evaluation of the stress level effect on the creep strain rates is conducted by keeping other parameters constant while changing the stress levels. The stress level applied on the salt rock range between 14.1 MPa – 26 MPa and it is observed that the stress level rise has an incremental effect on the strain rates (Figure A 3a). Additionally, the creep strain response of the marble subjected to an incremental applied stress level (125.5 MPa - 160 MPa) is shown in Figure A 3b. It is drawn from these illustrations that an increment in the applied stress level upsurges the creep strain rates.

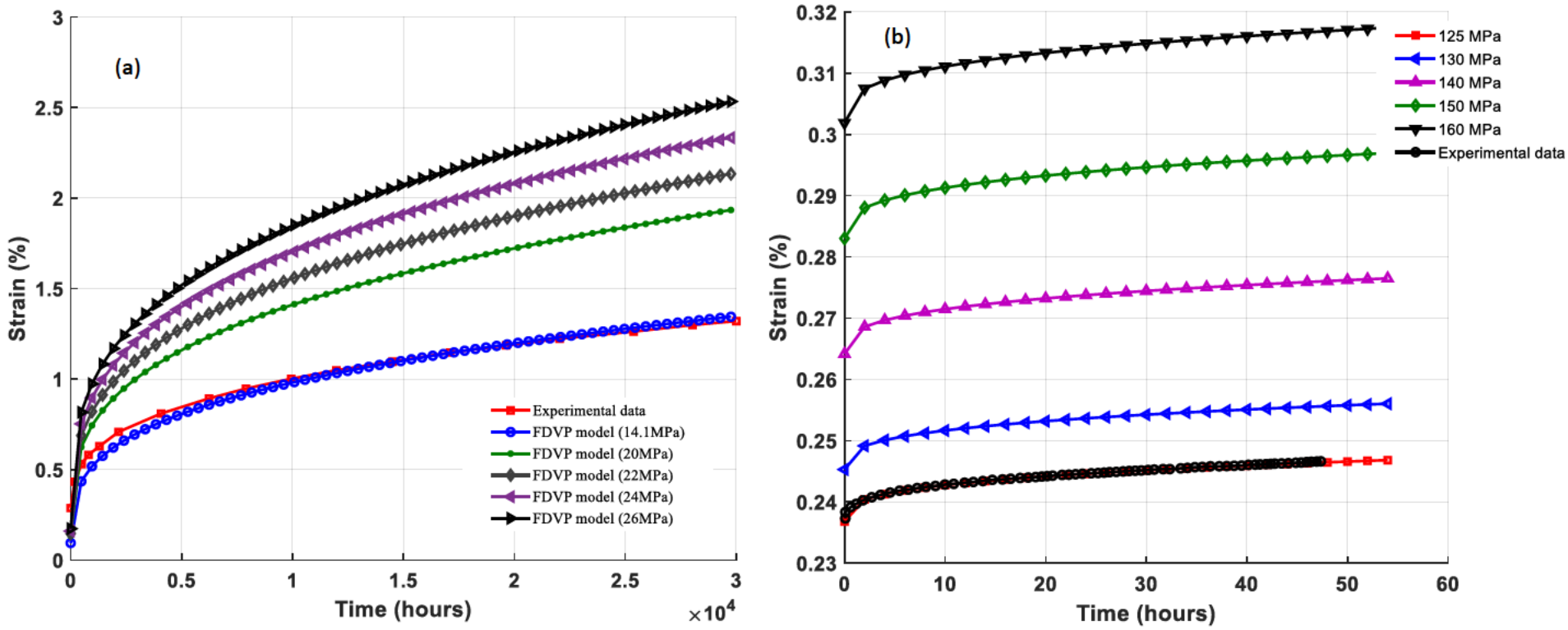

Figure A 3. Stress change effect on the FDVP model: (a) salt rock[52] and (b) Jinping marble[53]

Appendix C: Estimation of the Support capacity

The formulations for support element capacity estimation employed in this study are expressed by:

$$p_{ssmax} = \frac{A\sigma_{ys}}{\omega R} \tag{A8}$$

$$K_{ss} = \frac{E_s A}{\omega R^2} \tag{A9}$$

$$p_{scmax} = \frac{\sigma_{cc}}{2}\left[1 - \frac{(R-t)^2}{R^2}\right] \tag{A10}$$

$$K_{sc} = \frac{E_c(R^2 - (R-t)^2)}{2(1-v^2)(R-t)R^2} \tag{A11}$$

$$p_{sbmax} = \frac{T}{\omega_l R_c} \tag{A12}$$

$$K_{sb} = \frac{E_b \pi D^2}{4l\omega_l R_c} \tag{A13}$$

Where:

p_{ssmax} - maximum steel set support pressure

A - cross-section area

σ_{ys} - yield strength of steel

ω - set spacing along the tunnel

K_{ss} - stiffness of the steel sets

E_s - young modulus of the steel

p_{scmax} - maximum shotcrete support pressure

σ_{cc} - uniaxial compressive strength of the shotcrete

t – shotcrete thickness

K_{sc} – shotcrete stiffness

p_{sbmax} - maximum cable bolt pressure

T - ultimate cable load

ω_l - longitudinal cable bolt spacing

R_c - circumferential cable bolt spacing

K_{sb} - cable bolt stiffness

E_b - cable bolt young modulus

D^2 - cable diameter

l - cable bolt free length

Table C 1 presents the support structure properties employed in this study, Table C 3 present estimations of the SCCs, the p_{smax} , K_s , U_{io} values and their results are presented in Table C 4 – C 7.

Table C 1. Support element mechanical and geometrical properties

	Steel sets (without wood blocks)			**Shotcrete**			
A	109.27 m²	p_{ssmax}	4.61 MPa	A	109.27 m²	p_{scmax}	2.02 MPa
E_s	207000 MPa	K_{ss}	672.38 MPa/m	E_c	30000 MPa	K_{sc}	286.29 MPa/m
σ_y	245 MPa	p_{smax}/K_{ss}	0.0069 m	σ_{cc}	40 MPa	p_{scmax}/K_{sc}	0.0070 m
R_q	5.8 m			R_q	5.8 m	v	0.2
ω	1 m			t	0.3 m		
	Shotcrete						
A	109.27 m²	p_{scmax}	3.30 MPa	A	109.27 m²	p_{scmax}	6.30 MPa
E_c	30000 MPa	K_{sc}	486.39 MPa/m	E_c	30000 MPa	K_{sc}	1025.72 MPa/m
σ_{cc}	40 MPa	p_{scmax}/K_{sc}	0.00679 m	σ_{cc}	40 MPa	p_{scmax}/K_{sc}	0.00614 m
R_q	5.8 m	v	0.2	R_q	5.8 m	v	0.2
t	0.5 m			t	1.0 m		
	Cable bolts						
T	0.354 MN	l	14 m				
ω_b	1.0 m	R_q	5.8 m				
R_c	1.0 m	p_{sbmax}	0.354 MPa				
E_b	207000 MPa	K_{sb}	13.424 MPa/m				
D	0.034 m	p_{scmax}/K_{sb}	0.02637				

Table C 2. Convergence at a distance behind the tunnel face for different solutions

X (m)	**Fritz**[58]	**Duncan-Fama**[7]	**Carranza-Torres**[9]	**Time-dependent solution (Eq. 49)**
1	0.026	0.077	0.081	0.110
2	0.033	0.095	0.100	0.134
3	0.038	0.111	0.117	0.154
4	0.043	0.126	0.132	0.173
5	0.048	0.139	0.146	0.192

Table C 3. Calculated results for the support characteristic curve

	Steel sets		**shotcrete**					
			0.3 m		**0.5 m**		**1.0 m**	
	MPa	m	MPa	m	MPa	m	MPa	m
Duncan-Fama[7]	4.61	0.2	2.02	0.2	3.3	0.2	6.3	0.2
	4.61	0.133	2.02	0.133	3.3	0.133	6.3	0.132
	0	0.126	0	0.126	0	0.126	0	0.126
Fritz[58]	4.61	0.1	2.02	0.1	3.3	0.1	6.3	0.1
	4.61	0.050	2.02	0.050	3.3	0.050	6.3	0.0495
	0	0.043	0	0.043	0	0.043	0	0.043
Carranza-Torres[9]	4.61	0.2	2.02	0.2	3.3	0.2	6.3	0.2
	4.61	0.139	2.02	0.139	3.3	0.139	6.3	0.138
	0	0.132	0	0.132	0	0.132	0	0.132
Time-dependent solution (Eq. 49)	4.61	0.3	2.02	0.3	3.3	0.3	6.3	0.3

	4.61	0.1797	2.02	0.1798	3.3	0.1796	6.3	0.179
	0	0.173	0	0.173	0	0.173	0	0.173

Table C 4. Support elements SCC parameters

Support	p_{smax} **(MPa)**	K_s **(MPa/m)**	U_{im}**(m)**
Shotcrete (t = 0.3 m)	2.02	286.29	0.0070
Shotcrete (t = 0.5 m)	3.30	486.39	0.0068
Steel set	4.61	672.38	0.0069
Cable bolt	0.35	13.42	0.0264

Table C 5. Composite support structure SCC parameters

Support	p_{smax} **(MPa)**	K_{st} **(MPa/m)**	U_{im}**(m)**
Shotcrete (t = 0.3 m) + Cable bolt	2.10	299.714	0.0070
Shotcrete (t = 0.5 m) + Cable bolt	3.39	499.814	0.0068
Steel set + Cable bolt	4.73	685.804	0.0069
Shotcrete (t = 0.3 m) + Cable bolt + Steel set	6.71	972.094	0.0069

Table C 6. Displacement results at GRC-SCC equilibrium points for Individual support elements

			Fritz[58]	**Duncan-Fama**[7]	**Carranza-Torres**[9]	**Time-dependent solution (Eq. 49)**
	U_{io}		0.0433	0.126	0.132	0.173
Shotcrete	U_{iy}	0.3 m	0.050	0.133	0.139	0.180
		0.5 m	0.050	0.133	0.139	0.180
		1.0 m	0.050	0.132	0.138	0.179

Steel sets	U_{iy}	0.050	0.133	0.139	0.180

Table C 7. Displacement results at GRC-SCC equilibrium points for the composite support structure

		Fritz[58]	**Duncan-Fama**[7]	**Carranza-Torres**[9]	**Time-dependent solution (Eq. 49)**
	U_{io}	0.04	0.13	0.13	0.17
Shotcrete (t = 0.5 m) + Cable bolt	U_{iy}	0.05	0.13	0.14	0.18
Shotcrete (t = 0.3 m) + Cable bolt	U_{iy}	0.05	0.13	0.14	0.18
Steel set + Cable Bolt	U_{iy}	0.05	0.13	0.14	0.18
Shotcrete (t = 0.3 m) + Cable bolt + Steel set	U_{iy}	0.05	0.13	0.14	0.18

4.7 References

[1] Panet M. Understanding deformations in tunnels. Compr Rock Eng 1993;1:663–90.

[2] Barla G. Squeezing rocks in tunnels. ISRM News J 1995;2:44–9.

[3] Sulem J, Panet M, Guenot A. An analytical solution for time-dependent displacements in a circular tunnel. Int. J. rock Mech. Min. Sci. Geomech. Abstr., vol. 24, Elsevier; 1987, p. 155–64.

[4] Ladanyi B. Time-dependent response of rock around tunnels. In Analysis and Design Methods 1993;77-112. Pergamon.

[5] Gnirk PF, Johnson RE. The deformational behavior of a circular mine shaft situated in a viscoelastic medium under hydrostatic stress. 6th US Symp. Rock Mech., American Rock Mechanics Association; 1964.

[6] Ladanyi B, Gill DE. 3 Tunnel lining design in a creeping rock. Des. Perform. Undergr. Excav. ISRM Symp. UK, 3–6 Sept. 1984, Thomas Telford Publishing; 1984, p. 19–26.

[7] Duncan E. Fama. Numerical modeling of yield zones in weak rock. In Analysis and design methods. Pergamon. 1993:49–75.

[8] Brown ET, Bray JW, Ladanyi B, Hoek E. Ground response curves for rock tunnels. Journal of Geotechnical Engineering. 1983;109:15–39.

[9] Carranza-Torres C, Fairhurst C. The elasto-plastic response of underground excavations in rock masses that satisfy the Hoek–Brown failure criterion. Int J Rock Mech Min Sci 1999;36:777–809.

[10] Kabwe E, Karakus M, Chanda EK. Proposed solution for the ground reaction of non-circular tunnels in an elastic-perfectly plastic rock mass. Comput Geotech 2020;119:103354.

[11] Cui L, Zheng J-J, Zhang R-J, Lai H-J. A numerical procedure for the fictitious support pressure in the application of the convergence–confinement method for circular tunnel design. Int J Rock Mech Min Sci 2015;78:336–49.

[12] Pan YW, Dong JJ. Time-dependent tunnel convergence-I. Formulation of the model. Int J Rock Mech Min Sci 1991;28:469–75.

[13] Nomikos P, Rahmannejad R, Sofianos A. Supported Axisymmetric Tunnels Within Linear Viscoelastic Burgers Rocks. Rock Mech Rock Eng 2011;44:553–64.

[14] Birchall TJ, Osman AS. Response of a tunnel deeply embedded in a viscoelastic medium. Int J Numer Anal Methods Geomech 2012;36:1717–40.

[15] Fahimifar A, Tehrani FM, Hedayat A, Vakilzadeh A. Analytical solution for the excavation of circular tunnels in a visco-elastic Burger's material under hydrostatic stress field. Tunn Undergr Sp Technol 2010;25:297–304.

[16] Gschwandtner GG, Galler R. Input to the application of the convergence confinement method with time-dependent material behaviour of the support. Tunn Undergr Sp Technol Inc Trenchless Technol Res 2012;27:13–22.

[17] Wang HN, Jiang MJ, Zhao T, Zeng GS. Viscoelastic solutions for stresses and displacements around non-circular tunnels sequentially excavated at great depths. Acta Geotech 2019;14:111–39.

[18] Potvin, Y., & Hadjigeorgiou J. Ground support strategies to control large deformations in mining excavations. J South African Inst Min Metall 2008;108:397–404.

[19] Varden RP, Woods MJ. Design approach for squeezing ground. Proc. Int. Semin. Des. Methods Undergr. Min., Australian Centre for Geomechanics 2015; 489–504.

[20] Karampinos E, Hadjigeorgiou J, Turcotte P, Mercier-Langevin F. Large-scale deformation in underground hard-rock mines. J South African Inst Min Metall 2015;115:645–52.

[21] Roache B. Mining in extreme squeezing conditions at the Henty mine Mining in extreme squeezing conditions at the Henty mine 2016:0–13.

[22] Kabwe E. Mining Sequence Deformation and Failure Behaviour Analysis in the hangingwall and Orebody Rock Formations; A Continuum Approach. Geotech Geol Eng 2017;35.

[23] Kabwe E. Optimal mining method selection for Nchanga's Upper Orebody using analytic hierarchy process and Yager's method. Trans Institutions Min Metall Sect A Min Technol. 2017;126.

[24] Kabwe, Eugie & Karakus M. Creep constitutive model considering the overstress theory with an associative viscoplastic flow rule. Computers and Geotechnics. 2020;124:103629.

[25] Karakus M. Appraising the methods accounting for 3D tunnelling effects in 2D plane strain FE analysis. Tunn Undergr Sp Technol. 2007;22:47–56.

[26] Sadeghiyan R, Hashemi M, Moloudi E. Determination of longitudinal convergence profile considering effect of soil strength parameters. International Journal of Rock Mechanics and Mining Sciences. 2016;82:10-21

[27] Oke J, Vlachopoulos N, Diederichs M. Improvement to the convergence-confinement method: inclusion of support installation proximity and stiffness. Rock mechanics and rock engineering. 2018;51(5):1495-519

[28] Yan Q, Li SC, Xie C, Li Y. Analytical Solution for Bolted Tunnels in Expansive Loess Using the Convergence-Confinement Method 2018;18:1–16.

[29] Kirsch EG. The theory if elasticity and the need of the strength of materials (trans.). J Assoc Ger Eng

1898;42:797–807.

[30] Fenner R. Untersuchungen zur erkenntnis des gebirgsdrucks. Glückauf; 1938.

[31] Alejano LR, Rodriguez-dono A, Alonso E, Fdez G. Ground reaction curves for tunnels excavated in different quality rock masses showing several types of post-failure behaviour. Tunn Undergr Sp Technol Inc Trenchless Technol Res 2009;24:689–705.

[32] González-Nicieza C, Álvarez-Vigil AE, Menéndez-Díaz A, González-Palacio C. Influence of the depth and shape of a tunnel in the application of the convergence–confinement method. Tunn Undergr Sp Technol 2008;23:25–37.

[33] Vrakas A, Anagnostou G. A finite strain closed-form solution for the elastoplastic ground response curve in tunnelling. International Journal for Numerical and Analytical Methods in Geomechanics. 2014;38(11):1131-48.

[34] Barbosa RE. A Analytical solution for a deep tunnel excavated in a porous elasto-plastic material considering the effects of seepage forces. In Proceedings of the 3rd CANUS rock mechanics symposium. 2009:1–2.

[35] Lee Y, Pietruszczak S. A new numerical procedure for elasto-plastic analysis of a circular opening excavated in a strain-softening rock mass. Tunnelling and Underground Space Technology. 2008;23(5):588-99.

[36] Malan DF. Time-dependent Behaviour of Deep Level Tabular Excavations in Hard Rock. Rock Mech Rock Eng 1999;32:123–55.

[37] Barla G, Bonini M, Debernardi D. Time Dependent Deformations in Squeezing Tunnels. 12th Int Conf Int Assoc Comput Methods Adv Geomech 2008:1–6.

[38] Debernardi D, Barla G. New viscoplastic model for design analysis of tunnels in squeezing conditions. Rock Mech Rock Eng 2009;42:259–88.

[39] Panet M. Time-dependent deformations in underground works. 4th ISRM Congr., International Society for Rock Mechanics; 1979.

[40] Malan DF. Manuel Rocha medal recipient simulating the time-dependent behaviour of excavations in hard rock. Rock Mech Rock Eng 2002;35:225–54.

[41] Barla G, Bonini M, Debernardi D. Time Dependent Deformations in Squeezing Tunnels. 12th Int Conf Int Assoc Comput Methods Adv Geomech 2008;2:1–6.

[42] Kabwe E, Karakus M, Chanda E. Assessment of analytical solutions for time-dependent behavior of unlined tunnels. In: Proceedings of 4th International Symposium on Underground Excavation. 2018; vols. 1–9. Istanbul, Turkey.

[43] Khalil R, Al Horani M, Yousef A, Sababheh M. A new definition of fractional derivative. J Comput Appl Math 2014;264:65–70.

[44] Abdeljawad T. On Riemann and Caputo fractional differences. Comput Math with Appl. 2011;62:1602– 1611.

[45] Kilbas AAA, Srivastava HM, Trujillo JJ. Theory and applications of fractional differential equations. vol. 204. Elsevier Science Limited; 2006.

[46] Xu Z, Chen W. Fractional-order modeling of linear viscoelastic creep in hami melon. 13th Int Conf Fract 2013, ICF 2013 2013;6:1–7.

[47] Zhang L, Liu Y, Yang Q. Mechanics of Materials A creep model with damage based on internal variable theory and its fundamental properties. Int J Mech Mater 2014;78:44–55.

[48] Hui LI, Zhang QJ, Lian-Seng NI, Ying XU. Fractional Order Derivative Nishihara Model of Artificial Frozen Soil. In 2014 International Conference on Mechanics and Civil Engineering (icmce-14) 2014. Atlantis Press.

[49] Zhou HW, Wang CP, Mishnaevsky L, Duan ZQ, Ding JY. A fractional derivative approach to full creep regions in salt rock. Mech Time-Dependent Mater 2013;17:413–25.

[50] Cai W, Chen W, Xu W. Characterizing the creep of viscoelastic materials by fractal derivative models. Int J Non Linear Mech 2016;87:58–63.

[51] Bagley RL, Torvik PJ. A theoretical basis for the application of fractional calculus to viscoelasticity. Journal of Rheology. 1983;27(3):201-10.

[52] Zhou HW, Wang CP, Han BB, Duan ZQ. A creep constitutive model for salt rock based on fractional derivatives. Int J Rock Mech Min Sci 2011;48:116–21.

[53] Chen BR, Zhao XJ, Feng XT, Zhao HB, Wang SY. Time-dependent damage constitutive model for the marble in the Jinping II hydropower station in China. Bull Eng Geol Environ 2014;73:499–515.

[54] Zhang J-Z, Zhou X-P, Yin P. Visco-plastic deformation analysis of rock tunnels based on fractional derivatives. Tunn Undergr Sp Technol 2019;85:209–19.

[55] Panet M, Guenot A. Analysis of convergence behind the face of a tunnel: Tunnelling 82, proceedings of the 3rd international symposium, Brighton, 7–11 June 1982, P197–204. Publ London: IMM, 1982. Int. J. Rock Mech. Min. Sci. Geomech. Abstr., vol. 20, Pergamon; 1983, p. A16.

[56] Jean HT, Didier S, Tunnel ÁTÁ. Progressive degradation of rock properties and time-dependent behavior of deep tunnels. Acta Geotech 2016;11:693–711.

[57] Cui L, Zheng JJ, Sheng Q, Pan Y. A simplified procedure for the interaction between fully-grouted

bolts and rock mass for circular tunnels. Computers and Geotechnics. 2019;106:177-92.

[58] Fritz P. An analytical solution for axisymmetric tunnel problems in elasto-viscoplastic media. International journal for numerical and analytical methods in geomechanics. 1984;8(4):325-42.

[59] Vlachopoulos N, Diederichs MS. Improved longitudinal displacement profiles for convergence confinement analysis of deep tunnels. Rock mechanics and rock engineering. 2009;42(2):131-46.

Statement of Authorship

Title of Paper	Creep constitutive model considering the overstress theory with an associative viscoplastic flow rule,
Publication Status	☑ Published ☐ Accepted for Publication ☐ Submitted for Publication ☐ Unpublished and Unsubmitted w ork w ritten in manuscript style
Publication Details	Eugie Kabwe, Murat Karakus, Emmanuel K. Chanda, Creep constitutive model considering the overstress theory with an associative viscoplastic flow rule, Computers and Geotechnics,Volume 124,2020,103629, ISSN 0266-352X,https://doi.org/10.1016/j.compgeo.2020.103629.

Principal Author

Name of Principal Author (Candidate)	EUGIE KABWE		
Contribution to the Paper	Conceptualization, Formal analysis, Methodology, Investigation, Writing - original draft, Writing - review & editing and as the corresponding author		
Overall percentage (%)	80%		
Certification:	This paper reports on original research I conducted during the period of my Higher Degree by Research candidature and is not subject to any obligations or contractual agreements with a third party that would constrain its inclusion in this thesis. I am the primary author of this paper.		
Signature		Date	17/08/2020

Co-Author Contributions

By signing the Statement of Authorship, each author certifies that:

i. the candidate's stated contribution to the publication is accurate (as detailed above);

ii. permission is granted for the candidate in include the publication in the thesis; and

iii. the sum of all co-author contr butions is equal to 100% less the candidate's stated contribution.

Name of Co-Author	MURAT KARAKUS		
Contribution to the Paper	Supervision of the work; Identification of the problem and methodology, reviewing & editing		
Signature		Date	18/08/2020

Name of Co-Author	EMMANUEL K. CHANDA		
Contribution to the Paper	Supervision, review & editing		
Signature		Date	18/08/2020

Chapter 5

Creep Constitutive Model Considering the Overstress Theory with an Associative Viscoplastic Flow Rule *(Paper 3)*

Eugie Kabwe, Murat Karakus, Emmanuel K Chanda

Published in Computer and Geotechnics

Abstract

Tunnel excavation in squeezing ground is very challenging due to the difficulty in making reliable predictions at the preliminary design stage. Tunnel response in squeezing ground is made possible by employing creep constitutive models. However, literature outlines the limitations of the conventional creep constitutive models in estimating delayed deformations due to the squeezing mechanism. Hence this paper presents, a fractional-order derivative viscoelastic viscoplastic (FDVP) constitutive model capable of estimating delayed deformations characterized by squeezing. The FDVP constitutive equations are derived as an extension to the Burgers model and adjusted Perzyna overstress function with an associated viscoplastic flow rule. The constitutive model validation and verification are conducted by using the experimental data obtained from literature and monitored tunnel convergence data, respectively. Thereafter, the constitutive equations are implemented in FLAC^{3D} and applied to simulate deformations responsible for squeezing within a tunnel employing in-built constitutive models for verification purposes. The constitutive model shows very good agreement with experimental data and yields close results with monitored tunnel convergence data. The model can be successfully used in numerical code for tunnel stability analysis in squeezing ground.

Keywords: Creep; Delayed deformation; FLAC^{3D}; Fractional-order derivative; Viscoplastic flow rule

5.1 Introduction

Excavation of tunnels in squeezing ground is very challenging because it is difficult in making reliable estimation of the squeezing mechanism at the preliminary design stage. Throughout excavation, this phenomenon is not predicted, the experience is only gained on the squeezing problems encountered. This makes the selection and design of the most appropriate excavations in squeezing conditions more cumbersome [1]. Squeezing is a large time-dependent (TD) deformation encountered during tunnel excavation. It arises when a certain combination of induced stresses and material properties initiates tunnel boundary closure at which TD behaviour emanates. This TD deformation tends to occur instantaneously during excavation or continue over time and it is related to creep [2,3] (Figure 5-1). Impacts of squeezing consists of large tunnel closure, considerable deformation of the tunnel face, support structure overload and in extreme cases, the total collapse of tunnels. In engineering practice difficulties encountered with this phenomenon are attributed to: (1) the employment of inappropriate constitutive model to describe the squeezing mechanism and (2) the design of a suitable excavation and its support structure.

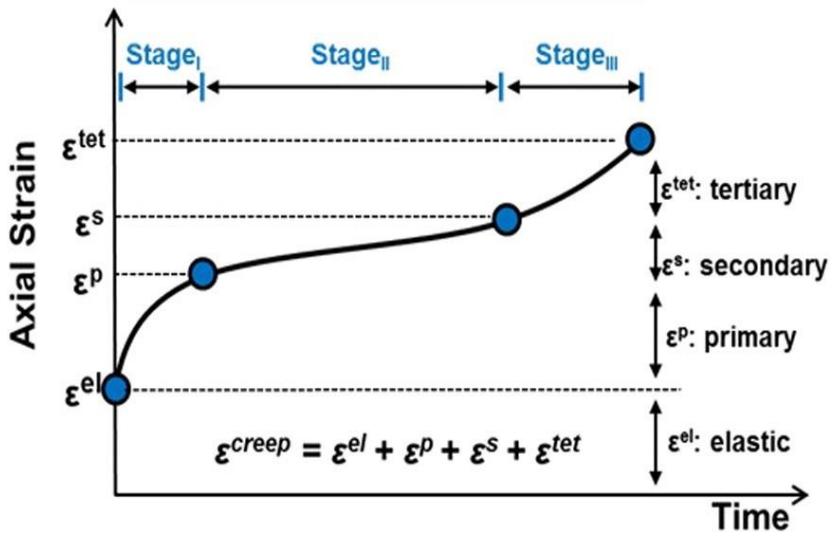

Figure 5-1. 3-stage creep behaviour

This entails consideration of the viscoplastic (VP) creep behaviour and most importantly that exhibited in the accelerated creep stage responsible for squeezing related delayed deformations. To describe the 3-

stage creep behaviour, researchers suggested rheological model combinations. The Burgers model connected in series with a VP component is one such combination proposed to predict the VP irreversible deformation [4–7]. The Burgers VP (CVISC) constitutive model is another example able to replicate the 3-stage creep behaviour of a rock mass [8]. The constitutive relation of the CVISC model is characterised by an elasto-plastic (EP) volumetric behaviour and an elasto-viscoplastic (EVP) deviatoric behaviour. The viscoelastic (Kelvin) and viscoplastic (Maxwell and slider) strain rate components act in series (Figure 5-2). The viscoelastic and plastic constitutive laws are given by the Burgers model and the Mohr-Coulomb (MC) yield surface respectively. The CVISC constitutive model estimates deformation in the transient and steady-state creep stages represented by the Burgers model. The MC yield surface governed plastic slider estimates permanent plastic strain rates in the accelerated creep stage. However, these estimated permanent strain rates are dependent on stress rather than on time. Overall, these strains develop overtime in tunnels driven in weak rocks and subjected to high in situ stress. They are characterised by the TD deformation referred to as squeezing [2]. Hence, it is important to estimate the TD viscoplastic strains in the accelerated creep stage that are responsible for delayed deformations to better understand the squeezing mechanism. These constitutive models fail to satisfactorily describe the entire creep related TD behaviour involved in tunnel excavation [9,10].

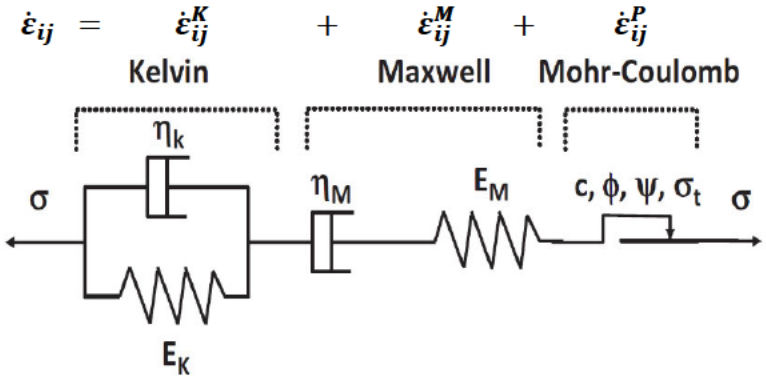

Figure 5-2. CVISC model accounting for viscoelastic and viscoplastic behaviour

Hence, the focus of this study is to improve the functionality of the Burgers and CVISC models to account for the TD delayed deformations. The improvement is conducted by developing a constitutive model applicable in the estimation of delayed tunnel deformation in squeezing ground. To achieve this task, the

FDVP constitutive model is presented by coupling the Burgers model and the VP component. Additionally, contribution to the understanding of tunnel response in squeezing ground through formulating a constitutive model requires presentation of simple constitutive laws applicable in research and design practice. However, the mathematical theory and constitutive laws employed in the existing non-linear creep models are not adequate to satisfactorily describe the TD behaviour most prominently the accelerated creep stage. The commonly used differential constitutive equations to describe TD behaviour in these models employs integral calculus based on integer-order derivatives. In this regard, it is important to propose a creep model for squeezing ground governed by fractional-order derivative capable of describing the power-law mechanism of geomaterials. Fractional-order calculus is a concept of integrals and derivatives of random real and even complex numbers [11,12]. It is a generalization of integer-order derivative calculus and therefore preserves most of the basic functions.

As an intensively developing area of calculus during the last couple of decades, it offers new features for research and other applications such as rheological models. Some classic creep models such as Maxwell and Kelvin models have been improved by using fractional-order derivatives [13–17]. Zhang et al.,[18] presented the FVP constitutive model based on fractional-order derivatives to capture deformations in tunnels. However, their model used so many parameters, considered the Hoek-Brown strength criterion and neglected numerical implementation. Furthermore, the FVP constitutive model employed the fractional Maxwell coupled with the fractional VP components and neglected the Kelvin component effect. Lu et al., [19] employed fractional-order derivatives to develop an EP constitutive model for soils governed by a fractional plastic flow rule. Lu et al., [20] further employed fractional plastic flow rule and developed a fractional EP constitutive model for concrete material. In the application of these models, the fractional-order derivative is adopted by an element called “spring-pot”. The spring-pot exhibits characteristic amid an ideal Newtonian dashpot and an ideal spring addresses limitations faced by both elements [14,16,21,22]. However, these fractional-order derivatives based constitutive models have not been applied in the estimation of delayed deformations responsible for squeezing in tunnels. Furthermore, they

are constrained to a more solitary degree of freedom approach and under simple loading conditions. Neglect the three-dimensional (3D) numerical code implementation with intricate initial boundary and heterogeneous stress-strain conditions to verify their applicability [11]. These models display advantages and limitations which are mainly dependent on their applicability. Some are relatively simple but neglect the time effect and others describe actual rock mass behaviour but are complex.

Besides, the FDVP constitutive model presented in this paper takes advantage of the Perzyna [23] overstress theory to describe the viscoplastic strains. There are several time-dependent constitutive models based on this overstress theory and they are classified into two categories [24]: (1) conventional overstress constitutive models [25–28], assume a static yield surface in which state stress occur within and only elastic strains develop. The determination of viscosity parameters in these constitutive models require laboratory tests at low-stress levels. This has proved to be a limitation in the actual in-situ application of these models. Regards to this (2), the extended overstress constitutive models [29–31] were introduced to address this limitation. In overcoming this curb, these constitutive models assume viscoplastic strain development even though the stress state occurs inside the static yield surface. Hence, the determination of the viscosity parameters and yield surface evolution is straight forward. Therefore, in this paper, the limitation of the conventional overstress constitutive model is addressed by the extension of the Perzyna [23] overstress function. This is achieved by incorporating the fractional-order derivative function and the time-independent yield surface.

The FDVP constitutive model presented in this paper comprises of the following features and assumptions:

1) The model adopts an adjusted Perzyna [23] overstress function using fractional-order derivatives as such its parameters can be calibrated using conventional creep test data.
2) The model ignores the viscoplastic flow rule assumption that governs the conventional overstress constitutive models as such addresses their limitation.

3) The model is governed and restricted to the associated viscoplastic flow rule in which the potential function is given as the yield function.
4) The model ignores the assumption of the conventional creep constitutive models governed by the integer-order derivatives as such addresses their limitation.
5) The model assumes ideal viscoplasticity in that it overlooks the isotropic and kinematic hardening constitutive laws.

Hence, a not exceedingly complicated creep constitutive model capable of describing the power-law mechanism of geomaterials is proposed with the intent of estimating delayed deformations in squeezing ground. The constitutive model is derived as an extension to the Burgers model and Perzyna [23] overstress theory with an associated viscoplastic flow rule. It is worth mentioning that the presented form of this creep constitutive model is presently under development. The further enhancement will include the integration of constitutive equations able to describe the accelerated creep stage explicitly, account for creep damage effect and hardening viscoplasticity.

5.2 Fractional-order derivative application

The viability of employing fractional-order derivatives to describe the EVP behaviour of rocks stems from its application to represent viscoelasticity and elastoplasticity which include [11,19,20,32–35] among others. The fractional-order derivatives are applied in rheological models (Kelvin and Maxwell) by substitution of a dashpot with a spring-pot. It is correctly established that ideal solids (spring) abide by Hooke's law and Newtonian fluids (dashpot) comply with Newton's law of viscosity [11,33]. In the hypothesis of viscoelasticity, it is considered that the Hooke's law is defined by the zero-order derivative of strain relative to time (Eq. (5-1)) and Newton's law is defined by the first-order derivative of strain relative to time (Eq. (5-2)).

$$\sigma(t) = \frac{d^0[\varepsilon(t)]}{dt^0} \tag{5-1}$$

$$\sigma(t) = \frac{d^1[\varepsilon(t)]}{dt^1} \tag{5-2}$$

The spring-pot represent the element that obeys the fractional-order derivative amid Eq. (5-1) and Eq. (5-2), and it is represented by the fractional relation (Eq. (5-3)). The relation is defined by the fractional-order derivative coefficient (β) which satisfy the condition $0 \leq \beta \leq 1$:

$$\sigma(t) = \eta^{\beta} \frac{d^{\beta}[\varepsilon(t)]}{dt^{\beta}} \qquad (0 \leq \beta \leq 1) \tag{5-3}$$

Where η^{β} is the spring-pot viscosity coefficient and it has been verified that employing fractional-order derivative governed constitutive models can describe the rheological behaviour of materials in a better way as compared to classical constitutive models.

5.2.1 The Riemann-Liouville operator

Fractional-order calculus is a branch of mathematics that investigates the likelihood of considering power-law of the differential and integral operators of real or complex numbers [11,33,36]. Definitions of fractional-order calculus include Grunwald-Letnikov, Riemann-Liouville and Caputo among others [11,32,33]. At this point, the Riemann-Liouville definition is presented because it is used to propose the model that will be able to describe the 3-stage creep behaviour of geomaterials. The Riemann-Liouville fractional-order differential operator assumes that $f(t)$ is continuous in $(0, +\infty)$ and is integrated into any finite subdomain of $(0, +\infty)$ for $t > 0$ and $Re(\beta) > 0$ where β is the order integral of the function $f(t)$ [37–39]. The Riemann–Liouville fractional-order integral of the function $f(\tau)$ is expressed as [40]:

$$\frac{d^{-\beta} f(t)}{dt^{-\beta}} = \frac{1}{\Gamma(\beta)} \int_{t_0}^{t} (t - \tau)^{\beta - 1} f(\tau) d\tau \tag{5-4}$$

Where t_0 is the lower integration limit, β lies between $0 \leq \beta \leq 1$ and $\Gamma(\beta)$ is the gamma function of argument β and this function is calculated as:

$$\Gamma(\beta) = \int_0^\infty x^{\beta-1} e^{-x} dx \,, \qquad Re(\beta) > 0 \quad (5\text{-}5)$$

The $\frac{d^\beta}{dt^\beta}$ with the order $\beta \in (0,1)$ of the function $f(t)$ is defined by:

$$\frac{d^\beta f(t)}{dt^\beta} = \left(\frac{1}{\Gamma(1-\beta)} \int_{t_0}^{t} (t-\tau)^{1-\beta} f(t) d\tau\right) \frac{df(t)}{dt} \quad (5\text{-}6)$$

and the $\frac{d^\beta}{dt^\beta}$ with the order $\beta \in (n-1, n)$ of the function $f(t)$ is defined by:

$$\frac{d^\beta f(t)}{dt^\beta} = \left(\frac{1}{\Gamma(n-\beta)} \int_{t_0}^{t} (t-\tau)^{n-\beta} f(t) d\tau\right) \frac{d^n f(t)}{dt^n} \quad (5\text{-}7)$$

In this relation, the gamma function characterizes a continuous extension of the factorial function. It is defined for non-negative numbers and displays a concave response for positive real numbers as illustrated in Figure 5-3. Figure 5-3 draws the comparison with the factorial function, and it is observed that the factorial function always maintains the constant output of 2.0 when the fractional-order derivative coefficient is increased from 1.0 to 2.0. Whereas the gamma function experiences a continuous increment of the output from 2.0 to 6.0. This clearly shows that the gamma function can describe the power-law characteristic when applied to describe the rheological behaviour of materials.

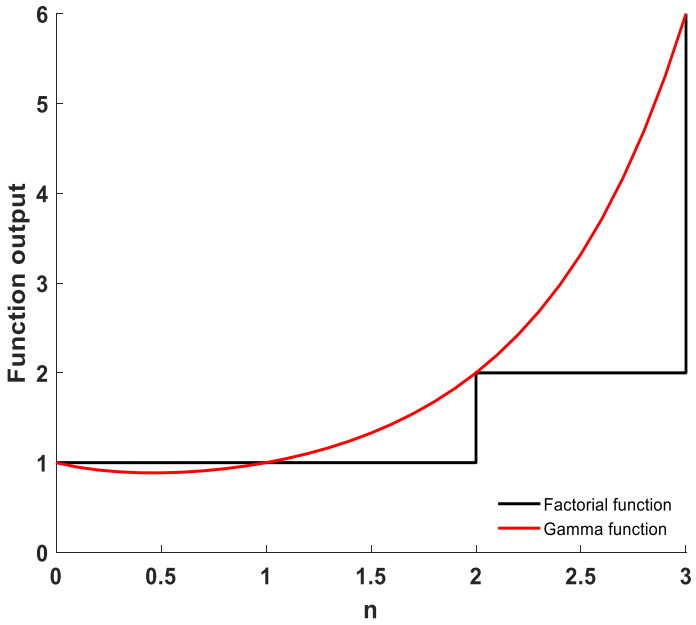

Figure 5-3. The gamma function

Fractional-order derivative is an exceptional mathematical tool for modelling viscoelastic behaviour and especially appropriate for building the EVP constitutive models. In the following section, a brief derivation of the stress-strain constitutive equations in an EVP medium is conducted which utilizes the fractional-order derivatives. Thereafter, the FDVP constitutive model is proposed and employs the fractional-order derivative function which incorporates an adjusted Perzyna [23] overstress function with an associative flow rule.

5.3 Fractional-order viscoplasticity model

In Section 5.2, the total stress in the spring-pot was represented by the constitutive relation (Eq. (5-3)). When we set $\sigma(t) = \sigma$ (constant stress) and employing the fractional-order derivative attributed to Reimann-Liouville operation. Thereafter, applying Laplace transformation on either side of Eq. (5-3), the following expression can be obtained:

$$F_{\beta_{1,2}}(s) = \frac{\sigma}{\eta^{\beta_{1,2}}} \frac{1}{s^{1+\beta_{1,2}}} \tag{5-8}$$

Where $\beta_{1,2}$ represents the fractional-order derivative coefficients for different spring-pots. In this case β_1 and β_2 are the fractional-order derivative coefficients of the Maxwell and VP spring-pots respectively. Conducting an inverse Laplace transformation on Eq. (5-8), the strain in the spring-pot is represented by the constitutive relation:

$$\varepsilon(t) = \frac{\sigma}{\eta^{\beta_{1,2}}} \frac{t^{\beta_{1,2}}}{\Gamma(1+\beta_{1,2})} \qquad (0 \leq \beta_{1,2} \leq 1) \quad (5\text{-}9)$$

The constitutive relation employs the gamma function and its effect on the spring-pot response over several time scales are illustrated in Figure 5-4.

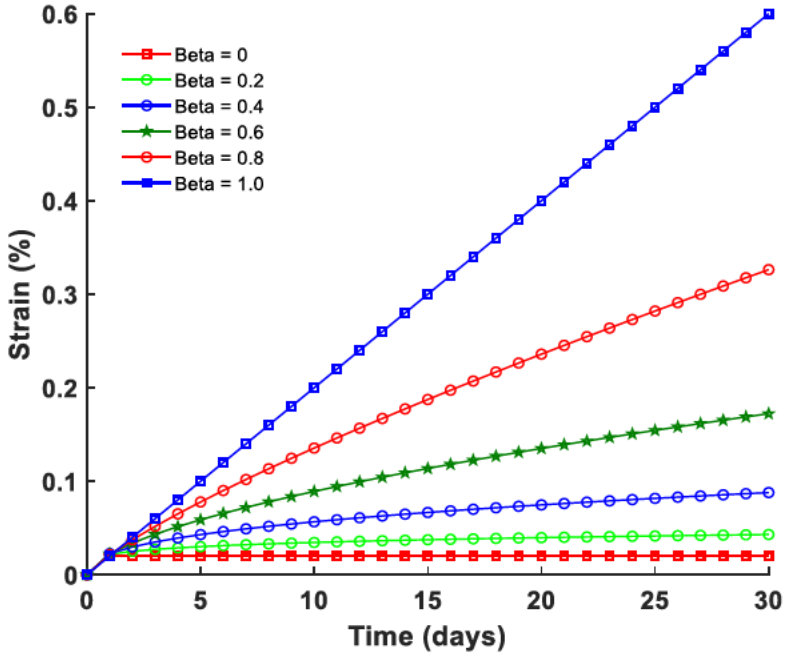

Figure 5-4. Strain response of the spring-pot

Substitution of the Newtonian element with a spring-pot in the Maxwell component and coupling a VP component which consists of a spring-pot and MC plastic slider, a new model is constructed. The model is constructed to estimate the TD strains related to the 3-stage creep behaviour. Figure 5-4 draws a schematic representation of the model composed of the Kelvin, Maxwell and VP components all connected in series.

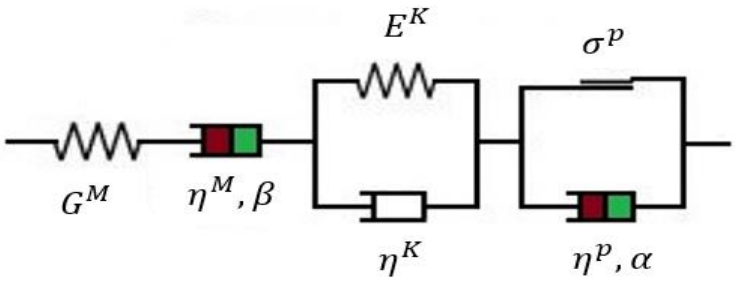

Figure 5-5. Schematic view of the FDVP model. Note: β = $\boldsymbol{\beta_1}$ & α = $\boldsymbol{\beta_2}$

The stress-strain partition in the model is expressed by:

$$\sigma(t) = \sigma^K = \sigma^M = \sigma^{vp}; \qquad \varepsilon(t) = \varepsilon^K + \varepsilon^M + \varepsilon^{vp} \tag{5-10}$$

Where σ^K, σ^M and σ^{vp} are the stress acting in the Kelvin, Maxwell and VP components respectively. ε^K, ε^M and ε^{vp} are the strain in the Kelvin, Maxwell and VP components respectively. The total stress in the VP component σ^{vp} is computed by:

$$\sigma^{vp} = \sigma^p + \sigma^v \tag{5-11}$$

Where σ^p is the stress in the plastic slider, σ^v is the stress in the spring-pot and σ^p is partitioned in the form:

$$\sigma^p = \begin{cases} \sigma & \sigma < \sigma_Y \\ \sigma_Y, & \sigma \geq \sigma_Y \end{cases} \tag{5-12}$$

When $\sigma < \sigma_Y$, combining Eq. (5-9) and Eq. (5-10) then $\sigma^v = 0$ and $\varepsilon^{vp} = 0$. When $\sigma \geq \sigma_Y$, the total stress in the VP component is expressed as:

$$\sigma^{vp} = \eta^{\beta_2}\left(\frac{\sigma - \sigma_Y}{\eta^{\beta_2}}\right) + \sigma_Y \tag{5-13}$$

Where β_2 is the VP spring-pot fractional-order derivative coefficient and η^{β_2} is the VP spring-pot viscosity coefficient. Considering the fractional-order relation Eq. (5-8) and setting initial condition as ε^{vp} = 0 and t = 0, Eq. (5-11) in terms of the fractional-order derivatives is further expressed as:

$$\varepsilon^{VP} = \frac{\sigma - \sigma_Y}{\eta^{\beta_2}} \frac{t^{\beta_2}}{\Gamma(1+\beta_2)} \qquad \sigma \geq \sigma_Y, (0 \leq \beta_2 \leq 1) \tag{5-14}$$

Substituting Eq.(5-14) into Eq. A7 (Appendix A) the strain and time relationship befit:

$$\varepsilon(t) = \begin{cases} \left\{\frac{\sigma}{G_M} + \frac{\sigma t}{\eta_M} + \frac{\sigma}{G_K}\left[1 - exp\left(-\frac{G_K t}{\eta_K}\right)\right]\right\}, & \sigma < \sigma_Y \\ \left\{\frac{\sigma}{G_M} + \frac{\sigma t}{\eta_M} + \frac{\sigma}{G_K}\left[1 - exp\left(-\frac{G_K t}{\eta_K}\right)\right] + \left(\frac{\sigma - \sigma_Y}{\eta^{\beta_2}} \frac{t^{\beta_2}}{\Gamma(1+\beta_2)}\right)\right\}, & \sigma \geq \sigma_Y \end{cases} \tag{5-15}$$

As mentioned earlier in Section 5.2, the fractional-order derivatives can realistically describe the rheological behaviour of geomaterials. Additionally, the gamma function adopted in these derivatives describes the power-law mechanism due to its power-law characteristic. Whereas the conventional integer-order solutions assume linearity in the rheological behaviour of geomaterials. Hence, the gamma function employment in the fractional-order solution provides a realistic estimation of the delayed deformations responsible for squeezing.

5.3.1 Viscoelastic and Viscoplastic constitutive equations

It is important to emphasize that the results presented in this section represent the fractional-order derivative viscoplasticity formulation based on Perzyna [23] overstress theory. The FDVP constitutive model is presented in a form exemplified by the three components (Figure 5-5) and serves as a Burgers

creep model extension which is characterised by an EVP deviatoric and volumetric behaviour. Substituting the Maxwell and VP dashpots with the spring-pot constitutive relations in Eq.(5-15), one gets the FDVP constitutive equations expressed as:

$$\begin{cases} \varepsilon = \dfrac{\sigma}{G_M} + \dfrac{\sigma t^{\beta_1}}{\eta^{\beta_1}\Gamma(1+\beta_1)} + \dfrac{\sigma}{G_K}\left[1 - exp\left(-\dfrac{G_K t}{\eta_K}\right)\right], \sigma < \sigma_Y \\ \varepsilon = \dfrac{\sigma}{G_M} + \dfrac{\sigma t^{\beta_1}}{\eta^{\beta_1}\Gamma(1+\beta_1)} + \dfrac{\sigma}{G_K}\left[1 - exp\left(-\dfrac{G_K t}{\eta_K}\right)\right] + \left(\dfrac{\sigma - \sigma_Y}{\eta^{\beta_2}}\dfrac{t^{\beta_2}}{\Gamma(1+\beta_2)}\right), \sigma \geq \sigma \end{cases} \quad (5\text{-}16)$$

Where η^{β_1} is the fractional-order Maxwell viscosity coefficient and in Eq (5-16), when $\sigma < \sigma_Y$ transient creep and steady-state creep exhibit, when $\sigma \geq \sigma_Y$ the transient creep, steady-state creep and accelerated creep exhibit. Realistically, a rock mass exists under triaxial stress state as such the model's constitutive equations are expressed in a 3D stress state. In which the rock stress tensor (σ_{ij}) is comprised of the mean stress tensor (σ_m), deviatoric stress tensor (S_{ij}) and these are expressed by:

$$\sigma_m = \frac{\sigma_{kk}}{3} \quad (5\text{-}17)$$

$$S_{ij} = \sigma_{ij} - \sigma_m \delta_{ij} \quad (5\text{-}18)$$

Where δ_{ij} is the Kronecker delta, σ_m is responsible for volume change of a rock mass and S_{ij} is responsible for the change in the shape of the rock mass. The strain tensor (ε_{ij}) can also be decomposed into mean strain tensor (ε_m) and deviatoric strain tensor (e_{ij}):

$$\varepsilon_m = \frac{\varepsilon_{kk}}{3} \quad (5\text{-}19)$$

$$e_{ij} = \varepsilon_{ij} - \varepsilon_m \delta_{ij} \quad (5\text{-}20)$$

Based on Hooke's law the σ_m and S_{ij} in a 3D stress state is computed by:

$$\sigma_m = 3K\varepsilon_m \tag{5-21}$$

$$S_{ij} = 2Ge_{ij} \tag{5-22}$$

Where K is the bulk modulus and substituting Eqs (5-21) and (5-22) into Eq. (5-16) and assuming S_{ij} is less than the 3D long-term strength (S_Y) the creep constitutive equation with the VP component deactivated is expressed as:

$$\varepsilon_{ij} = \frac{S_{ij}}{2G_M} + \frac{\sigma_m \delta_{ij}}{3K} + \frac{S_{ij} t^{\beta_1}}{2\eta^{\beta_1}\Gamma(1+\beta_1)} + \frac{S_{ij}}{2G_K}\left[1 - exp\left(-\frac{G_K t}{\eta_K}\right)\right] \quad S_{ij} < S_Y \tag{5-23}$$

When $S_{ij} \geq S_Y$ the VP component is activated and Eq (5-25) becomes:

$$\varepsilon_{ij} = \frac{S_{ij}}{2G_M} + \frac{\sigma_m \delta_{ij}}{3K} + \frac{S_{ij} t^{\beta_1}}{2\eta^{\beta_1}\Gamma(1+\beta_1)} + \frac{S_{ij}}{2G_K}\left[1 - exp\left(-\frac{G_K t}{\eta_K}\right)\right] + \left(\frac{S_{ij} - S_Y}{2\eta^{\beta_2}\Gamma(1+\beta_2)}\right) t^{\beta_2} \quad S_{ij} \geq S_Y \tag{5-24}$$

In this case, the viscoplastic strains initiate as such the viscoplastic potential function (Q_{vp}) and viscoplastic flow rule is introduced in the constitutive equations. Constitutive equations of viscoplasticity also referred to as the TD plasticity are formulated in the same way as the time-independent plasticity. For instance, in viscoplasticity theory, the flow rule constitutive equation can be postulated as Eq (5-25) which is similar to the plastic flow rule.

$$\dot{\varepsilon}_{ij}^{vp} = \lambda \frac{\partial Q_{vp}}{\partial \sigma_{ij}} \tag{5-25}$$

Where λ is the scalar multiplier which determines the flow intensity. However, there is a distinction in this flow rule definition that describes the evolution of the effective plastic strain [41,42]. It must be emphasized that in the time-independent constitutive models the plastic strain rate is a pseudo-time rate

and its derivative to this pseudo-time is irrelevant [41]. Whereas the viscoplastic strain rate is the actual time derivative of the viscoplastic strain. Additionally, in plasticity theory, the scalar multiplier is determined by the consistency condition whereas in the viscoplasticity theory it is given by the explicit function based on S_{ij} and S_Y. In the TD theory the viscoplastic strain rate is further expressed by the Perzyna [23] overstress function:

$$\dot{\varepsilon}_{ij}^{vp} = \frac{\langle \phi(F) \rangle}{\eta} \frac{\partial Q_{vp}}{\partial \sigma_{ij}} \tag{5-26}$$

Where η is the viscosity parameter, $\langle \phi(F) \rangle$ is the viscoplastic nucleus that regulates the extent of the viscoplastic strain, F is the overstress function, Q_{vp} describes the viscoplastic strain rate tensor's direction and $\langle \quad \rangle$ are the Macaulay brackets defined by:

$$\langle \phi(F) \rangle = \begin{cases} 0, & F < 0 \\ \phi(F), & F \geq 0 \end{cases} \tag{5-27}$$

A full description of the viscoplastic strain rates requires comprehensive clarification. Hence, in classical viscoplasticity, it is hypothesized that the rate of viscoplastic strains is obtainable from Perzyna [23] overstress function. Equating Eq (5-25) to Eq (5-26) it can be observed that the scalar multiplier is determined by the constitutive equation (Eq (5-28)) as opposed to time-independent plasticity which employs the consistency condition.

$$\lambda = \frac{\langle \phi(F) \rangle}{\eta} \tag{5-28}$$

In time-independent plasticity when the state stress lies above the yield surface the scalar multiplier is obtained from the consistency condition. In viscoplasticity when the state stress is above the failure surface the constitutive relation (Eq (5-28)) is used to obtain the scalar multiplier. It has been argued that during viscoplasticity stress correction the consistency condition is not pertinent as such certain state

stress conditions are irrelevant. However, the fact that the overstress theory postulates that the stress state always lies above the yield surface. This signifies a consistency condition that needs to be satisfied for viscoplastic strains to occur. Additionally, the plastic stress return mapping computation is similar to the viscoplastic return mapping procedure. This numerical framework of the viscoplastic return mapping can be described as:

1. ***Elastic predictor***. The geomaterial behaves elastically in this state in a given time interval $[t_n, t_{n+1}]$. The elastic trail state is calculated by:

$$\varepsilon_{n+1}^{trial} = \varepsilon_n + \Delta\varepsilon$$

$$\varepsilon_{n+1}^{vp\ trial} = \varepsilon_n^{vp}$$

$$\sigma_{n+1}^{trial} = C_e\left(\varepsilon - \varepsilon^{vp}\right) \tag{5-29}$$

$$f_{n+1}^{trial} = \left|\sigma_{n+1}^{trial}\right| - \sigma_Y$$

If $f^{trial} \leq 0$, then the procedure is elastic within the stipulated interval $[t_n, t_{n+1}]$ and variable at $[t_{n+1}]$ are assigned the values of the trial variables.

Set:

$$\sigma_{n+1} = \sigma_{n+1}^{trial}$$

$$C_{vp} = C_e \tag{5-30}$$

Else $f^{trial} > 0$, hence the load step is viscoplastic and we apply the viscoplastic return mapping as described below.

2. ***Viscoplastic corrector.*** In this state, a system of equations is computed as follows:

$$\sigma_{n+1} = \sigma_{n+1}^{trial} - \Delta\lambda C_e : \left.\frac{\partial f}{\partial \sigma}\right|_{n+1} \tag{5-31}$$

Where the viscoplastic scalar multiplier *(Δλ)* is given by

$$\Delta\lambda = \frac{\langle\phi(F)\rangle}{\eta} \tag{5-32}$$

Hence we solve Eq (5-31) for the stress and strain update

$$\varepsilon_{n+1}^{vp} = \varepsilon_n^{vp} + \Delta\lambda \left.\frac{\partial f}{\partial \sigma}\right|_{n+1}, \qquad \varepsilon_{n+1}^{e} = \varepsilon_{n+1}^{trial} - \Delta\lambda \left.\frac{\partial f}{\partial \sigma}\right|_{n+1} \tag{5-33}$$

As outlined above the stress return mapping procedure is similar only that Eq (5-32) is employed to account for the viscous time effect as opposed to the time-independent plasticity. In the viscoplastic correction procedure, the failure surface is considered just like in time-independent plasticity [43]. It also considers the same assumption, that if the stress state occurs below the failure surface then it is admissible or else it violates the condition. Hence, the scalar multipliers for both are expressed as:

$$\lambda = \begin{cases} \dfrac{f}{C_e}, & f \geq 0 \\ 0, & f < 0 \end{cases} \Bigg| \; Plasticity\,, \qquad \lambda = \begin{cases} \dfrac{\langle\phi(F)\rangle}{\eta}, & f > 0 \\ 0, & f \leq 0 \end{cases} \Bigg| \; Viscoplasticity \tag{5-34}$$

5.3.1.1 Adjustment of the overstress constitutive equation

In this section, the viscoplastic constitutive equation a product of an adjusted Perzyna [23] overstress function is presented. The equation accounts for the viscoplastic strain rates, it considers an MC yield surface and neglects hardening constitutive law as such assumes ideal viscoplasticity. According to Perzyna [23], the total strain rate is an additive resulting from the elastic and viscoplastic strain rates. In this constitutive equation, the assumption considered is that the viscoplastic strain rates obey an associative flow rule (Eq (5-26)). The Perzyna [23] overstress function is adjusted by incorporating the fractional-order derivatives to represent the 3D viscoplastic constitutive relation as:

$$\dot{\varepsilon}_{ij}^{vp} = \frac{\langle\phi(F)\rangle}{2\eta^{\beta_2}\Gamma(1+\beta_2)} t^{\beta_2} \frac{\partial Q_{vp}}{\partial \sigma_{ij}} \tag{5-35}$$

The overstress function exemplifies the state of overstressing inside the rock mass defined by the yield surface and it is reliant on the time-independent yield surface [42]. Hence, In the presented model, F is assumed to be equal to f and It is widely assumed in classical viscoplasticity theory that the yield direction is normal to the failure surface [34,44–46]. Therefore, an associated viscoplastic flow rule $\left(F = Q_{vp}\right)$ is assigned and Eq (5-35) is further expressed as:

$$\dot{\varepsilon}_{ij}^{vp} = \left(\frac{f}{2\eta^{\beta_2}\Gamma(1+\beta_2)}\right)\frac{\partial f}{\partial \sigma_{ij}}t^{\beta_2} \qquad (f \geq 0) \quad (5\text{-}36)$$

In Eq (5-36), the overstress function is substituted with the time-independent yield surface and the fractional-order derivative function to address the limitation of the conventional overstress models. Hence, the presented viscoplastic constitutive equation (Eq (5-36)) acts as an extended Perzyna [23] overstress function. As a result, there is no viscoplastic strain development constraint when the stress state occurs within or above the yield surface. Subsequently, the 3D FDVP constitutive equation is further expressed as:

$$\begin{aligned}\varepsilon_{ij} = \frac{S_{ij}}{2G_M} + \frac{\sigma_m \delta_{ij}}{3K} + \frac{S_{ij}t^{\beta_1}}{2\eta^{\beta_1}\Gamma(1+\beta_1)} + \frac{S_{ij}}{2G_K}\left[1 - exp\left(-\frac{G_K t}{\eta_K}\right)\right] \\ + \left(\frac{f}{2\eta^{\beta_2}\Gamma(1+\beta_2)}\right)\frac{\partial f}{\partial \sigma_{ij}}t^{\beta_2} \qquad (f \geq 0)\end{aligned} \quad (5\text{-}37)$$

Whereas f is assumed to be the MC yield surface expressed as:

$$f = \sigma_1 - \sigma_3 N_\phi + 2c\sqrt{N_\phi} \quad (5\text{-}38)$$

Where σ_1 is the major principal stress, σ_3 is the minor principal stress, c is the cohesion, $N_\phi = 1 + \sin\phi/1 - \sin\phi$ and ϕ is the internal friction angle. Even though the MC yield surface adopted for the FDVP constitutive model provides a relatively simple approach in constitutive behaviour simulation. Its implementation in finite element solutions is complicated due to its hexagonal shape apex on the deviatoric plane [47,48]. Specific treatment is required for the intersection of its yield surfaces during implementation for the general stress state [49]. The singularity posed at the apex can be addressed by considering each yield surface and implementing its constitutive equation as a multi-surface yield function. Additionally, this singularity can be removed by the smooth approximation techniques such as the hyperbolic approximation [50]. The hyperbolic approximation involves the surface asymptotical approach to the MC yield surface apex as the mean stress increases on a $(\sigma_m, \bar{\sigma})$ space. This surface approach is usually very close to model the MC yield surface, its accuracy is controlled by the alteration of the distance (a) between the apex of the MC yield surface and the tip of the hyperbolic surface (Figure 5-6).

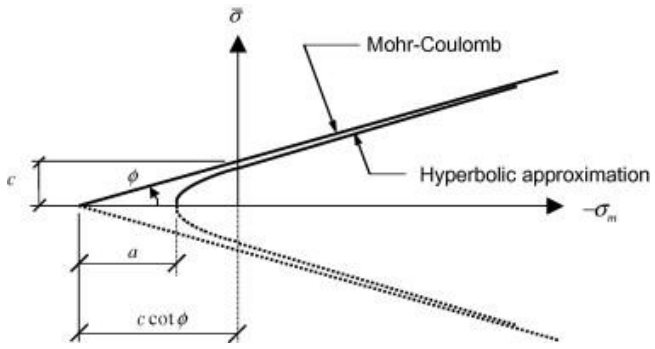

Figure 5-6. Hyperbolic approximation of the MC yield surface on the $(\boldsymbol{\sigma_m}, \boldsymbol{\bar{\sigma}})$ plane [50].

In this procedure, the hyperbolic surface lies within the MC yield surface at all stress states as such it underestimates the strength of geomaterials as compared to the original MC yield surface. However, the hyperbolic approximation has been implemented in the commercial finite volume code (FLAC^{3D}) as an inbuilt feature. As such the limitation posed by the singularity effect of the MC yield surface apex has been addressed in this paper. Therefore, in the sections that follow, the model is; (1) validated through a curve comparison procedure between its computed strain rates and creep test results accessible in

literature; (2) verified on an in-situ scale employing a real tunnel case; (3) written in the object-oriented C++ as a user-defined constitutive model source code which is then implemented in FLAC^{3D} as a compiled DLL.

5.4 Calibration of the FDVP constitutive model

In this section, the procedure to calibrate the FDVP constitutive model is presented conferring to the experimental data achieved from salt rock and Jinping marble sample creep tests. The experimental data of the rock salt sample is attained from the literature provided by Zhou et al [15]. Whereas that of the Jinping marble sample is obtained from two creep tests conducted by Chen et al [17].

5.4.1 Viscoelastic and viscoplastic model parameters

It is worthing mentioning that damage evolution in this model attained either under low or high-stress levels is neglected. Therefore, the salt rock and Jinping marble merely exhibit the transient, steady-state and part of the accelerated creep stages. Even though, the accelerated creep stage is not fully captured the viscoplastic strains characterized by the TD delayed deformations in squeezing ground are described by the FDVP constitutive equations. The constitutive model parameters are calibrated by curve comparison with experimental data over 1256 days using Eq (5-16). Additionally, the experimental data

of the salt rock and compared curves assume ideal viscoplasticity as well as neglect damage evolution under uniaxial stress load σ_0 = 14.1 MPa with σ_Y = 8.46 MPa are shown in Figure 5-7 and Table 5-1.

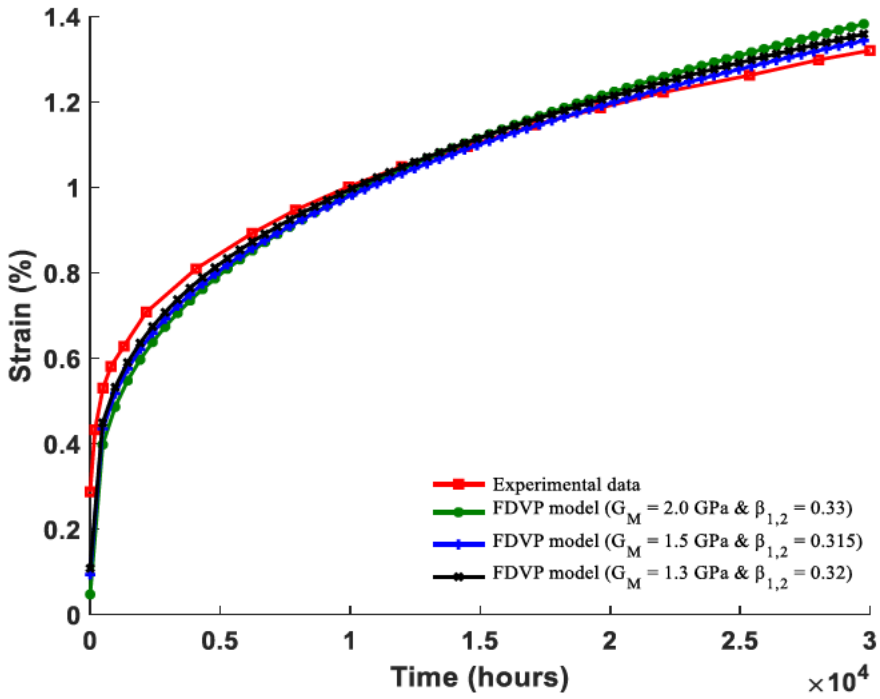

Figure 5-7. Experimental data of the salt rock [15] with the FDVP model prediction

Table 5-1. FDVP constitutive model parameters of salt rock

η_M(GPa.h)	G_K(GPa)	η_K(GPa.h)	G_M(GPa)	η^{β_1}(GPa.h)	η^{β_2}(GPa.h)	$\beta_{1,2}$	$\Gamma(1+\beta_{1,2})$
1.23	4.52	2.98	1.5	1.23	13.76	0.315	0.896

Calibration of the parameters using marble is employed by experimental data attained from a series of creep tests conducted by Chen et al [17] on a Jinping marble sample obtained from the Jinping tunnel. Fig 8 illustrates compared curves of the creep model and experimental data at a stress level σ_0 = 130.6 MPa with σ_Y = 130.1 MPa over 60 hours. The determined creep parameters and different $\beta_{1,2}$ values employed in the spring-pots of the Maxwell and VP components are presented in Table 5-2. Additionally, Figure 5-8 draws that the curves of the FDVP constitutive model agree very well with the newly proposed FVP constitutive model and only close with the experimental data after 25 hours. This further led to the model calibration using additional experimental data set of the Jinping marble under uniaxial stress load

σ_0 = 125.5 MPa. Further curve comparison of the FDVP constitutive model with its determined parameters is illustrated and presented in Figure 5-9 and Table 5-3 respectively.

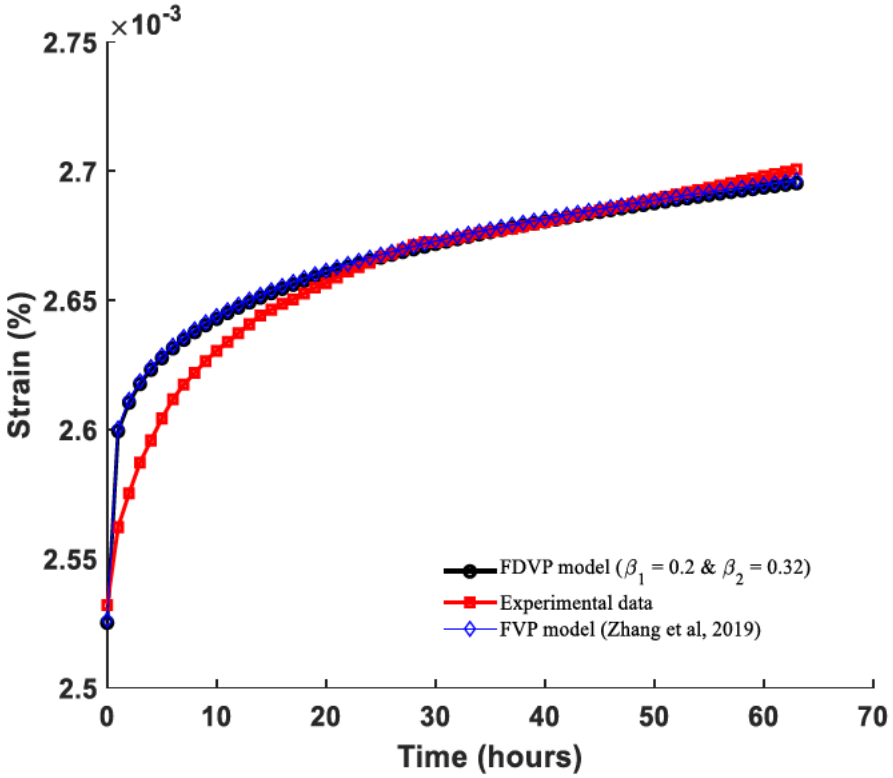

Figure 5-8. Experimental data of the Jinping marble by [17] with the FDVP model prediction

Table 5-2. FDVP constitutive model parameters of Jinping marble

η_M(GPa.h)	η_K(GPa.h)	G_K(GPa)	G_M(GPa)	η^{β_1}(GPa.h)	η^{β_2}(GPa.h)	β_1	β_2	$\Gamma(1+\beta_1)$	$\Gamma(1+\beta_2)$
1920	1961	2610	51.7	1920	3545	0.2	0.32	0.918	0.895

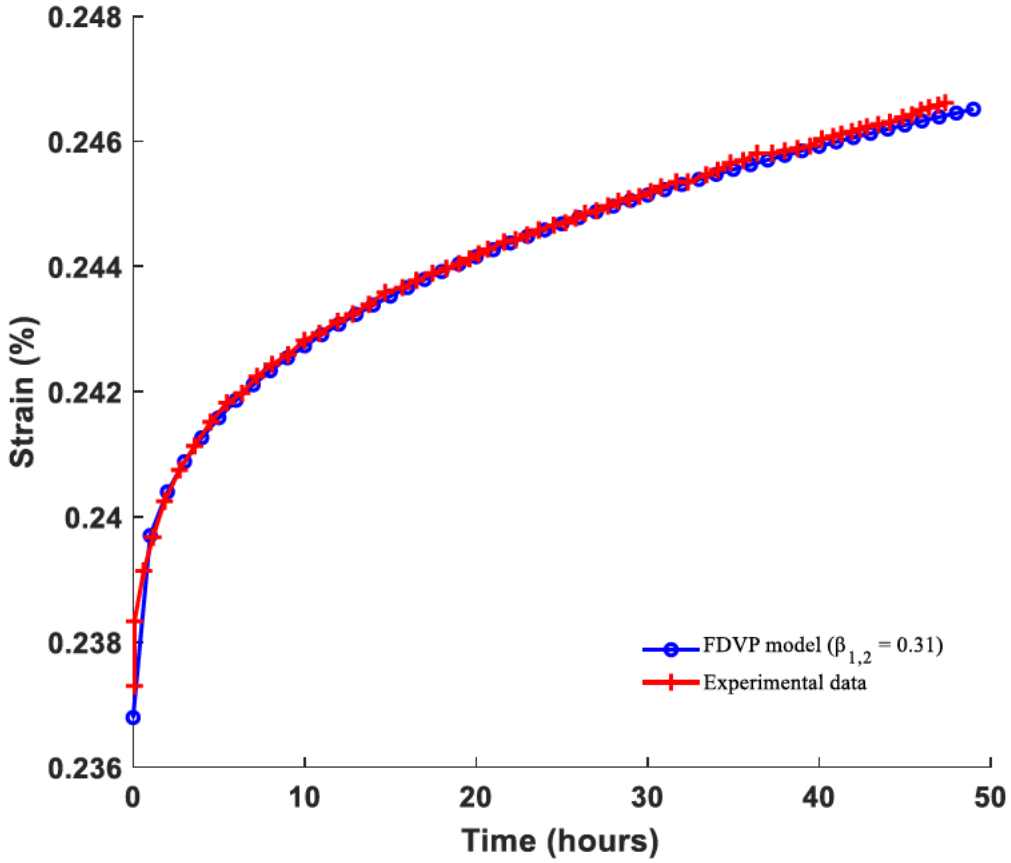

Figure 5-9. Additional experimental data of the Jinping marble [17] with the FDVP model prediction

Table 5-3. Additional FDVP constitutive model parameters of Jinping marble

η_M(GPa.h)	G_K(GPa)	η_K(GPa.h)	G_M(GPa)	η^{β_1}(GPa.h)	η^{β_2}(GPa.h)	$\beta_{1,2}$	$\Gamma(1+\beta_{1,2})$
4650	2610	1961	53	4650	4959	0.31	0.895

The validation results indicate that the constitutive equations of the model can satisfactorily replicate the TD behaviour. Even though the constitutive model can describe the creep behaviour which is associated with the TD deformation experienced by rocks or rock masses. It does not fully describe the 3-stage creep behaviour especially the accelerated creep stage responsible for the long-term deformation herein referred to as squeezing. Hence, this indicates that this preliminary constitutive model will require further development to explicitly capture the 3-stage creep behaviour.

5.4.2 Parametric analysis of the constitutive model

This analysis is conducted to identify the most sensitive and critical parameters in the creep curve description. It is observed that the TD strain of salt rock and Jinping marble depends on these parameters such as $\beta_{1,2}$ and applied stress levels. To gain a better understanding of the influence of these parameters on the TD behaviour, a parametric investigation is performed to evaluate their effects on the creep strain rates.

5.4.2.1 Effects of the fractional derivative order on the creep strain

The effect of the critical parameters $\beta_{1,2}$ on the creep curves of the salt rock and Jinping marble are evaluated and the results presented in this section. Figure 5-10 illustrates a series of creep curves obtained from salt rock indicating the influence of these critical parameters. It is drawn that the higher the values of $\beta_{1,2}$ the greater the creep strain. The variation of the creep curves with time attained from the Jinping marble using the two data sets under different values of $\beta_{1,2}$ are illustrated in Figure 5-11a & Figure 5-11b. It is observed that an increment in the β_1 values lead to an increase in the strain rates in all the creep stages while the steady-state creep strain rates are reduced. Furthermore, an increment in β_2 values showed a small change in the transient and steady-state creep strain rates. The creep curves attained from the additional data set of the Jinping marble shows that the rise in the $\beta_{1,2}$ values have an incremental effect on the creep strain rates (Figure 5-11c).

These results indicate the importance of selecting an appropriate value of $\beta_{1,2}$ to realistically describe the viscoelastic and viscoplastic behaviour of salt rock and marble. Hence, it is necessary to optimize the $\beta_{1,2}$ values when the FDVP constitutive model is employed to estimate the TD deformation of tunnels in squeezing ground. The compared curve results of the FDVP constitutive model are most appropriate when $\beta_{1,2}$ values are between 0.2 - 0.32 and most accurately when $\beta_{1,2}$ = 0.315.

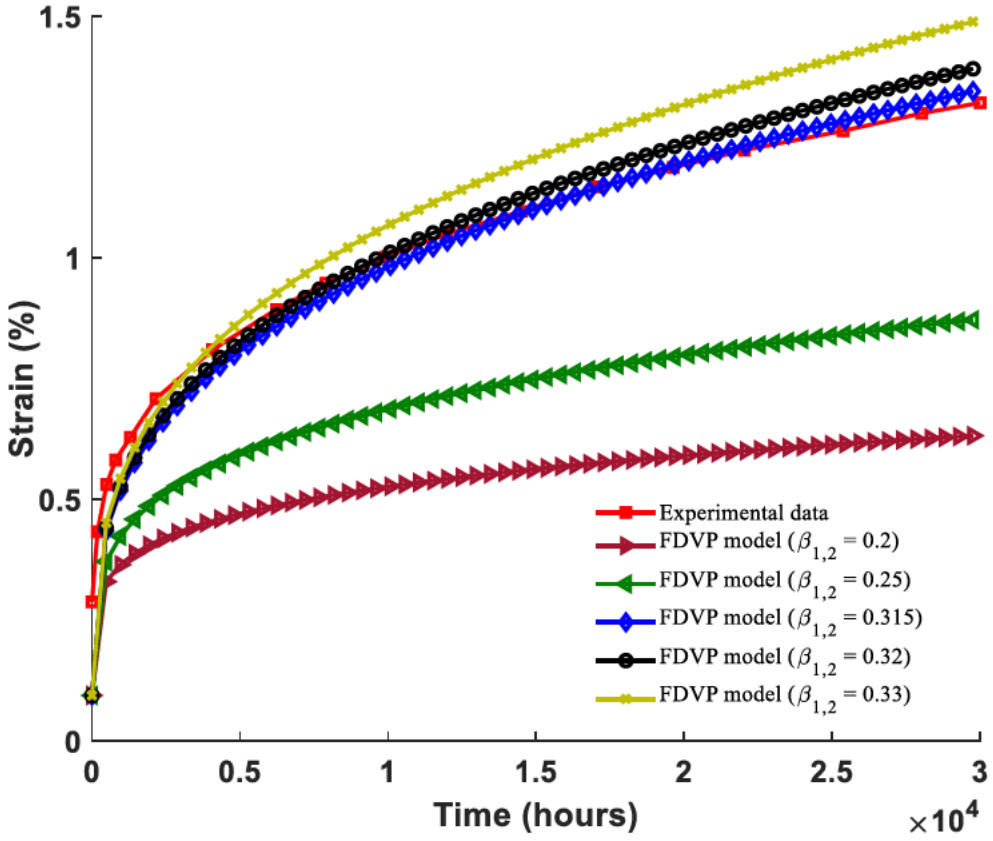

Figure 5-10. Creep strain sensitivity to the different values of $\boldsymbol{\beta_{1,2}}$ on the salt rock

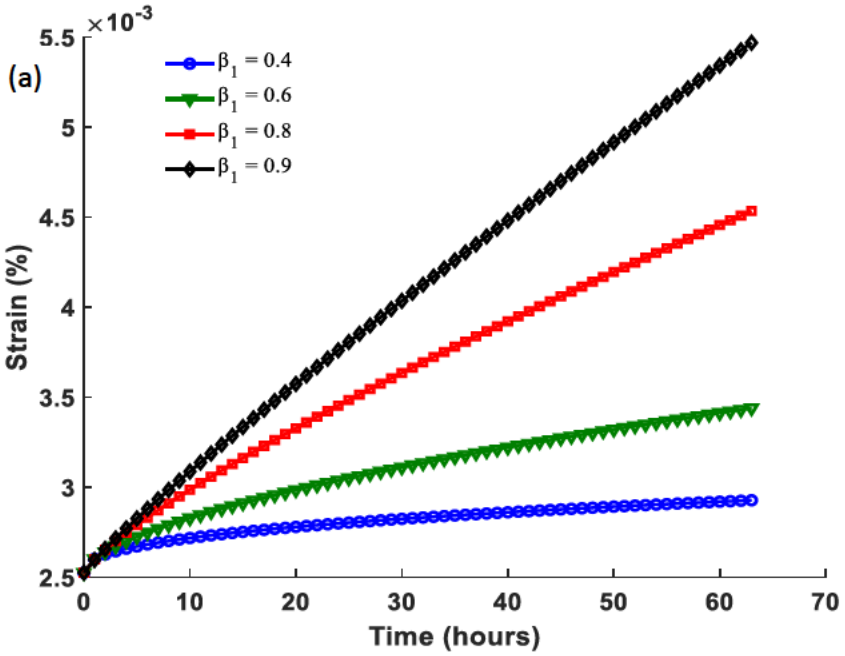

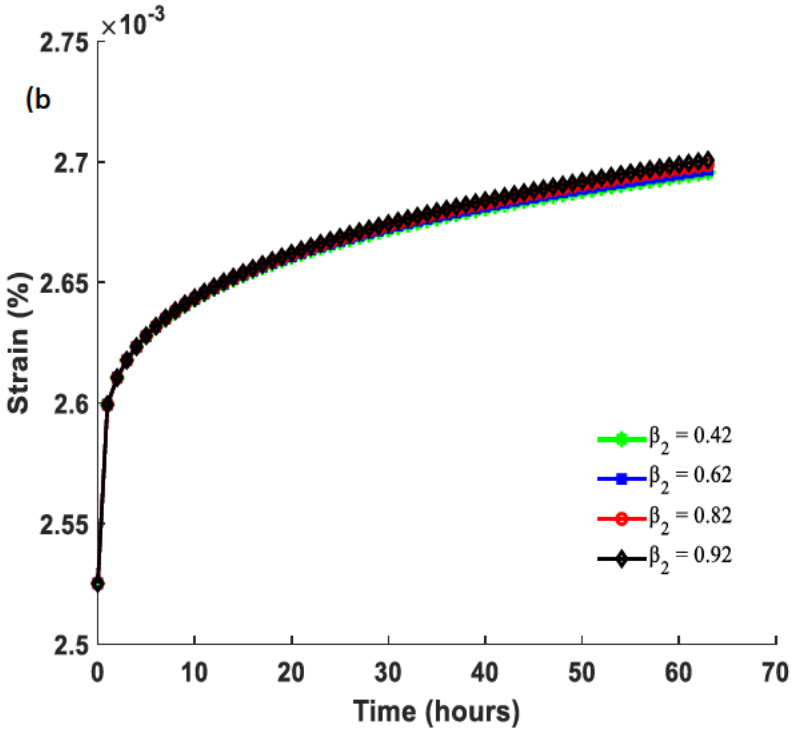

(c)

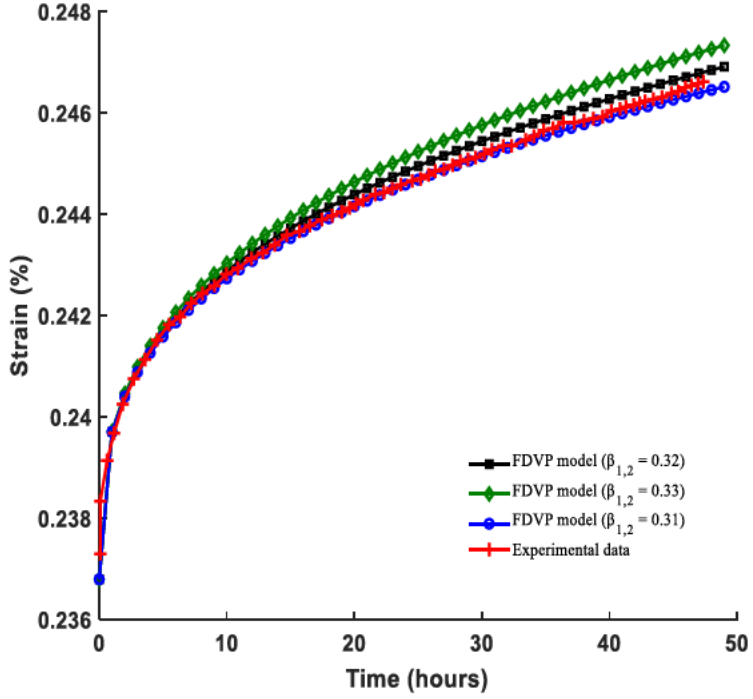

Figure 5-11. Creep strain sensitivity to the different values of (a) β_1 on the Jinping marble, (b) β_2 on the Jinping marble and (c) $\beta_{1,2}$ on the additional Jinping marble

5.4.2.2 Effects of the stress level on the creep strain

The evaluation of the stress level effect on the creep strain rates is conducted by letting the other parameters be constant while changing the stress levels. The stress level applied on the salt rock ranged between 14.1 MPa – 26 MPa and it is observed that a rise in its level had an incremental effect on the strain rates (Figure 5-12a). Additionally, the creep strain response of the Jinping marble subjected to an incremental applied stress level (125.5 MPa - 160 MPa) is illustrated in Figure 5-12b & Figure 5-12c. It is drawn from these depictions that an increment in the applied stress level upsurges the creep strain rates.

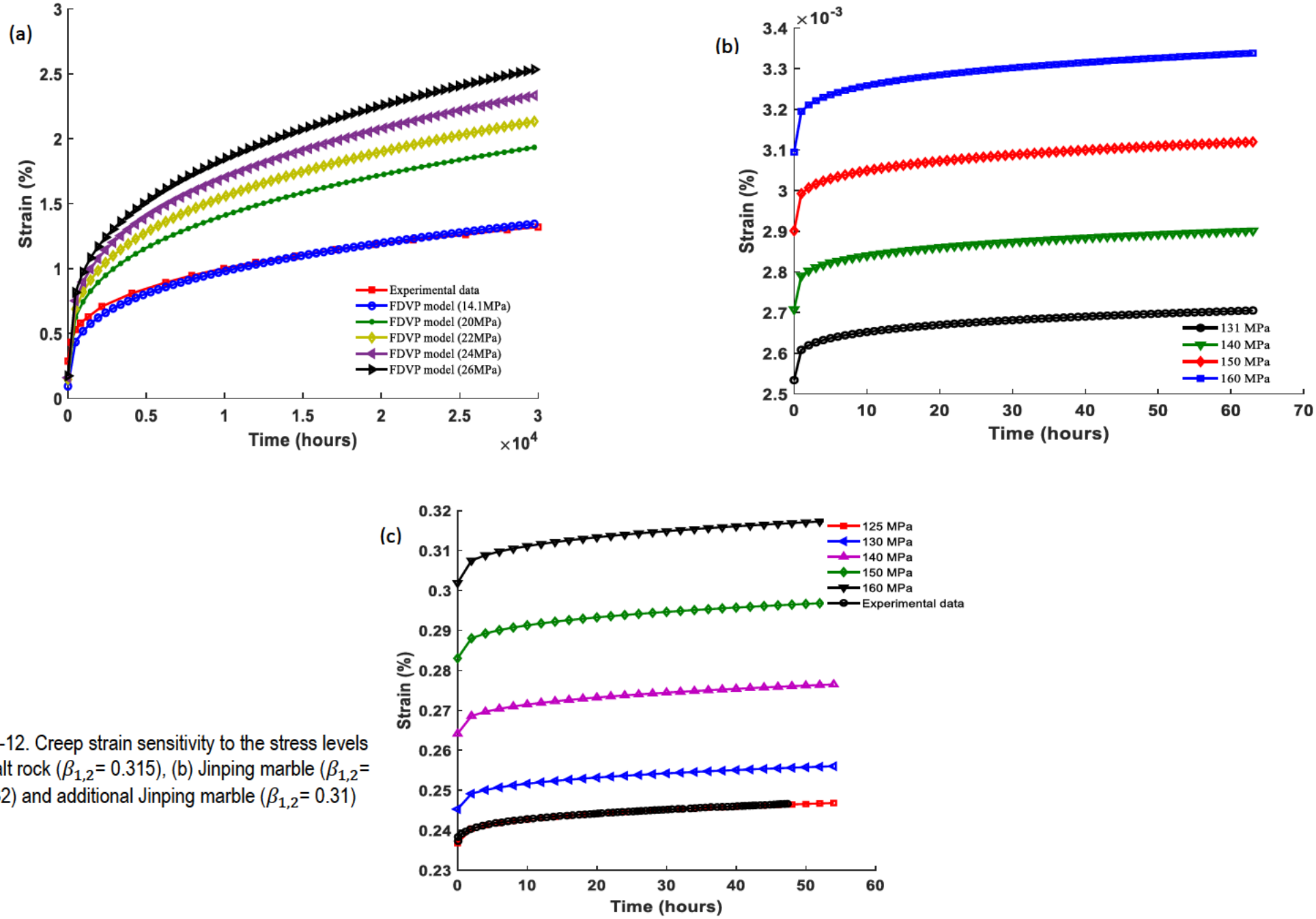

Figure 5-12. Creep strain sensitivity to the stress levels on (a) salt rock ($\beta_{1,2}$= 0.315), (b) Jinping marble ($\beta_{1,2}$= 0.2,0.32) and additional Jinping marble ($\beta_{1,2}$= 0.31)

5.5 In-situ scale verification and numerical implementation

The numerical implementation of the FDVP constitutive model in FLAC^{3D} follows the procedure outlined in the FLAC^{3D} user manual [51] (Appendix C). The implementation flowchart of the developed FDVP constitutive model is shown in Figure 5-13. It is programmed for ITASCA code FLAC^{3D}/3DEC and it can be loaded as a user-defined creep constitutive model by the following commands:

model configure creep

model configure plugin

zone cmodel load "cmodelFDVP006_64" (for FLAC 3D version 6.0)

zone cmodel assign FDVP

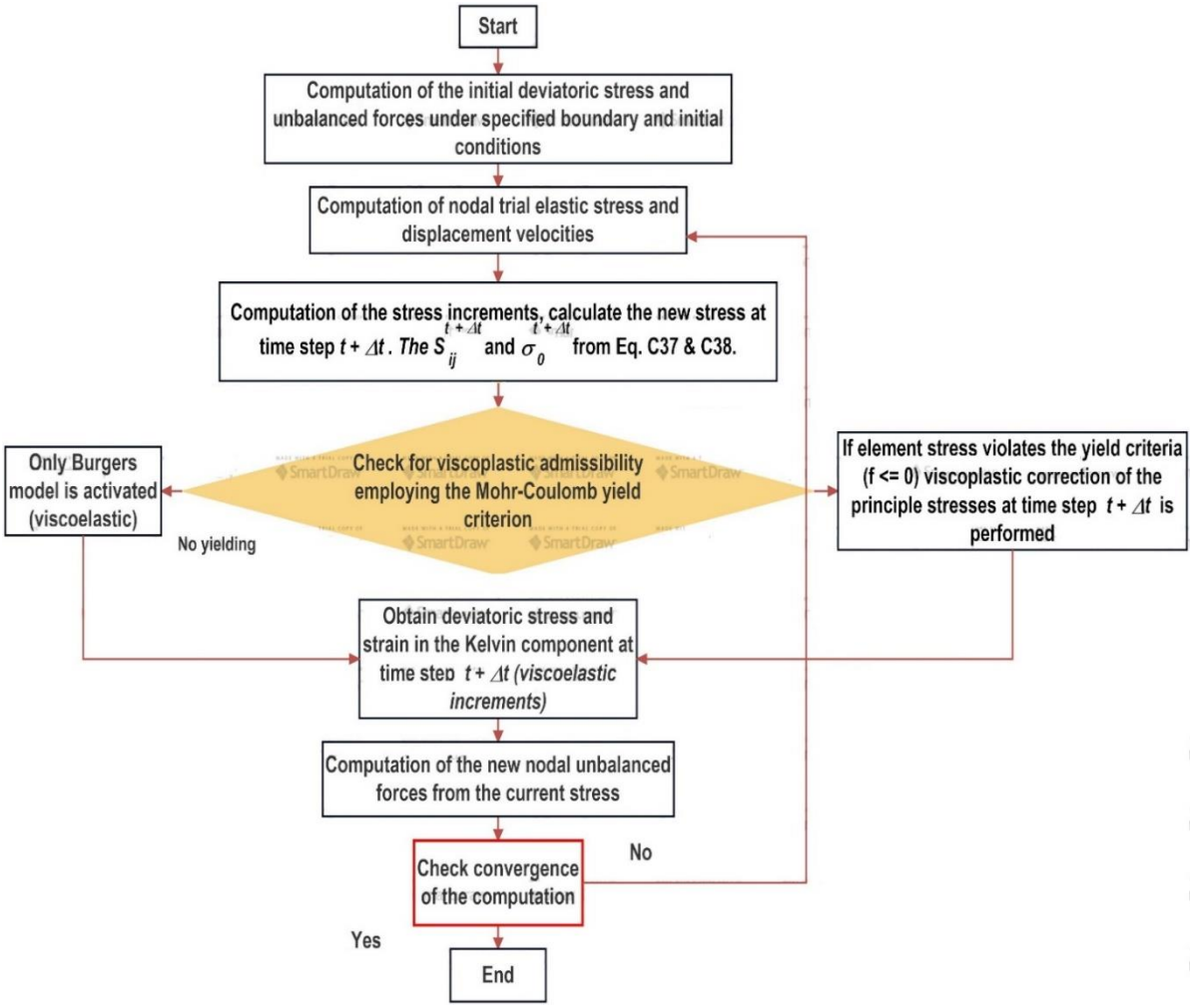

Figure 5-13. FDVP constitutive model implementation

In FLAC^{3D} numerical code, the implementation and running of time-independent constitutive models are different from the creep constitutive models. The dissimilarity is attributed to the numerical simulation time-step, for creep simulation, time-step represent real-time while in static analysis represents virtual values required to reach steady-state conditions [52]. Time-stepping is required in creep analysis to ensure TD simulation stability [6,53]. The conditions for the effective simulation using the FDVP constitutive model require mechanical equilibrium state. The other condition that should be considered in the efficient running of the FDVP constitutive model is the increment of the TD stress. This increment should have a higher value as compared to stress increment dependent on the strain. If this condition is not considered unbalanced forces tend to elevate and inertia effects may affect the outcome of the simulation.

5.5.1 Estimation of tunnel boundary deformation

Real tunnel verification of the proposed model is conducted through field deformation estimated in the Jinping underground tunnel [17,18] at a depth of 2500 m with rock mass parameters of the white marble with green schist's weak planes (Table 5-4). The in-situ stress around the tunnel is assumed to be uniform (36.36 MPa) and the tunnel cross-section layout and deformation monitoring points are illustrated in Figure 5-14. Deformation was estimated around the tunnel boundary using deformation gauges placed at points (1-5) around the tunnel.

Table 5-4. Rock strength, tunnel and creep parameters

ϕ(°)	σ_{cm}(MPa)	GSI	m_i	m_b	s	a	ρ(kg/m^3)	R_q(m)	σ_0(MPa)
9.9	85.2	55	9	0.432	0.000791	0.5	2700	3.68	36.36

Note: ν = Poisson ratio, c = Cohesion ϕ = Friction angle, σ_{cm}= Rock mass strength, GSI= Geological strength index.

β_1	η_M(GPa.h)	β_2	G_M(GPa)	η^{β_1}(GPa.h)	η^{β_2}(GPa.h)	η_K(GPa.h)	G_K(GPa)
0.2	53	0.32	51.7	1920	147.7	81.7	2610

Figure 5-14 illustrates the comparison between deformation from different tunnel monitored points and the FDVP constitutive model over 20 days. However, the main emphasis is placed on the mean monitored deformation with time [1,2,54]. It is observed that the FDVP constitutive model yield results which are closer to the mean monitored deformation as compared to the FVP constitutive model. The monitored deformation is actual in-situ deformation captured by extensometers fixed on specific points along the tunnel boundary.

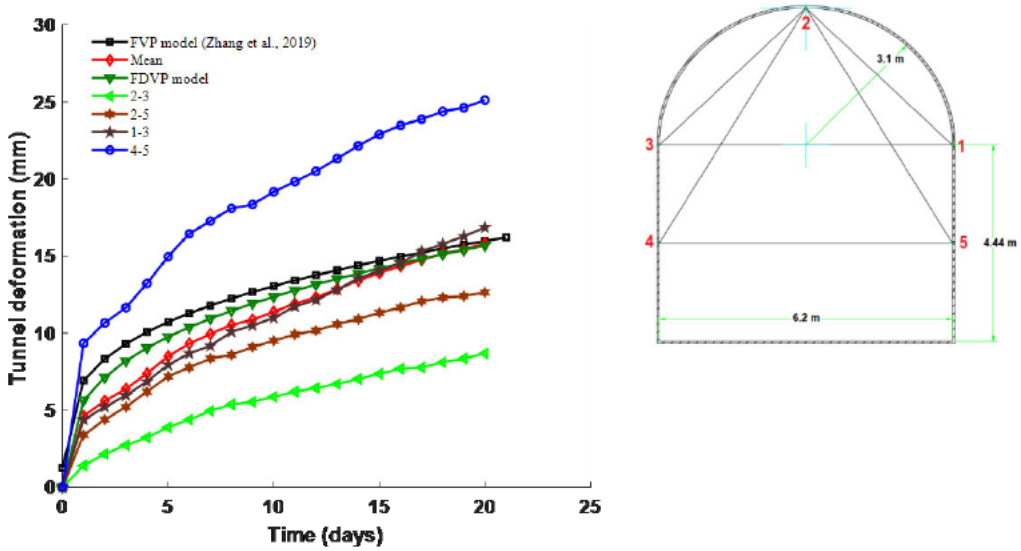

Figure 5-14. Layout of the horseshoe tunnel cross section

5.5.2 Numerical simulation

In this section, the applicability of the FDVP constitutive model in estimating delayed tunnel deformations is conducted within a FLAC^{3D} numerical simulation. The geometrical model considered in the simulation is a real tunnel case excavated in a block (100 m x 80 m x 50 m) constructed symmetrically to reduce the simulation time (Figure 5-15). The boundary and initial conditions of the constructed model are set as zero normal displacements at all the faces as well as the symmetrical plane and initial stress of 8.4 MPa.

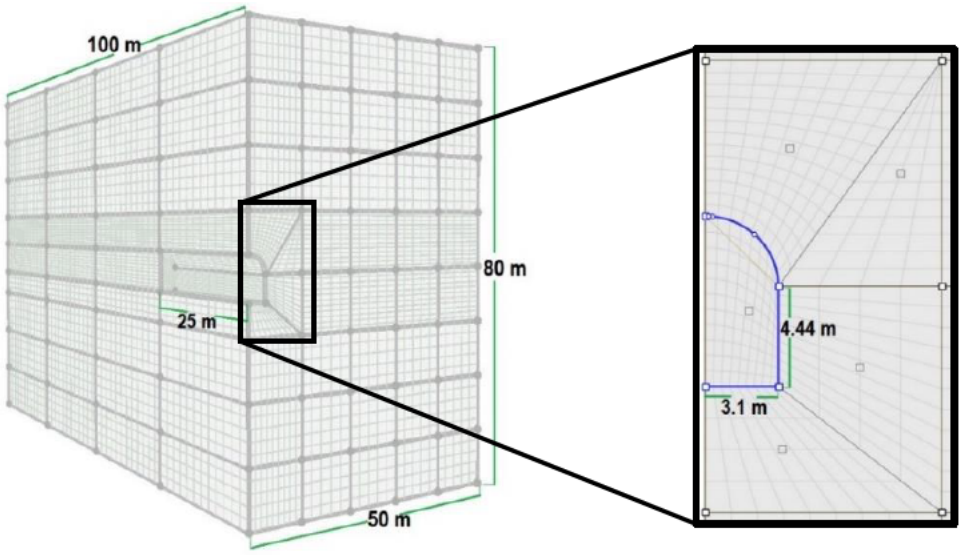

Figure 5-15. Model geometry

The numerical simulation aims to compare the FDVP constitutive model's functionality with the time-independent and creep constitutive models. The in-built creep constitutive model (CVISC) selected for comparison can compute both instantaneous strains as well as the TD strains. It is composed of a plastic slider and Burgers model coupled in series that enables it to estimate instantaneous strains and to some extent delayed deformations characterized by TD behaviour [55]. The instantaneous strains are estimated by the EP component governed by the MC yield surface. The TD strains are estimated by the Burgers model (Kelvin and Maxwell components) capable of describing the transient and steady-state creep stage respectively. The last feature is the accelerated creep stage characterized by delayed deformations responsible for squeezing. However, delayed deformations estimated by the CVISC

constitutive model are highly dependent on stress rather than on time. It must be noted that creep parameters used in this numerical analysis must correspond closely to the field scale values. The laboratory scaled creep parameters should not be employed directly in models for full-scale simulation. They should be scaled to account for the influence of rock mass discontinuities and heterogeneities [51,56]. Therefore, the first step to address this limitation is by employing creep parameters already calibrated on an in-situ scale (Table 5-5).

Table 5-5. FDVP creep model parameters (after Barla et al [57])

η_K(MPa.y)	G_K(MPa)	G_M(MPa)	η^{β_1}(MPa.y)	η^{β_2}(MPa.y)	β_1	β_2	c (MPa)	ϕ	ν	K(MPa)	σ^t(MPa)
4.26	498.1	566	27.98	0.64	0.9	0.65	0.61	28	0.2	942	0.0085

CVISC creep model parameters (after Barla et al., 2010)

η_K(MPa.y)	G_K(MPa)	G_M(MPa)	η_M(MPa.y)	σ^t(MPa)	c (MPa)	ϕ	ν	K(MPa)
4.26	498.1	566	27.98	0.0085	0.61	28	0.2	942

In the numerical simulation, the tunnel employed for the analysis is excavated in stages. After stress was initialized during simulation, the excavation of the tunnel was conducted in stages of 5 m every advance (length of excavation at each step). The tunnel advance simulation commenced with an EP analysis and after 200 steps the simulation reached an equilibrium of which the creep model was activated. The creep period employed in the creep simulation was equivalent to 5 days (4.32E5 s). Figure 5-16 & Figure 5-17 draw results attained after simulation convergence.

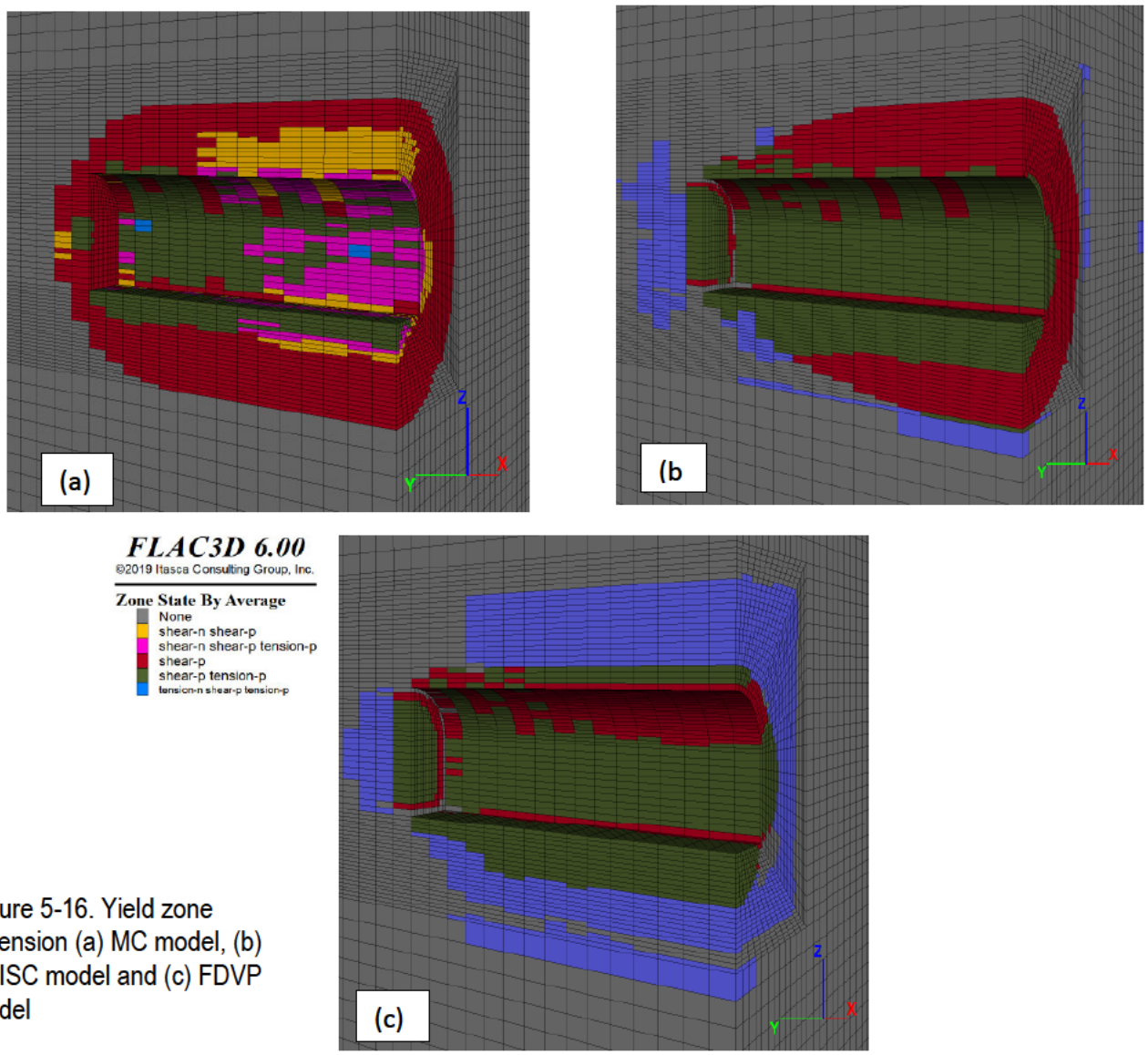

Figure 5-16. Yield zone extension (a) MC model, (b) CVISC model and (c) FDVP model

Figure 5-16 shows the yield zone extension around the tunnel using the time-independent MC, the CVISC and the FDVP constitutive models. The maximum yield zone radii estimated by the MC, the CVISC and the FDVP constitutive models are 7.18 m, 8.18 m and 10.59 m respectively (Table 5-6). Figure 5-17 shows that the total deformation is more around the tunnel simulated using the FDVP constitutive model as compared to the MC and CVISC constitutive models. The total deformation calculated is approximately 1582 mm and accounts for 1418 mm and 42 mm more than the MC and CVISC constitutive model estimations respectively, the variance between the estimations is attributed to the delayed deformations (Table 5-6). This further shows that the CVISC constitutive model underestimates the squeezing related delayed deformations as compared to the FDVP constitutive model.

(a)

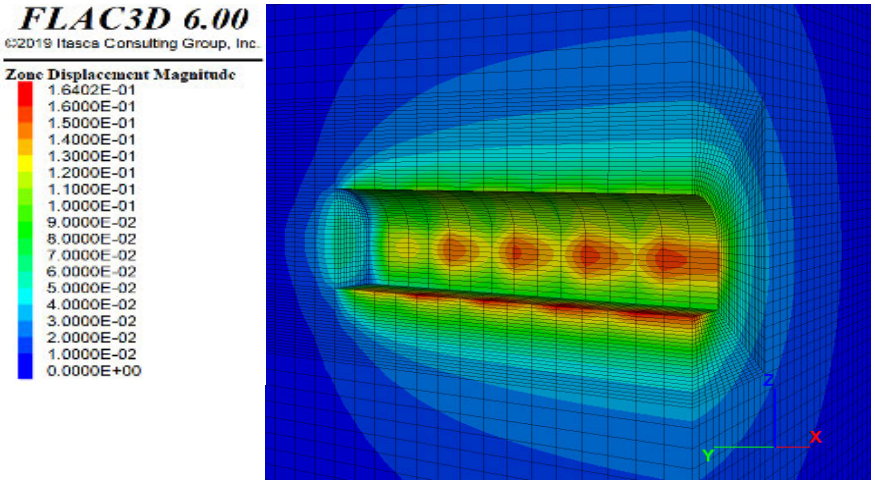

(b)

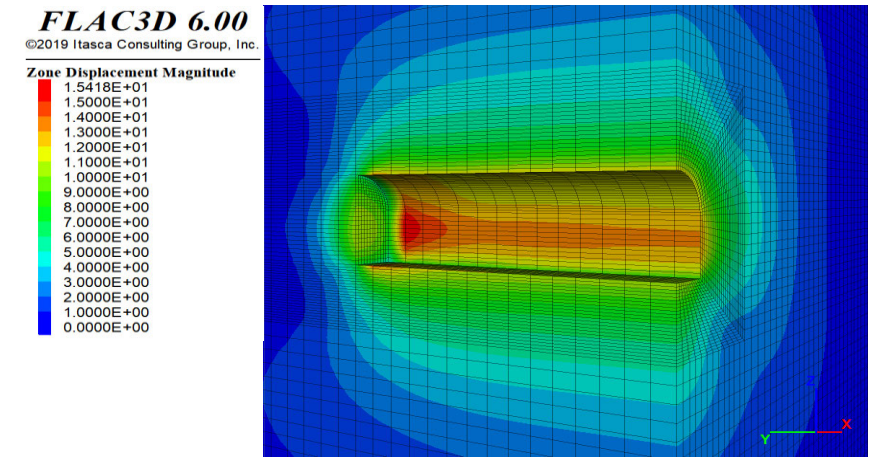

(c)

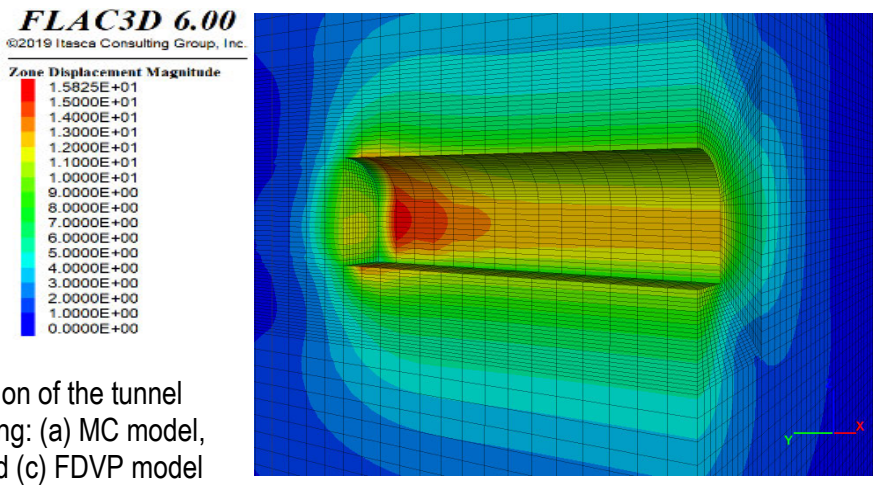

Figure 5-17. Estimation of the tunnel deformation employing: (a) MC model, (b) CVISC model and (c) FDVP model

Table 5-6.Tunnel deformation and viscoplastic extension

Constitutive model	MC model	CVISC model	FDVP model (This study)
Yield extension radius (m)	7.18	8.18	10.59
Tunnel deformation (mm)	164	1540	1582

5.6 Discussion

In this paper, the four rheological elements of the Kelvin and Maxwell components of the Burgers model are utilized to describe the viscoelastic strains whereas the two elements of the VP component are used to replicate the viscoplastic strains. This combination of components gives the FDVP constitutive model its rheological structure. It is presented to describe the TD behaviour related to creep that occurs during tunnel excavation in squeezing ground. Its mathematical derivation has been elucidated to address the shortfall of the existing constitutive laws that describe the TD behavioural feature. Attention is focused on the major issue of the existing constitutive law based on integer-order derivatives incapability of describing the power-law mechanism of geomaterials.

The constitutive equations based on the FDVP rheological structure are derived in 1D then further transformed to 3D by the integration of an adjusted Perzyna [23] overstress function. This adjusted viscoplastic constitutive equation employs the fractional-order derivative theory and the MC yield surface substitution. The important attribute about this adjusted constitutive equation is its capability in estimating the viscoplastic strain rates when the stress state occurs within or above the time-independent yield surface. Consequently, addresses the limitation of the conventional overstress constitutive models based on the classic Perzyna [23] overstress theory.

The validation procedure conducted which involves the experimental data of salt rock by Zhou et al [15] and constitutive model predictions of the creep strain shows close agreement. It is observed that the constitutive model agrees very well when the $\beta_{1,2}$= 0.31 and overall prediction of the transient, steady-state and part of the accelerated creep stages is substantiated. The experimental data provided by Chen et al [17] and the constitutive model indicates that it yields quite close results after 20 hours but very close with the FVP constitutive model. However, this deemed insufficient as such an extended verification is conducted by including additional experimental data set. The additional experimental data set provided, and the constitutive model predicted curves shows very good agreement when $\beta_{1,2}$= 0.31.

The constitutive parameters can be obtained directly from the conventional mechanical and creep tests whereas the $\beta_{1,2}$ values can be calculated between 0 and 1 as a rule of thumb. The three experimental data sets of different rock specimens subjected to different confining pressure provide a comprehensive set of experimental data which can only be replicated by a robust constitutive model. Besides, it is observed that the FDVP constitutive model prediction of the creep curves show very good agreement with these data sets. They employ different creep parameters and subjected to different stress levels but with almost the same values of $\beta_{1,2}$.

After the validation with experimental data, the constitutive model proved to be robust for numerical implementation within FLAC^{3D}. Further verification of its application on an in-situ scale proved to be successful after a series of parametric scaling of the $\beta_{1,2}$ values to accommodate the effect of rock mass discontinuities and heterogeneities. Thereafter, the implemented constitutive model applicability was evaluated by carrying out a large-scale numerical simulation of a tunnel case. In the simulation, the model employed scaled parameters β_1 = 0.9 and β_2 = 0.65 which provided a realistic estimation of the delayed deformation. The completed simulation signified the implemented model was robust for stability analysis of tunnels in squeezing ground.

The FDVP constitutive equations presented are straightforward as such can simply be executed in any numerical code especially ITASCA code (FLAC^{3D}/3DEC). Additionally, estimation of squeezing within tunnels through numerical computation can readily be achieved with the numerical code. Section 5.5.2 presented numerical simulations of the TD behaviour within a tunnel and results show discrepancies in tunnel deformation and yielding zone extension. The results show more deformation and yielding when employing the FDVP constitutive model as compared to the MC and CVISC constitutive models.

However, the FDVP constitutive model assumes ideal viscoplasticity in which the isotropic and kinematic hardening constitutive laws are ignored. Hardening viscoplasticity is characterized by the transient creep, ideal viscoplasticity by the steady-state creep and softening viscoplasticity by the accelerated creep.

Hence, incorporating their constitutive laws and effects is very important for the accurate description of the 3-stage creep mechanism. Although it lacks the consideration of these constitutive laws and the capability to explicitly capture the 3-stage creep mechanism. The constitutive model can be employed with confidence in estimating delayed deformations associated with squeezing ground. Nevertheless, the presented constitutive equations are relatively straightforward to allow for further implementation. As such they have the potential for further integrating the hardening and softening viscoplasticity laws.

5.7 Conclusion

The proposed constitutive model applies fractional-order derivatives to realistically describe the creep behaviour characterised by the power-law mechanism. In addition to that, it employs an adjusted associated viscoplastic flow rule based on the overstress theory which establishes the onset of the delayed deformations. Its mathematical formulation, experimental validation and in-situ verification draw that it can describe the most significant features characterised by the squeezing related TD behaviour. This includes the transient, the steady-state and the accelerated creep stage to some extent. It is shown from this study that:

- The validation results indicate that the model yield close results with experimental data attained from salt rock and marble. Whereas the in-situ verification draws a closer match to the mean tunnel monitored deformation as compared to the FVP constitutive model. As such it describes the TD behaviour associated with squeezing ground more realistically. The sensitivity parameter analysis performed shows that $\beta_{1,2}$ values had a relatively large influence on the constitutive model's viscoelastic viscoplastic characteristics. The constitutive model best describes the creep behaviour and TD characteristic of squeezing rock and rock masses when $\beta_{1,2}$= 0.315. Further on, in-situ verification shows that the model estimates the mean delayed deformation within a tunnel reasonably well when $\beta_{1,2}$ values are between 0.2 - 0.32.

- The FDVP constitutive equations are written in code using C++ for FLAC^{3D} implementation as a user-defined constitutive model. It is drawn that the implemented constitutive model can estimate delayed deformations as compared to the existing CVISC creep constitutive model. However, the $\beta_{1,2}$ values and creep parameters require upscaling to account for the influence of rock mass discontinuities and heterogeneities. The constitutive model estimates more deformation and yielding as compared to the other constitutive models. This is attributed to its capability in estimating the delayed deformation characterized by squeezing.

5.8 Further constitutive model enhancement

The FDVP constitutive equations are not complex as they are readily applicable in research and engineering practice. This allows them to be used with confidence in describing the creep behaviour responsible for delayed deformations in squeezing ground. However, the full explicit description of the 3-stage creep mechanism is a limitation that needs to be addressed. As such further enhancement on the constitutive equations is considered to aid in the explicit 3-stage creep description and currently in progress to include:

- the isotropic and kinematic hardening viscoplasticity and creep damage effect.
- the softening viscoplasticity characterised by the explicit accelerated creep description.
- the dynamic effects governed by the material forces and time-dependent properties.
- the temperature dependency and its effect on the squeezing mechanism.

5.9 References

[1] Debernardi D, Barla G. New viscoplastic model for design analysis of tunnels in squeezing conditions. Rock Mech Rock Eng 2009;42:259–88.

[2] Barla G, Debernardi D, Sterpi D. Time-dependent modeling of tunnels in squeezing conditions. Int J Geomech 2012;12:697–710.

[3] Kodama J, Mitsui Y, Hara S, Fukuda D, Fujii Y, Sainoki A, et al. Time-dependence of mechanical behavior of Shikotsu welded tuff at sub-zero temperatures. Cold Reg Sci Technol 2019;168:102868.

[4] Barla G, Bonini M, Semeraro M. Analysis of the behaviour of a yield-control support system in squeezing rock. Tunn Undergr Sp Technol 2011;26:146–54. https://doi.org/10.1016/j.tust.2010.08.001.

[5] Malan DF. Time-dependent Behaviour of Deep Level Tabular Excavations in Hard Rock. Rock Mech Rock Eng 1999;32:123–55.

[6] Pellet FL. Contact between a tunnel lining and a damage-susceptible viscoplastic medium. C - Comput Model Eng Sci 2009;52:279–95.

[7] Sterpi D, Gioda G. Visco-Plastic behaviour around advancing tunnels in squeezing rock. Rock Mech Rock Eng 2009;42:319–39.

[8] Fahimifar A, Karami M, Fahimifar A. Modifications to an elasto-visco-plastic constitutive model for prediction of creep deformation of rock samples. Soils Found 2015;55:1364–71.

[9] Paraskevopoulou C, Perras M, Diederichs M, Loew S, Lam T, Jensen M. Time-Dependent Behaviour of Brittle Rocks Based on Static Load Laboratory Tests. Geotech Geol Eng 2018;36:337–76.

[10] Kabwe E, Karakus M, Chanda E. Assessment of analytical solutions for time-dependent behavior of unlined tunnels. In: Proceedings of 4th International Symposium on Underground Excavation 2018; 1–9. Istanbul, Turkey.

[11] Yin D, Wu H, Cheng C, Chen Y. Fractional order constitutive model of geomaterials under the condition of triaxial test. Int J Numer Anal Methods Geomech 2013;37:961–72.

[12] Tarasov VE. Review of some promising fractional physical models. International Journal of Modern Physics B. 2013;27(09).

[13] Hou F, Li Q, Liu E, Zhou C, Liao M, Luo H, Liu X. A fractional creep constitutive model for frozen soil in consideration of the strengthening and weakening effects. Advances in Materials Science and Engineering. 2016.

[14] Hui LI, Zhang QJ, Lian-Seng NI, Ying XU. Fractional Order Derivative Nishihara Model of Artificial Frozen Soil. In2014 International Conference on Mechanics and Civil Engineering (icmce-14) 2014. Atlantis Press.

[15] Zhou HW, Wang CP, Han BB, Duan ZQ. A creep constitutive model for salt rock based on fractional derivatives. Int J Rock Mech Min Sci 2011;48:116–21.

[16] Zhou HW, Wang CP, Mishnaevsky L, Duan ZQ, Ding JY. A fractional derivative approach to full creep regions in salt rock. Mech Time-Dependent Mater 2013;17:413–25.

[17] Chen BR, Zhao XJ, Feng XT, Zhao HB, Wang SY. Time-dependent damage constitutive model for the marble in the Jinping II hydropower station in China. Bull Eng Geol Environ 2014;73:499–515.

[18] Zhang J-Z, Zhou X-P, Yin P. Visco-plastic deformation analysis of rock tunnels based on fractional derivatives. Tunn Undergr Sp Technol 2019;85:209–19.

[19] Lu D, Liang J, Du X, Ma C, Gao Z. Fractional elastoplastic constitutive model for soils based on

a novel 3D fractional plastic flow rule. Comput Geotech 2019;105:277–90.

[20] Lu D, Zhou X, Du X, Wang G. A 3D fractional elastoplastic constitutive model for concrete material. Int J Solids Struct 2019;165:160–75.

[21] Zhang L, Liu Y, Yang Q. Mechanics of Materials A creep model with damage based on internal variable theory and its fundamental properties. Int J Mech Mater 2014;78:44–55.

[22] Su X, Chen W, Xu W. Characterizing the rheological behaviors of non-Newtonian fluid via a viscoelastic component: Fractal dashpot. Adv Mech Eng 2017;9:1–12.

[23] Perzyna P. Fundamental problems in viscoplasticity. Adv. Appl. Mech., vol. 9, Elsevier; 1966, p. 243–377.

[24] Yin ZY, Chang CS, Karstunen M, Hicher PY. An anisotropic elastic-viscoplastic model for soft clays. Int J Solids Struct 2010;47:665–77.

[25] Adachi T, Oka F. Constitutive equations for normally consolidated clay based on elasto-viscoplasticity. Soils Found 1982;22:57–7.

[26] Mabssout M, Herreros MI, Pastor M. Wave propagation and localization problems in saturated viscoplastic geomaterials. Int J Numer Methods Eng 2006;68:425–47.

[27] Shahrour I, Meimon Y. Calculation of marine foundations subjected to repeated loads by means of the homogenization method. Comput Geotech 1995;17:93–106.

[28] Yin Z-Y, Hicher P-Y. Identifying parameters controlling soil delayed behaviour from laboratory and in situ pressuremeter testing. Int J Numer Anal Methods Geomech 2008;32:1515–35.

[29] Kimoto S, Oka F. An Elasto-Viscoplastic Model for Clay Considering Destructuralization and Consolidation Analysis of Unstable Behavior. Soils Found 2005;45:29–42.

[30] Kutter BL, Sathialingam N. Elastic-viscoplastic modelling of the rate-dependent behaviour of

clays. Géotechnique 1992;42:427–41.

[31] Yin J-H, Zhu J-G, Graham J. A new elastic viscoplastic model for time-dependent behaviour of normally and overconsolidated clays: theory and verification. Can Geotech J 2002;39:157–73.

[32] Mendiguren J, Cortés F, Galdos L. A generalised fractional derivative model to represent elastoplastic behaviour of metals. Int J Mech Sci 2012;65:12–7.

[33] Yin D, Duan X, Zhou X. Fractional time-dependent deformation component models for characterizing viscoelastic Poisson's ratio. Eur J Mech - A/Solids 2013;42:422–9.

[34] Sumelka W. Fractional viscoplasticity. Mech Res Commun 2014;56:31–6.

[35] Cai W, Chen W, Xu W. Characterizing the creep of viscoelastic materials by fractal derivative models. Int J Non Linear Mech 2016;87:58–63.

[36] Khalil R, Al Horani M, Yousef A, Sababheh M. A new definition of fractional derivative. J Comput Appl Math 2014;264:65–70.

[37] Bagley RL, Torvik PJ. A theoretical basis for the application of fractional calculus to viscoelasticity. Journal of Rheology. 1983;27(3):201-10.

[38] Abdeljawad T. On Riemann and Caputo fractional differences. Comput Math with Appl 2011;62:1602–11.

[39] Zheng Z, Zhao W, Dai H. A new definition of fractional derivative. Int J Non Linear Mech 2019;108:1–6.

[40] Kilbas AAA, Srivastava HM, Trujillo JJ. Theory and applications of fractional differential equations. vol. 204. Elsevier Science Limited; 2006.

[41] Souza Neto E de, Peric D, Owen DRJ. Computational Methods for Plasticity. vol. 55. 2008.

[42] de Borst R, Heeres OM. A unified approach to the implicit integration of standard, non-standard

and viscous plasticity models. Int J Numer Anal Methods Geomech 2002;26:1059–70.

[43] Govindjee S, Kay GJ, Simo JC. Anisotropic modelling and numerical simulation of brittle damage in concrete. Int J Numer Methods Eng 1995;38:3611–33.

[44] Liu HZ, Xie HQ, He JD, Xiao ML, Zhuo L. Nonlinear creep damage constitutive model for soft rocks. Mech Time-Dependent Mater 2017;21:73–96.

[45] Bruning T, Karakus M, Nguyen GD, Goodchild D. Experimental Study on the Damage Evolution of Brittle Rock Under Triaxial Confinement with Full Circumferential Strain Control. Rock Mech Rock Eng 2018;51:3321–41..

[46] Bruning T, Karakus M, Nguyen GD, Goodchild D. An experimental and theoretical stress-strain-damage correlation procedure for constitutive modelling of granite. Int J Rock Mech Min Sci 2019;116:1–12.

[47] Kabwe E, Karakus M, Chanda EK. Proposed solution for the ground reaction of non-circular tunnels in an elastic-perfectly plastic rock mass. Comput Geotech 2020;119:103354.

[48] Kabwe E. Confining stress effect on the elastoplastic ground reaction considering the Lode angle dependence. Int J Min Sci Technol 2020. https://doi.org/https://doi.org/10.1016/j.ijmst.2020.04.002.

[49] Clausen J, Damkilde L, Andersen L. Efficient return algorithms for associated plasticity with multiple yield planes. Int J Numer Methods Eng 2006;66:1036–59.

[50] Abbo AJ, Lyamin A V, Sloan SW, Hambleton JP. A C2 continuous approximation to the Mohr–Coulomb yield surface. Int J Solids Struct 2011;48:3001–10.

[51] Itasca Consulting Group. FLAC3D 6.0 Theory and Background 2017.

[52] Sharifzadeh M, Tarifard A, Ali M. Time-dependent behavior of tunnel lining in weak rock mass

based on displacement back analysis method. Tunn Undergr Sp Technol Inc Trenchless Technol Res 2013;38:348–56.

[53] Salmi EF, Karakus M, Nazem M. Assessing the effects of rock mass gradual deterioration on the long-term stability of abandoned mine workings and the mechanisms of post-mining subsidence – A case study of Castle Fields mine. Tunn Undergr Sp Technol 2019;88:169–85.

[54] Bonini M, Debernardi D, Barla M, Barla G. The Mechanical Behaviour of Clay Shales and Implications on the Design of Tunnels. Rock Mech Rock Eng 2007;42:361.

[55] Boidy E, Bouvard A, Pellet F. Back analysis of time-dependent behaviour of a test gallery in claystone. Tunn Undergr Sp Technol 2002;17:415–24.

[56] Fabre G, Pellet F. Creep and time-dependent damage in argillaceous rocks. Int J Rock Mech Min Sci 2006;43:950–60.

[57] Barla G, Bonini M, Debernardi D. Time Dependent Deformations in Squeezing Tunnels. 12th Int Conf Int Assoc Comput Methods Adv Geomech 2008;2:1–6.

[58] Owen DRJ, Hinton E. Finite elements plasticity: Theory and Practice 1980:603.

[59] Fahimifar A, Tehrani FM, Hedayat A, Vakilzadeh A. Analytical solution for the excavation of circular tunnels in a visco-elastic Burger's material under hydrostatic stress field. Tunn Undergr Sp Technol 2010;25:297–304.

5.10 Appendix: Script

```
#include "modelFDVP.h"
#include "state.h"
#include "convert.h"
#include "version.txt"
#include <algorithm>
#include <limits>

#ifdef FDVP_EXPORTS
  int stdcall DllMain(void *,unsigned, void *) {
  return(1);
  }

  extern "C" EXPORT_TAG const char *getName() {
  return("cmodelfdvp");
  }

  extern "C" EXPORT_TAG unsigned getMajorVersion() {
  return(MAJOR_VERSION);
  }

  extern "C" EXPORT_TAG unsigned getMinorVersion(){
  return(MINOR_VERSION);
  }

  extern "C" EXPORT_TAG void *createInstance() {
    models::ModelFDVP *m = NEWC(models::ModelFDVP());
  return((void *)m);
  }
#endif // FDVP_EXPORTS

namespace models
 {
  static const unsigned long mShearNow    = 0x01;   /* state logic */
  static const unsigned long mTensionNow  = 0x02;
  static const unsigned long mShearPast   = 0x04;
  static const unsigned long mTensionPast = 0x08;
  static const Double pi =  3.14159265358979323846264338327950288419716939937;
  static const Double degrad = pi / 180.0;
  static const Double dC1d3 = 1.0 / 3.0;
  static const Double time = 1.0;
  //static const Double gamma = 0.988;
  //static const Double d4d3 = 4.0 / 3.0;

  ModelFDVP::ModelFDVP() : Bulk_(0.0),
              Kshear_(0.0), Mshear_(0.0), Kviscosity_(0.0),  Mviscosity_(0.0),
              Fdviscosity_(0.0),cohesion_(0.0), friction_(0.0), dilation_
                (0.0), tension_(0.0),
              gamma_(0.0),beta_(0.0),alpha_(0.0),AccshearE_(0.0),AcctensE_
                (0.0), Mnphi_(0.0), Mnpsi_(0.0), Mcsnp_(0.0)
{
    Mekd_[0]= 0.0;
    Mekd_[1]= 0.0;
    Mekd_[2]= 0.0;
    Mekd_[3]= 0.0;
    Mekd_[4]= 0.0;
    Mekd_[5]= 0.0;
```

```
}

UInt ModelFDVP::getMinorVersion() const{
return MINOR_VERSION;
}

String ModelFDVP::getProperties() const{
  return
    (L"bulk,kshear,mshear,kviscosity,mviscosity,fdviscosity,cohesion,frictio
    n,dilation,tension,gamma,beta,alpha,"
L"k_exx,k_eyy,k_ezz,k_exy,k_exz,k_eyz"); 64     }

String ModelFDVP::getStates(void) const {
return L"shear-n,tension-n,shear-p,tension-p"; 68
}

Variant ModelFDVP::getProperty(UInt ul) const {
    switch (ul) {
    case 1:  return(Bulk_);
    case 2:  return(Kshear_);
    case 3:  return(Mshear_);
    case 4:  return(Kviscosity_);
    case 5:  return(Mviscosity_);
    case 6:  return(Fdviscosity_);
    case 7:  return(cohesion_);
    case 8:  return(friction_);
    case 9:  return(dilation_);
    case 10: return(tension_);
    case 11: return(gamma_);
    case 12: return(beta_);
    case 13: return(alpha_);
    case 14:  return(Mekd_[0]);
    case 15:  return(Mekd_[1]);
    case 16:  return(Mekd_[2]);
    case 17:  return(Mekd_[3]);
    case 18:  return(Mekd_[4]);
  case 19: return(Mekd_[5]);
  }
  return(0.0);
}

void ModelFDVP::setProperty(UInt ul,const Variant &p,UInt  restoreVersion){
  ConstitutiveModel::setProperty(ul,p,restoreVersion);
  switch (ul) {
    case 1: { // BULK
      Bulk_ = p.toDouble();
      break;
    }
    case 2: { // KELVIN SHEAR
      Kshear_ = p.toDouble();
      break;
    }
    case 3: { // MAXWELL SHEAR
      Mshear_ = p.toDouble();
      break;
```

```
109         }
110         case 4: {  // KELVIN VISCOSITY
111           Kviscosity_ = p.toDouble();
112           break;
113         }
114         case 5: {  // MAXWELL VISCOSITY
115           Mviscosity_ = p.toDouble();
116           break;
117         }
118         case 6: {  // FD VISCOSITY
119           Fdviscosity_ = p.toDouble();
120           break;
121         }
122         case 7: {  // COHESION
123           cohesion_ = p.toDouble();
124           break;
125         }
126         case 8: {  // FRICTION ANGLE
127           friction_ = p.toDouble();
128           break;
129         }
130         case 9: {  // DILATION ANGLE
131           dilation_ = p.toDouble();
132           break;
133         }
134         case 10:{ // TENSION
135           tension_ = p.toDouble();
136           break;
137         }
138         case 11:{ // GAMMA
139           gamma_ = p.toDouble();
140           break;
141         }
142         case 12:{ // BETA
143           beta_ = p.toDouble();
144           break;
145           }
146         case 13:{ // ALPHA
147           alpha_ = p.toDouble();
148           break;
149           }
150         case 14: {  // Kelvin strain 11
151           Mekd_[0] = p.toDouble();
152           break;
153         }
154         case 15: {  // Kelvin strain 22
155           Mekd_[1] = p.toDouble();
156           break;
157         }
158         case 16: {  // Kelvin strain 33
159           Mekd_[2] = p.toDouble();
160           break;
161         }
162         case 17: {  // Kelvin strain 12
163           Mekd_[3] = p.toDouble();
164           break;
```

```
}
166         case 18: {  // Kelvin strain 13
167           Mekd_[4] = p.toDouble();
168           break;
169         }
170         case 19: {  // Kelvin strain 23
171           Mekd_[5] = p.toDouble();
172           break;
173         }
174       }
175     }
176
177     void ModelFDVP::copy(const ConstitutiveModel *cm)
178     {
179       ConstitutiveModel::copy(cm);
180       const ModelFDVP *vm = dynamic_cast<const ModelFDVP  *>(cm);
181       if (!vm) throw std::runtime_error("Internal error: constitutive model
            dynamic cast failed.");
182       Bulk_       = vm->Bulk_;
183       Kshear_     = vm->Kshear_;
184       Mshear_     = vm->Mshear_;
185       Kviscosity_ = vm->Kviscosity_;
186       Mviscosity_ = vm->Mviscosity_;
187       Fdviscosity_ = vm->Fdviscosity_;
188       cohesion_   = vm->cohesion_;
189       friction_   = vm->friction_;
190       dilation_   = vm->dilation_;
191       tension_    = vm->tension_;
192       gamma_      = vm->gamma_;
193       beta_       = vm->beta_;
194       alpha_      = vm->alpha_;
195       AccshearE_  =  vm->AccshearE_;
196       AcctensE_   =  vm->AcctensE_;
197       Mnphi_      =  vm->Mnphi_;
198       Mnpsi_      =  vm->Mnpsi_;
199       Mcsnp_      =  vm->Mcsnp_;
200       Mekd_[0]    = vm->Mekd_[0];
201       Mekd_[1]    = vm->Mekd_[1];
202       Mekd_[2]    = vm->Mekd_[2];
203       Mekd_[3]    = vm->Mekd_[3];
204       Mekd_[4]    = vm->Mekd_[4];
205       Mekd_[5]    = vm->Mekd_[5];
206     }
207
208     void ModelFDVP::initialize(UByte  dim,State  *s)  {
209       ConstitutiveModel::initialize(dim,s);
210       if (Mshear_ <= 0.0) Mshear_ = 1e-20 ;
211       if (Kshear_ <= 0.0) Kshear_ = 0.0;
212       if (Kviscosity_ <= 0.0)  Kshear_ = 0.0;
213       //if (yield_<= 0.0) yield_ = 0.0;
214       //if (gamma_<= 0.0) gamma_ = 0.0;
215       //iMerr = 0;
216       //if (friction_ > 89.0) iMerr = 1;
217       //if (fabs(dilation_)  > 89.0) iMerr = 2;
218       //if (cohesion_  < 0.0) iMerr = 3;
219       //if (tension_ < 0.0) iMerr = 4;
```

```
220       //if (iMerr != 0) {
221       //  iNerr = 126;
222       //  iErr = 1 ;
223       //}
224       Double dSphi = sin(friction_ * degrad);
225       Double dSpsi = sin(dilation_ * degrad);
226       Mnphi_  = (1.0 + dSphi) / (1.0 -  dSphi);
227       Mnpsi_  = (1.0 + dSpsi) / (1.0 -  dSpsi);
228       Mcsnp_  = 2.0 * cohesion_ * sqrt(std::max(Mnphi_, 0.0));
229
230       // --- set tension to prism apex if larger than apex ---
231       Double apex = tension_;
232       if (friction_ != 0.0) apex = cohesion_ / tan(friction_ *  degrad);
233       tension_ = ((apex < tension_) ? apex : tension_);
234     }
235
236     static const UInt eps = 6;
237     static const UInt ept = 7;
238
239     void ModelFDVP::run(UByte dim,State *s) {
240       ConstitutiveModel::run(dim,s);
241       UInt iplas = 0;
242       Double e1=0,e2=0,x1=0;
243       Double tempk=0, tempm=0;
244
245       if (!s->sub_zone_) {
246         s->working_[0] = 0.0;
247         s->working_[1] = 0.0;
248         s->working_[2] = 0.0;
249         s->working_[3] = 0.0;
250         s->working_[4] = 0.0;
251         s->working_[5] = 0.0;
252         s->working_[eps] =0.0;
253         s->working_[ept] =0.0;
254       }
255
256       Double dCrtdel =  (s->isCreep() ? s->getTimeStep() : 0.0);
257
258       /* --- plasticity indicator:                                    */
259       /*     store 'now' info. as 'past' and turn 'now' info off ---*/
260       if (s->state_ & mShearNow) s->state_ |= mShearPast;
261       s->state_ = s->state_ & ~mShearNow;
262       if (s->state_ & mTensionNow) s->state_ |= mTensionPast;
263       s->state_ = s->state_ & ~mTensionNow;
264
265       if (Kviscosity_ <= 0.0) tempk = 0.0;
266       else tempk = 1.0 / Kviscosity_ ;
267       if (Mviscosity_ <= 0.0) tempm = 0.0;
268       //else tempm = pow (time,beta_)*(1.0 / Mviscosity_*gamma_);
269       //else tempm = 1.0 / Mviscosity_ *gamma_ ;
270       else tempm = 1.0 / Mviscosity_ ;
271
272       Double temp  = 0.5 * Kshear_ * dCrtdel * tempk;
273       Double a_con = 1.0 + temp;
274       Double b_con = 1.0 - temp;
275       Double ba    =  b_con / a_con;
```

```
329     if (canFail())
330     {
331       /* --- calculate and sort principal stresses and principal  directions
            --- */
332       // Calculate principal stresses
333       SymTensorInfo info;
334       DVect3 prin = s->stnS_.getEigenInfo(&info);
335       //; --- shear yield criterion ---
336       Double fs    = prin.x() - prin.z() * anphi + amc;
337       Double alams = 0.0;
338       //; --- tensile yield criterion ---
339       Double ft    = tension_ - prin.z();
340       Double alamt = 0.0;
341       Double bisc = sqrt(1.0 + anphi * anphi) + anphi;
342       Double pdiv = - ft + (prin.x() - anphi * tension_ + amc) * bisc;
343       //; --- tests for failure ---
344       if (fs < 0.0 && pdiv <= 0.0) {
345         //; ---     shear failure ---
346         e1 = Bulk_ + (2*dC1d3) * c1dxc;
347         e2 = Bulk_ - dC1d3 * c1dxc;
348         x1 = 2.0 * Fdviscosity_*gamma_;
349         alams = (fs / x1) * deriv * dCrtdel;
350         prin.rx() -= alams * (e1 - e2 * anpsi);//sigma1
351         prin.ry() -= alams *  e2 * (1.0 - anpsi);
352         prin.rz() -= alams * (e2 -  e1 *  anpsi);//sigma3
353         s->state_ |= mShearNow;
354         iplas = 1;
355       }
356       else  {
357         if (ft < 0.0 && pdiv > 0.0) {
358           //; ---     tension failure ---
359           e1 = Bulk_ + (2*dC1d3) * c1dxc;
360           e2 = Bulk_ - dC1d3 * c1dxc;
361           //alamt = ft / e1 ;
362           alamt = (ft / x1) * deriv * dCrtdel;
363           Double tco=  alamt * e2 ;
364           prin.rx() += tco;
365           prin.ry() += tco ;
366           prin.rz() = tension_;
367           s->state_ |= mTensionNow;
368           iplas = 2;
369         }
370       }
371       //simple apex correction
372       if (friction_)
373       {
374         Double dApex = cohesion_ / tan(friction_*degrad);
375         if  ((prin.x()>=dApex)||(prin.y()>=dApex)||(prin.z()>=dApex))
376         {
377           if(prin.x()>=dApex) prin.rx() = tension_;
378           if(prin.y()>=dApex) prin.ry() = tension_;
379           if(prin.z()>=dApex) prin.rz() = tension_;
380           iplas = 2;
381           s->state_ |=  mTensionNow;
382         }
383       }
```

```
384         //; --- resolve back to global axes ---
385         if (iplas != 0)
386         {
387           /* --- resolve back to global axes --- */
388           s->stnS_ = info.resolve(prin);// transform back to refrence  frame
389         }
390
391         //; --- accumulate hardening parameter increments ---
392         if  (iplas == 1)
393         {
394           Double de1ps = alams;
395           Double de3ps = -alams * anpsi;
396           Double depm  =  dC1d3 * (de1ps + de3ps);
397           de1ps =  de1ps - depm;
398           de3ps =  de3ps - depm;
399           s->working_[eps] += (sqrt(0.5*(de1ps*de1ps+depm*depm+de3ps*de3ps))  *
                s->getSubZoneVolume());
400         }
401         if (iplas == 2)
402         {
403           s->working_[ept] -= (alamt * s->getSubZoneVolume());
404         }
405       } // if (canFail())


 //;--- sub-zone contribution to Kelvin-strains ---
 407       s0    = dC1d3 * (s->stnS_.s11() + s->stnS_.s22() + s->stnS_.s33());
 408       s->working_[0] += (Mekd_[0] * ba  +  (s->stnS_.s11() - s0 + s11old) *
           z_con)  * s->getSubZoneVolume();
 409       s->working_[1] += (Mekd_[1] * ba  +  (s->stnS_.s22() - s0 + s22old) *
           z_con) * s->getSubZoneVolume();
 410       s->working_[2] += (Mekd_[2] * ba  +  (s->stnS_.s33() - s0 + s33old) *
           z_con) * s->getSubZoneVolume();
 411       s->working_[3] += (Mekd_[3] * ba  +  (s->stnS_.s12()      + s12old) *
           z_con) * s->getSubZoneVolume();
 412       s->working_[4] += (Mekd_[4] * ba  +  (s->stnS_.s13()      + s13old) *
           z_con) * s->getSubZoneVolume();
 413       s->working_[5] += (Mekd_[5] * ba  +  (s->stnS_.s23()      + s23old) *
           z_con) * s->getSubZoneVolume();
 414       //;--- update stored Kelvin-strains and plastic strain ---
 415       if (s->sub_zone_ == s->total_sub_zones_-1) {
 416         Double Aux = 1./s->getZoneVolume();
 417         if (s->overlay_==2) Aux *= 0.5;
 418         Mekd_[0]= s->working_[0] * Aux;
 419         Mekd_[1]= s->working_[1] * Aux;
 420         Mekd_[2]= s->working_[2] * Aux;
 421         Mekd_[3]= s->working_[3] * Aux;
 422         Mekd_[4]= s->working_[4] * Aux;
 423         Mekd_[5]= s->working_[5] * Aux;
 424         if (canFail())
 425         {
 426           AccshearE_ += s->working_[eps]*Aux;
 427           AcctensE_  += s->working_[ept]*Aux;
 428         }
 429       }
 430
 431       if( (s->state_ & mShearNow) || (s->state_ & mTensionNow) )
 432         s->viscous_ = false; // inhibit viscous strains
```

```
433       else
434         s->viscous_ = true;  // allow viscous strains
435     }
436
437     Double ModelFDVP::getStressStrengthRatio(const SymTensor &st) const {
438       DVect3 prin = st.getEigenInfo();
439       Double rat = 10.0;
440       Double tanf = std::tan(friction_*degrad);
441       Double tcut = friction_ ? std::min(tension_,(cohesion_/tanf)) : tension_;
442       if (tcut - prin.z() <= 0.0)
443         rat = 0.0;
444       else
445       {
446         Double sinf = std::sin(friction_*degrad);
447         Double denom = 1.0 - sinf;
448         Double nph = limits<Double>::max();
449         if (denom) nph = (1.0 + sinf) / denom;
450         Double sig1f = nph*prin.z() - 2.0*cohesion_*std::sqrt(nph);
451         denom = prin.z() - prin.x();
452         if (denom) rat = (prin.z() - sig1f) / denom;
453       }
454       rat = std::min(rat,10.0);
455       return(rat);
456     }
457
458     void ModelFDVP::scaleProperties(const Double &scale,const  std::vector<UInt>
        &props) {
459       for (UInt u=0;u<props.size();++u) {
460         switch (props[u]) {
461           case 1: Bulk_ *= scale;  break;
462           case 2: Kshear_ *= scale;  break;
463           case 3: Mshear_ *= scale;  break;
464           case 7: cohesion_ *= scale;  break;
465           case 8: friction_ =  std::max(0.0,std::min(85.0,std::atan(std::tan
              (friction_*degrad) * scale)/ degrad));  break;
466           case 9: dilation_ = std::max(0.0,std::min(85.0,std::atan(std::tan
              (dilation_*degrad) * scale)/ degrad));  break;
467           case 10: tension_ *= scale;  break;
468           default: break;
469         }
470       }
471       setValid(0);
472     }
473   }
474   // EOF
475
476
```

Statement of Authorship

Title of Paper	Isotropic Damage Constitutive Model for Time-Dependent Behaviour of Tunnels in Squeezing Ground
Publication Status	☑ Published ☐ Accepted for Publication ☐ Submitted for Publication ☐ Unpublished and Unsubmitted w ork w ritten in manuscript style
Publication Details	Eugie Kabwe, Murat Karakus, Emmanuel K. Chanda, Isotropic Damage Constitutive Model for Time-Dependent Behaviour of Tunnels in Squeezing Ground. Computers and Geotechnics, Volume 120, (2020).103738. https://doi.org/10.1016/j.compgeo.2020.103738

Principal Author

Name of Principal Author (Candidate)	EUGIE KABWE		
Contribution to the Paper	Conceptualization, Formal analysis, Methodology, Investigation, Writing - original draft, Writing - review & editing and as the corresponding author		
Overall percentage (%)	80%		
Certification:	This paper reports on original research I conducted during the period of my Higher Degree by Research candidature and is not subject to any obligations or contractual agreements with a third party that would constrain its inclusion in this thesis. I am the primary author of this paper.		
Signature		Date	17/08/2020

Co-Author Contributions

By signing the Statement of Authorship, each author certifies that:

i. the candidate's stated contr bution to the publication is accurate (as detailed above);
ii. permission is granted for the candidate in include the publication in the thesis; and
iii. the sum of all co-author contributions is equal to 100% less the candidate's stated contribution.

Name of Co-Author	MURAT KARAKUS		
Contribution to the Paper	Supervision of the work; Identification of the problem and methodology, reviewing & editing		
Signature		Date	18/08/2020

Name of Co-Author	EMMANUEL K. CHANDA		
Contribution to the Paper	Supervision, review & editing		
Signature		Date	18/08/2020

Chapter 6

Isotropic Damage Constitutive Model for Time-Dependent Behaviour of Tunnels in Squeezing Ground *(Paper 4)*

Eugie Kabwe, Murat Karakus, Emmanuel K Chanda

Published in Computer and Geotechnics

Abstract

The conventional constitutive models employed to describe rock mass creep behaviour under the squeezing mechanism are widely adopted in research and design practice. However, these models fail to replicate the 3-phase creep behaviour especially the accelerated creep phase; only the transient and steady creep phase are described explicitly. Hence, this paper presents an elasto-viscoplastic with isotropic damage (EVPD) constitutive model that describes the 3-phase behaviour. This is achieved by the Newtonian dashpot replacement with the fractal-order spring-pot that incorporates isotropic damage effect. Derivation of the fractal-order derivative-based creep constitutive equations is conducted using scaling transformations. The model is then calibrated using experimental data and its derived constitutive equation is implemented in FLAC^{3D} using C++ code. Furthermore, its numerical implementation is employed to simulate delayed response of a tunnel excavated in squeezing ground. The average radii of yield zone around the tunnel estimated by the CVISC and EVPD constitutive models are approximately 8.7 m and 14.7 m, respectively. Whereas the deformation is approximately 29% and accounts for 8% more than the CVISC estimation, the disparity attributed to time-dependent behaviour. It is observed that the EVPD constitutive model describes the creep mechanism and mean deformation in squeezing ground reasonably well.

Keywords: Accelerated creep; Isotropic damage; Delayed deformations; Fractal-order derivative; Squeezing ground

6.1 Introduction

The time-dependent behaviour of rocks and rock masses in response to stress has a significant impact on the stability of underground tunnels. The behaviour might occur instantaneously after tunnel excavation and continue over time and it is often referred to as creep. Hence, estimation and numerical modelling of the time-dependent behaviour of rocks and rock masses is of great importance in tunnel design and stability analysis [1]. There are several constitutive models developed with different assumptions employed to estimate creep related time-dependent behaviour in tunnels. Reversible deformation is one aspect considered in the classical constitutive model for time-dependent behaviour estimation. Conventional viscoelastic models have been developed and used by a great number of researchers by employing analytical formulations [2]. In line with this, time-dependent rheological components have been integrated into these conventional viscoelastic models by different researchers such as Debernardi & Barla [3] and Fahimifar et al., [1]. conventional viscoelastic models are only capable of capturing the irrecoverable viscoplastic strains by incorporating the classic Bingham component [4,5].

The accurate estimation of these irrecoverable creep strains requires a proper and explicit description of the 3-phase (3-stage) creep behaviour (Figure 1). This entails that the elastic-viscoplastic (EVP) creep behaviour of the rock masses should be taken into consideration. Most importantly the viscoplastic behaviour exhibited in accelerated creep phase characterised by delayed deformation and damage responsible for squeezing. The idealised creep behaviour consists of the instantaneous elastic strain which tends to occur immediately upon the subjection of load or stress, then followed by the 3-phases. The 3-phase creep behaviour is interpreted as follows [6]: (1) Stage 1 or primary (transient) creep is represented by the Kelvin component where viscoelastic (reversible) deformation occurs sometimes accompanied by irreversible deformation this results in strain accumulation with decreasing rate over time. In this phase, the rock undergoes strain hardening and deformation is characterised by sliding and breakage of material weak bonds. (2) Stage 2 or secondary (steady-state) creep is represented by the Maxwell component, this phase exhibits a consistent strain accumulation over time. It is also

characterised by the intermediate behaviour between strain hardening and strain softening mechanism of the transient and accelerated creep phases respectively, and (3) Stage 3 or tertiary (accelerated) creep is a phase where there is a non-linear rapid strain increment leading to rupture and commonly represented by viscoplastic (VP) models. It is characterised by rock failure (Figure 6-1).

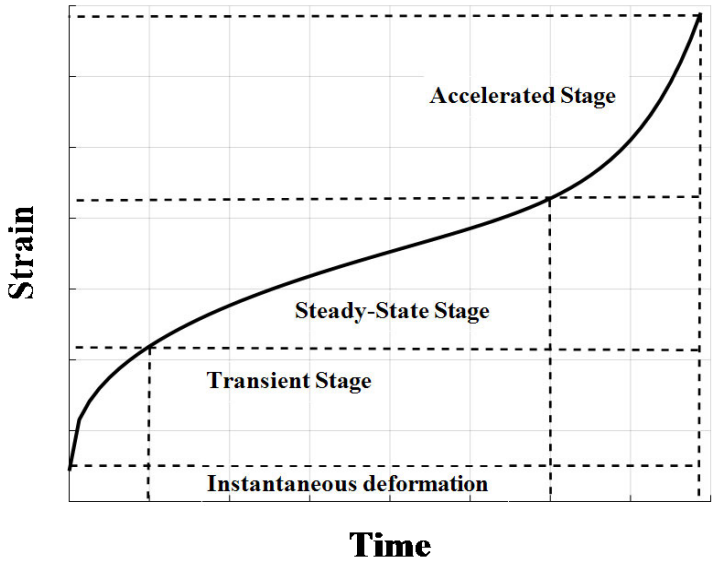

Figure 6-1. The 3-phase creep mechanism

The transient and steady creep phase combination can be represented by merging the Kelvin and Maxwell components into a Burgers model. However, representation of the entire 3-phase creep behaviour requires a combination of more rheological components, as discussed below.

To describe the 3-phase creep behaviour, research has been conducted on modelling the accelerated creep phase. Modelling is divided into two broad categories which involve the non-linear rheological and damage rheological modelling [7]. The non-linear rheological models that have been built to describe the accelerated creep phase include Boukharov et al [8] creep model which described the 3-phase creep behaviour of brittle rocks by employing a strain-triggered non-linear viscous dashpot. Lemaitre and Chaboche [9] VIPLA creep model estimated the VP irreversible deformation. The Burgers model connected in series with a Bingham component [4,10,11], the Burgers VP (CVISC) creep model [12], Zhou et al [13,14] creep model that describes the 3-phase creep behaviour by employing fractional

calculus theory and Newtonian dashpot replacement with the Abel dashpot. Yang et al [15] creep model which combines a viscoelastic-plastic Schiffman component with a Bingham and classic elastic Hooke components in series. The model describes the creep behaviour of a diabase under variable stress loading. However, some of these models fail to explicitly describe the 3-phase creep behaviour especially the accelerated creep phase [16]. Additionally, it is considered that the accelerated creep phase is a rapid growth of micro-cracks which can be described by the damage evolution [7]. Hence, the study has been conducted by researchers on the 3-phase creep behaviour by introducing the damage variable. For example, Chan et al [17], Mazzotti & Savoia [18], Hou [19], Verstrynge et al [20] and Ma et al [21]. The mathematical theory used in these non-linear and damage creep models is however not adequate to explain the 3-phase creep behaviour most significantly the accelerated creep. When the damage variable is directly integrated into the constitutive equations of the non-linear and damage governed dashpots it is a function of not only stress but time [7,22]. In such models, the widely used differential constitutive equations to explain 3-phase creep process use integral calculus Based on integer-order derivatives, and there exist the fractional-order and fractal-order derivatives.

Fractional-order derivatives have long been employed to model the transient and steady creep behaviour of rocks and rock masses. The employment has been feasible and successful in establishing the creep constitutive relation. Additionally, it has satisfactorily modelled the power-law rheological mechanism of these rocks and rock masses [23,24]. The consideration of fractional-order derivative theory in describing creep mechanism is interesting and motivating by the fact that it requires fewer parameters to achieve validation with experimental data as compared to integer-order derivative models [25]. However, fractional-order derivatives require expensive computations and memory allocation during numerical implementation [23]. As an alternative, this paper adopts fractal-order derivatives simpler and computationally efficient as compared to fractional-order derivatives. It requires less time in carrying out numerical computations and its efficacy can be drawn from the Maxwell and Kelvin creep constitutive equations (Section 6.3; Table 6-2). Besides, the constitutive model that is being presented takes

advantage of the overstress function represented by Perzyna [26]. However, there exist constitutive models based on this overstress hypothesis. Include the conventional overstress constitutive models [27–29] which consider a static yield surface where the state of stress occurs within and allows solely elastic strains to develop. The extended overstress constitutive models [30–32] proposed to address the drawback of the traditional overstress constitutive models. They assume the production of viscoplastic strain as the stress condition occurs within the surface of the static yield [25]. Hence, an efficient creep constitutive model must be developed able to address the above limitations and describe the 3-phase creep mechanism explicitly. Hence the limitation of traditional overstress constitutive models is addressed in this paper by tweaking the Perzyna [26] overstress function. In this paper, a time-based fractal derivative creep constitutive model that considers isotropic damage is presented. It must be emphasised that the constitutive model presented in this paper is the build-up on the earlier proposed constitutive model by Kabwe et al [25]. Extension of this constitutive model employs the fractal-order derivatives, softening viscoplasticity, and damage effects. Besides, it considers the following:

- Adopts an adjusted Perzyna [26] overstress function by integrating the fractal-order isotropic damage factor and neglects tensile and shear damage.
- Ignores the assumptions that govern the conventional overstress constitutive models.
- Obeys the associative viscoplastic flow rule under which the potential function is equivalent to the yield.
- Neglects the integer-order and fractional-order derivative constitutive model assumptions.
- Adopts ideal and softening viscoplasticity and overlooks isotropic and kinematic hardening constitutive laws.

The presented constitutive model is constructed by coupling the Burgers model with a rheological component that incorporates a fractal-order derivative spring-pot (variable dashpot) that considers isotropic damage. This component is required to describe the accelerated creep phase characterized by damage evolution in squeezing ground, which is responsible for delayed deformations.

6.2 Conventional creep constitutive models

The widely adopted conventional constitutive models for the 3-phase creep mechanism description associated with squeezing include the Nishihara [33], CVISC and Burgers model. However, they (including those presented in Table 6-1 below) can only describe the transient and steady creep phase explicitly [34,35]. Additionally, they assume isotropic deformation in homogeneous rock material which is unrealistic. It shows that they cannot describe the accelerated creep phase explicitly, in that irreversible deformations estimated in this phase are mainly dependent on stress rather than on time. More notably, apart from the model presented by Kabwe et al [25], they cannot predict the time when accelerated creep phase initiates and damage evolution.

Table 6-1. Conventional creep constitutive model.

Researcher	**Constitutive model**	**Accelerated creep simulation**
Norton (1929)	Two-Component Power Law	None
Herrmann et al., (1980)	WIPP viscoelastic model	None
Sjaardema & Kreig (1987)	WIPP creep law model	None
Callahan & DeVries (1991)	Crushed Salt Model	None
Lemaitre and Chaboche (1996)	VIPLA	None
Okubo & Fukui (2006)	Okubo and Fukui model	Dependent on stress
ITASCA (2006)	CVISC model and Power Law VP model	Dependent on stress
Sterpi & Gioda (2009)	3-stage creep model	Dependent on stress
Debernardi & Barla (2009)	SHELVIP	None
Weng et al (2010)	Modified Burgers model	None
Moghadam et al (2013)	EVP model	None

Tran et al (2015)	Modified CVISC model	Dependent on stress
Causse et al (2015)	Burger-creep VP model	None
Fahimifar et al (2015)	Modified 3-stage creep model	None
Ofoegbu & Dasgupta (2017)	FZK-INE creep model	Dependent on stress
Sainoki et al (2017)	Modified Okubo and Fukui model	Dependent on stress
Zhang et al (2019).	FVP model	Dependent on stress
Kabwe et al (2020)	FDVP model	Neglected damage evolution

However, the accelerated creep phase responsible for squeezing can be considered with models that incorporate VP behaviour and damage evolution [25,45]. It is observed from experimental studies that creep strains in the accelerated creep phase increase non-linearly with a varying viscosity coefficient [46]. Therefore, to address the above limitations, a constitutive model in this paper able to describe the non-linear and unsteady creep behaviour in the accelerated creep phase is presented. It is devised as an extension of the Burgers model and the recently proposed FDVP [25] constitutive model by incorporating damage evolution.

6.2.1 Burgers viscoplastic creep model

The conventionally employed CVISC model is comprised of a classic Burgers model able to replicate the transient and steady-state creep phases and a Mohr Coulomb (MC) frictional slider (Figure 6-2). Its constitutive equations are characterized by volumetric elasto-plastic and deviatoric EVP behaviour. Therefore, the strain levels of this component function in sequence, the viscoelastic constitutive laws are provided by the classic Burgers model and the plastic constitutive laws by the MC failure surface. It can describe creep strains of the transient and steady-state creep phases represented by the Kelvin and Maxwell rheological components, respectively. However, In the accelerated creep process, the frictional slider estimates the instantaneous plastic deformation, yielding and permanent strain rates. However, the estimated plastic strain levels in this process are highly dependent on stress and not time. But it has been

observed through experimental studies that permanent strains develop overtime especially in weak rocks subjected to high stress. In tunnels excavated in weak rock mass under high in-situ stress, the developed permanent strains are characterized by the time-dependent squeezing behaviour [48]. It is therefore necessary to estimate the time-dependent VP stresses in the accelerated creep process to reliably predict squeezing.

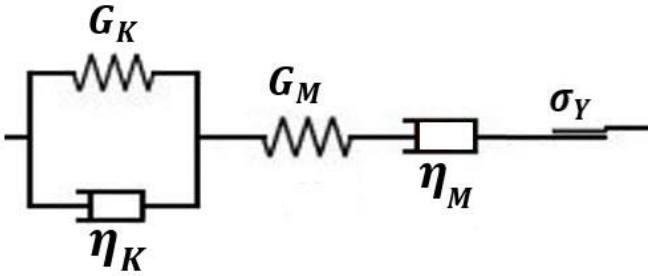

Figure 6-2. Schematic representation of the CVISC rheological model

6.2.2 FDVP creep constitutive model

The FDVP constitutive model employs four rheological elements of the Burgers model for defining viscoelastic strains and two VP component elements for replicating viscoplastic strains (Figure 6-3). It employs fractional-order derivatives for the realistic description of the power-law related creep mechanism. Which involves to some extent the creep strains of the transient, the steady-state and the accelerated creep stages. The constitutive model is based on an adjusted overstress function with a related viscoplastic flow rule that sets the delayed deformations. However, this constitutive model obeys ideal viscoplasticity and ignores isotropic and kinematic hardening laws. Furthermore, it does not account for softening viscoplasticity associated with the accelerated creep stage and damage evolution.

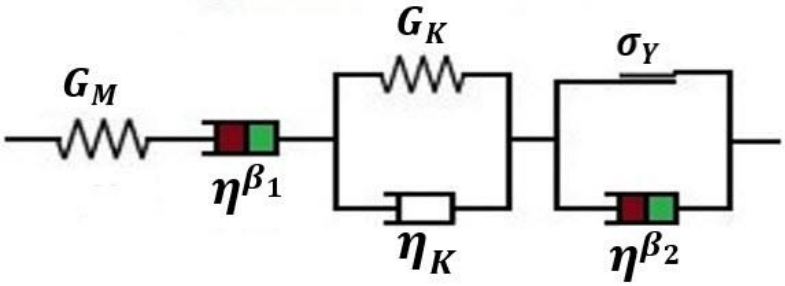

Figure 6-3. Schematic representation of the FDVP rheological

As such integrating these constitutive laws will aid in a full creep description. Hence, in this paper, the improved version of this constitutive model is presented which includes ideal viscoplasticity, softening viscoplasticity and visco-damage laws.

6.3 Fractal-order derivative creep constitutive model

6.3.1 Visco-plastic component with damage evolution

When rocks and or rock masses are subjected to stress level which exceeds their yield strength failure initiates which leads to accelerated creep stage. To estimate this mechanism, a VPD (viscoplastic with damage) component composed of an MC frictional slider and a fractal-order spring-pot is presented. However, damage evolution tends to occur during this creep mechanism, this is often referred to as creep damage. During this process, the viscosity coefficient of the dashpot reduces as damage accumulates. Hence, it is important to consider damage evolution in the VPD component for an accurate estimation of the accelerated creep phase. Considering damage in the accelerated creep phase entails the viscosity coefficient of the fractal-order spring-pot may not be constant. The fractal-order coefficient employed in this spring-pot is assumed to obey the exponential decay law for non-constant viscosity and permanent viscous deformation [25,47,48], which is expressed by;

$$\eta(t) = \eta_0(1 - D) \tag{6-1}$$

Where η_0 is the initial viscosity coefficient and D is the damage variable computed by:

$$D = 1 - e^{-\omega t} \tag{6-2}$$

Where ω is the damage factor, t is the time and D varies between 0.0 – 1.0. This signifies that the rock or rock masses can be either in an undamaged (D = 0.0) or completely damaged (D = 1.0) state. The viscosity coefficient ($\eta(t)$) can be expressed as Eq. (6-3) by substituting Eq. (6-2) into Eq. (6-1).

$$\eta(t) = \eta_0 e^{-\omega t} \tag{6-3}$$

Hence, the constitutive equation of the VPD component considering isotropic damage evolution is expressed as:

$$\sigma - \sigma_Y = \eta_0 e^{-\omega t} \frac{d\varepsilon(t)}{dt} \qquad \sigma \geq \sigma_Y \tag{6-4}$$

Where σ_Y is the rock yield strength, Laplace transformation of Eq. 4 and further inverse transformation expresses the constitutive equation for the VPD component incorporating isotropic damage evolution as:

$$\varepsilon(t) = \frac{\sigma - \sigma_Y}{\eta_0 \omega} e^{\omega t} \tag{6-5}$$

There is a certain level of stress for damage to initiate in rocks (soft and hard), it tends to initiate when the applied stress is greater than σ_Y [49,50]. During the time-dependent material deformation process and when loading stress is greater than σ_Y the material undergoes all the 3-phase creep behaviour. In this creep process damage initiates after steady-state and during the accelerated creep phase but not at the initial phase of the accelerated creep. When damage accumulates change in material deformation tends to occur and D can be expressed by:

$$D = 1 - e^{-\omega t} \qquad t > t_a \tag{6-6}$$

Where t_a is the starting time for the accelerated creep phase and the constitutive equation of the VPD component incorporating damage can now be expressed by:

$$\varepsilon(t) \begin{cases} 0 & \sigma < \sigma_Y \\ 0 & \sigma \geq \sigma_Y \quad 0 \leq t \leq t_a \\ \dfrac{\sigma - \sigma_Y}{\eta_0 \omega} e^{\omega t} & \sigma \geq \sigma_Y \quad t > t_a \end{cases} \tag{6-7}$$

Regarding Eq. (6-7), the accumulation of damage is not entirely dependent on σ_Y but also on t. The EVPD constitutive model is represented by three rheological components connected in series these are the Kelvin, Maxwell and VPD (Figure 6-4).

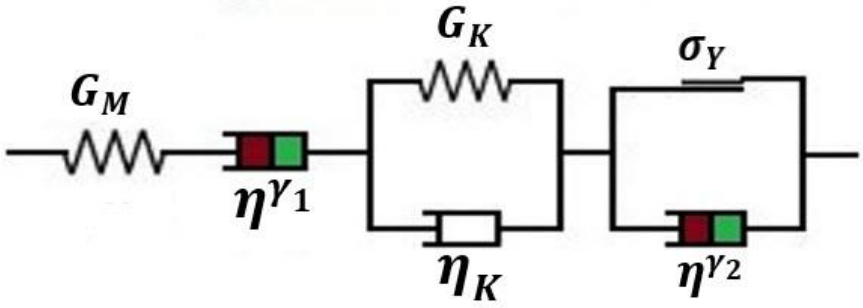

Figure 6-4. Schematic representation of the EVPD consitutive

This combination can be represented by the constitutive equations (Eq (6-8)) expressed in one-dimension (1D):

$$\begin{cases} \varepsilon = \varepsilon^K + \varepsilon^M + \varepsilon^{vpd} \\ \sigma = \sigma^K = \sigma^M = \sigma^{vpd} \\ \sigma^K = \eta_K \dot{\varepsilon}_K + G_K \varepsilon_K \\ \sigma^M = \eta_M \dot{\varepsilon}^M + G_M \varepsilon^M \\ \sigma^{VPD} = \eta_0 e^{-\omega t} \dfrac{d\varepsilon(t)}{dt} + \sigma_Y \end{cases} \qquad 0 \le t \le t_a \tag{6-8}$$

Where σ^K, ε^K, $\dot{\varepsilon}_K$, G_K and η_K are the stress, strain, strain rate, shear modulus and viscosity coefficient of the Kelvin component respectively. σ^M, ε^M, $\dot{\varepsilon}^M$, η_M and G_M are the stress, strain, strain rate, shear modulus and viscosity coefficient of the Maxwell component respectively. Whereas the $\varepsilon^{vpd}$and σ^{vpd} are the strain and stress of the VPD component. When the deviatoric stress is below σ_Y the VPD component is ineffective and when increased to more or equal to σ_Y it is activated.

6.3.2 Fractal-order derivative application

In this section, the theory of fractal-order derivatives is adopted to formulate a time-dependent constitutive model for EVP materials. The rheological behaviour of materials can be accurately described by employing the fractional-order derivative constitutive equations. However, as mentioned earlier fractional-order derivatives require a lot of computational time. Hence, compared to fractal-order derivatives they are less efficient in numerical computation [51]. By employing the time scaling transformation fractal derivatives can be defined as:

$$\frac{df(t)}{dt^{\gamma}} = \lim_{t' \to t} \frac{f(t) - f(t')}{t^{\gamma} - t'^{\gamma}} \tag{6-9}$$

Where γ is the fractal-order derivative coefficient which represents the fractal-order time in space. It can be seen from Eq (6-9) that the fractal-order derivative is a local operator without convolution integrals. While fractional-order derivatives employ convolution integrals as such fractal-order derivatives can be easily transformed into classical integer-order derivatives by employing scaling transformation [51]. They coincide with these classical derivatives employed in most constitutive equations by using a metric transform $t = t^{\gamma}$ [52]. The fractal-order derivative has successfully been employed to characterize the viscoelastic behaviour of materials, for instance, Cai et al [51] proposed the Maxwell and Kelvin models based on fractal-order derivatives to describe the material's creep modulus. Thereafter, compared the creep modulus results attained with those of the integer-order and fractional-order derivative models (Table 6-2)

Table 6-2. Creep modulus relation based on classical, fractal-order and fractional-order derivative components

Component	Integer-order derivative	Fractal-order derivative	Fractional-order derivative
Maxwell	$J(t) = \frac{1}{E_M} + \frac{t}{\eta_M}$	$J(t) = \frac{1}{E_M} + \frac{t^{\gamma}}{\eta_M}$	$J(t) = \frac{1}{E_M} + \frac{t^{\alpha}}{\eta_M \Gamma(1+\alpha)}$

Kelvin	$J(t) = \frac{1}{E_K}\left[1 - exp\left(-\frac{G_K\, t}{\eta_K}\right)\right]$	$J(t) = \frac{1}{E_K}\left[1 - exp\left(-\frac{G_K\, t^{\gamma}}{\eta_K}\right)\right]$	$J(t) = \frac{1}{E_K} + \sum_{k=0}^{\infty}\left(-\frac{G_K}{\eta_K}\right)^{k} \frac{t^{\alpha(k+1)}}{\Gamma(\alpha k + 1 + \alpha)}$

Note: $J(t)$ = Creep modulus, α = Fractional-order derivative coefficient, E_M = Maxwell modulus, E_K = Kelvin modulus, Γ = Gamma function and k = non-negative integer

It can be drawn from Table 6-2, that fractal-order derivatives require few parameters this enhances their computational time in numerical simulations. Figure 6-5 illustrates the Maxwell creep modulus results of the integer-order, fractal-order and fractional-order derivative models. It is drawn from the illustration that, fractal-order derivative models are as accurate as fractional-order derivative models in describing the power-law rheological mechanism of rocks and rock masses.

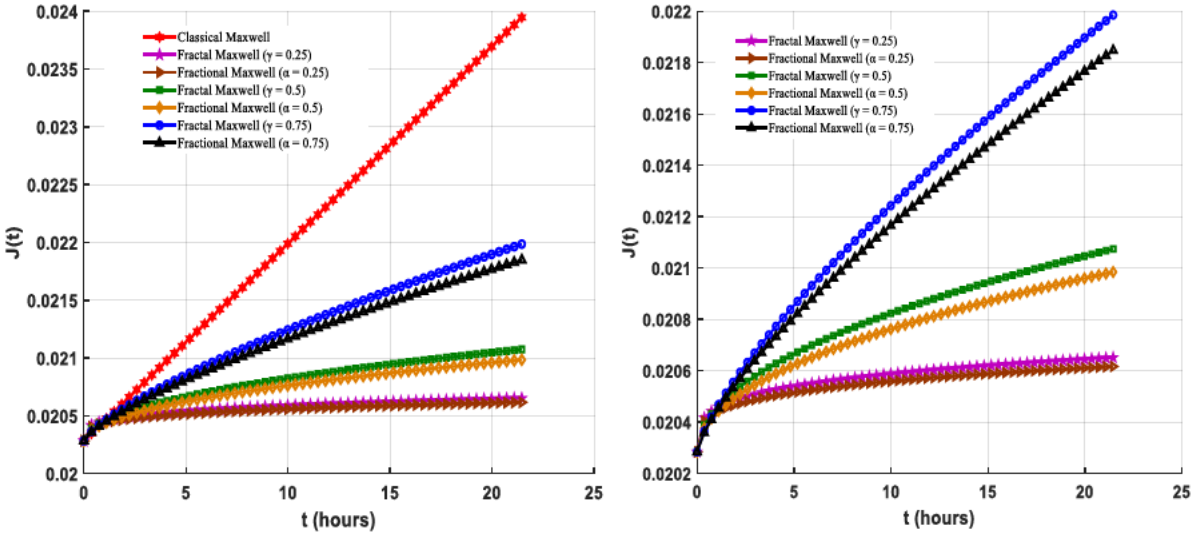

Figure 6-5. Comparison of classical, fractal-order and fractional-order Maxwell with varying γ and α values

6.3.3 Derivation of the fractal-order derivatives with damage

Application of fractal-order derivatives in rheological models is presented as a spring-pot which experiences a spring or Newtonian dashpot response when different coefficient $(\gamma_{1,2})$ values are assigned. The spring is a solid governed by Hooke's law whereas the Newtonian dashpot is a fluid which abides by Newton's law of viscosity [47]. Viscoelastic law hypothetically defines Hooke's law as a zero-order derivative of the strain rate (Eq (6-10)) and Newtonian law as a first-order derivative of the strain rate (Eq. (6-11)).

$$\sigma(t) = \frac{d^0[\varepsilon(t)]}{dt^0} \tag{6-10}$$

$$\sigma(t) = \frac{d^1[\varepsilon(t)]}{dt^1} \tag{6-11}$$

The spring-pot represents an element with the derivative order amid Eq. (6-10) and Eq. (6-11), and it is represented by the fractal-order derivative relation (Eq.(6-12)) which satisfies the condition $0 \leq \gamma_{1,2} \leq 1$.

$$\sigma(t) = \eta \frac{d\varepsilon(t)}{dt^{\gamma_{1,2}}} \qquad \left(0 \leq \gamma_{1,2} \leq 1\right) \tag{6-12}$$

When $\gamma_{1,2} = 0$ the spring-pot is a spring represented as an ideal solid and when $\gamma_{1,2} = 1$, it is a Newtonian dashpot represented as an ideal fluid. If we consider constant stress which occurs during creep and applying scaling transformation, $t = t^{\gamma_{1,2}}$ we obtain an expression for strain as:

$$\varepsilon(t) = \frac{\sigma}{\eta} t^{\gamma_{1,2}} \qquad \left(0 \leq \gamma_{1,2} \leq 1\right) \tag{6-13}$$

Eq. (6-13) shows that the strain rate obeys the power-law mechanism and incorporating damage evolution, the fractal-order derivative formulation can be expressed in the form of fractal time. Applying the scaling transformation $t = t^{\gamma_{1,2}}$ on Eq. (6-3), fractal-order damage variable (D_{FD}) is expressed by Eq. (6-14) and the influence of the fractal-order coefficient and the damage factor on the D_{FD} can be illustrated in Figure 6-6.

$$D_{FD} = 1 - e^{-\omega t^{\gamma_2}} \qquad (0 \leq \gamma_2 \leq 1) \tag{6-14}$$

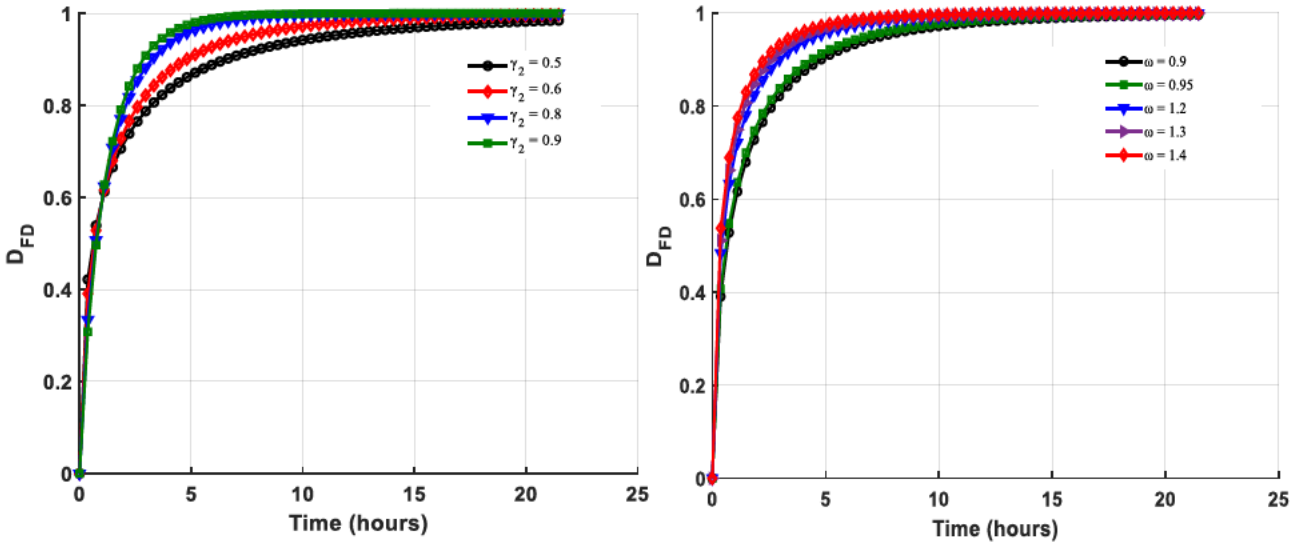

Figure 6-6. Damage evolution with different values of (a) γ_2 and (b) ω

It is drawn from the illustration (Figure 6-6a) that an increase in ω has a progression effect on the material's rate of D_{FD}. It shows that using ω = 1.4 material damage reaches 90% within 3 hours while at ω = 0.9 it reaches 90% after 5 hours and also shown in Figure 6-6b that γ_2 increment influences the rate of the D_{FD}. There is more material damage when higher-order values of ω and γ_2 are employed. The degree of D_{FD} determines the extent of damage evolution responsible for delayed deformations associated with squeezing mechanism. In that, it determines the rate of damage initiation which influences the long-term behaviour of the rock mass. The appropriate parameter values to characterize delayed deformations are those that attribute to a low rate of the D_{FD}, in this case, values $\omega < 1$ and $\gamma_2 < 0.6$. However, these can be accurately determined through calibration with experimental data which is conducted in section 6.5. In this section the parameter sensitivity on the rate of D_{FD} is evaluated and observed that an increase in these parameter values has an incremental effect on the D_{FD}. Additionally, the constitutive expression (Eq. (6-4)) incorporating D_{FD} is further given by:

$$\sigma(t) = \eta_0 e^{-\omega t^{\gamma_2}} \frac{d\varepsilon(t)}{dt^{\gamma_2}} \tag{6-15}$$

If we consider a stress level $\sigma(t) = \sigma$ and initial strain as $\varepsilon(0) = 0$ we further obtain a constitutive expression for strain in the spring-pot incorporating D_{FD} as:

$$\varepsilon(t) = \frac{\sigma}{\eta_0 \omega}\left(e^{\omega t^{\gamma_2}} - 1\right) \tag{6-16}$$

In section 6.3, the derived fractal-order derivative with damage equation (Eq.(6-16)) for the spring-pot is integrated into the creep constitutive equations to construct the EVPD constitutive model.

6.4 The EVPD creep constitutive equations

The EVPD rheological model is represented by the Kelvin, Maxwell and VPD components which consists of 14 parameters. It is an extension of the Burgers rheological model characterised by an EVP deviatoric behaviour, EVP volumetric behaviour and an improvement to the FDVP rheological model.

6.4.1 Viscoelastic and viscoplastic constitutive equations

The viscoelastic viscoplastic constitutive equations presented in this section takes the form of the recently proposed FDVP constitutive model. They employ fractal-order derivatives with a few creep parameters for computational time reduction during numerical implementation and offers the same power-law description of rock mass response in 1D (Eq. (6-17)).

$$\begin{cases} \varepsilon = \dfrac{\sigma}{G_M} + \dfrac{\sigma t^{\gamma_1}}{\eta^{\gamma_1}} + \dfrac{\sigma}{G_K}\left[1 - exp\left(-\dfrac{G_K\, t^{\gamma_1}}{\eta_K}\right)\right], \sigma < \sigma_Y \\ \varepsilon = \dfrac{\sigma}{G_M} + \dfrac{\sigma t^{\gamma_1}}{\eta^{\gamma_1}} + \dfrac{\sigma}{G_K}\left[1 - exp\left(-\dfrac{G_K\, t^{\gamma_1}}{\eta_K}\right)\right] + \left(\dfrac{\sigma - \sigma_Y}{\eta^{\gamma_2}} t^{\gamma_2}\right), \sigma \geq \sigma_Y \qquad 0 \leq t \leq t_a \end{cases} \tag{6-17}$$

Where η^{γ_1} is the Maxwell spring-pot viscosity coefficient, η^{γ_2} is the VPD spring-pot viscosity coefficient and Eq (6-17) can describe the 3-stage creep mechanism to some extent. The transient creep and steady-state creep exhibit ($\sigma < \sigma_Y$), the transient creep, steady-state creep and accelerated creep display ($\sigma \geq \sigma_Y$ & $0 \leq t \leq t_a$)[25]. Further on, the fact that on an in-situ scale a rock mass is subjected to a triaxial state of stress. In a general state of three-dimension (3D) stress, a point can be represented by three principal stresses σ_1, σ_2 and σ_3 which are the major, intermediate, and minor acting on mutual orthogonal planes. Hence, it is prudent to express these constitutive equations in 3D stress state to realistically represent the rock mass behaviour. Where the stress tensor (σ_{ij}) is composed of the deviatoric stress tensor (S_{ij}) and spherical stress tensor (σ_m).

$$\sigma_m = \frac{\sigma_{kk}}{3} \tag{6-18}$$

$$S_{ij} = \sigma_{ij} - \sigma_m \delta_{ij} \tag{6-19}$$

Where σ_{kk}= σ_1+σ_2+σ_3 and δ_{ij} is the Kronecker delta. The strain tensor (ε_{ij}) can also be decomposed into spherical strain tensor (ε_m) and deviatoric strain tensor $\left(e_{ij}\right)$.

$$\varepsilon_m = \frac{\varepsilon_{kk}}{3} \tag{6-20}$$

$$e_{ij} = \varepsilon_{ij} - \varepsilon_m \delta_{ij} \tag{6-21}$$

Based on Hooke's law σ_m and S_{ij} in 3D stress state is computed by:

$$\sigma_m = 3K\varepsilon_m \tag{6-22}$$

$$S_{ij} = 2Ge_{ij} \tag{6-23}$$

Substitution of Eq. (6-17) with Eq (6-22) and (6-23) where S_{ij} < S_Y the 3D viscoelastic constitutive equation is expressed by Eq (6-24). The constitutive equation determines the current deviatoric stress and the total accumulated viscoelastic strains characterised by the Burgers model viscoelasticity.

$$\varepsilon_{ij} = \frac{S_{ij}}{2G_M} + \frac{\sigma_m \delta_{ij}}{3K} + \frac{S_{ij} t^{\gamma_1}}{2\eta^{\gamma_1}} + \frac{S_{ij}}{2G_K}\left[1 - exp\left(-\frac{G_K\, t^{\gamma_1}}{\eta_K}\right)\right] \quad S_{ij} < S_Y \tag{6-24}$$

Where S_Y is the 3D long-term strength (yield strength). Besides when $S_{ij} \geq S_Y$ and $t \leq t_a$ the irreversible viscoplastic strain initiates It introduces the viscoplastic potential function $\left(Q_{vp}\right)$ and the viscoplastic flow rule [15]. In classical viscoplasticity, it is hypothesized that the rate of viscoplastic strains is achieved by Perzyna [26] overstress function. In this theory the constitutive equations for viscoplastic strain rate ($\dot{\varepsilon}_{ij}^{vp}$) estimation is represented by this overstress function.

$$\dot{\varepsilon}_{ij}^{vp} = \lambda \frac{\partial Q_{vp}}{\partial \sigma_{ij}} \tag{6-25}$$

Where λ Is the scalar multiplier that defines the rate of flow. Hence, in this stage, we adopt the 3D viscoplastic constitutive law represented by an adjusted Perzyna [26] overstress function to estimate the viscoplastic strain rates. In this definition of the flow rule, however, there is a distinction which depicts the effective plastic strain evolution [54,55]. In plasticity concept, the plastic strain rate is a quasi-time factor, and its derivative is unrelated to this quasi-time [54]. However, the viscoplastic strain intensity is the time derivative of the real viscoplastic strain. Furthermore, the state of consistency is calculated in the plasticity theory, while in the viscoplasticity hypothesis it is calculated by the specific function dependent on S_{ij} and S_Y. As such, the viscoplastic strain rate is represented by an explicit function based on Perzyna [26] overstress theory (Eq.(6-26)).

$$\dot{\varepsilon}_{ij}^{vp} = \frac{\langle \phi(F) \rangle}{\eta} \frac{\partial Q_{vp}}{\partial \sigma_{ij}} \tag{6-26}$$

Where η is the viscosity parameter, $\langle \phi(F) \rangle$ Is the viscoplastic nucleus that controls the viscoplastic strain range, Q_{vp} the tensor direction of the viscoplastic strain rate and the Macaulay brackets $\langle \quad \rangle$ is determined by;

$$\langle \phi(F) \rangle = \begin{cases} 0, & F < 0 \\ \phi(F), & F \geq 0 \end{cases} \tag{6-27}$$

Where $\phi(F)$ is the overstress function illustrates the overstress state inside the rock mass and expressed in terms of the yield function (F). The constitutive relationship (Eq. (6-28)) is used to determine λ in viscoplasticity when the state stress is above the surface of the failure.

$$\lambda = \frac{\langle \phi(F) \rangle}{\eta} \tag{6-28}$$

Additionally, to account for the fractal-order derivative power-law effect of the viscoplastic spring-pot while neglecting the isotropic damage variable. Thus, the adjusted 3D viscoplastic constitutive law incorporating the fractal-order coefficient is expressed by.

$$\dot{\varepsilon}_{ij}^{vp} = \frac{\langle \phi(F) \rangle}{2\eta^{\gamma_2}} \frac{\partial Q_{vp}}{\partial \sigma_{ij}} t^{\gamma_2} \tag{6-29}$$

In this case, F is presumed to be equal to f and an associated viscoplastic flow rule $\left(F = Q_{vp}\right)$ is assigned commonly assumed in rock plasticity [7]. Hence, the adjusted 3D viscoplastic constitutive law (Eq. (6-29)) is reduced to Eq. (6-30).

$$\dot{\varepsilon}_{ij}^{vp} = \left(\frac{f}{2\eta^{\gamma_2}}\right) \frac{\partial f}{\partial \sigma_{ij}} t^{\gamma_2} \qquad (f \geq 0) \tag{6-30}$$

Where f is the MC failure surface represented by Eq (6-31).

$$f = \sigma_1 - \sigma_3 N_\vartheta + 2c\sqrt{N_\vartheta} \tag{6-31}$$

Where c is the cohesion, $N_\vartheta = \frac{1+\sin\vartheta}{1-\sin\vartheta}$ and ϑ is the internal friction angle. In viscoplasticity when the state of stress lies above f the scalar multiplier (λ) is obtained from Eq (6-32) and the 3D viscoelastic viscoplastic constitutive equation is expressed by Eq (6-33).

$$\lambda = \left(\frac{f}{2\eta^{\gamma_2}}\right) t^{\gamma_2} \tag{6-32}$$

$$\begin{aligned} \varepsilon_{ij} = \frac{S_{ij}}{2G_M} + \frac{\sigma_m \delta_{ij}}{3K} + \frac{S_{ij} t^{\gamma_1}}{2\eta^{\gamma_1}} + \frac{S_{ij}}{2G_K}\left[1 - exp\left(-\frac{G_K\, t^{\gamma_1}}{\eta_K}\right)\right] \\ + \left(\frac{f}{2\eta^{\gamma_2}}\right) \frac{\partial f}{\partial \sigma_{ij}} t^{\gamma_2} \quad (f \geq 0) \end{aligned} \tag{6-33}$$

6.4.2 Visco-damage constitutive equations

In section 6.3, it was highlighted that the damage evolution is a significant factor and should be considered in estimating the accelerated creep phase. Research has postulated that damage evolution subjected to variable loading condition is highly dependent on the stress level and strain accumulation. In this study, the damage evolution is represented by the derived constitutive equation of the viscous stress and strain rate. The stress effect is embodied in a power-law function characterised by the fractal-order derivative integrated with the damage variable. The damage variable is a significant factor that is considered in estimating the long-term deformations characterised by visco-damage strains. Hence, coupling the viscoelastic and viscoplastic constitutive equation with visco-damage effect will enable the explicit description of the accelerated creep stage. Therefore, substitution of the Newtonian dashpot with a fractal-order spring-pot an enhanced time-based constitutive model which incorporates isotropic damage effect is presented. In this constitutive law, when $\sigma \geq \sigma_Y$ and $t > t_a$ the transient creep, steady-state creep, accelerated creep and creep damage display. In the accelerated phase ($t \leq t_a$) the non-linear part of the dashpot is triggered, and the viscosity coefficient is no longer constant but varies with time. Hence, damage accumulation sets in as such incorporating the variable viscosity coefficient with damage is important and the damage associated viscoplastic strain is obtained from Eq (6-34).

$$\varepsilon = \frac{\sigma - \sigma_Y}{\eta^{\gamma_2}\omega}\left(e^{\omega t^{\gamma_2}} - 1\right) \qquad \sigma \geq \sigma_Y \qquad t > t_a \quad \text{(6-34)}$$

Therefore, the 1D viscoelastic viscoplastic visco-damage strain is estimated by the constitutive equation (Eq (6-35)) when $\sigma \geq \sigma_Y$ and $t > t_a$.

$$\varepsilon = \frac{\sigma}{G_M} + \frac{\sigma t^{\gamma_1}}{\eta^{\gamma_1}} + \frac{\sigma}{G_K}\left[1 - exp\left(-\frac{G_K\, t^{\gamma_1}}{\eta_K}\right)\right] + \frac{\sigma - \sigma_Y}{\eta^{\gamma_2}\omega}\left(e^{\omega t^{\gamma_2}} - 1\right), \quad \sigma \geq \sigma_Y \qquad t > t_a \quad \text{(6-35)}$$

When $S_{ij} \geq S_Y$ and $t > t_a$ viscoplastic strains associated with damage evolution occurs which represents the accelerated creep stage and the strain is characterised by both stress and time. The

viscoplastic strain rate estimation in this creep stage is determined by the adjusted Perzyna [26] overstress constitutive relation incorporated with isotropic damage evolution.

6.4.3 Perzyna overstress function adjustment

Coupling of the viscoplastic law and the isotropic damage law is possible in this section for the explicit definition of the 3-stage creep mechanism. This is essential in that the stress-strain response of the rock/rock mass depends not on the viscoelastic viscoplastic behaviour but also on damage evolution. Combining these constitutive equations will provide the means of attaining stress, strain, and damage evolution at an instance. Therefore, description of the viscoplastic with damage behaviour we adopt Eq. 34 which accounts for the viscous time effect and damage evolution. Additionally, when $S_{ij} \geq S_Y$ and $t > t_a$ damage evolution initiates and the viscoplastic strains are determined by the adjusted overstress function which incorporates fractal-order damage evolution (Eq. (6-36)).

$$\dot{\varepsilon}_{ij}^{vpd} = \frac{\langle \phi(F) \rangle}{2\eta^{\gamma_2}\omega}\left(e^{\omega t^{\gamma_2}} - 1\right)\frac{\partial f}{\partial \sigma_{ij}} \tag{6-36}$$

As well as being governed by the condition that if the stress state occurs below the yield surface then it is admissible, otherwise the condition is violated and, in this case, λ is determined by Eq. (6-37).

$$\lambda = \left\{ \begin{array}{ll} \dfrac{\langle \phi(F) \rangle}{2\eta^{\gamma_2}\omega}\left(e^{\omega t^{\gamma_2}} - 1\right), & f > 0 \\ 0, & f \leq 0 \end{array} \right| \text{Visco-damage} \tag{6-37}$$

Therefore, considering isotropic damage 3D constitutive equation (Eq. (6-36)) with an associated viscoplastic flow rule $\left(F = Q_{vp}\right)$ and assuming F is equal to f is expressed by.

$$\dot{\varepsilon}_{ij}^{vpd} = \frac{f}{2\eta^{\gamma_2}\omega}\left(e^{\omega t^{\gamma_2}} - 1\right)\frac{\partial f}{\partial \sigma_{ij}} \tag{6-38}$$

6.4.4 Coupling of the viscoelastic, viscoplastic and visco-damage constitutive equations

Damage evolution develops overtime under high-stress levels, as a result, the primary, steady-state and accelerated creep occurs. Because the accelerated creep is influenced by the damage evolution integration of the visco-damage component in the model's constitutive equations is required. The viscoelastic-viscoplastic constitutive equations employed to describe the 3-stage creep behaviour underestimate the behaviour including the explicit accelerated creep description. However, the addition of the visco-damage constitutive equation to the viscoelastic-viscoplastic model compensates this shortfall and explicitly describes the damage evolution-based creep stage. Therefore, the integrated EVPD creep constitutive equation under 3D stress state is expressed by (6-39).

$$\varepsilon_{ij} = \frac{S_{ij}}{2G_M} + \frac{\sigma_m \delta_{ij}}{3K} + \frac{S_{ij} t^{\gamma_1}}{2\eta^{\gamma_1}} + \frac{S_{ij}}{2G_K}\left[1 - exp\left(-\frac{G_K\, t^{\gamma_1}}{\eta_K}\right)\right] + \left(\frac{f}{2\eta^{\gamma_2}\omega}\right)\left(e^{\omega t^{\gamma_2}} - 1\right)\frac{\partial f}{\partial \sigma_{ij}} \quad (f \geq 0) \tag{6-39}$$

In the section that follows, the presented EVPD constitutive model is calibrated with experimental data attained from literature.

6.5 The constitutive model calibration

In this section, the calibration procedure of the EVPD constitutive model is presented per the experimental data set attained from salt rock and Marble. The experimental data set of salt rock is attained from Zhou et al., [13] and of Marble attained from Chen et al.,[53]. The mechanical rock mass parameters of the experimental samples are presented in Table Table 6-3,Table 6-4 and Table 6-5. Table Table 6-3 & Table 6-4 creep parameters are used to calibrate the viscoelastic – viscoplastic component of the EVPD constitutive model. Whereas those in Table Table 6-5 are utilised for the entire calibration of the EVPD constitutive model which includes the viscoelastic, viscoplastic and visco-damage constitutive laws.

Table 6-3. Calibrated creep parameters with salt rock

η_M(GPa.h)	G_K(GPa)	η_K(GPa.h)	G_M(GPa)	η^{γ_1}(GPa.h)	η^{γ_2}(GPa.h)	$\gamma_{1,2}$
1.23	4.52	2.98	2.0	1.23	13.76	0.32

Table 6-4. Calibrated creep parameters with marble

η_M(GPa.h)	G_K(GPa)	η_K(GPa.h)	G_M(GPa)	η^{γ_1}(GPa.h)	η^{γ_2}(GPa.h)	$\gamma_{1,2}$
4650	2610	1961	53	4650	4959	0.31

Table 6-5. Employed creep parameters:

(a) EVPD constitutive model

η_K(GPa.h)	G_K(GPa)	G_M(GPa)	η^{γ_1}(GPa.h)	η^{γ_2}(GPa.h)	γ_1	γ_2	ω	σ_Y(MPa)
2552	73.6	49.3	5860	7567	0.56	0.6	0.9	130.1

(b) CVISC constitutive model

η_K(GPa.h)	G_K(GPa)	G_M(GPa)	η_M(GPa.h)	K(GPa)
2552	73.6	49.3	5860	50

6.5.1 Viscoelasticity and viscoplasticity constitutive model parameters

In this model state, the isotropic damage effect has not yet been initiated or is insignificant and neglected under low-stress levels in the short term. Hence, the salt rock and Jinping marble in this state exhibits

transient, steady-state and to some extent accelerated creep neglecting visco-damage. Constitutive equations employed for the calibration in this section are represented by Eq. (6-29) which obeys an associative viscoplastic flow rule and ideal viscoplasticity whereas neglecting the isotropic and kinematic hardening laws. The creep strain rate calibrated curves of the constitutive model with experimental data as well as comparison with the recently proposed FDVP constitutive model is illustrated in Figure 6-7.

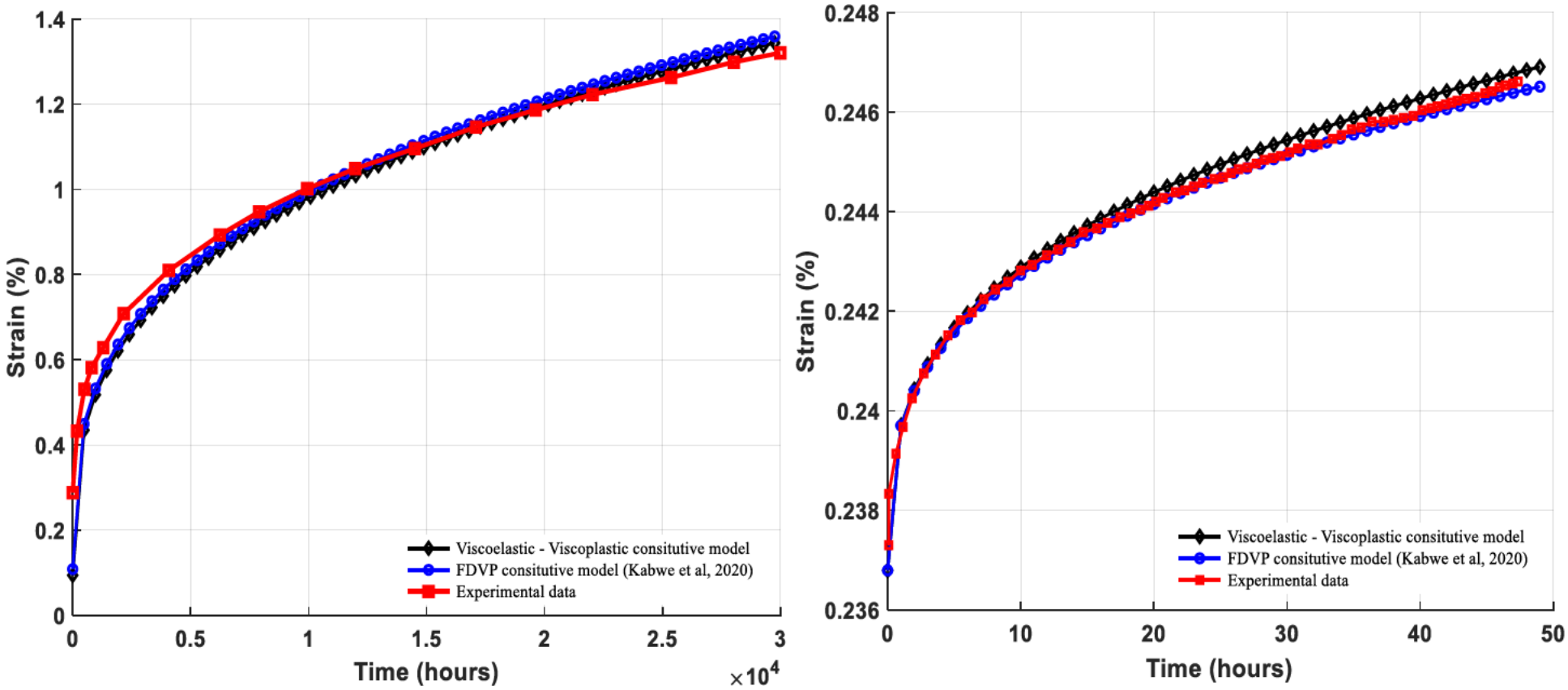

Figure 6-7. Constitutive model without damage prediction with experimental data (a) Zhou et al., [13] and (b) Chen et al.,[53]

6.5.1.1 Sensitivity analysis of the viscoelasticity and viscoplasticity constitutive parameters

The purpose of this section is to define the most sensitive and important parameter in the definition of the viscoelasticity and viscoplasticity creep curves. For a better understanding of the effects of these parameters on the creep strain rates, a parametric analysis is carried out. It is observed that the salt rock and marble strain rates are entirely dependent on these parameters ($\gamma_{1,2}$) and the subjected stress levels.

6.5.1.1.1 Effects of the fractal-order derivative coefficient on the creep strain

The influence of the essential parameters $\gamma_{1,2}$ on the salt rock/Jinping marble creep strain rates are evaluated in this section. Figure 6-8a shows the effect of these important parameters by a sequence of creep curves acquired from the salt rock. It is illustrated that the greater the $\gamma_{1,2}$ values, the more extensive the creep strain. Figure 6-8b reveals the variance of the creep curves with the time reached from the marble under different values of $\gamma_{1,2}$. It is seen that an increase in these parameter values leads to an increment of the creep strain levels while the rate of steady-state creep strain is reduced. Also, an increase in $\gamma_{1,2}$ values revealed a slight change in the rate of transient and steady-state creep strains. The creep curves obtained indicate that the increase in the values of $\gamma_{1,2}$ has a gradual impact on the creep strain levels. These findings signify the significance of opting for a suitable value of $\gamma_{1,2}$ to depict the viscoelastic and viscoplastic behavior of salt rock and marble realistically. Therefore, when employing the viscoelasticity and viscoplasticity constitutive model for TD tunnel reaction in squeezing ground, it is necessary to optimize the $\gamma_{1,2}$ values. The comparative curve results of shows that the most appropriate values of $\gamma_{1,2}$ are between 0.2 - 0.32 and most accurate when $\gamma_{1,2}$ = 0.315.

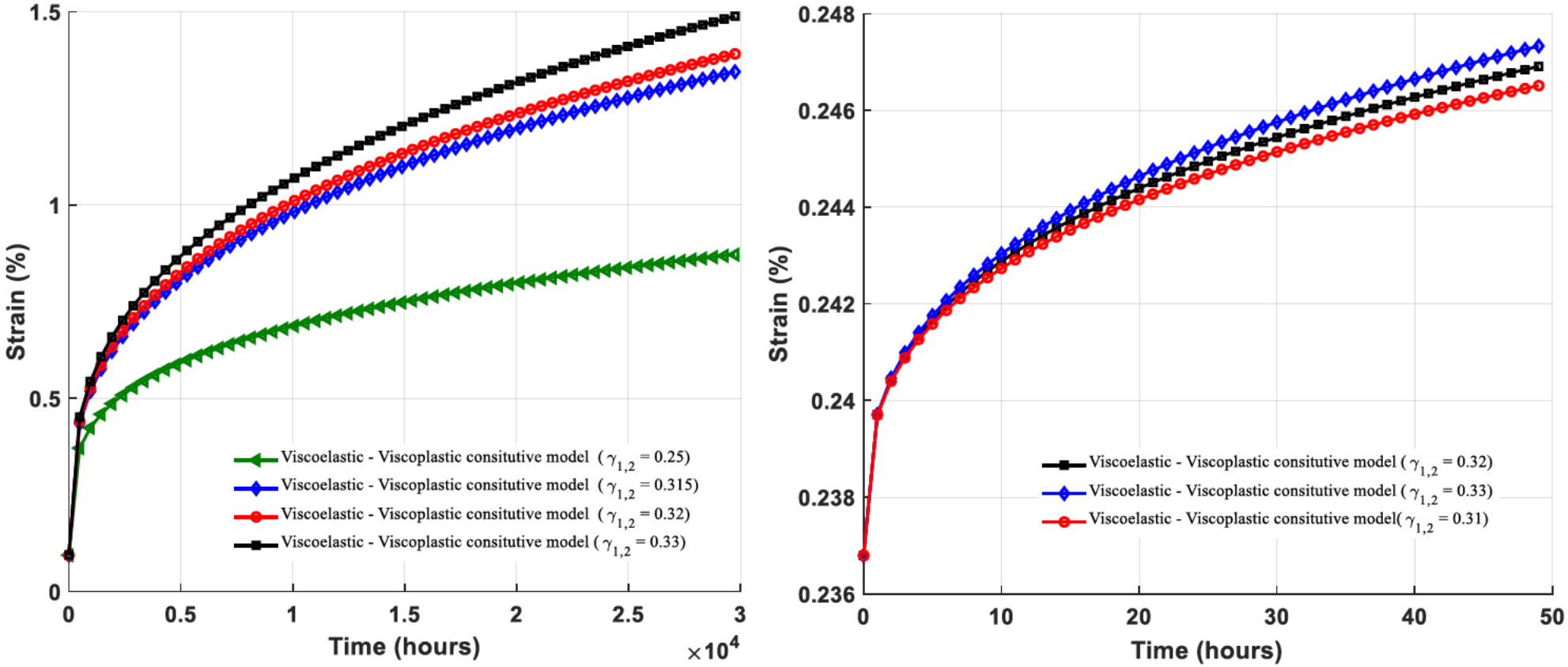

Figure 6-8. Constitutive model without damage sensitivity to $\boldsymbol{\gamma_{1,2}}$ with experimental calibrated (a) Zhou et al., [13] and (b) Chen et al.,[53]

6.5.1.1.2 Effects of the stress level on the creep strain

The estimation of the stress level effect on the rates of creep strain is achieved by allowing the other parameters to be constant while the stress levels change. The level of stress applied to salt rock ranged from 14.1 MPa to 26 MPa and an increase in its level is observed to have an incremental effect on the strain rate (Figure 6-9a). Also, the Jinping marble's creep strain response under incremental applied stress level (125.5 -160 MPa) is shown in Figure 6-9b. From these depictions, it is derived that an increase in the applied stress level increases the rates of creep strain.

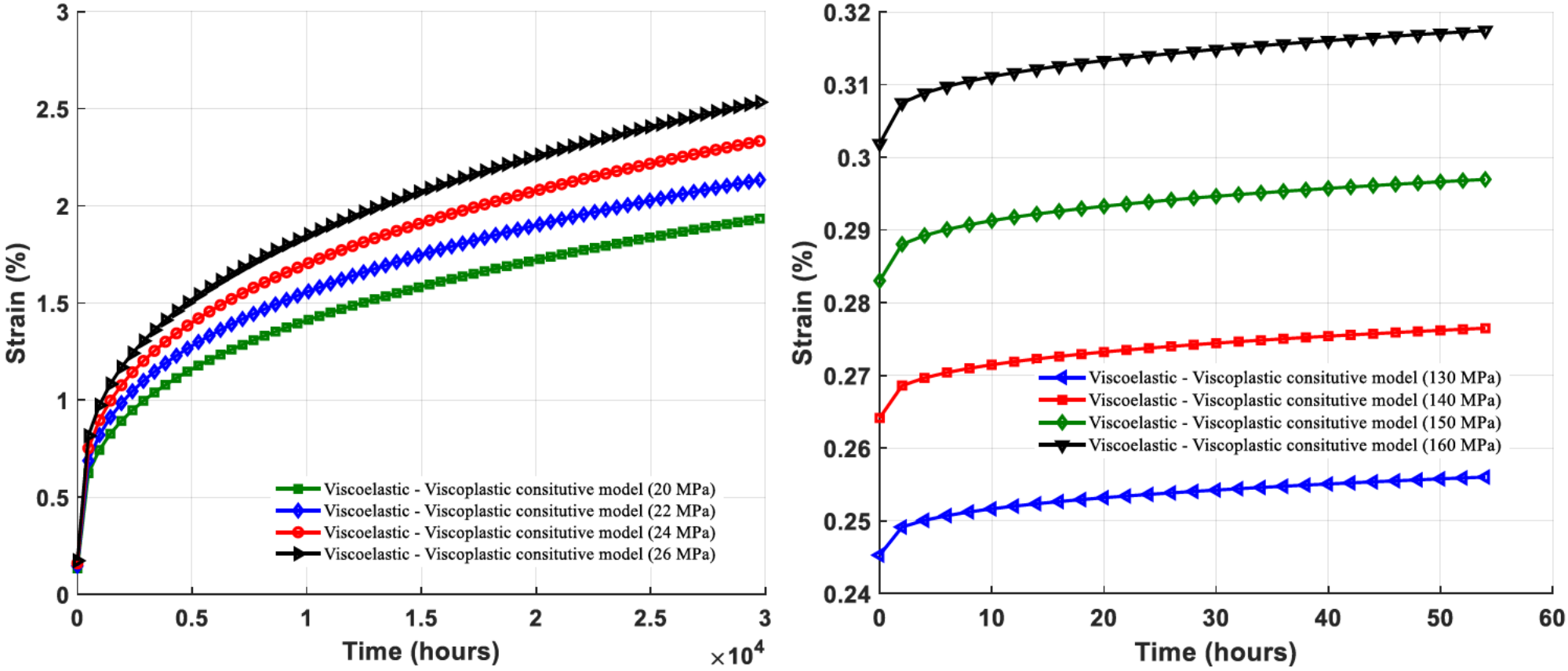

Figure 6-9. Constitutive model without damage sensitivity to stress level with experimental calibrated (a) Zhou et al., [13] and (b) Chen et al.,[53]

6.5.2 Visco-damage constitutive model parameters

When a rock mass is subjected to high stress level sufficient to initiate damage evolution, at this instant in time both the transient, steady-state, and accelerated creep occurs. Thus, the calibrated parameters in section 6.5.1 considered for the viscoelastic viscoplastic constitutive model can be used to calibrate the viscoelastic viscoplastic viscodamage constitutive model. However, the fact that it neglects visco-damage it underrates the creep mechanism most importantly accelerated creep associated with damage evolution. Hence, the visco damage constitutive law is coupled with the viscoelastic and viscoplastic constitutive model to address the above limitation. Calibration of this coupled constitutive model is based on experimental data attained from a 3-stage creep mechanism test conducted by Chen et al.,[53] and these calibrated creep parameters are presented in Table 6-5. The results attained from the coupled viscoelastic, viscoplastic and visco-damage constitutive equation (Eq. (6-20)) and the experimental data are compared in an illustration (Figure 6-10). The illustration also shows that the creep strain curve at the stress level 135.7 MPa obtained from the CVISC and EVPD constitutive models is in close agreement with experimental data up to 20 hours. Beyond that, the rock material exhibits the accelerated creep stage which is further explicitly described by the EVPD constitutive model.

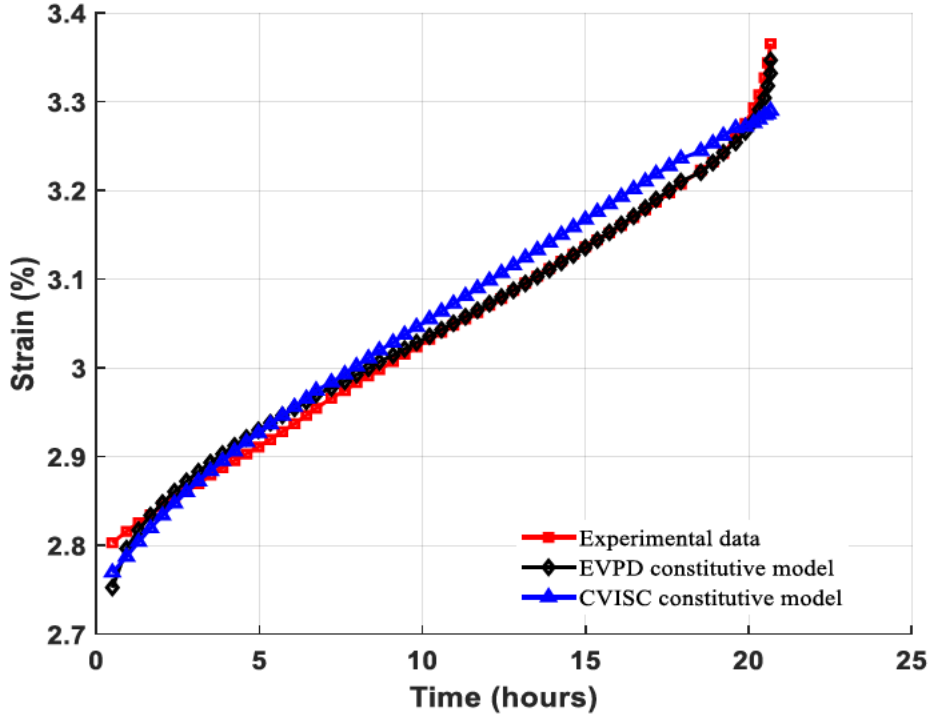

Figure 6-10. CVISC and EVPD consitutive model prediction with experimental data

6.5.2.1 Sensitivity analysis of the EVPD constitutive parameters

It is obvious that the time-dependent strain of the specimen depends on creep parameters, among which are $\gamma_{1,2}$ and ω. To get a better understanding of the sensitivity of these parameters on the specimen's deformation. A parametric analysis is performed to identify the most sensitive and the results of the critical creep parameters $\gamma_{1,2}$ and ω effect on the creep curves is illustrated in Figure 6-11.

6.5.2.1.1 Effects of the stress level on the creep strain

The illustration also shows the creep strain response of the specimen from the effect of the applied stress level change (131-160 MPa) while $\gamma_{1,2}$ and ω are kept constant (Figure 6-11a). It is observed that an increment in the applied stress level, there is an increase in the creep strain rates while the steady creep phase is reduced. It is also drawn that the accelerated creep phase initiation is characterised by high-stress levels.

6.5.2.1.2 Effects of the fractal-order derivative coefficient and damage variable on the creep strain

The variation of the creep curves with time attained under a few $\gamma_{1,2}$ values are illustrated in Figure 6-11b & c. It is observed that when there is an increment in the γ_1 values the creep strains in all phases increases. While an increment in γ_2 values, the transient and steady creep strain rates are hardly affected. This is attributed to the damage progression which is the key role in the accelerated creep phase when the fractal-order dashpot in the VPD component is activated. Figure 6-11d illustrates the increase of the ω values which influences the initiation of the accelerated creep phase early. This signifies the importance of the ω values regulatory effect on the damage progression of the creep model. It also shows that the greater the ω value leads to an early transient creep phase transition into steady creep phase.

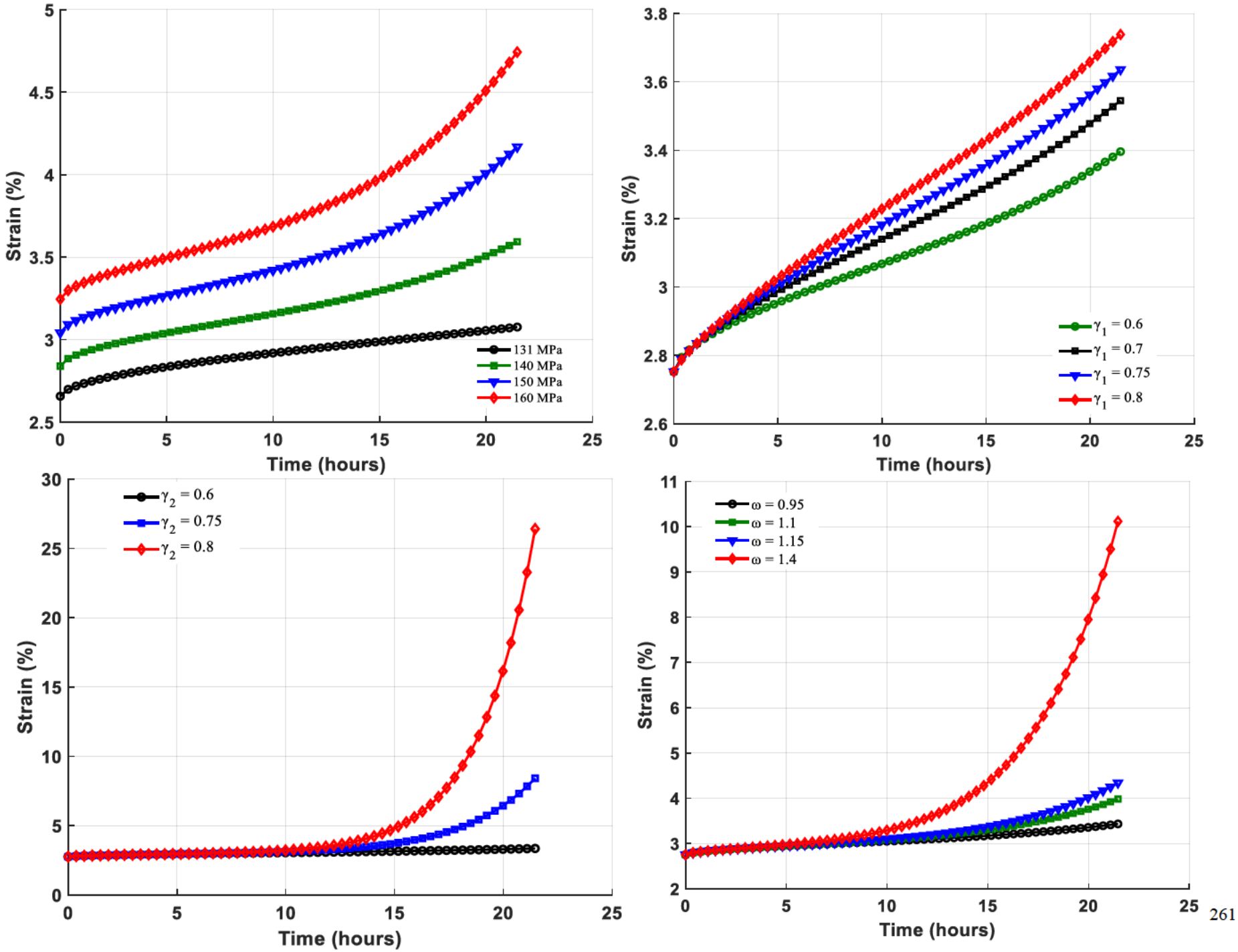

Figure 6-11. EVPD constitutive model sensitivity to (a) stress level (b) γ_1, (c) γ_2 and (d) ω.

6.6 Numerical implementation of the constitutive equations

In this section, the basic ingredients to implement the viscoelastic viscoplastic visco-damage constitutive model in a finite volume numerical framework the following requirements are needed.

- an algorithm for numerical integration of the EVPD constitutive equations to be employed to update stresses and other state variables.
- the correlated viscoplastic modulus to be employed in the assemblage of the finite volume stiffness matrix.

6.6.1 Explicit solution scheme (Integration algorithm)

To illustrate the application of the EVPD constitutive model by constructing a numerical framework which provides components to its computational implementation in a finite volume numerical code. An algorithm comprised of the elastic predictor and the viscoplastic with damage return mapping is presented. The iteration algorithm is based on the closest point projection method (CCPM) which describes the behaviour of the viscoelastic viscoplastic and visco-damage material. An adjusted associated viscoplastic constitutive function is considered and assume that all initial variables at time (t_n) are known and Δt denotes their change in the interval (t_n, t_{n+1}).

1. **Elastic prediction**. *In this state, the purely elastic behaviour occurs within a stipulated time interval [t_n,t_{n+1}]. In this state the variables are calculated as follows*

$$\begin{aligned} \varepsilon_{n+1}^{trial} &= \varepsilon_n + \Delta\varepsilon \\ \varepsilon_{n+1}^{vp\ trial} &= \varepsilon_n^{vp} \\ \sigma_{n+1}^{trial} &= D^e\left(\varepsilon - \varepsilon^{vp}\right) \\ f_{n+1}^{trial} &= \left|\sigma_{n+1}^{trial}\right| - \sigma_Y \end{aligned} \tag{6-40}$$

Check the yielding function.

If $f_{n+1}^{trial} \leq 0$, *this iteration lies in the elastic range within the interval* $[t_n, t_{n+1}]$. *In this case, the state variables are assigned values equal to the trial variables.*

Then set:

$$\sigma_{n+1} = \sigma_{n+1}^{trial}$$
$$D^{vp} = D^{e} \tag{6-41}$$

And exit

Else $f_{n+1}^{trial} \geq 0$, *therefore the loading phase is viscoplastic otherwise we employ the viscoplastic return mapping procedure.*

2. **Viscoplastic correction.** *In this state using the consistency condition* $f_{n+1}^{trial} - \left(\left|\sigma_{n+1}^{trial}\right| - \sigma_Y\right) = 0$ *we solve for the incremental viscoplastic scalar multiplier (*$\Delta\lambda$*) and employ the Newton-Raphson backward Euler solution then update the state variables.*

$$\Rightarrow \quad \Delta\lambda = \frac{\left\langle \phi(F) \right\rangle}{2\eta^{\gamma_2}\omega}\left(e^{\omega t^{\gamma_2}} - 1\right)\Delta t \tag{6-42}$$

$$\sigma_{n+1} = \sigma_{n+1}^{trial} - D^{vp} : \Delta\lambda \left.\frac{\partial f}{\partial \sigma}\right|_{n+1} \tag{6-43}$$

With the time increment (Δt*) within time interval the system of equations (Eq (6-40)) is used to calculate the viscoplastic and elastic strain updates.*

$$\varepsilon_{n+1}^{vp} = \varepsilon_n^{vp} + \Delta\lambda \left.\frac{\partial f}{\partial \sigma}\right|_{n+1}, \qquad \varepsilon_{n+1}^{e} = \varepsilon_{n+1}^{trial} - \Delta\lambda \left.\frac{\partial f}{\partial \sigma}\right|_{n+1} \tag{6-44}$$

Then exit the scheme

6.6.2 Finite volume implementation

The formulated EVPD constitutive equations are transcribed in object-oriented C++ as a user-defined constitutive model (UDM). This UDM is then executed as a compiled Dynamic Library Link (DLL) in a finite volume numerical code FLAC^{3D} and it is loaded on startup as:

model configure creep

model configure plugin

zone cmodel load "cmodelEVPD007_64" (FLAC^{3D} version 7.0)

zone cmodel assign EVPD

This numerical code allows the ability to build the EVPD user-defined material behaviour through the UDM. It employs an explicit material scheme using a time-step based solution more appropriate for computing non-linear material associated with large strain in squeezing ground. The solution computes the increment in strain and stress state at a time ($t + \Delta t$) given initial stress state at the time (t). The implemented model measure perfectly elastic trial stress and then compare the results at a time ($t + \Delta t$) to the nonlinear parameters considered. Additionally, to evaluate the true stress condition an adjustment is made to the trial stress where necessary and implementation of the established constitutive model is illustrated in a flowchart below (Figure 6-12).

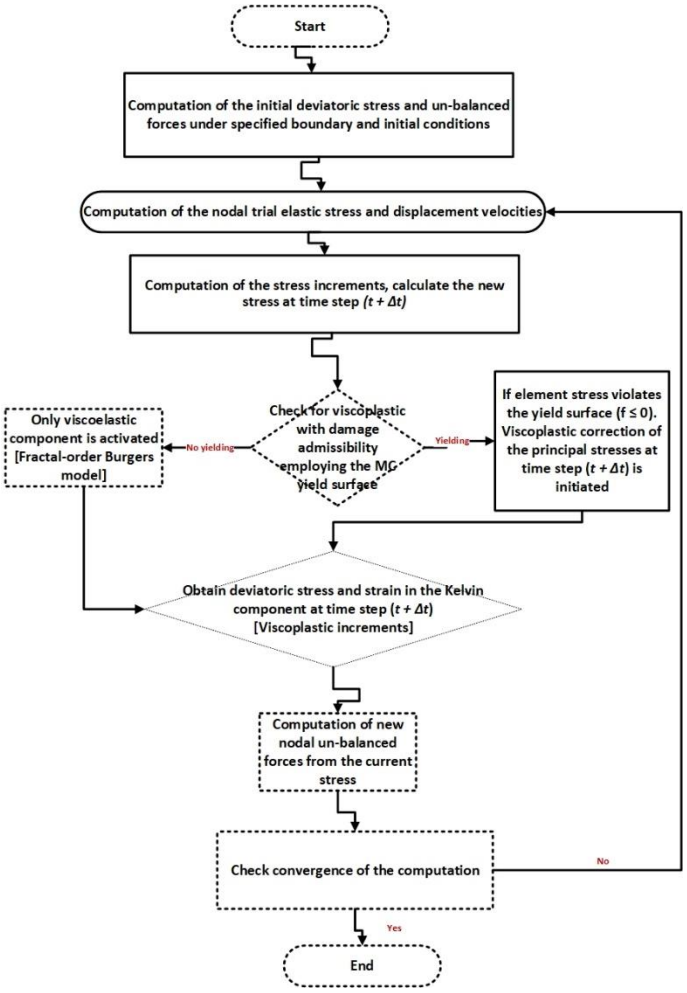

Figure 6-12. Implementation steps in FLAC3D

Implementing and running this model in FLAC3D is distinct from the time-independent constitutive models which employ static analysis. This discrepancy is due to the time-step of the creep simulation, which represents real-time, while in the static analysis it represents the virtual values required to attain the conditions of a stable state. Successful EVPD constitutive model simulation requires a mechanical state of equilibrium condition and creep time steps. In the numerical simulation to guarantee a quasi-static equilibrium is reached a sufficient and smaller time step is considered governed by $\Delta t_{\max}^{cr} \le \min\left(\frac{\eta_K}{G_K}, \frac{\eta^{\gamma_1}}{G_M}\right)$ as the maximum creep time step. Whereas strain-dependent stress increment should be as low as possible compared to time-dependent stress increment to avert unbalanced forces rising.

6.7 Application of the constitutive model

6.7.1 Numerical scale application

In the section, the 3D tunnel case study numerical analysis is conducted within FLAC^{3D} to simulate the time-dependent behaviour. Figure 6-13 illustrates the constructed meshed 3D numerical model geometry large enough for simulation and minimize boundary effects. The far-field boundaries are placed at an average distance of 10 and 20 radii (R = 5.8 m), the model axial length is 50 m and the mesh are discretised into 0.45 m elements. Additionally, fixed boundary conditions are adopted in which all displacements on the boundaries are static in the perpendicular direction to their surfaces. Additionally, half of the model as a symmetrical geometry is adopted in order to reduce the simulation time [54]. The applied boundary conditions are similar in both the CVISC and EVPD constitutive model simulations and the state of stress (S_x = S_y = S_z = 23.3 MPa) is initialized on every model zones. It is assumed that the depth at which the circular tunnel is considered for stability analysis is 700 m, average ground specific gravity is 2700 kN/m^3 and the gravity effect is neglected. The excavation step adopted is 5 m every 2000 numerical steps to a maximum of 10 m tunnel advance which follows the actual rate of 5 m/day tunnel advance observed at the mine. The material strength and creep properties used the tunnel yield zone extent and deformation in response to the 3-phase creep behaviour are adopted from the Nchanga underground (NUG) back analysis [55,56](Table 6-6).

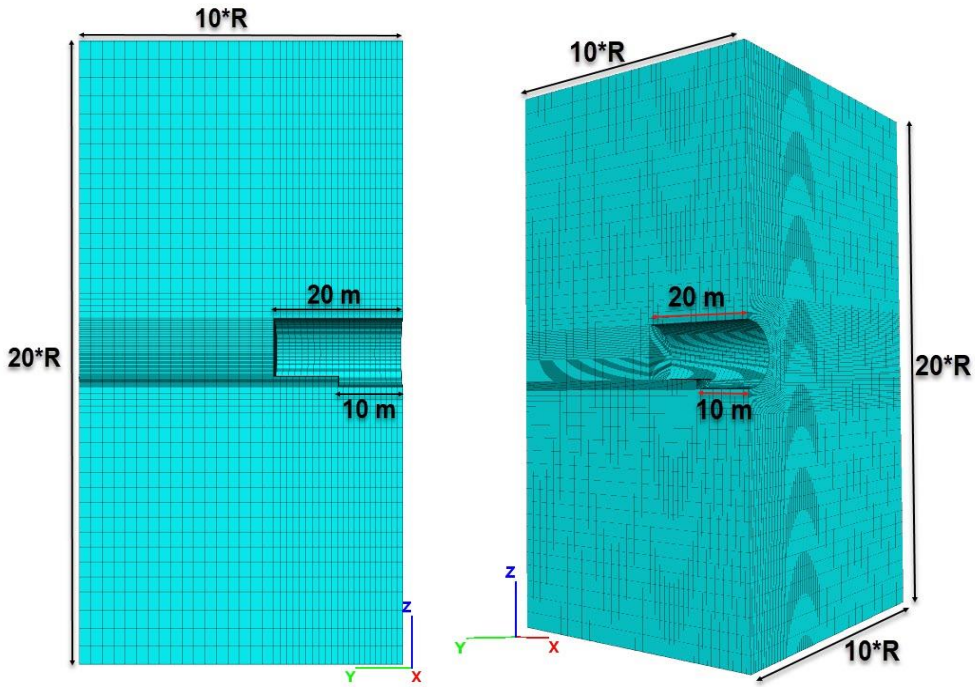

Figure 6-13. Meshed and discretised geometry

Table 6-6. Strength and creep parameters for the EVPD constitutive model

η_K(GPa.h)	G_K(GPa)	G_M(GPa)	η^{γ_1}(GPa.h)	η^{γ_2}(GPa.h)	γ_1	γ_2	ω	c(MPa)	ϑ(°)	ψ(°)	ν	K(GPa)	σ^t(MPa)
2552	73.6	49.3	5860	7567	0.56	0.6	0.9	1.28	26.6	0.0	0.2	50	0.05

Strength and creep parameters for the CVISC constitutive model

η_K(GPa.h)	G_K(GPa)	G_M(GPa)	η_M(GPa.h)	c(MPa)	ϑ(°)	ψ(°)	ν	K(GPa)	σ^t(MPa)
2552	73.6	49.3	5860	1.28	26.6	0.0	0.2	50	0.05

The simulation adopts the EVPD and CVISC constitutive models for comparative analysis. The results of this simulation show that the deformation and yield zone extension around the tunnel in a CVISC and EVPD simulation is extensive in the latter than the former (Figure 6-14). In the CVISC simulated tunnel, the yield zone is about 9 m, 8 m and 9 m for the roof, wall, and floor, respectively. Whereas, for the EVPD simulated tunnel it is not more than 18 m, 10 m, and 16 m. On the other hand, the tunnel wall to wall deformation in the EVPD simulation as compared to the CVISC simulation is approximately 29% and accounts for 8% (29% - 21%) more. This variance is attributed to delayed deformations which occur in squeezing ground characterised by the accelerated creep phase.

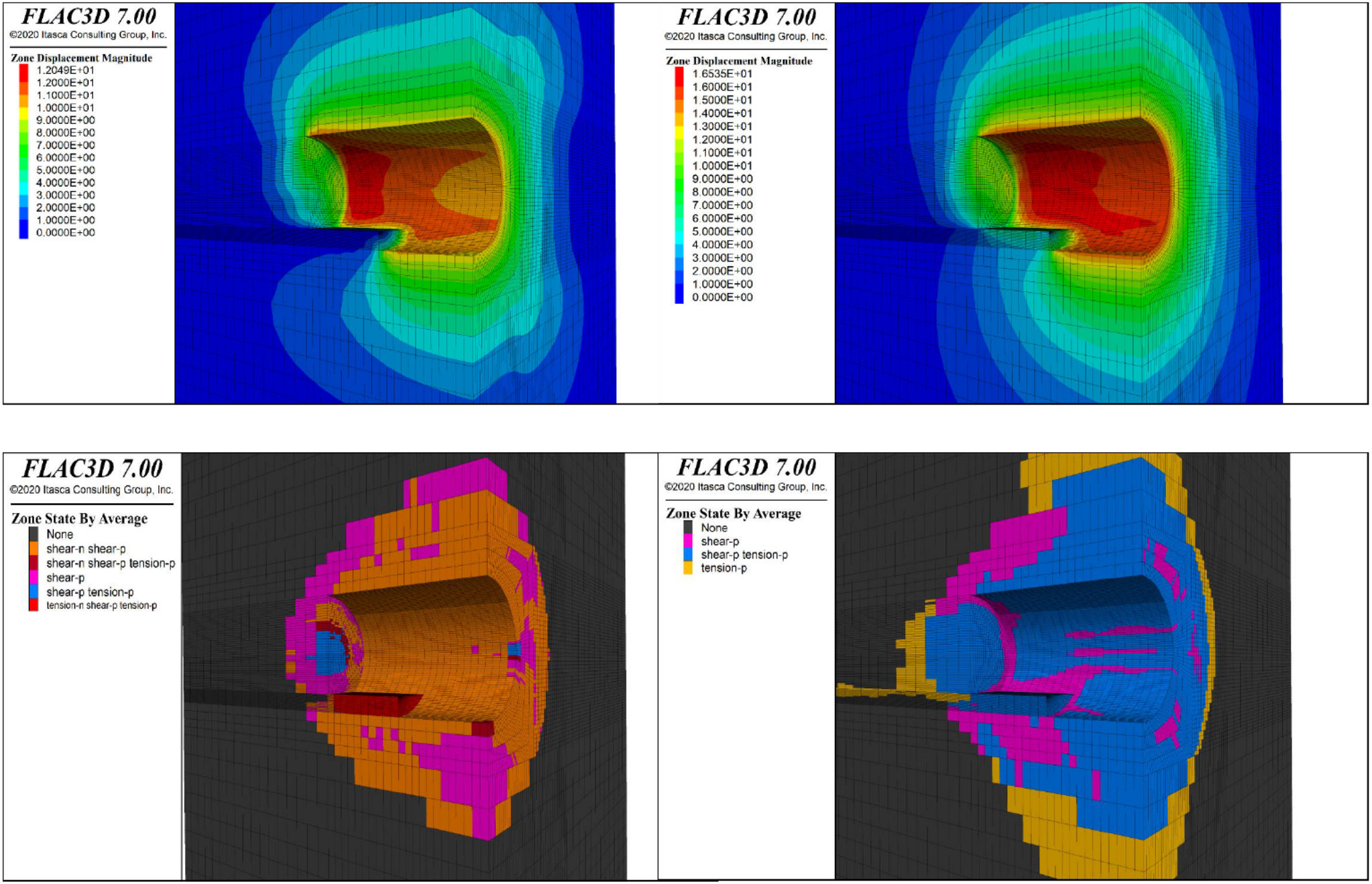

Figure 6-14. Simulation results (a) Deformation using CVISC model, (b) deformation using the EVPD model, (c) yielding using CVISC model and (d) yielding using the EVPD model

6.7.2 In-situ scale application

In this section, a tunnel case at the Jinping hydropower station excavated at a depth of 2500 m is considered for time-dependent convergence estimation [58]. Its dimension and designed convergence monitor positions (1, 2, 3, 4 & 5) are illustrated in Figure 6-15. The illustration also shows attained results from the comparison between the EVPD, FDVP estimated and monitored time-dependent convergence. The convergence between monitor positions 1 and 2 is represented by 1-3, between positions 2 and 3 by 2-3, between positions 2 and 5 by 2-5 and between positions 4 and 5 by 4-5. This comparative analysis is conducted with an emphasis on the mean tunnel convergence which occurs over time [3]. The preliminary analysis verified that the EVPD constitutive model does not satisfactorily replicate the time-dependent tunnel scale (in-situ scale) response if experimental calibrated creep parameters (Table 6-5) are employed. This limitation is addressed by conducting a sequence of parametric analyses to assess the appropriate creep parameters to match monitoring data at an in-situ scale. The suitable and calibrated creep parameters for the constitutive model to describe the time-dependent tunnel deformation on an in-situ scale are presented in Table 6-7 below.

Table 6-7. Calibrated in-situ creep and rock strength parameters for the EVPD constitutive model

η_K(GPa.h)	G_K(GPa)	G_M(GPa)	η^{γ_1}(GPa.h)	η^{γ_2}(GPa.h)	γ_1	γ_2	ω	c	ϑ	ψ	ν	σ_Y(MPa)
81.7	2610	53	4470.83	141.7	0.56	0.6	0.66	6	32.6	0	0.2	130.1

In section 6.4, the EVPD constitutive model was calibrated with experimental data employing the value ω = 0.9. However, matching monitored data at an in-situ scale required adjustment of this value to approximately 70% (ω = 0.66). This adjustment considered the rock mass characteristics' (joints, anisotropy, and heterogeneity) influence, neglected at the experimental scale calibration with an intact rock specimen. Additionally, this adjusted value enables the EVPD constitutive model to attain a good agreement with the in-situ mean tunnel convergence. Therefore, the presented EVPD constitutive model represents the 3-phase creep behaviour reasonably well and estimates tunnel convergence in squeezing ground by scaling up/down parameters calibrated on an experimental scale.

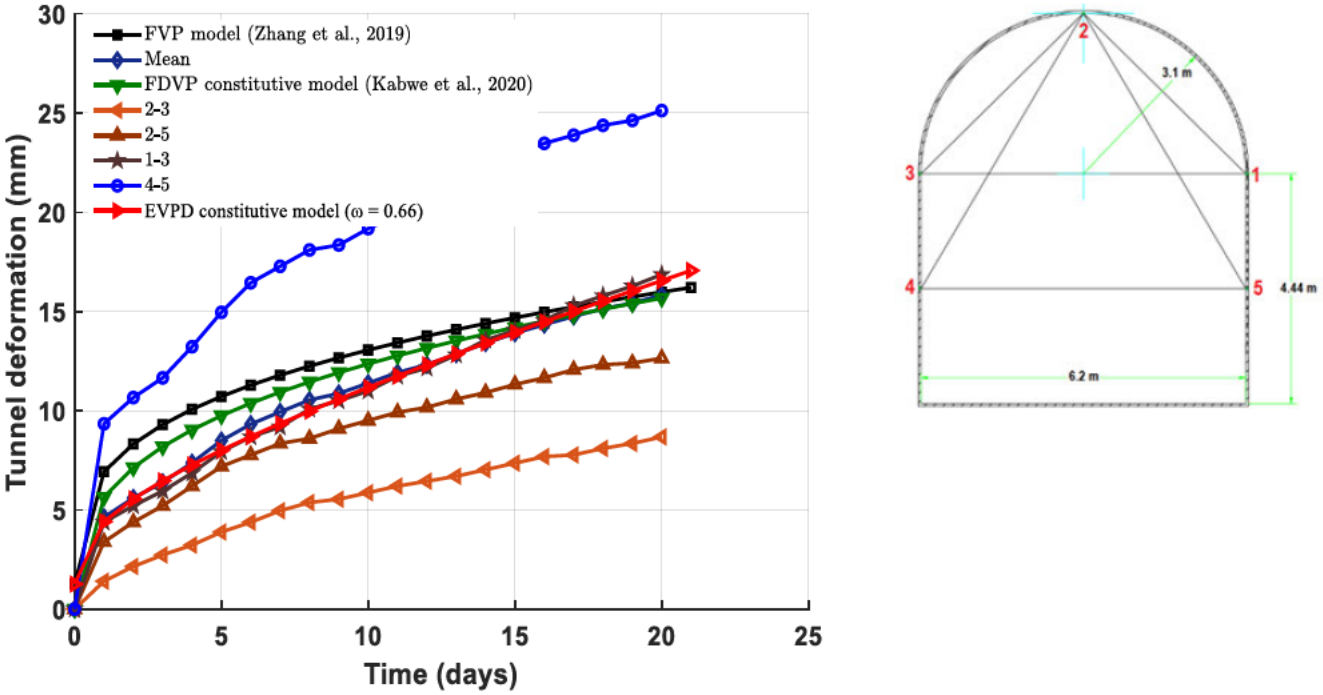

Figure 6-15. Estimated deformation using the EVPD model in comparison with the monitored deformations

6.8 Discussion

The integer-order derivative constitutive models fail to fully describe the 3-phase creep behaviour most importantly the tertiary creep phase. This phase is characterised by the time-dependent behaviour responsible for squeezing. Hence, a time-dependent constitutive model for squeezing ground conditions based on fractal-order derivatives constitutive equations is presented. This constitutive model is derived to efficiently estimate the time-dependent (delayed deformation) in squeezing ground. An extension and adjustment of the FDVP [25] model coupled with a time-dependent viscoplastic component with a visco-damage element. The visco-damage element is governed by the derived time scaling transformation constitutive equation established on fractal-order derivative hypothesis and Perzyna [26] fundamental constitutive law.

The different values of the fractal-order parameters can be determined by the fractal mathematical law based on the condition $0.0 \leq \gamma_{1,2} \leq 1.0$. This condition determines the behaviour of the spring-pot strain derivation characterised by a zero-order derivative as a spring and first-order derivative as a dashpot. Important for damage development consideration in the spring-pot which entails explicit creep mechanism description. However, it can be mentioned that the calibration of the fractal-order parameters $\gamma_{1,2}$ will be different for different rock masses due to different response when subjected to stress. Seeing that validation in this study is based on different rock specimens, the calibrated fractal-order parameters for salt rock and marble are 0.31 and 0.32 respectively. As such further research will be conducted to determine the appropriate fractal-order derivative for different rock masses prone to squeezing.

Additionally, modelling the 3-stage creep behaviour is very ambiguous with few or lesser parameters it is almost impossible to attain that delayed time-dependent response characterised by the accelerated creep stage associated with squeezing. Therefore, additional parameters are required to explicitly describe this mechanism as such 14 parameters are adopted in the EVPD constitutive model. To this regard, results attained from the constitutive model validation, calibration and response show very close alignment with

experimental data. It must be mentioned that to achieve the explicit description of the 3-stage creep mechanism, specified rocks/rock masses should be selected, and experimental conditions critically designed. Hence, the selected rocks employed in this study are those attained from an underground operation which experiences squeezing mechanism associated with creep. Additionally, the experimental setting adopted and data attained are from experiment set conditions by [13] and [53]. Whereas the constitutive parameters can be derived directly from traditional mechanical and creep tests and $\gamma_{1,2}$ values can be determined as rule of thumb between 0.0 and 1.0. The three experimental data sets of the rock specimens under specific confining pressure provide a detailed collection of experimental data which can only be reproduced by a reliable constitutive model. As such the EVPD constitutive model shows good agreement with experimental data and replication of the 3-creep phases.

Its finite volume numerical implementation proved successful as well as actual simulation of the delayed deformation of a tunnel excavated in squeezing ground. The constitutive model was intended to describe the squeezing mechanism characterised by the 3-phase creep behaviour and its occurrence during tunnelling in squeezing ground. The soft rock tunnel case study adopted in the numerical simulation to verify the constitutive model applicability is one which experiences severe squeezing occurrences. The 3D numerical model considers a staged excavation option and design analysis based on experience gained during excavation at a mine. Finally, the simulation result shows that the CVISC model underestimates the squeezing based delayed deformations compared to the EVPD model.

Thus, the presented constitutive equations will allow for the appropriate excavation and tunnel support structure design in squeezing ground. Furthermore, damage evolution consideration is critical in modelling and estimating the delayed deformation characterised by squeezing.

6.9 Conclusions

The strain rate curves of the EVPD constitutive model indicate near alignment with the experimental creep results. Hence, this validation signifies that its constitutive equations can describe not only the transient creep and steady-state creep but also the accelerated creep process. As such the following conclusion are drawn from this study.

- The results from the undertaken calibration, validation and verification demonstrated that the constitutive model provides an efficient tool for describing 3-stage creep mechanism, delayed deformation estimation and tunnel stability in squeezing ground. The model perfectly described the accelerated creep phase and its time-dependent characteristics when γ_1 = 0.56, γ_2 = 0.6 and ω = 0.9. Findings obtained from the sensitivity analysis of these constitutive parameters indicate that different values of $\gamma_{1,2}$, ω and stress level have a major effect on the rate of creep strain and the shape of the creep curves. However, on an in-situ scale, the model required parameter scaling of these constitutive parameters to match the monitoring data.

- The constitutive model is shown to stimulate the time-dependent tunnel deformation perfectly by comparing its performance with the built-in CVISC constitutive model. The yield extension was, according to the numerical calculation, more across the tunnel simulated by the constitutive model (14.7 m) relative to the constitutive model CVISC (8.7 m). Whereas the deformation is approximately 29% and accounts for 8% more than the CVISC estimation (21%), delayed (time-dependent) deformations are attributed to the disparity between the two results. The CVISC constitutive model underestimates the squeezing related delayed deformations in comparison with the EVPD constitutive model.

- The constitutive model employs rather simple and powerful fractal-order derivative constitutive laws which improves the estimation of squeezing mechanism associated with the 3-phase creep

behaviour. It shows that fractal-order derivatives can serve as a bridge between the fractional-order and integer-order derivative models by employing scaling transformation. As such preserves the integer-order derivative functionality and describes the power-law mechanism with few parameters.

6.10 Further enhancement

The EVPD constitutive model's not too simple and not complex characteristic simply makes it a good fit in both research and design practice. This allows the model to be used with confidence in estimating the time-dependent deformation in squeezing ground. However, some limitation of the constitutive model which will require further research and improvement include:

- The constitutive model neglected heterogeneity influence on damage evolution characterized by the VP behaviour of rock mass joints, discontinuities, and fractures. Which plays a major role on the extent of delayed deformations responsible for squeezing.
- The constitutive model considered static and quasistatic conditions neglected dynamic effects (attributed to blasting and seismic events) governed by material forces and time-dependent rock mass properties.
- The assumption adopted by the constitutive model neglects temperature effects even though its impact is significant. However, in cases of deep underground tunnels, influence of temperature on squeezing should be taken into consideration.

Therefore, further work on the constitutive equations should consider the heterogeneity, dynamic and temperature effects on squeezing.

6.11 References

[1] Fahimifar A, Karami M, Fahimifar A. Modifications to an elasto-visco-plastic constitutive model for prediction of creep deformation of rock samples. Soils Found 2015;55:1364–71.

[2] Fahimifar A, Tehrani FM, Hedayat A, Vakilzadeh A. Analytical solution for the excavation of circular tunnels in a visco-elastic Burger's material under hydrostatic stress field. Tunn Undergr Sp Technol 2010;25:297–304.

[3] Debernardi D, Barla G. New viscoplastic model for design analysis of tunnels in squeezing conditions. Rock Mech Rock Eng 2009;42:259–88.

[4] Malan DF. Time-dependent Behaviour of Deep Level Tabular Excavations in Hard Rock. Rock Mech Rock Eng 1999;32:123–55.

[5] Sterpi D, Gioda G. Visco-Plastic behaviour around advancing tunnels in squeezing rock. Rock Mech Rock Eng 2009;42:319–39.

[6] Cristescu N, Gioda G. Visco-plastic behaviour of geomaterials. Springer; 1994.

[7] Liu HZ, Xie HQ, He JD, Xiao ML, Zhuo L. Nonlinear creep damage constitutive model for soft rocks. Mech Time-Dependent Mater 2017;21:73–96.

[8] Boukharov GN, Chanda MW, Boukharov NG. The three processes of brittle crystalline rock creep. Int. J. rock Mech. Min. Sci. Geomech. Abstr., vol. 32, Elsevier; 1995, p. 325–35.

[9] Chaboche J-L, Lemaitre J. Mécanique des matériaux solides. Dunod; 2009.

[10] Barla G, Bonini M, Debernardi D. Time Dependent Deformations in Squeezing Tunnels. 12th Int Conf Int Assoc Comput Methods Adv Geomech 2008;2:1–6.

[11] Pellet F, Roosefid M, Deleruyelle F. On the 3D numerical modelling of the time-dependent development of the damage zone around underground galleries during and after excavation.

Tunn Undergr Sp Technol Inc Trenchless Technol Res 2009;24:665–74.

[12] Itasca Consulting Group Inc. Flac 5 Fast Lagrangian Analysis of Continua Manual 2005:3058.

[13] Zhou HW, Wang CP, Han BB, Duan ZQ. A creep constitutive model for salt rock based on fractional derivatives. Int J Rock Mech Min Sci 2011;48:116–21.

[14] Zhou HW, Wang CP, Mishnaevsky L, Duan ZQ, Ding JY. A fractional derivative approach to full creep regions in salt rock. Mech Time-Dependent Mater 2013;17:413–25.

[15] Yang W, Zhang Q. Time-Dependent Behavior of Diabase and a Nonlinear Creep Model 2014;3:1211–24.

[16] Paraskevopoulou C, Diederichs M. Analysis of time-dependent deformation in tunnels using the Convergence-Confinement Method. Tunn Undergr Sp Technol 2018;71:62–80.

[17] Chan KS, Bodner SR, Fossum AF, Munson DE. A damage mechanics treatment of creep failure in rock salt. Int J Damage Mech 1997;6:121–52.

[18] Mazzotti C, Savoia M. Nonlinear creep damage model for concrete under uniaxial compression. J Eng Mech 2003;129:1065–75.

[19] Hou Z. Mechanical and hydraulic behavior of rock salt in the excavation disturbed zone around underground facilities. Int J Rock Mech Min Sci 2003;40:725–38.

[20] Verstrynge E, Schueremans L, Van Gemert D. Time-dependent mechanical behavior of lime-mortar masonry. Mater Struct 2011;44:29–42.

[21] Ma LJ, Liu XY, Fang Q, Xu HF, Xia HM, Li EB, et al. A new elasto-viscoplastic damage model combined with the generalized hoek-brown failure criterion for bedded rock salt and its application. Rock Mech Rock Eng 2013;46:53–66.

[22] Chen L, Wang CP, Liu JF, Liu YM, Liu J, Su R, et al. A damage-mechanism-based creep model

considering temperature effect in granite. Mech Res Commun 2014;56:76–82.

[23] Cai W, Chen W, Xu W. Characterizing the creep of viscoelastic materials by fractal derivative models. Int J Non Linear Mech 2016;87:58–63.

[24] Kabwe E, Karakus M, Chanda EK. Time-dependent solution for non-circular tunnels considering the elasto-viscoplastic rockmass. International Journal of Rock Mechanics and Mining Sciences. 2020 ;133:104395.

[25] Kabwe E, Karakus M, Chanda EK. Creep constitutive model considering the overstress theory with an associative viscoplastic flow rule. Comput Geotech 2020;124:103629.

[26] Perzyna P. Fundamental problems in viscoplasticity. Adv. Appl. Mech., vol. 9, Elsevier; 1966, p. 243–377.

[27] ADACHI T, OKA F. Constitutive equations for normally consolidated clay based on elasto-viscoplasticity. Soils Found 1982;22:57–70.

[28] Mabssout M, Herreros MI, Pastor M. Wave propagation and localization problems in saturated viscoplastic geomaterials. International journal for numerical methods in engineering. 2006; 68(4):425-47.

[29] Yin ZY, Hicher PY. Identifying parameters controlling soil delayed behaviour from laboratory and in situ pressuremeter testing. International Journal for Numerical and Analytical Methods in Geomechanics. 2008;32(12):1515-35.

[30] Kimoto S, Oka F. An elasto-viscoplastic model for clay considering destructuralization and consolidation analysis of unstable behavior. Soils and Foundations. 2005;45(2):29-42.

[31] Kutter BL, Sathialingam N. Elastic-viscoplastic modelling of the rate-dependent behaviour of clays. Géotechnique. 1992;42(3):427-41.

[32] Yin JH, Zhu JG, Graham J. A new elastic viscoplastic model for time-dependent behaviour of normally and overconsolidated clays: theory and verification. Canadian Geotechnical Journal. 2002;39(1):157-73.

[33] Nishihara M. Creep of shale and sandy-shale. J Geol Soc Japan 1952;58:373–7.

[34] Kabwe E, Karakus M, Chanda E. Assessment of analytical solutions for time-dependent behavior of unlined tunnels. In Proceedings of 4th International Symposium on Underground Excavation 2018;1-9.

[35] Xu G, He C, Yan J, Ma G. A new transversely isotropic nonlinear creep model for layered phyllite and its application. Bull Eng Geol Environ 2019;78:5387–408.

[36] Herrmann W, Wawersik WR, Lauson HS. Analysis of steady state creep of southeastern New Mexico bedded salt. Sandia National Labs., Albuquerque, NM (USA); 1980.

[37] Sjaardema GD, Kreig RD. A constitutive model for the consolidation of WIPP [Waste Isolation Pilot Plant] crushed salt and its use in analyses of backfilled shaft and drift configurations. Sandia National Labs.; 1987.

[38] Okubo S, Fukui K. An Analytical Investigation of a Variable- Compliance-type Constitutive Equation 2006;39:233–53.

[39] Pellet FL. Contact between a tunnel lining and a damage-susceptible viscoplastic medium. C - Comput Model Eng Sci 2009;52:279–95.

[40] Weng MC, Tsai LS, Liao CY, Jeng FS. Numerical modeling of tunnel excavation in weak sandstone using a time-dependent anisotropic degradation model. Tunn Undergr Sp Technol 2010;25:397–406.

[41] Nazary Moghadam S, Mirzabozorg H, Noorzad A. Modeling time-dependent behavior of gas caverns in rock salt considering creep, dilatancy and failure. Tunn Undergr Sp Technol

2013;33:171–85.

[42] Tran H, Jean M, Didier S, Billaux D, Abstr G, Mech IJR. Anisotropic Time-Dependent Modeling of Tunnel Excavation in Squeezing Ground. Rock Mech Rock Eng 2015:2301–17.

[43] Causse L, Cojean R, Fleurisson J-A. Interaction between tunnel and unstable slope – Influence of time-dependent behavior of a tunnel excavation in a deep-seated gravitational slope deformation. Tunn Undergr Sp Technol 2015;50:270–81.

[44] Ofoegbu G, Dasgupta B. implementation of a creep model in flac to study the thermomechanical response of salt as a host repository medium—2nd progress report 2017.

[45] Sainoki A, Tabata S, Mitri HS, Fukuda D, Kodama J ichi. Time-dependent tunnel deformations in homogeneous and heterogeneous weak rock formations. Comput Geotech 2017;92:186–200.

[46] Wang X, Yin Y, Wang J, Lian B, Qiu H, Gu T. A nonstationary parameter model for the sandstone creep tests 2018.

[47] Yin D, Wu H, Cheng C, Chen Y. Fractional order constitutive model of geomaterials under the condition of triaxial test. Int J Numer Anal Methods Geomech 2013;37:961–72.

[48] Wang R, Zhuo Z, Zhou HW, Liu JF. A fractal derivative constitutive model for three stages in granite creep. Results Phys 2017;7:2632–8.

[49] Xu XL, Karakus M. A coupled thermo-mechanical damage model for granite. Int J Rock Mech Min Sci 2018;103:195–204.

[50] Bruning T, Karakus M, Nguyen GD, Goodchild D. An experimental and theoretical stress-strain-damage correlation procedure for constitutive modelling of granite. Int J Rock Mech Min Sci 2019;116:1–12.

[51] Cai W, Chen W, Xu W. Characterizing the creep of viscoelastic materials by fractal derivative

models. Int J Non Linear Mech 2016;87:58–63.

[52] Kilbas AAA, Srivastava HM, Trujillo JJ. Theory and applications of fractional differential equations. vol. 204. Elsevier Science Limited; 2006.

[53] Chen BR, Zhao XJ, Feng XT, Zhao HB, Wang SY. Time-dependent damage constitutive model for the marble in the Jinping II hydropower station in China. Bull Eng Geol Environ 2014;73:499–515.

[54] Kabwe E, Karakus M, Chanda EK. Proposed solution for the ground reaction of non-circular tunnels in an elastic-perfectly plastic rock mass. Comput Geotech 2020;119:103354.

[55] Kabwe E. Optimal mining method selection for Nchanga's Upper Orebody using analytic hierarchy process and Yager's method. Trans Institutions Min Metall Sect A Min Technol 2017;126:151–62.

[56] Kabwe E. Mining Sequence Deformation and Failure Behaviour Analysis in the hangingwall and Orebody Rock Formations; A Continuum Approach. Geotech Geol Eng 2017;35.

[57] Zhang J-Z, Zhou X-P, Yin P. Visco-plastic deformation analysis of rock tunnels based on fractional derivatives. Tunn Undergr Sp Technol 2019;85:209–19.

6.12 Appendix A: Formulation of the constitutive model

The EVPD constitutive equations are formulated by coupling the VPD component and the Burgers model, the strain rate relationship of the coupling is expressed by:

$$\dot{e}_{ij} = \dot{e}_{ij}^{K} + \dot{e}_{ij}^{M} + \dot{e}_{ij}^{vpd} \tag{A1}$$

Where $\dot{e}_{ij}$ is the total strain, $\dot{e}_{ij}^{M}$ is the Maxwell strain rate, $\dot{e}_{ij}^{K}$ is the Kelvin strain rate and $\dot{e}_{ij}^{vpd}$ is the VPD component strain rate. The Maxwell, Kelvin components' strain and stress rates are expressed by:

$$S_{ij} = 2\eta_K \dot{e}_{ij}^{K} + 2G_K e_{ij}^{K} \tag{A2}$$

$$\dot{e}_{ij}^{M} = \frac{S_{ij}^{M}}{2\eta^{\gamma_1}} t^{\gamma_1} + \frac{\dot{S}_{ij}^{M}}{2G_M} \qquad (0 \le \gamma_1 \le 1) \tag{A3}$$

Where $\dot{e}_{ij}^{M}$ is the deviatoric strain rate, S_{ij}^{M} is the deviatoric stress acting on the Maxwell component, η^{γ_1} is the viscosity of the fractal order dashpot. The stress-strain relationship in the VPD component is computed from:

$$\dot{e}_{ij}^{vpd} = \lambda \frac{\partial Q_{vp}}{\partial \sigma'_{ij}} - \frac{\dot{e}_{vol}^{vpd}}{3}\delta_{ij} \tag{A4}$$

$$\dot{e}_{vol}^{vpd} = \lambda \left[\frac{\partial Q_{vp}}{\partial \sigma'_{11}} + \frac{\partial Q_{vp}}{\partial \sigma'_{22}} + \frac{\partial Q_{vp}}{\partial \sigma'_{33}} \right] \tag{A5}$$

Where e_{ij}^{VPD} is the deviatoric strain and σ'_{ij} is the total stress acting in the VPD component plastic slider respectively while the fractal derivative dashpot is represented by the constitutive relation given by;

$$\dot{e}_{ij}^{vpd} = \frac{S_{ij}^{vpd}}{2\eta^{\gamma_2}\omega}\left(e^{\omega t^{\gamma_2}} - 1\right) \qquad (0 \le \gamma_2 \le 1) \tag{A6}$$

Where S_{ij}^{vpd} is the deviatoric stress partition and e_{ij}^{VPD} is the deviatoric strain in the fractal-order derivative spring-pot. Computations of the strain in the VPD component is obtained by calculating the stress acting on the spring-pot, slider and λ. These are computed from the stress equilibrium between the fractal dashpot and

slider, the deviatoric strain rates contributed by the VPD component. The deviatoric strain rate of the slider and the dashpot in the VPD component are equal because the elements are connected in parallel.

$$\lambda \frac{\partial Q_{vp}}{\partial \sigma'_{ij}} - \frac{\dot{e}_{vol}^{vpd}}{3}\delta_{ij} = \frac{S_{ij}^{vpd}}{2\eta^{\gamma_2}\omega}\left(e^{\omega t^{\gamma_2}} - 1\right) \tag{A7}$$

and the stress equilibrium for the VPD component is represented by;

$$\sigma_{ij} = \sigma'_{ij} + S_{ij}^{vpd} \tag{A8}$$

Alternatively, the strain rate acting in both the plastic slider and dashpot of the VPD component can be integrated into one relation expressed as;

$$\dot{e}_{ij}^{vpd} = \frac{S_{ij}^{vpd} - S_Y}{2\eta^{\gamma_2}\omega}\left(e^{\omega t^{\gamma_2}} - 1\right) \tag{A9}$$

The VPD component strain rate is further represented by the rock yield function $\left(\langle\phi(F)\rangle = S_{ij}^{vpd} - S_Y\right)$ and the flow rule:

$$\dot{e}_{ij}^{vpd} = \frac{\langle\phi(F)\rangle}{2\eta^{\gamma_2}\omega}\left(e^{\omega t^{\gamma_2}} - 1\right)\frac{\partial Q_{vp}}{\partial \sigma_{ij}} \tag{A10}$$

Where e_{ij}^{vpd} is the total strain rate of the VPD component and the plastic slider is represented by Eqs. A11, A12 & A13;

$$\dot{e}_{ij}^{p} = \lambda \frac{\partial Q_p}{\partial \sigma_{ij}} - \frac{\dot{e}_{vol}^{p}}{3}\delta_{ij} \tag{A11}$$

$$\dot{e}_{vol}^{p} = \lambda\left[\frac{\partial Q_p}{\partial \sigma_{11}} + \frac{\partial Q_p}{\partial \sigma_{22}} + \frac{\partial Q_p}{\partial \sigma_{33}}\right] \tag{A12}$$

$$\sigma_0 = K\left(e_{vol} + e_{vol}^{p}\right) \tag{A13}$$

Where Q_{vp} is the plastic potential and the MC yield criterion $(f = 0)$ employed is comprised of the shear and tensile yielding (Eq A14 & A15).

$$f^s = \sigma_1 - \sigma_3 N_\vartheta + 2c\sqrt{N_\vartheta} \quad \text{(A14)}$$

$$f^t = \sigma^t - \sigma_3 \quad \text{(A15)}$$

Where f^s is the shear yielding, f^t is the tension yielding, σ^t is the tensile strength and their potential functions are represented by Eqs A16 & A A17.

$$Q^s_{vp} = \sigma_1 - \sigma_3 N_\psi \quad \text{(A16)}$$

$$Q^t_{vp} = -\sigma_3 \quad \text{(A17)}$$

Where Q^s_{vp} is the shear yielding potential function, Q^t_{vp} is the tension yielding potential function, $N_\psi = (1 + \sin\psi/1 - \sin\psi)$ whereas λ for shear and tensile yielding is determined by Eq A18 & A19.

$$\lambda^s = \frac{f^s}{2\eta^{\gamma_2}\omega}\left(e^{\omega t^{\gamma_2}} - 1\right) \quad \text{(A18)}$$

$$\lambda^t = \frac{f^t}{2\eta^{\gamma_2}\omega}\left(e^{\omega t^{\gamma_2}} - 1\right) \quad \text{(A19)}$$

6.13 Appendix B: Script

```
#include "modelEVPDF.h"
#include "state.h"
#include "convert.h"
#include "version.txt"
#include <algorithm>
#include <limits>

#ifdef EVPDF_EXPORTS
  int stdcall DllMain(void *,unsigned, void *) {
  return(1);
  }

  extern "C" EXPORT_TAG const char *getName() {
  return("cmodelEVPDF");
  }

  extern "C" EXPORT_TAG unsigned getMajorVersion() {
  return(MAJOR_VERSION);
  }

  extern "C" EXPORT_TAG unsigned getMinorVersion(){
  return(MINOR_VERSION);
  }

  extern "C" EXPORT_TAG void *createInstance() {
    models::ModelEVPDF *m = NEWC(models::ModelEVPDF());
  return((void *)m);
  }

#endif // EVPDF_EXPORTS

namespace models {

  static const unsigned long mShearNow    = 0x01;   /* state logic */
  static const unsigned long mTensionNow  = 0x02;
  static const unsigned long mShearPast   = 0x04;
  static const unsigned long mTensionPast = 0x08;
  static const Double pi = 3.14159265358979323846264338327950288419716939937;
  static const Double degrad = pi / 180.0;
  static const Double dC1d3 = 1.0 / 3.0;
  static const Double time = 1.0;
  //static const Double d4d3 = 4.0 / 3.0;

  ModelEVPDF::ModelEVPDF(): Bulk_(0.0),
                Kshear_(0.0), Mshear_(0.0), Kviscosity_(0.0), Mviscosity_
                  (0.0),Fdviscosity_(0.0),
                cohesion_(0.0), friction_(0.0), dilation_(0.0), tension_(0.0),
                   dvariable_(0.0), gamma_(0.0),
                        AccshearE_(0.0), AcctensE_(0.0), Mnphi_(0.0), Mnpsi_
                    (0.0), Mcsnp_(0.0) {
    Mekd_[0]= 0.0;
    Mekd_[1]= 0.0;
    Mekd_[2]= 0.0;
    Mekd_[3]= 0.0;
    Mekd_[4]= 0.0;
    Mekd_[5]= 0.0;
```

Note: EVPDF refers to the EVPD_final (this is because i could not create an updated C++ code with the same name)

```
}

UInt ModelEVPDF::getMinorVersion() const{
return(MINOR_VERSION); 58
}

String ModelEVPDF::getProperties(void) const {
  return
    (L"bulk,kshear,mshear,kviscosity,mviscosity,Fdviscosity,cohesion,frictio
    n,dilation,tension,dvariable,gamma,"
L"k_exx,k_eyy,k_ezz,k_exy,k_exz,k_eyz"); 63     }

String ModelEVPDF::getStates(void) const {
return(L"shear-n,tension-n,shear-p,tension-p"); 67
}

Variant ModelEVPDF::getProperty(UInt ul) const {
  switch (ul) {
    case 1:  return(Bulk_);
    case 2:  return(Kshear_);
    case 3:  return(Mshear_);
    case 4:  return(Kviscosity_);
    case 5:  return(Mviscosity_);
    case 6:  return(Fdviscosity_);
    case 7:  return(cohesion_);
    case 8:  return(friction_);
    case 9:  return(dilation_);
    case 10: return(tension_);
    case 11: return(dvariable_);
    case 12: return(gamma_);
    case 13:  return(Mekd_[0]);
    case 14:  return(Mekd_[1]);
    case 15:  return(Mekd_[2]);
    case 16:  return(Mekd_[3]);
    case 17:  return(Mekd_[4]);
  case 18: return(Mekd_[5]);
  }
  return(0.0);
}

void ModelEVPDF::setProperty(UInt ul, const Variant &p,UInt restoreVersion)
  {
  ConstitutiveModel::setProperty(ul,p,restoreVersion);
  switch (ul) {
    case 1: { // BULK
      Bulk_ = p.toDouble();
      break;
    }
    case 2: { // KELVIN SHEAR
      Kshear_ = p.toDouble();
      break;
    }
    case 3: { // MAXWELL SHEAR
      Mshear_ = p.toDouble();
      break;
```

```
107         }
108         case 4: {  //
109           Kviscosity_
110           break;
111         }
112         case 5: {  //
113           Mviscosity_
114           break;
115           }
116         case 6: {  //
117           Fdviscosity_ = p.toDouble();
118           break;
119         }
120         case 7: {  // COHESION
121           cohesion_ = p.toDouble();
122           break;
123         }
124         case 8: {  // FRICTION ANGLE
125           friction_ = p.toDouble();
126           break;
127         }
128         case 9: {  // DILATION ANGLE
129           dilation_ = p.toDouble();
130           break;
131         }
132         case 10:{ // TENSION
133           tension_ = p.toDouble();
134           break;
135           }
136         case 11: { // DVARIABLE
137           dvariable_ = p.toDouble();
138           break;
139         }
140         case 12:{ // GAMMA
141           gamma_ = p.toDouble();
142           break;
143           }
144         case 13: {  // Kelvin strain 11
145           Mekd_[0] = p.toDouble();
146           break;
147         }
148         case 14: {  // Kelvin strain 22
149           Mekd_[1] = p.toDouble();
150           break;
151         }
152         case 15: {  // Kelvin strain 33
153           Mekd_[2] = p.toDouble();
154           break;
155         }
156         case 16: {  // Kelvin strain 12
157           Mekd_[3] = p.toDouble();
158           break;
159         }
160         case 17: {  // Kelvin strain 13
161           Mekd_[4] = p.toDouble();
162           break;
```

```
}
164         case 18: {  // Kelvin strain 23
165           Mekd_[5] = p.toDouble();
166           break;
167         }
168       }
169     }
170
171     void ModelEVPDF::copy(const ConstitutiveModel *cm) {
172       ConstitutiveModel::copy(cm);
173       const ModelEVPDF *vm = dynamic_cast<const ModelEVPDF *>(cm);
174       if (!vm) throw std::runtime_error("Internal error: constitutive model
            dynamic cast failed.");
175       Bulk_       = vm->Bulk_;
176       Kshear_     = vm->Kshear_;
177       Mshear_     = vm->Mshear_;
178       Kviscosity_ = vm->Kviscosity_;
179       Mviscosity_ = vm->Mviscosity_;
180       Fdviscosity_ = vm->Fdviscosity_;
181       cohesion_   = vm->cohesion_;
182       friction_   = vm->friction_;
183       dilation_   = vm->dilation_;
184       tension_    = vm->tension_;
185       dvariable_ = vm->dvariable_;
186       gamma_      = vm->gamma_;
187       AccshearE_  =  vm->AccshearE_;
188       AcctensE_   =  vm->AcctensE_;
189       Mnphi_      =  vm->Mnphi_;
190       Mnpsi_      =  vm->Mnpsi_;
191       Mcsnp_      =  vm->Mcsnp_;
192       Mekd_[0]    = vm->Mekd_[0];
193       Mekd_[1]    = vm->Mekd_[1];
194       Mekd_[2]    = vm->Mekd_[2];
195       Mekd_[3]    = vm->Mekd_[3];
196       Mekd_[4]    = vm->Mekd_[4];
197       Mekd_[5]    = vm->Mekd_[5];
198     }
199
200
201     void ModelEVPDF::initialize(UByte dim,State *s)  {
202       ConstitutiveModel::initialize(dim,s);
203       if (Mshear_ <= 0.0) Mshear_ = 1e-20 ;
204       if (Kshear_ <= 0.0) Kshear_ = 0.0;
205       if (Kviscosity_ <= 0.0)  Kshear_ = 0.0;
206       //iMerr = 0;
207       //if (friction_ > 89.0) iMerr = 1;
208       //if (fabs(dilation_)  > 89.0) iMerr = 2;
209       //if (cohesion_  < 0.0) iMerr = 3;
210       //if (tension_ < 0.0) iMerr = 4;
211       //if (iMerr != 0) {
212       //  iNerr = 126;
213       //  iErr = 1 ;
214       //}
215       Double dSphi = sin(friction_ * degrad);
216       Double dSpsi = sin(dilation_ * degrad);
217       Mnphi_  = (1.0 +  dSphi) / (1.0 -  dSphi);
```

```
274     //; --- define constants locally ---
275     Double anphi = Mnphi_;
276     Double anpsi = Mnpsi_;
277     Double amc   = Mcsnp_;
278     //;--- partition strains ---
279     Double dev   = s->stnE_.s11() + s->stnE_.s22() + s->stnE_.s33() ;
280     Double dev3  = dC1d3 * dev;
281     Double de11d = s->stnE_.s11() -  dev3;
282     Double de22d = s->stnE_.s22() -  dev3;
283     Double de33d = s->stnE_.s33() -  dev3;
284     //;--- partition stresses---
285     Double s0    = dC1d3 * (s->stnS_.s11() + s->stnS_.s22() + s->stnS_.s33());
286     Double s11d  = s->stnS_.s11() - s0;
287     Double s22d  = s->stnS_.s22() - s0;
288     Double s33d  = s->stnS_.s33() - s0;
289     //;--- remember old stresses ---
290     Double s11old = s11d;
291     Double s22old = s22d;
292     Double s33old = s33d;
293     Double s12old = s->stnS_.s12();
294     Double s13old = s->stnS_.s13();
295     Double s23old = s->stnS_.s23();
296     //;--- new trial deviator stresses assuming viscoelastic increments ---
297     s11d = (de11d + s11d * y_con - Mekd_[0] * bal) * c1dxc ;
298     s22d = (de22d + s22d * y_con - Mekd_[1]* bal) * c1dxc  ;
299     s33d = (de33d + s33d * y_con - Mekd_[2]* bal) * c1dxc  ;
300     Double s12i  = (s->stnE_.s12()  +  s->stnS_.s12() * y_con  - Mekd_[3]  *
          bal) * c1dxc ;
301     Double s13i  = (s->stnE_.s13()  +  s->stnS_.s13() * y_con  - Mekd_[4]  *
          bal) * c1dxc ;
302     Double s23i  = (s->stnE_.s23()  +  s->stnS_.s23() * y_con  - Mekd_[5]  *
          bal) * c1dxc ;
303     //;--- new trial isotropic stress assuming elastic increment ---
304     s0 += Bulk_ * dev;
305     //;--- convert back to x-y components ---
306     Double s11i  = s11d + s0;
307     Double s22i  = s22d + s0;
308     Double s33i  = s33d + s0;
309     //; --- trial stresses ---
310     s->stnS_.rs11()   = s11i;
311     s->stnS_.rs22()   = s22i;
312     s->stnS_.rs33()   = s33i;
313     s->stnS_.rs12()   = s12i;
314     s->stnS_.rs13()   = s13i;
315     s->stnS_.rs23()   = s23i;
316
317     if (canFail())
318     {
319       /* --- calculate and sort principal stresses and principal directions
            --- */
320       // Calculate principal stresses
321       SymTensorInfo info;
322       DVect3 prin = s->stnS_.getEigenInfo(&info);
323       //; --- shear yield criterion ---
324       Double fs    = prin.x() - prin.z() * anphi + amc;
325       Double alams = 0.0;
```

```
382       //; --- accumulate hardening parameter increments ---
383       if  (iplas == 1)
384       {
385         Double de1ps = alams;
386         Double de3ps = -alams * anpsi;
387         Double depm  =  dC1d3 * (de1ps + de3ps);
388         de1ps =  de1ps - depm;
389         de3ps =  de3ps - depm;
390         s->working_[eps] += (sqrt(0.5*(de1ps*de1ps+depm*depm+de3ps*de3ps))  *
              s->getSubZoneVolume());
391       }
392       if (iplas == 2)
393       {
394         s->working_[ept] -= (alamt * s->getSubZoneVolume());
395       }
396     } // if (canFail())
397     //;--- sub-zone contribution to Kelvin-strains ---
398     s0    = dC1d3 * (s->stnS_.s11() + s->stnS_.s22() +  s->stnS_.s33());
399     s->working_[0] += (Mekd_[0] * ba  +  (s->stnS_.s11() - s0 + s11old) *
        z_con) * s->getSubZoneVolume();
400     s->working_[1] += (Mekd_[1] * ba  +  (s->stnS_.s22() - s0 + s22old) *
        z_con) * s->getSubZoneVolume();
401     s->working_[2] += (Mekd_[2] * ba  +  (s->stnS_.s33() - s0 + s33old) *
        z_con) * s->getSubZoneVolume();
402     s->working_[3] += (Mekd_[3] * ba  +  (s->stnS_.s12()      + s12old) *
        z_con) * s->getSubZoneVolume();
403     s->working_[4] += (Mekd_[4] * ba  +  (s->stnS_.s13()      + s13old) *
        z_con) * s->getSubZoneVolume();
404     s->working_[5] += (Mekd_[5] * ba  +  (s->stnS_.s23()      + s23old) *
        z_con) * s->getSubZoneVolume();
405     //;--- update stored Kelvin-strains and plastic strain ---
406     if (s->sub_zone_ == s->total_sub_zones_-1) {
407       Double Aux = 1./s->getZoneVolume();
408       if (s->overlay_==2) Aux *= 0.5;
409       Mekd_[0]= s->working_[0] * Aux;
410       Mekd_[1]= s->working_[1] * Aux;
411       Mekd_[2]= s->working_[2] * Aux;
412       Mekd_[3]= s->working_[3] * Aux;
413       Mekd_[4]= s->working_[4] * Aux;
414       Mekd_[5]= s->working_[5] * Aux;
415       if (canFail())
416       {
417         AccshearE_ += s->working_[eps]*Aux;
418         AcctensE_  += s->working_[ept]*Aux;
419       }
420     }
421
422     if( (s->state_ & mShearNow) || (s->state_ & mTensionNow) )
423       s->viscous_ = false; // inhibit viscous strains
424     else
425       s->viscous_ = true;  // allow viscous strains
426   }
427
428   Double ModelEVPDF::getStressStrengthRatio(const SymTensor &st) const {
429     DVect3 prin = st.getEigenInfo();
430     Double rat = 10.0;
```

```
431       Double tanf = std::tan(friction_*degrad);
432       Double tcut = friction_ ? std::min(tension_,(cohesion_/tanf)) : tension_;
433       if (tcut - prin.z() <= 0.0)
434         rat = 0.0;
435       else
436       {
437         Double sinf = std::sin(friction_*degrad);
438         Double denom = 1.0 - sinf;
439         Double nph = limits<Double>::max();
440         if (denom) nph = (1.0 + sinf) / denom;
441         Double sig1f = nph*prin.z() - 2.0*cohesion_*std::sqrt(nph);
442         denom = prin.z() - prin.x();
443         if (denom) rat = (prin.z() - sig1f) / denom;
444       }
445       rat = std::min(rat,10.0);
446       return(rat);
447     }
448
449     void ModelEVPDF::scaleProperties(const Double &scale,const std::vector<UInt>
          &props) {
450       for (UInt u=0;u<props.size();++u) {
451         switch (props[u]) {
452           case 1: Bulk_ *= scale;  break;
453           case 2: Kshear_ *= scale;  break;
454           case 3: Mshear_ *= scale;  break;
455           case 7: cohesion_ *= scale;  break;
456           case 8: friction_ = std::max(0.0,std::min(85.0,std::atan(std::tan
              (friction_*degrad) * scale)/ degrad));  break;
457           case 9: dilation_ = std::max(0.0,std::min(85.0,std::atan(std::tan
              (dilation_*degrad) * scale)/ degrad));  break;
458           case 10: tension_ *= scale;   break;
459           default: break;
460         }
461       }
462       setValid(0);
463     }
464   }
465   // EOF
```

Statement of Authorship

Title of Paper	Identifying the Minimum Support Requirements for a Tunnel in Squeezing Ground of an Underground Mine: A Case Study
Publication Status	☐ Published ☐ Accepted for Publication ☐ Submitted for Publication ☑ Unpublished and Unsubmitted work written in manuscript style
Publication Details	Eugie Kabwe, Murat Karakus, Emmanuel K. Chanda Identifying the Minimum Support Requirements for a Tunnel in Squeezing Ground of an Underground Mine: A Case Study. To be submitted.

Principal Author

Name of Principal Author (Candidate)	EUGIE KABWE		
Contribution to the Paper	Conceptualization, Formal analysis, Methodology, Investigation, Writing - original draft, Writing - review & editing and as the corresponding author		
Overall percentage (%)	80%		
Certification:	This paper reports on original research I conducted during the period of my Higher Degree by Research candidature and is not subject to any obligations or contractual agreements with a third party that would constrain its inclusion in this thesis. I am the primary author of this paper.		
Signature		Date	17/08/2020

Co-Author Contributions

By signing the Statement of Authorship, each author certifies that:

i. the candidate's stated contribution to the publication is accurate (as detailed above);

ii. permission is granted for the candidate in include the publication in the thesis; and

iii. the sum of all co-author contr butions is equal to 100% less the candidate's stated contribution.

Name of Co-Author	MURAT KARAKUS		
Contribution to the Paper	Supervision of the work; Identification of the problem and methodology, reviewing & editing		
Signature		Date	18/08/2020

Name of Co-Author	EMMANUEL K. CHANDA		
Contribution to the Paper	Supervision, review & editing		
Signature		Date	18/08/2020

Chapter 7

Identifying the Minimum Support Requirements for a Tunnel in Squeezing Ground of an Underground Mine: A Case Study *(Paper 5)*

Eugie Kabwe, Murat Karakus, Emmanuel K Chanda

To be submitted to an International Journal

Abstract

Tunnel closure due to squeezing ground conditions poses a significant challenge in the support structure set up, maintenance and tunnel stability. It is associated with excessive rehabilitation, rock reinforcement and support element failure. In this paper, the schematic support system design for tunnel stability in squeezing ground by employing a newly proposed analytical and numerical solutions is presented. This analytical solution considers the strengthening effect of the intermediate principal stress on the ground reaction of non-circular tunnels as well as employs strength degradation to represent squeezing. The solution quantifies squeezing as a consequence of high stresses, yielding, strength deterioration and determines the required support structure for tunnel ground response restraint at the preliminary stage. In addition, a finite element numerical simulation in RS^2 is performed to estimate the ground response and support structure performance. It is drawn from the simulation results that after installation of the determined support structure, ground response and plastic flow radii around the tunnel decreased considerably. This indicates that a combination of the analytical solution and numerical simulation is required for a reliable tunnel support structure design in squeezing ground. It is also drawn that the analytical solution determines a preliminary ground response estimation which is further verified by the numerical simulation.

Keywords: Analytical solution; Ground reaction; Intermediate principal stress; Non-circular tunnels; Squeezing

7.1 Introduction

Excavation and stability of tunnels require a thorough understanding of the surrounding weak rock mass behaviour. This understanding enables the appropriate support structure design and installation. The support structure design is highly dependent on the rock mass classification and the drift design experience. Excessive tunnel closure due to squeezing ground conditions in weak rock masses may pose a significant challenge for support structure installation, maintenance and tunnel stability. Large deformation associated with these conditions is characterized by the tunnel cross-section area reduction due to the combination of induced stress and weak rock mass [1]. This squeezing associated long-term deformation is usually in the form of roof sagging, wall extrusion and floor heave (Figure 7-1).

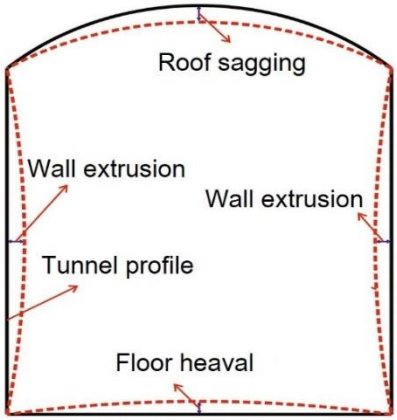

Figure 7-1. Profile deformation associated with squeezing

Squeezing mechanism is a major challenge when excavating tunnels in weak rock mass associated with high induced stress fields. It is usually not identified and predicted at an early stage of tunnel excavation [2]. Tunnelling under this ground condition is frequently associated with excessive rehabilitation, rock reinforcement and support element failure. Based on the extent of the squeezing process, considerable investment is needed in extra rock reinforcement and support installation and time-consuming rehabilitation to keep tunnels serviceable [1,3,4]. When a tunnel is driven in a high-stressed rock mass stress redistribution occurs around its boundary depending on the geometry of its opening. This stress redistribution leads to the increase in deviatoric stresses which in turn induce squeezing.

Several conducted studies about squeezing ground conditions are associated with civil engineering projects, for instance [5–9]. They analysed the squeezing mechanism in tunnels and concluded that squeezing is a long-term behaviour of rocks that can be predicted using constitutive modelling and numerical analyses. This estimation is centred on the rock mass strength and in situ state of stress. Estimation of the rock mass response requires an accurate illustration of its long-term behaviour and adjustment of its mechanical properties [10].

Tunnels in mining experience squeezing when the ore bodies are in weak rock formations and as they continue going deeper tunnel stability under these ground conditions is becoming a major challenge. There are few documented case studies on squeezing in mines as opposed to civil engineering projects. Some squeezing occurrences in mines include the Blackwater mine of New Zealand which experienced severe squeezing behaviour in the 1940s [11]. In Australia the Henty mine of Tasmania experienced severe squeezing conditions, up to 50% above wall strain was recorded [4], the Wattle Dam Gold Mine reported by [12] experienced strains up to 2.8%, the Perseverance mine in Kalgoorlie reported by [13] and Rio Tinto's Argyle Diamond mine reported by [14] among others. The Canadian Lapa and La Rhonde mines' experience with squeezing ground conditions has been discussed by [3,15,16]. South African experience with squeezing is also described by [17]. The Zambia's Nchanga Under Ground (NUG) which is our focus in this study also experienced severe squeezing [18]. Based on [18,19] these conditions led to large deformation and collapse of several tunnels, consequently shutdown of the entire underground mine operation. This paper highlights the practical approach of employing the new analytical solution and the RS^2 numerical simulation in determining the appropriate tunnel support structures. This approach is used in the stability analysis and suggests an appropriate tunnel support system in the NUG squeezing ground. The analytical solution estimates the elastoplastic ground reaction with strength degradation as a representation of the long-term behaviour associated with squeezing. It is further employed to estimate the support system capacity at the preliminary stage. Whereas the numerical solution verifies this ground response and the performance of the analytically suggested support system.

7.2 Convergence quantification

Tunnel deformation associated with squeezing can be quantified using approaches classified as empirical methods, semi empirical methods, analytical continuum elastoplastic models (closed-form solutions), analytical discontinuum elastoplastic models, analytical continuum and discontinuum models based on material degradation and damage and continuum and discontinuum rheological models among others. In this paper we consider the analytical continuum model based on material degradation. This is because we want to gain preliminary insight into tunnel response when excavated in a rockmass that exhibits squeezing mechanism. It is worth mentioning that this study and analysis does not consider time-dependency of the squeezing mechanism. Rather considers the material degradation and strength characteristic of the rockmass represented by the cohesion, internal friction angle and material stiffness. Since material degradation or deterioration takes place overtime due to the aspect of weathering, squeezing, swelling and stress relief [10]. This employs an elastoplastic analytical solution that neglects time-dependency assumes the behaviour is a simple result of high stress, yielding and linked to the strength degradation overtime. This solution is based on the widely employed Convergence Confinement Method (CCM). Which is originally based on a hole-in-a-plate theory [20] with assumptions restricted to (1) continuous, homogenous and isotropic rock mass, (2) initial isotropic state stress (3) plane strain condition and (4) circular tunnel cross-section. The applicability of this method in estimating tunnel deformation associated with squeezing is well clarified in several publications [21–27]. It considers three basic components the ground reaction curve (GRC), support characteristic curve (SCC) and Longitudinal Displacement Profile (LDP). The GRC describes a curve which represents the tunnel inner boundary stress relaxation with an incremental convergence. The SCC is characterised by the tunnel support structure deformation because of the internal support pressure action and the LDP relates tunnel displacement to the position of the tunnel face. Whereas, numerical estimation is conducted by using elasto-plastic, visco-elastic and more complex elasto visco-plastic constitutive models [26,28,29]. In this study, the elastoplastic constitutive model is adopted to verify the analytically estimated tunnel

convergence and verify the support structure performance. Additionally, the CCM based solution which addresses an assumption considered a limitation for non-circular tunnels is employed.

7.3 Nchanga background

Nchanga mine lies on the Zambian Copperbelt with three overlaid orebodies namely, the Lower Orebody (LOB), Intermediate Orebody (IOB) and Upper Orebody (UOB) [30]. Generally, two of these orebodies has been the source of ore production for the Nchanga open pit (NOP) while the LOB is sorely sourced by the NUG. Mass mining in the NUG is mainly achieved by the conventional block caving technique. There has been a significant decline in the LOB ore production, as a result, the UOB is the main source of production which will also extend the Life of Mine (LOM). However, the highly folded UOB is characterised by fissures, strength degrading rock mass which poses uneconomical extraction [31].

7.3.1 Geological structure

The LOB lies in the argillaceous shale rock type referred to as the Lower Banded Shale (LBS) while the UOB lies in the Feldspathic Quartzite (TFQ) [31]. The LOB is mainly extracted from the NUG however in the direction of the eastern syncline section the argillaceous shale is exposed on the surface and it is extracted from the Nchanga Open Pit (NOP) [32,33]. Ore extraction in the LOB is achieved through footwall drives excavated in the Arkose rock formation while development and haulage tunnels are excavated in the Nchanga Red Granite a basement of the Nchanga's Lower roan group. Overlaying the LBS is the friable banded sandstone (BSS) which is a very weak semi-coherent rock type. The BSS is comprised of two forms which are the Upper Sandstone (BSSU) and Lower Sandstone (BSSL) these are split by a special kind of pink quartzite and shale marker [34]. While the TFQ, Dolomitic Schist (Dolschist) and Upper Banded Shale (UBS) all overlay the BSS [35]. The TFQ predominates much of the UOB while the UBS formation exists in the upper part. Even though the TFQ is characterised by its moderately competent state it has long been exposed to considerable folding and occurs in a profoundly jointed structure. The TFQ in its heavily jointed structure cannot be compared to the UBS which is significantly

weaker. The Dolschist, on the other hand, is slightly more competent and less jointed as compared to the UBS [36]. Mechanically, lithologies in the UOB exist in the form of asymmetric extensive folds which are not displayed below in the lithologies overlain by the TFQ. Ore extraction in the UOB is achieved through tunnels excavated in the footwall mainly comprised of the BSS which acts as the LOB faulting effect absorber and provides the UOB folding lower limit. The significant folds which occur in the UOB are the northern fold and overthrust fold the former affects most of the deeper sections while the latter affects the upper section of the UOB [35,37]. The adverse ground conditions as well as folding in the UOB present a significant challenge to efficient tunnel design and ore extraction.

7.3.2 Long-term deformations at the Nchanga mine

The NUG tunnel development is excavated in the geological footwall at a depth 700 m which is the current mining level. Tunnel excavation faces significant challenges due to the NUG adverse and high stressed ground conditions. The UOB rock mass forms an inclined bedding structure that deforms and shears under the high-stress state effect. Even though the tunnel support structures are installed during tunnelling in this high-stress rock mass significant deformations tend to occur. tunnelling in this high-stress surrounding rock mass induces stress redistribution which leads to squeezing related deformations. Squeezing related deformations can be observed through floor heave, significant sidewall and roof extrusion characterised buckling and roof sagging which causes shotcrete liner distortion and flaking (Figure 7-2).

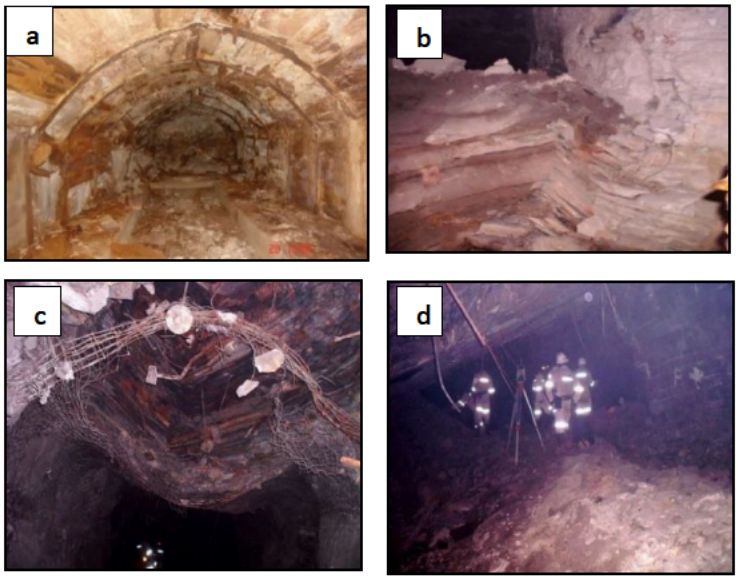

Figure 7-2. Long-term deformation associated with squeezing (a) Collapsed tunnel, (b) side wall buckling, (c) roof sagging and (d) floor heave (Photos taken by the author).

7.3.3 Support structure employed at Nchanga mine

The effective tunnel support structure installation requires analysis of the stress redistributions because of the UOB high-stress state. In conventionally supported tunnels the stress redistribution on the sides is usually transferred to the floor the effect observed through significant floor heave. However, the ground control support structures employed in the NUG tunnels ineffectively control floor heave which is a combination of conventional bolting, meshing and lacing. The bolts are mostly fully grouted rebar (2.0 m and 2.4 m) installed in horseshoe-shaped tunnels (3.7 m × 4.5 m). However, permasetts, Hydra bolts a friction bolt similar to swellex bolt but less expensive, Tendon straps and mesh are the most commonly employed. The installation of mesh within footwall tunnels and crosscuts is mostly preferred to shotcrete because it is efficiently installed. Additional support elements installed are 16 mm U shaped steel bars/steel arch sets, 4 mm wire mesh coupled with shotcrete and rock reinforcements (Table 7-1).

Table 7-1. Support elements employed at the Nchanga Underground [18,19]

Rock formation	Support system	Compliance
BSS, highly fissured zones	Resin injection or fore poling, elliptical steel setts, 100 – 200 mm fibrecrete	Steel sett every 1 m advance
LBS, TFQ, UBS/TFQ contact, minor fissure zone	2.4 m permasetts (0.5 - 1.0 m spacing), weldmesh, wetcrete (100 - 150 mm) Shotcrete arch setts	Permasetts and weldmesh within 1.0 m of the face, wetcrete 5 m from the face. 1 m face advance
UBS, DolSch	2.4 m permasetts (0.5 - 1.0 m spacing), weldmesh, wetcrete (75-100 mm)	Permasetts and weldmesh within 1.0 m of the face, wetcrete 5 m from the face.
TFQ	2.4 m permasetts (1.0 m spacing), weldmesh, wetcrete (50 mm)	Permasetts and weldmesh within 1.0 m of the face, Wetcrete 10 m from the face.
Arkose	Permasetts (1.2 m spacing)	Permasetts within 1.0 of the face.
Nchanga Red Granite	Spot bolting	

The UOB footwall tunnel support structure design considers fibrecrete/mesh reinforced shotcrete (200 mm) and split set bolts (2.4 m) at 0.6 m spacing from the floor. In addition, permasets (2.4 m) at 1.0 m spacing, grouted rock bolts (2.4 m) coupled with fibrecrete (200 mm) are usually installed in the dry/wet rock mass conditions (Figure 7-3).

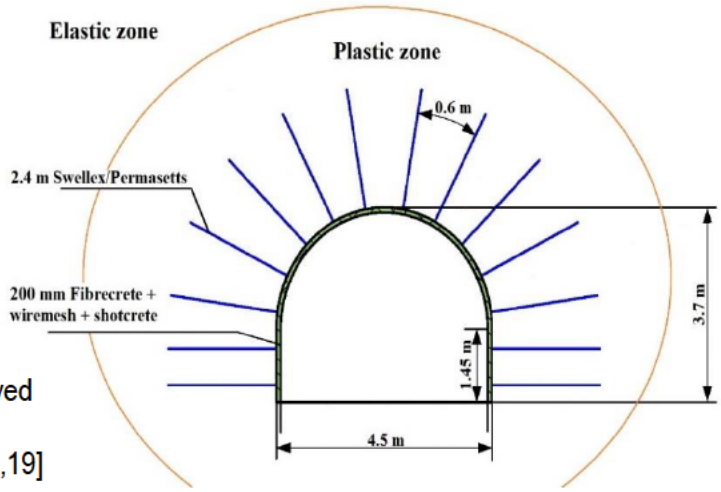

Figure 7-3. Current employed tunnel support structure at Nchanga Underground [18,19]

However, these support structure can only provide effective deformation restraint around the tunnel roof and sidewalls which is observed when deformation shifts to the unsupported floor in the form of heave (Figure 7-4). Hence, the current support structure installation within the NUG tunnels is not adequate to effectively control floor heave. Figure 7-4 illustrates a numerical estimation of the plastic flow extension around the unsupported and supported NUG tunnel which is usually beyond the rock bolts (permasetts) reach for the unsupported case. It shows that the bolt-reinforced zone cannot be anchored to the competent rock mass or stratum (elastic zone) beyond the plastic flow. The current support structure as so far proved to be ineffective in restraining tunnel convergence due to squeezing at the NUG [38]. Hence, in this study, an analytical solution is employed to analyze convergence and suggest the appropriate support structure to effectively restrain NUG tunnel convergence.

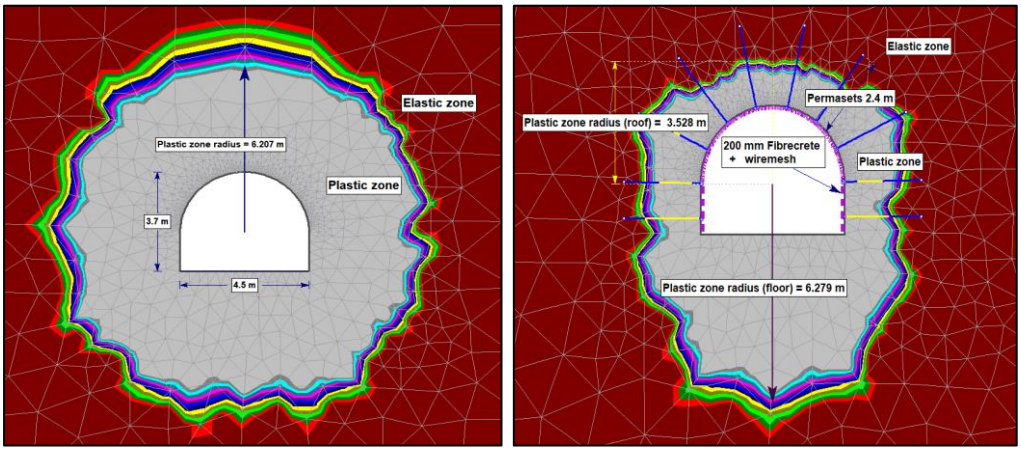

Figure 7-4. Plastic zone extension (a) unsupported tunnel case and (b) supported tunnel case

7.3.4 Support system strategy in squeezing ground

Determination of the optimized and appropriate tunnel support structure the GRC-SCC interaction is required which considers tunnel convergence and the load on the structures. These support structures and their capacity are directly dependent on the extension of the plastic flow usually extensive in poor rock masses. In such cases, conventional rock bolts with limited length tend not to be effectively anchored into the elastic stable stratum. In such conditions, they are effective when installed in a closely spaced arrangement which induces an unnatural arch in the failure zone (Figure 7-5).

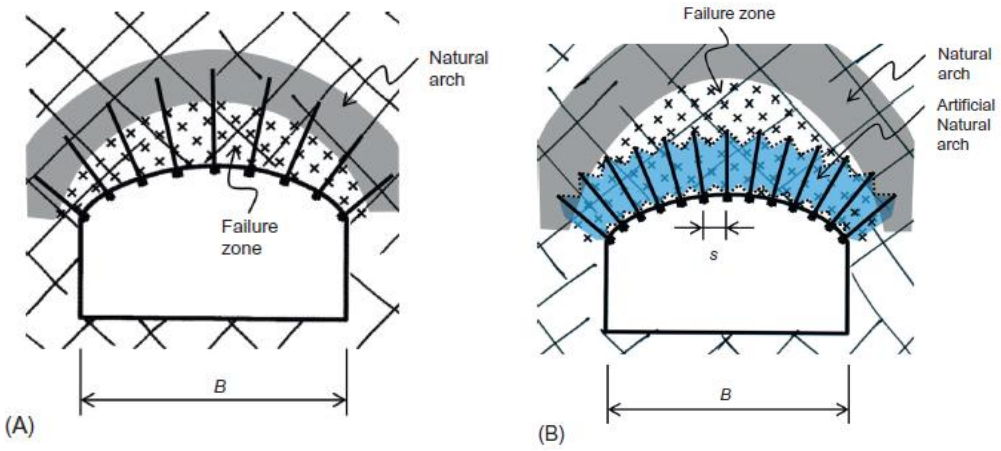

Figure 7-5. Rock bolt setup (A) normal spaced pattern and (B) tightly spaced pattern [39]

However, in exceedingly poor rock masses the most effective approach is by employing an integrated support structure comprised of steel sets, shotcrete and cable bolts capable to anchor into the stable elastic zone (Figure 7-6). This integration is most effective in restraining rock dilation in delayed plastic extension experienced around tunnels in squeezing ground conditions.

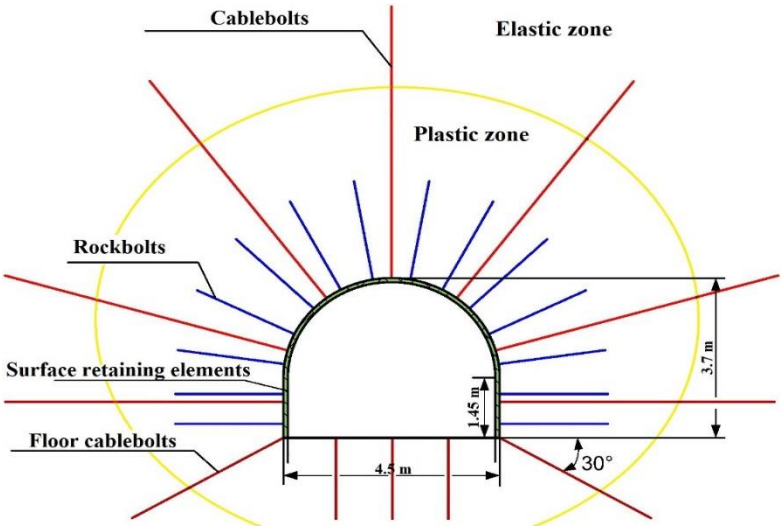

Figure 7-6. Composite support structure design

7.4 Tunnel convergence analysis

Determination of the appropriate tunnel support structure design in the NUG we employ a recently proposed analytical solution [27]. Which considers the Lode angle dependence and non-circular tunnels in a hydrostatic stress field.

7.4.1 Yield criterion description

In this section, the DP yield criterion (Eq. (7-1)) is reformulated in the spherical coordinate system by incorporating the Lode angle parameter to account for the intermediate principal stress strengthening effect on the rock mass.

$$f = \alpha_{\varphi} I_1 + \sqrt{J_2} - k_{\varphi} \tag{7-1}$$

Where α_φ and k_φ are material constants, J_2 is the second invariant of the stress deviator tensor and I_1 is the first invariant of the stress tensor defined by:

$$I_1 = \sigma_1 + \sigma_2 + \sigma_3 \tag{7-2}$$

$$J_2 = \frac{1}{6}[(\sigma_1 - \sigma_2)^2 + (\sigma_2 - \sigma_3)^2 + (\sigma_1 - \sigma_3)^2] \tag{7-3}$$

$$\alpha_\varphi = \frac{2\,sin\,\varphi}{\sqrt{3}(3 - sin\,\varphi)} \tag{7-4}$$

$$k_\varphi = \frac{6\,ccos\,\varphi}{\sqrt{3}(3 - sin\,\varphi)} \tag{7-5}$$

Where σ_1, σ_2 and σ_3 represents the major, intermediate and minor principal stresses respectively. Whereas c and φ are the cohesion and internal friction angle respectively. Rock mass under stress is subjected to elastic behavior exemplified by Hooke's law in which the change in stress-strain depends on the elastic modulus (E) and ν. Further on, the behaviour extends into plasticity represented by elastoplastic constitutive equation governed models. The plastic flow attained from plasticity is controlled by a parameter described by the hydrostatic stress-von Mises equivalent stress ratio [40]. The Lode angle related to the third invariant of the stress tensor deviator (J_3) on the deviatoric plane will affect this plastic flow [41]. The Lode angle (θ) on this plane is represented by a coordinate system associated with the three stress invariants (p, q, r)). This normalized Lode angle obeys the condition ($-1 \leq \bar{\theta} \leq 1$) and defined in different forms [42,43]. Additionally, in-plane stress state ($\sigma_3 = 0$) it can be expressed by the relation Eq (7-6) below.

$$\cos\left[\frac{\pi}{2}(1-\bar{\theta})\right] = \frac{2\sigma_2 - (\sigma_1 + \sigma_3)}{(\sigma_1 - \sigma_3)} = \xi \tag{7-6}$$

The DP yield criterion (Eq. (7-1)) is expressed in terms of the radial stress (σ_r) stress, hoop stress (σ_θ) and the Lode angle parameter as:

$$\frac{(\sigma_r + \sigma_\theta)}{2}\left[\left(1 + \frac{\left(\cos\left[\frac{\pi}{2}(1-\bar{\theta})\right]\right)^2}{3}\right)^{0.5} - \frac{\alpha_\varphi\left(\cos\left[\frac{\pi}{2}(1-\bar{\theta})\right]\right)}{2}\right] - \frac{3\alpha_\varphi(\sigma_r + \sigma_\theta)}{2} - k_\varphi = 0 \tag{7-7}$$

7.4.2 Ground reaction curves

During the excavation of tunnels, they tend to occur peripheral convergence towards its centre attributed to the elastic behaviour of the surrounding rock mass. When this convergence extends it satisfies the yield criterion as a result plastic flow emanates which is represented by the plastic radius (R_p). This extension due to the yield criterion satisfaction occurs when the internal support pressure is less the critical pressure. The critical pressure, on the other hand, has an equal magnitude with the elastic-plastic interface stress (σ_{RP}) expressed by:

$$\sigma_{RP} = \sigma_0 - \frac{3\alpha_\varphi\sigma_0 + k_\varphi}{\left(1 + \frac{\left(\cos\left[\frac{\pi}{2}(1-\bar{\theta})\right]\right)^2}{3}\right)^{0.5} - \frac{\alpha_\varphi\left(\cos\left[\frac{\pi}{2}(1-\bar{\theta})\right]\right)}{2}} \tag{7-8}$$

If σ_{RP} is less than the internal support pressure no failure of the rock mass arises and is associated with the rock mass elastic convergence (u_e).

$$u_e = \frac{1+v}{E}(R_q)(\sigma_0 - \sigma_R) \tag{7-9}$$

Where R_q is the equivalent radius of a tunnel attained by employing the equal area method [27]:

$$R_q = \left[\left(\frac{\frac{1}{2}(\pi R^2 + LR)}{\pi}\right)^{0.5}\right] \tag{7-10}$$

Where R is the radius of the horseshoe-shaped tunnel arc, π is the radial constant and L is the tunnel wall height. When σ_{RP} is greater than the internal support pressure failure arises and R_p develops by adhering to the conditions $\left(R_p = R_q, \sigma_R = \sigma_{RP}\right)$:

$$R_p = R_q \left[\frac{\sigma_{RP} + \left(\frac{\rho}{\beta}\right)}{\sigma_R + \left(\frac{\rho}{\beta}\right)}\right]^{\frac{1}{\beta}} \tag{7-11}$$

Where:

$$\beta = \frac{6\alpha_\varphi - \left(1 + \frac{\left(\cos\left[\frac{\pi}{2}(1-\bar{\theta})\right]\right)^2}{3}\right)^{0.5}}{\left(1 + \frac{\left(\cos\left[\frac{\pi}{2}(1-\bar{\theta})\right]\right)^2}{3}\right)^{0.5} - \frac{\alpha_\varphi\left(\cos\left[\frac{\pi}{2}(1-\bar{\theta})\right]\right)}{2} - 3\alpha_\varphi} \tag{7-12}$$

$$\rho = \frac{2k_\varphi}{\left(1 + \frac{\left(\cos\left[\frac{\pi}{2}(1-\bar{\theta})\right]\right)^2}{3}\right)^{0.5} - \frac{\alpha_\varphi\left(\cos\left[\frac{\pi}{2}(1-\bar{\theta})\right]\right)}{2} - 3\alpha_\varphi} \tag{7-13}$$

When $R_p = R_q$ the surrounding rock mass undergoes plasticity and tunnel convergence associated with it is estimated by:

$$u_r = \frac{1+v}{E}\left(\frac{R_p^2}{R_q}\right)\frac{3\alpha_\varphi\sigma_0 + k_\varphi}{\left(1+\frac{\left(\cos\left[\frac{\pi}{2}(1-\bar{\theta})\right]\right)^2}{3}\right)^{0.5}} - \frac{\alpha_\varphi\left(\cos\left[\frac{\pi}{2}(1-\bar{\theta})\right]\right)}{2} \quad (7\text{-}14)$$

In this section, the convergence and plastic extension estimated by the analytical formulations (Eq. (7-9), (7-11) & (7-14)) are verified using numerical simulation results (Figure 7-7 & Table 7-2). Which employed the actual rock mass and geometrical parameters attained from the NUG (Table 7-3).

.

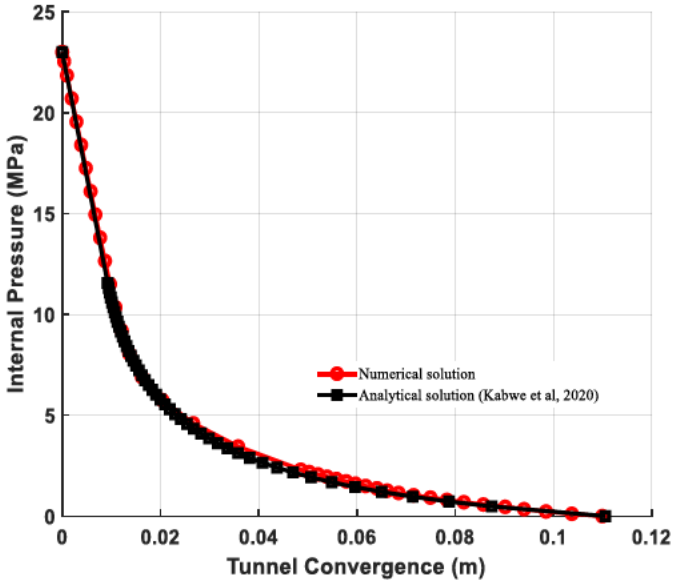

Figure 7-7. Analytically determined ground response verification

Figure 7-8 illustrates the results attained which indicate that the analytical solution is capable of estimating convergence reliably. Additionally, Table 7-2 presents the results of tunnel convergence and plastic flow radius with θ, whereas θ = 6°is the determined optimum value.

Table 7-2. Plastic extension and convergence estimations

	$\theta(°)$				Numerical solution
	15	12	9	6	

Maximum plastic extension (m)	5.16	5.60	5.88	6.21	6.31
Maximum tunnel convergence (m)	0.071	0.082	0.090	0.111	0.110

Table 7-3. Ground reaction rock mass and geometrical parameters

Parameters		**Mohr coulomb**		**Drucker-Prager**	
Specific weight (kN/m^3)	27	c (MPa)	1.28	Tensile strength (MPa)	0.05
Depth (m)	700	φ (°)	26.6	α_φ	0.4478
R_q (m)	2.15	UCS (MPa)	1.15	k_φ	1.553
v	0.20	E (MPa)	3193	ϑ (°)	0
Global strength (MPa)	4.38	v	0.20		

7.4.3 Longitudinal displacement profile

Estimation of the GRC and plastic flow around the tunnel is based on a two-dimensional (2D) analysis. However, the LDP is required to establish the relative position of the tunnel face and support structures. It is determined by a three-dimensional (3D) analysis, in this case, the LDP solution [44] in an EPP rock mass is adopted. Based on this solution the tunnel face convergence (U_{rf}) is determined by:

$$U_{rf} = \left(\frac{U_{rm}}{3}\right) e^{-0.15\left(\frac{R_m}{R}\right)} \tag{7-15}$$

Where R_m maximum plastic radius, U_{rm} is the maximum tunnel displacement and convergence ahead of the face $(X < 0)$ and behind the face $(X > 0)$ are defined by Eqs. (7-16) and (7-17) respectively:

$$U_{rX} = \left(\frac{U_{if}}{U_{rm}}\right) e^{\left(\frac{X}{R}\right)} \tag{7-16}$$

$$U_{rX} = 1 - \left(1 - \frac{U_{if}}{U_{rm}}\right) e^{\left(\frac{-3X}{R} \Big/ \frac{2R_m}{R}\right)} \tag{7-17}$$

Where U_{rX} is the tunnel convergence at distance (X) and Figure 7-8 shows the estimated LDP.

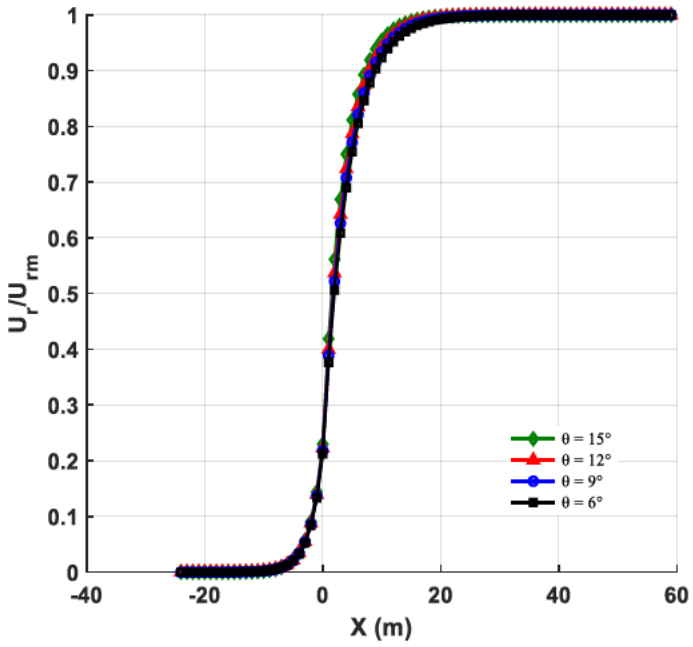

Figure 7-8. Longitudinal displacement profile of the Nchanga Underground tunnel

It is drawn from these LDP curves that the maximum deformation is attained at 25 m behind the face and least at 10 m ahead of the face. The results of the scaled convergence, maximum plastic radius, face and tunnel deformation attained are presented in Appendix A (Tables A1 & A2).

7.5 Tunnel support analysis

Support structure installation in tunnels usually takes place after excavation when a certain amount of convergence has already occurred. The relation of the pressure provided by the support installation with the tunnel convergence is usually determined by the SCC.

7.5.1 Support reaction curves

Support pressure provided by support elements can restrain convergence and plastic flow extent around tunnels. The support element stiffness (K_s) and the distance behind the face at which support elements are installed is an important aspect in tunnel convergence restraint and the rock mass-support element interaction. This rock mass-support element interaction is determined by the employment of the GRC and SCC. On the other hand, the LDP determines the tunnel convergence (U_{io}) at a specific distance behind the face at which support elements are installed. The installed support elements tend to yield during stages of excavation and this yielding extent $\left(U_{iy}\right)$ is determined by:

$$U_{iy} = U_{io} + U_{im} = U_{io} + \frac{p_{smax}}{K_s} \tag{7-17}$$

Where U_{im} is the support elastic deformation and p_{smax} represents the support structure capacity. When the GRC and SCC are used they tend to intersect at a point that determines the equilibrium point. This point verifies the tunnel convergence of a lined tunnel and the pressure provided by the support installed. this, in turn, estimates the support safety coefficient (FS):

$$FS = \frac{p_{smax}}{p_{se}} \tag{7-18}$$

Support elements with the safety coefficient more than the allowable limit $(FS \geq F_{s\,min})$ are considered appropriate for a tunnel. The critical aspect of tunnel design in squeezing ground conditions is the sequence and installation timing of support elements and to avert overload or failure but able to maintain a safe working environment. Support structures are installed at the earliest time to provide safety and be delayed sufficiently to avert support load build-up. Early tunnel support structure installation results in support buckling, support failure and extension of the plastic flow.

7.5.2 Construction of the support characteristic curves

This section considers the GRC and SCC interaction to determine the appropriate support structure capacity for tunnels in the NUG squeezing ground. This interaction is dependent on the LDP which allows support structure installation at distance behind the face.

7.5.2.1 Current support reaction curves

The stiff support structures employed at the NUG cannot allow the redistribution of stress (yielding principle). Also, the installed rock bolts cannot be anchored in the stable stratum beyond the plastic flow radius. Therefore, in this section, the current support structure capacity is evaluated in the short-term and long-term. A horseshoe-shaped tunnel excavated subjected to isometric stress field is assumed in this analysis. Its ground response is assumed to be instantaneous as such neglects the time-dependent (long-term) effect. A flaw that greatly affects the accuracy of the analysis in that an in-situ scale tunnelling is influenced by the rock mass time-dependent behaviour. However, to account for this tunnel behaviour it is observed that time-dependent parameter estimation without consideration of the creep behaviour is cumbersome. Therefore, a pragmatic approach considering the rock mass strength degradation overtime is undertaken in which the time-dependent strength parameters are attained from the reduction of the time-independent parameters (Table 7-4).

Table 7-4. Short-term and long-term strength parameters

Strength parameter	**Short-term**	**Long-term (67%)**
c (MPa)	1.28	0.86
φ (°)	26.6	17.8
E (MPa)	3193	2139

It is worth noting that the long-term strength parameters are applied to the plastic extension since the long-term change due to deformation is a measure of plastic yielding. Ideally, the installation of support

structures near the tunnel face is more effective to provide underground safety. It is determined in Section 3.4 that the appropriate support installation distance from the face is 2 m which corresponds to a tunnel convergence of 0.03 m (Figure 7-9). It is also drawn from the illustration that the SCC intersects the short-term rock mass reaction curve at a high equilibrium point. This point corresponds to 3.66 MPa support pressure which represents the capacity during the support installation.

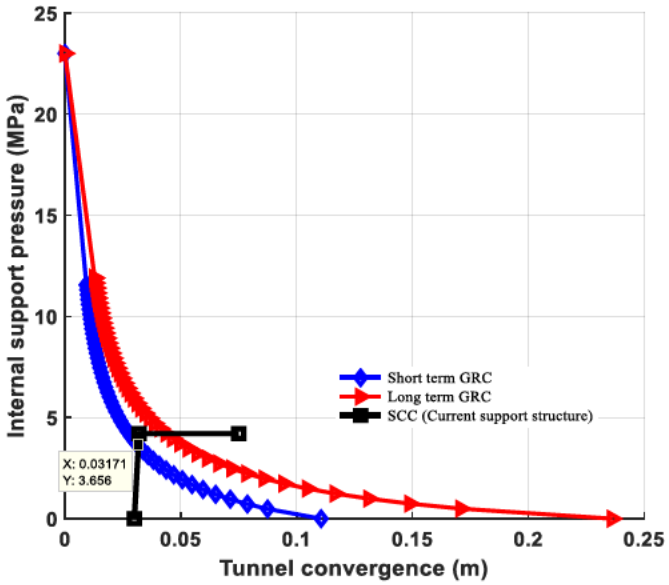

Figure 7-9. Ground reaction interaction with current support structure

This point can only be achieved if the SCC intersects the GRC before either of these curves have proceeded too far. Late installation of the support entails rock mass deformation to an extent that the failed material is irreversible. However, if the support structure capacity is inadequate, it yields before the GRC is intersected. In Figure 7-9 it is also shown that the current support structure SCC and short-term GRC interaction attribute to a safety coefficient of 1.2. The support capacity provided by this structure is lower than the required capacity for the long-term GRC. Therefore, the installation of this support structure in tunnels that exhibit long-term behaviour is susceptible to yielding. Hence, a feasible solution to this is the deferral of the support structure installation at 4 m behind the face which raises the long and short-term safety coefficient. However, this approach is unrealistic results in an acceptable level of risk to underground personnel as such the yielding support structure concept is adopted.

7.5.2.2 Proposed support reaction curves

The elastic deformation of the installed support in response to the tunnel convergence is dependent on the in-situ stress level, rock mass behaviour and support properties. It is worth noting that the rock reinforcement (rock and cable bolts) capacity cannot be effectively accounted for because its capacity is considered equivalent to the internal pressure. However, length can be determined by the radius of the plastic flow, this gives a rough estimation of how far they can be anchored into the stable elastic stratum. In this section, the tunnel support capacity of the surface retaining elements will be determined based on the allowable wall to wall strain ($\varepsilon_{\%}$). This is highly dependent on ether mining or civil tunnel design of which the former has a 2% allowable closure while the latter has no allowable closure. According to [45], an excess of $\varepsilon_{\%}$= 1% results in tunnel instability and difficulties in support structure installation. However, [46] later confirmed that some tunnels which experienced $\varepsilon_{\%}$= 5% did not exhibit instability. Hence, the 1% limit is an initial indication of tunnel instability signifying an immediate appropriate support structure installation to restrain further tunnel closure. Determination of the required support pressure (σ_i) requires the rock mass strength ($\sigma_{cm} = 2c\cos\varphi/(1-\sin\varphi)$) - stress (σ_0) ratio estimation. In the short-term, u_r attained for this tunnel is 0.11 m, translates to 5.2% wall to wall strain whereas the long-term records 0.24 m (11%) according to Eq. (7-19).

$$\varepsilon_{\%} = \frac{u_r}{R_{EQ}} \tag{7-19}$$

Based on the postulate [45] [46], the estimated 5.2% is unacceptable and appropriate support elements are required to avert further convergence (Figure 7-10).

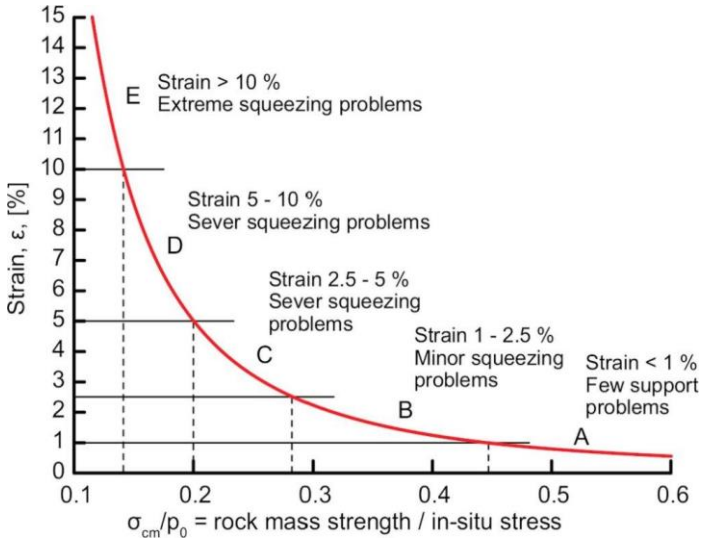

Figure 7-10. Expected strain and the rock mass strength to in-situ stress [45].

This is achieved by installing a support structure behind the tunnel face to restrict $\varepsilon_{\%}$ to an acceptable level. Considering the 2% allowable strain from Figure 7 in [47], it is observed that σ_{cm}/σ_0 = 0.086. Hence, an internal support pressure of σ_i/σ_0= 0.25 ≈ $\sigma_i/23$ is appropriate for tunnel stability. It is drawn from the analysis above that the least support pressure required is σ_i ≈ 5.75 MPa. This pressure can be attained from the stiffness and capacity estimation of the appropriate NUG tunnel support structure from simplistic analyses (Appendix B). The structure proposed from this analysis is the STSCCB (steel sets + shotcrete + cable bolts). This consists of yielding steel ribs with sliding joints (Toussaint-Heintzmann profile - TH 44/58-curve # 6), friction bolts (Swellex), bulbed and grouted cable bolts (JENNMAR 63 T sumo) and shotcrete (BN 450 shotcrete) designed in a horseshoe profile (Figure 7-11).

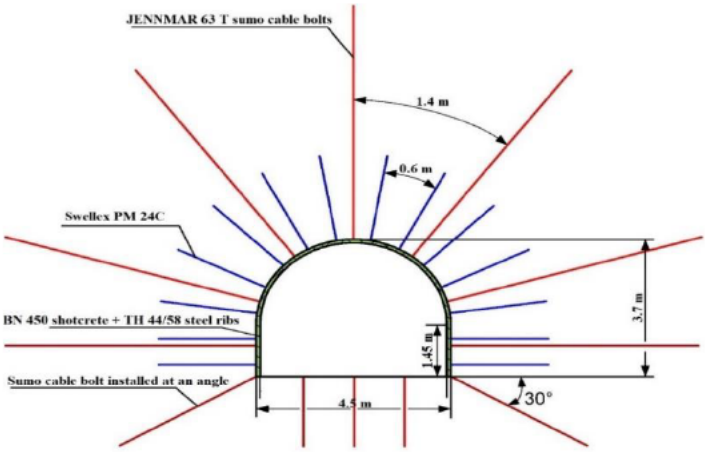

Figure 7-11. Proposed support structure design for the Nchanga

Figure 7-9 illustrates that the SCC of the current support structure indicates failure in the long-term and an unacceptable short-term safety coefficient. Hence, its employment is ineffective to restrict both short-term and long-term convergence. In this section, the relation between tunnel convergence and installed STSCCB location is estimated based on the LDP attained for a normalized plastic flow radius of 6.44 m (Appendix A; Table A2). Figure 7-12 below illustrates the SCC of the STSCCB installed at 2 m behind the advancing face results in an appropriate short-term and long-term safety coefficient. The safety coefficient is increased from 0.8 to 1.45 in the short-term and 1.15 to 2.23 in the long-term (Table 7-5). This shows that the STSCCB is appropriate and effective in restraining tunnel convergence both in the short-term and long-term.

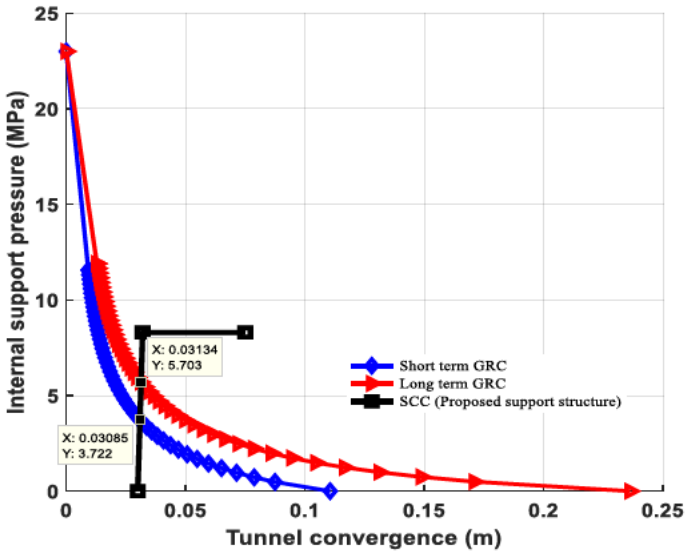

Figure 7-12. Ground reaction interaction with suggested support

Table 7-5. Current and proposed support structure safety coefficient

Safety coefficient (*FS*)		
GRC	**Current support structure**	**STSCCB**
Short-term	1.15	2.23
Long-term	0.8	1.45

7.5.3 Numerical verification of the proposed support structures

In this section, the numerical simulation is conducted in the 2D RS^2 to evaluate the tunnel stability and compare the effectiveness of the current and proposed support structures. The plane strain model is established using the actual geometrical standards set at of the NUG. The model dimension is 40 × 40 m with a 4.5 m × 3.7 m tunnel while boundary conditions of the model are set to restrain the vertical movement during the loading process and boundary displacements at the side walls (Figure 7-13). However, in the model, the initial stress acting on the tunnel boundary is assumed to be hydrostatic with the mean in-situ stress (23.3 MPa). Input parameters for the numerical simulation include the rock mass and support element mechanical parameters presented in Table 7-3, Table 7-6 & Table 7-7.

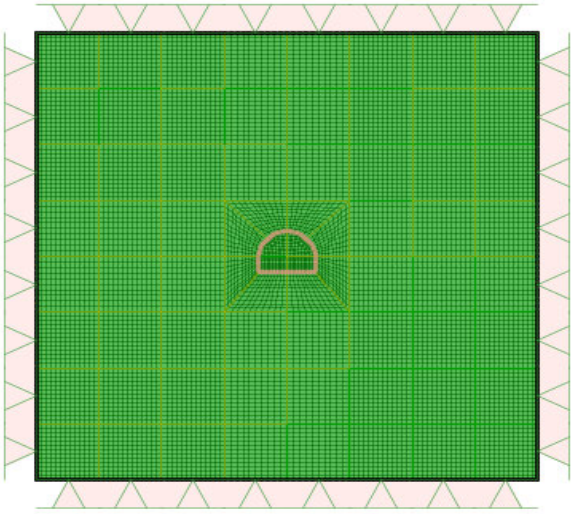

Figure 7-13. Boundary condition of the numerical model

Table 7-6. Current support element parameters

Support element	Elastic modulus (MPa)	Poisson's ratio	Compressive strength (MPa)	Tensile strength (MPa)
Permasets	200000	0.25		0.1
Wire mesh	200000	0.25	400	400
Shotcrete	30000	0.15	40	3
Steel sets	200000	0.25	400	400

Table 7-7. Proposed support element parameters

Support element	Elastic modulus (MPa)	Poisson's ratio	Compressive strength (MPa)	Tensile strength (MPa)
Swellex PM24C	207000	0.25		0.24
BN 450 concrete	36000	0.2	44	5
TH 44/58 steel ribs	200000	0.25	400	400
JENNMAR 63 T Cable bolts	207000	0.2		0.635

7.5.4 Numerical results

In this section, the results of the tunnel deformation and plastic flow around the unsupported, current supported and proposed supported tunnel case is presented. The total deformation estimated within the unsupported tunnel is 120 mm which translates to 5.6% wall to wall strain. This estimation comprises of the roof, wall and floor heave as 99 mm, 106 mm and 120 mm respectively. The numerical results attained from a tunnel installed with the current support structure shows a reduction in roof, wall and floor deformations at 40% (59 mm), 35% (69 mm) and 10% (108 mm) respectively (Figure 7-14). It is drawn from this analysis that the current support structure does not provide adequate tunnel stabilisation. The

deformation attained after installing the current support structure translates to unacceptable 4.8% wall to wall strain with floor heave (no significant reduction) as a major contributor. Therefore, the proposed support structure is installed to considerably reduce this wall strain to the allowable limit. Employing the proposed support structure shows a significant reduction in the wall to wall strain (Figure 7-15 & Table 7-8).

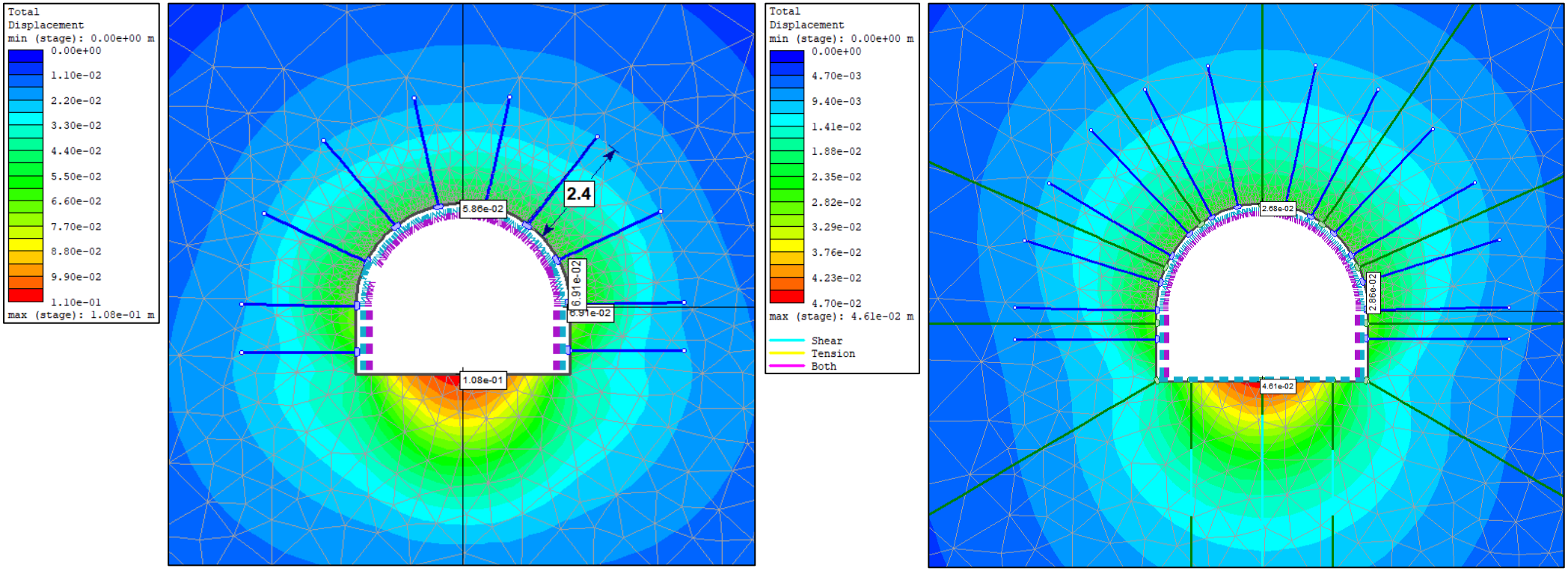

Figure 7-14. Tunnel convergence (a) current supported (b) proposed supported

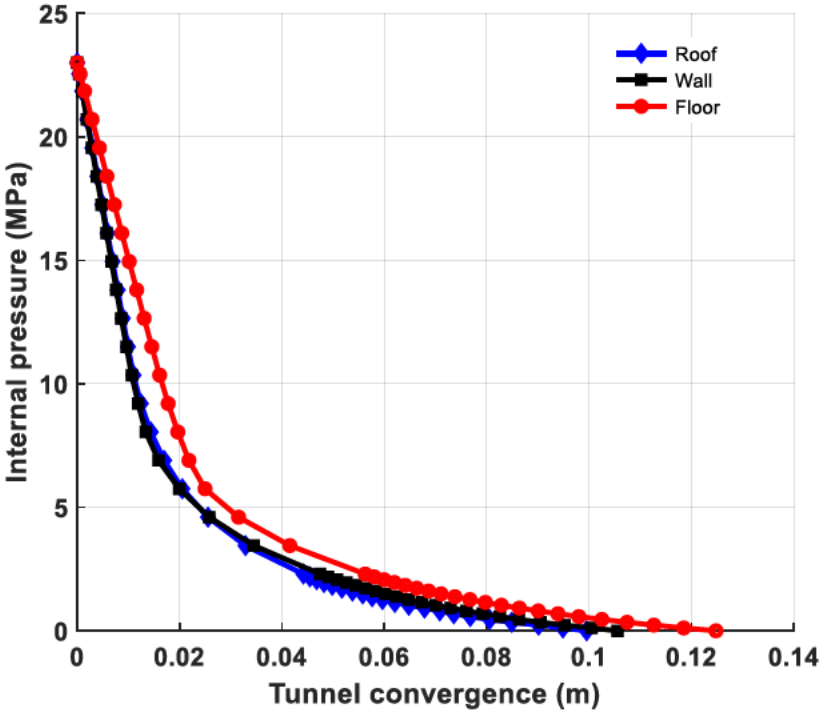

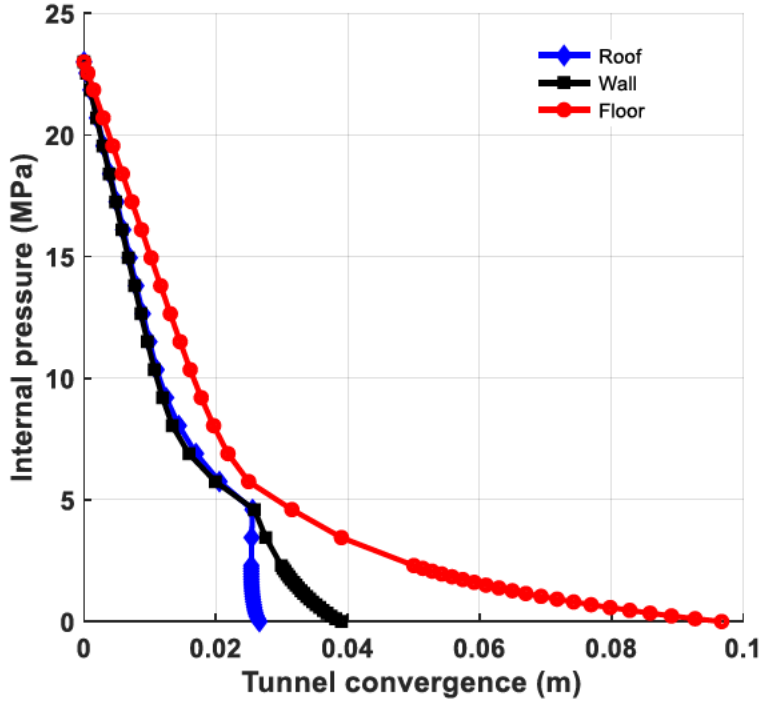

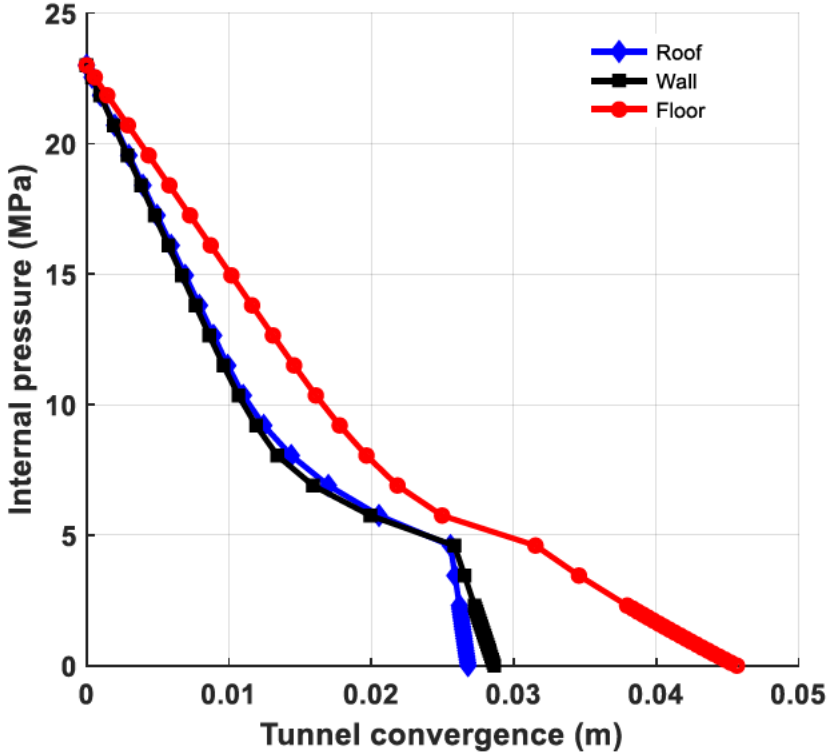

Figure 7-15. Tunnel ground response (a) unsupported (b) current supported and (c) proposed supported.

Table 7-8. Tunnel wall strain

	Short-term			**Long-term**		
	Unsupported	Current support structure	STSCCB	Unsupported	Current support structure	STSCCB
u_r (m)	0.13	0.11	0.046	0.24	0.22	0.044
ε (%)	5.6	4.8	2.0	11	10	2.0

The numerical analysis evaluates the practicability and efficacy of the proposed support structure. Through estimating deformation extent recorded from the monitoring points around the peripheral of the numerically simulated tunnel. Figure 7-16 shows these recorded deformations which depict extent into the surrounding rock mass. It is shown that the extent of deformation from the peripheral into the rock mass reduced when the current support structure is employed. Whereas, employing the proposed support structure shows further reduction with depth in the rock mass. This shows that the proposed support structure can further restrain rock dilation deep in the surrounding rock mass.

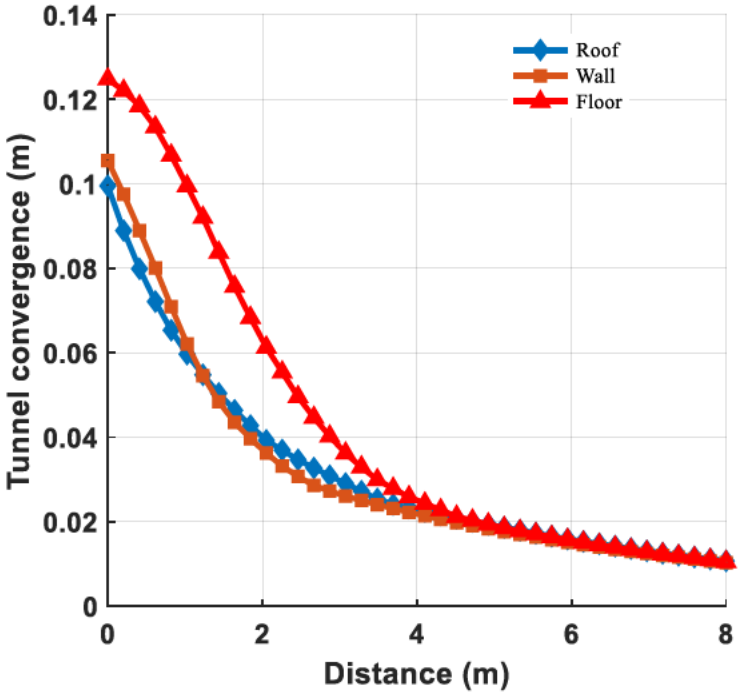

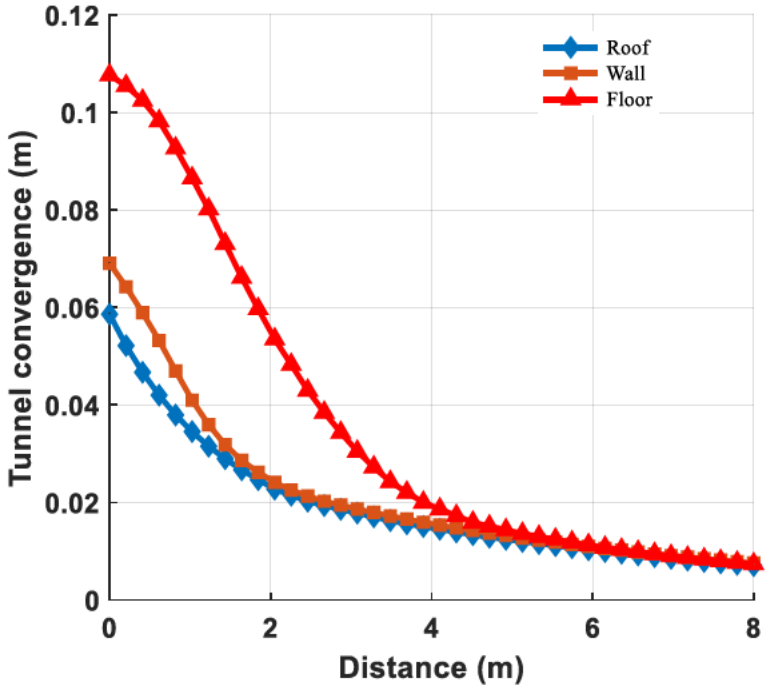

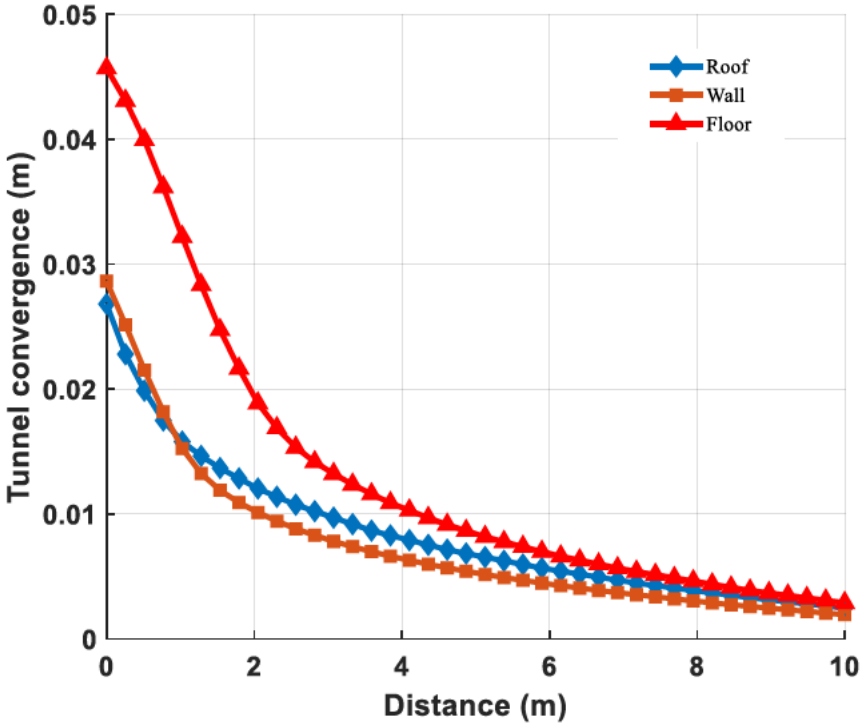

Figure 7-16. Tunnel deformation extent into surrounding rock mass (a) unsupported (b) current supported and (c) proposed supported.

Efficient tunnel support system design and installation require the understanding of the natural pressure arch which develops because of the tangential stress redistribution. This stress is oriented approximately parallel to the tunnel boundary in a tangential direction. During excavation, this boundary in unsupported tunnel experiences plastic flow defined by the plastic radius. Beyond the plastic flow region lies an intact stratum where stress extends to its maximum magnitude. Thereafter, further in the rock mass this stress steadily decreases to the level of the in-situ stress magnitude. The rock mass section subjected to a significant tangential stress increase experiences the maximum ground pressure which results in a natural pressure arch. When the tangential stress increases to reach its maximum the rock mass in this region yields due to shear or tension mechanism. Figure 7-17 illustrates the stress distribution around the unsupported tunnel excavated in the NUG rock mass. It is shown that the tangential stress achieved its maximum 5 m deep into the rock mass whereas current supported and proposed supported experience the maximum at 2.5 m and 1.2 m, respectively. It is drawn from the numerical results that the proposed supported tunnel experiences maximum tangential stress at a shallow depth into the rock mass signifies less plastic flow (Figure 7-18 & Figure 7-19).

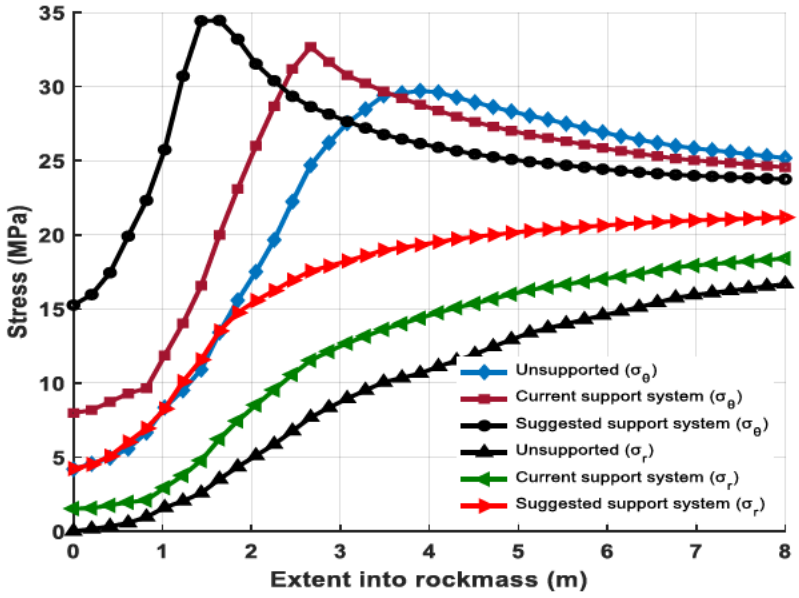

Figure 7-17. Tangential and radial distribution around the NUG tunnel

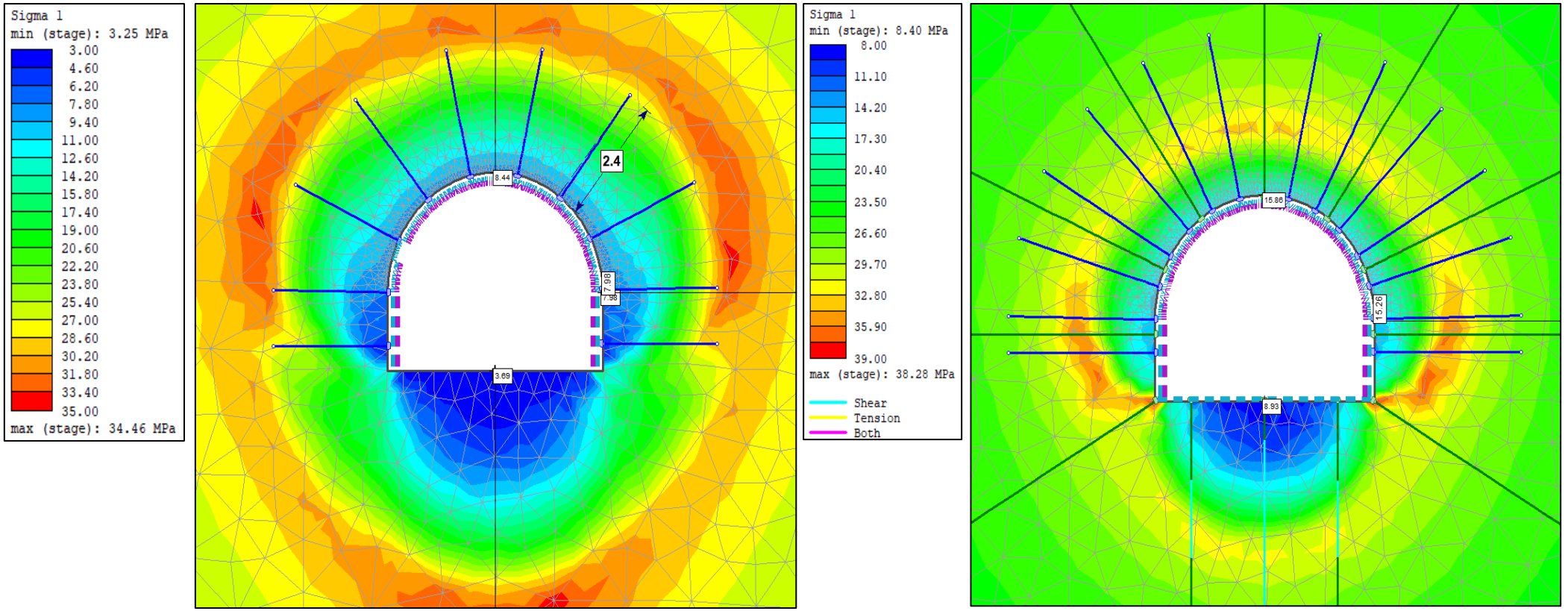

Figure 7-18. Tangential stress distribution (a) current supported tunnel (b) proposed supported tunnel

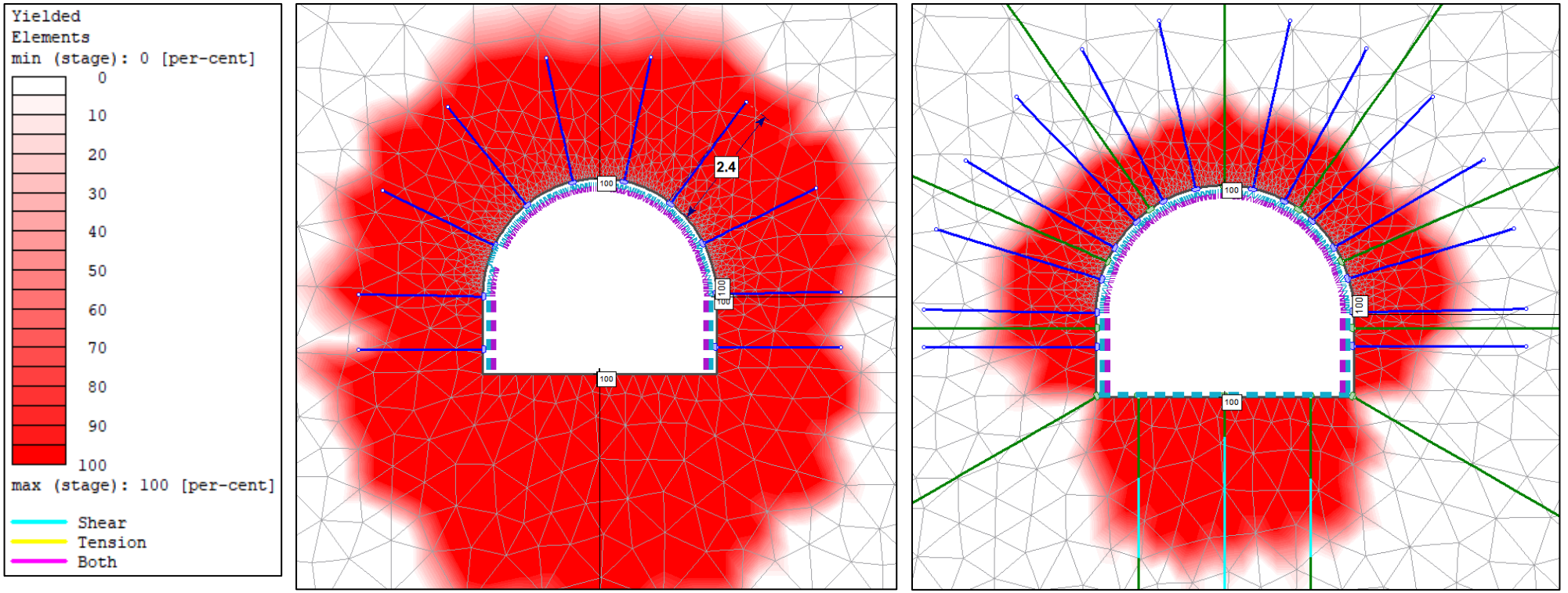

Figure 7-19. Plastic flow distribution around tunnels (a) current supported (b) proposed supported

7.6 Conclusion

The paper has shown that determining the support requirements for tunnelling through weak rock masses is not a trivial task but rather an iterative process. Integrating the newly proposed analytical solution and numerical simulation an adequate support structure design can be achieved for NUG tunnels in squeezing ground. The support structure-ground reaction interaction is conducted by using this proposed solution, it considers the effect of delayed support installation.

It is noteworthy that the solution does not associate squeezing with time rather the degradation of the rock mass strength characteristics. As such gives a preliminary insight of the tunnel response in the rockmass exhibiting squeezing mechanism.

The analytical GRC and LDP interaction assists in the determination of the appropriate time of support structures installation. This relationship verifies the long-term stability coefficient in squeezing grounds for the STSCCB system that is mounted at the right place and time behind the tunnel face. It is shown that the system constructed at tunnel convergence (0.03 m) indicates a higher safety coefficient of 2.23 in the short-term and 1.45 in the long-term. This shows that the structure is adequate for the effective restraint of both short-term and long-term convergence, most importantly that related to squeezing ground. Its design is based on the concept that allows for large deformation occurrence relating to that experienced in the NUG squeezing ground.

The STSCCB support structure significantly restrained tunnel convergence by 35% and 18% in the short-term and long-term. This reduction accounts for 2.0% wall to wall strain which lies on the allowable limit. The structure reduced the short-term deformation to approximately 27.8 mm (roof), 58.2 mm (wall) and 44.5 mm (floor) which accounts reduction of 72%, 45% and 63% respectively. Although employing this structure, tunnels experienced a certain degree of boundary deformation, it occurred within the allowable limit. Additionally, the support structure effectively restrained the plastic flow extension around the tunnel by approximately 34% in the short-term and 52% in the long-term.

Results from the numerical simulation show that the proposed support structure installation leads to a considerable tunnel convergence and plastic flow reduction. However, this outcome would be different if the support structure is installed too early (too close to the tunnel face) or too late (too far from the tunnel face). The paper reinforces that integrating the analytical solutions and numerical simulations are recommended for a reliable support structure design. The simplicity of the analytical solution may lead to the preliminary ground response estimation, while the numerical simulation is used to verify this ground reaction and the proposed support structure performance.

7.7 References

[1] Potvin, Y., & Hadjigeorgiou J. Ground support strategies to control large deformations in mining excavations. J South African Inst Min Metall 2008;108:397–404.

[2] Varden RP, Woods MJ. Design approach for squeezing ground. Proc. Int. Semin. Des. Methods Undergr. Min., Australian Centre for Geomechanics; 2015, p. 489–504.

[3] Karampinos, E., J. Hadjigeorgiou and PT. Management of squeezing ground conditions at LaRonde mine. 13th ISRM Int. Congr. Rock Mech., International Society for Rock Mechanics; 2015.

[4] Roache B. Mining in extreme squeezing conditions at the Henty mine Mining in extreme squeezing conditions at the Henty mine 2016:0–13.

[5] Aydan O, Akagi T, Kawamoto T. The squeezing potential of rocks around tunnels; Theory and prediction. Rock Mech Rock Eng 1993;26:137–63.

[6] Cristescu ND. Viscoplasticity of geomaterials. Visco-Plastic Behav. Geomaterials, Springer; 1994, p. 103–207.

[7] Ladanyi B. Time-dependent response of rock around tunnels. Anal. Des. Methods, Elsevier; 1995, p. 77–112.

[8] Gioda G, Cividini a. Numerical methods for the analysis of tunnel performance in squeezing rocks. Rock Mech Rock Eng 1996;29:171–93.

[9] Singh M, Singh B, Choudhari J. Critical strain and squeezing of rock mass in tunnels. Tunn Undergr Sp Technol 2007;22:343–50.

[10] Sterpi D, Gioda G. Visco-Plastic behaviour around advancing tunnels in squeezing rock. Rock Mech Rock Eng 2009;42:319–39.

[11] Pearson E. Thesis on the Blackwater Mine, Waiuta, New Zealand. University of Otago, Dunedin, 1946.

[12] Marlow P, and Mikula P. Shotcrete ribs and cemented rock fill ground control methods for stoping in weak squeezing rock at Wattle Dam Gold Mine 2013:133–48.

[13] Struthers MA, Turner MH, Mcnabb K, Jenkins PA. Rock Mechanics Design and Practice for Squeezing Ground and High Stress Conditions at Perseverance Mine. Proc Massmin 2000 2000;764:755–64.

[14] Fernandez F, Watt G, Ooi J. Strategic management for squeezing ground conditions at the Argyle Diamonds block cave project. Aust J Civ Eng 2012;10:193–206.

[15] Mercier-Langevin, F., & Hadjigeorgiou J. Towards a better understanding of squeezing potential in hard rock mines. Min Technol 2011;120:36–44.

[16] Karampinos E, Hadjigeorgiou J, Turcotte P, Mercier-Langevin F. Large-scale deformation in underground hard-rock mines. J South African Inst Min Metall 2015;115:645–52.

[17] Malan DF. Manuel Rocha medal recipient simulating the time-dependent behaviour of excavations in hard rock. Rock Mech Rock Eng 2002;35:225–54.

[18] Kabwe E, Yiming W. Production potential of Nchanga underground mine's collapsed blocks. Int J Sci Technol Res. 2015;4(10):289-301.

[19] AMC. Geological modelling and mineral resource evaluation, Nchanga underground Upper Orebody. Brisbane: 2007.

[20] Kirsch C. Die theorie der elastizitat und die bedurfnisse der festigkeitslehre. Zeitschrift Des Vereines Dtsch Ingenieure 1898;42:797–807.

[21] Panet M, Guenot A. Analysis of convergence behind the face of a tunnel: Tunnelling 82,

proceedings of the 3rd international symposium, Brighton, 7–11 June 1982, P197–204. Publ London: IMM, 1982. Int. J. Rock Mech. Min. Sci. Geomech. Abstr., vol. 20, Pergamon; 1983, p. A16.

[22] Carranza-Torres C, Fairhurst C. The elasto-plastic response of underground excavations in rock masses that satisfy the Hoek–Brown failure criterion. Int J Rock Mech Min Sci 1999;36:777–809.

[23] Lee YK, Pietruszczak S. A new numerical procedure for elasto-plastic analysis of a circular opening excavated in a strain-softening rock mass. Tunnelling and Underground Space Technology. 2008;23(5):588-99.

[24] Vrakas A, Anagnostou G. A finite strain closed-form solution for the elastoplastic ground response curve in tunnelling. International Journal for Numerical and Analytical Methods in Geomechanics. 2014;38(11):1131-48.

[25] Karakus M, Fowell RJ. Effects of different tunnel face advance excavation on the settlement by FEM. Tunnelling and Underground Space Technology. 2003;18(5):513-23..

[26] Kabwe E, Karakus M, Chanda E. Assessment of analytical solutions for time-dependent behavior of unlined tunnels. In Proceedings of 4th International Symposium on Underground Excavation 2018;1-9.

[27] Kabwe E, Karakus M, Chanda EK. Proposed solution for the ground reaction of non-circular tunnels in an elastic-perfectly plastic rock mass. Computers and Geotechnics. 2020;119:103354.

[28] Kabwe. E, Karakus. M, Chanda EK.. Fractal Derivative Constitutive Model for Time-Dependent Behaviour of Tunnels in Squeezing Ground. Comput Geotech 2020.

[29] Kabwe E, Karakus M, Chanda EK. Creep constitutive model considering the overstress theory with an associative viscoplastic flow rule. Computers and Geotechnics. 2020;124:103629.

[30] Pearson BN. The development and control of block caving at the Chingola division of Nchanga

consolidated copper mines limited, Zambia. Des Oper Caving Sublevel Stoping Mines, by DR Stewart 1981:211–23.

[31] Kabwe E. Optimal mining method selection for Nchanga's Upper Orebody using analytic hierarchy process and Yager's method. Trans Institutions Min Metall Sect A Min Technol 2017;126:151–62.

[32] Garrard P. The geology of the Chingola area, Zambia 1972.

[33] Binda PL. Stratigraphy of Zambian copperbelt orebodies. J African Earth Sci 1994;19:251–64.

[34] Haldane R. Biennial geological report for Chingola division. NCCM (Chingola Div) Geol Dept, Chingola 1974.

[35] Kabwe E. Mining Sequence Deformation and Failure Behaviour Analysis in the hangingwall and Orebody Rock Formations; A Continuum Approach. Geotech Geol Eng 2017;35.

[36] Diederix D. The geology of the Nchanga mining licence area. Unpubl Co Report—Nchanga Consol Copp Mines Ltd Chingola Div 1977;59.

[37] Kabwe E. Optimal mining method selection for Nchanga's Upper Orebody using analytic hierarchy process and Yager's method. Trans Institutions Min Metall Sect A Min Technol 2017;126.

[38] AMC Consultants Pty Ltd. Nchanga Mine Upper Orebody Mine Design-Konkola Copper Mines Plc. Brisbane: 2010.

[39] Charlie C. Li, Principles of rockbolting design, Journal of Rock Mechanics and Geotechnical Engineering. 2017;9(3):396-414,

[40] Li W, Liao F, Zhou T, Askes H. Ductile fracture of Q460 steel: Effects of stress triaxiality and Lode angle. J Constr Steel Res 2016;123:1–17.

[41] Bai Y, Wierzbicki T. A new model of metal plasticity and fracture with pressure and Lode dependence. Int J Plast 2008;24:1071–96.

[42] Lode W. Versuche über den Einfluß der mittleren Hauptspannung auf das Fließen der Metalle Eisen, Kupfer und Nickel. Zeitschrift Für Phys 1926;36:913–39.

[43] Wierzbicki T, Bao Y, Lee Y-W, Bai Y. Calibration and evaluation of seven fracture models. Int J Mech Sci 2005;47:719–43.

[44] Vlachopoulos N, Diederichs MS. Improved longitudinal displacement profiles for convergence confinement analysis of deep tunnels. Rock mechanics and rock engineering. 2009;42(2):131-46.

[45] Sakurai S. Displacement measurements associated with the design of underground openings. F. Meas. Geomech. Int. Symp., 1984, p. 1163–78.

[46] Chern JC, Yu CW, Shiao FY. Tunnelling in squeezing ground and support estimation. Proc. Reg. Symp. Sediment. Rock Eng. Taipei, 1998, p. 192–202.

[47] Hoek E. Tunnel support in weak rock. Keynote address, Symp. Sediment. Rock Eng. Taipei, Taiwan, 1998.

7.8 Appendix A: Longitudinal displacement profile estimated values

Table A 1. Scaled convergence at a normalized distance behind the tunnel face for different solutions

$\boldsymbol{\theta}(°)$	**15**	**12**	**9**	**6**
X (m)	$\boldsymbol{U_r/U_{rm}}$			
0	0.24	0.22	0.21	0.21
1	0.33	0.30	0.28	0.28
2	0.41	0.37	0.34	0.34
3	0.48	0.43	0.40	0.40
4	0.54	0.49	0.46	0.44
5	0.60	0.54	0.51	0.49

Table A 2. Maximum plastic radius, tunnel and face displacement for different solutions

$\boldsymbol{\theta}(°)$	**15**	**12**	**9**	**6**
R_m (m)	5.32939	5.79746	6.09144	6.43552
U_{rm} (m)	0.07568	0.08823	0.09661	0.10690
U_{if} (m)	0.01738	0.01961	0.02104	0.02273

7.9 Appendix B: Support structure capacity estimation

Table B 1. Mechanical and geometrical characteristic of proposed support elements

TH 44/58 steel ribs				**BN 450 shotcrete**			
A	0.00134 m^2	p_{ssmax}	0.638 MPa	A	0.00134 m^2	p_{scmax}	7.43 MPa
E_s	200000 MPa	K_{ss}	250.77 MPa/m	E_c	36000 MPa	K_{sc}	3615.85 MPa/m
σ_{ys}	245 MPa	p_{ssmax}/K_{ss}	0.00255	σ_{cc}	44 MPa	p_{scmax}/K_{s}	0.00205
R_q	2.15 m			R_q	2.15 m	v	0.2
ω	1 m			t	0.4 m		
JENNMAR 63 T sumo Cable bolts							**Swellex PM 24C**
T	0.635 MN	l	8.0 m	T	0.24 MN	l	3 m
ω_l	1.0 m	R_q	2.15 m	ω_l	1.0 m	R_q	2.15 m
R_c	2.0 m	p_{cbmax}	0.3175 MPa	R_c	1.0 m	p_{bmax}	0.24 MPa
E_b	207000 MPa	K_{cb}	7.87 MPa/m	E_b	207000 MPa	K_b	74.199 MPa/m
D	0.028 m	p_{cbmax}/K_{cb}	0.04035	D	0.037 m	p_{bmax}/K_b	0.00324

Table B 2. Tunnel convergence at a distance behind the tunnel face

	$\boldsymbol{\theta}$(°)			
X (m)	**15**	**12**	**9**	**6**
1	0.01816	0.01941	0.02029	0.02245
2	0.02497	0.02647	0.02705	0.02993
3	0.03103	0.03265	0.03285	0.03635

4	0.03633	0.03794	0.03865	0.04276
5	0.04087	0.04323	0.04444	0.04704

Table B 3. SCC parameters for the composite support structure

Combined support structure	p_{smax} **(MPa)**	K_{st} **(MPa/m)**	U_{im}**(m)**
STCB	0.66617	258.642	0.00258
STB	0.83699	324.963	0.00258
SCCB	7.44071	3623.723	0.00205
SCB	7.57689	3690.043	0.00205
STCBSCB	8.10797	3948.686	0.00205

Table B 4. Displacement results at GRC-SCC equilibrium points for the composite support structure

			Uiy X= 2m		
θ(°)	**STCB**	**STB**	**SCCB**	**SCB**	**STCBSCB**
15	0.02755	0.02755	0.02703	0.02703	0.02703
12	0.02905	0.02905	0.02852	0.02852	0.02852
9	0.02963	0.02963	0.02911	0.02911	0.02911
6	0.03251	0.03251	0.03199	0.03199	0.03199

Table B 5. Support characteristic curve computations

	STCB		**STB**		**SCCB**		**SCB**		**STCBSCB**	
θ(°)	MPa	**m**	MPa	**m**	MPa	**m**	MPa	**m**	MPa	**m**

15	0.66616 0.66616 0	0.2 0.02755 0.02497	0.83698 0.83698 0	0.2 0.02755 0.02497	7.44071 7.44071 0	0.2 0.02702 0.02497	7.57688 7.57688 0	0.2 0.02702 0.02497	8.10796 8.10796 0	0.2 0.02702 0.02497
12	0.66616 0.66616 0	0.1 0.02904 0.02647	0.83698 0.83698 0	0.1 0.02904 0.02647	7.44071 7.44071 0	0.1 0.02852 0.02647	7.57688 7.57688 0	0.1 0.02852 0.02647	8.10796 8.10796 0	0.1 0.02852 0.02647
9	0.66616 0.66616 0	0.2 0.02962 0.02705	0.83698 0.83698 0	0.2 0.02962 0.02705	7.44071 7.44071 0	0.2 0.02910 0.02705	7.57688 7.57688 0	0.2 0.02910 0.02705	8.10796 8.10796 0	0.2 0.02910 0.02705
6	0.66616 0.66616 0	0.6 0.03250 0.02993	0.83698 0.83698 0	0.6 0.03250 0.02993	7.44071 7.44071 0	0.6 0.03198 0.02993	7.57688 7.57688 0	0.6 0.03198 0.02993	8.10796 8.10796 0	0.6 0.03198 0.02993

Chapter 8.

8. Conclusions and Recommendations

8.1 Conclusions

The main objectives of this study are to understand the behaviour of tunnels excavated in squeezing ground with the main emphasis on the 3-phase creep phenomenon and efficient tools for its reliable estimation. Hence, a literature review on the conventional and numerical solutions is conducted and limitations are outlined. As such, this thesis addressed the limitations by presenting the closed-form solutions and the time-dependent constitutive model.

The two closed-form analytical solutions presented herein are derived and presented to predict the non-circular tunnel convergence influenced by the confining stress and time-dependent behaviour. The presented elasto-plastic solution governed by the Lode-dependent DP yield criterion can successfully be employed to estimate tunnel convergence. The most important part addressed by the solution is the consideration of the intermediate principal stress in convergence as well as non-circular tunnel geometry, which most analytical solutions neglect. Whereas, the second solution addresses the conventional analytical method limitation in considering the elasto-viscoplastic behaviour characterized by squeezing mechanism. This time-dependent solution can estimate the viscoplastic plastic strains in the accelerated creep phase. As such can be a good and reliable tool in estimating delayed tunnel convergence in squeezing ground.

The derived time-dependent constitutive equations presented herein are based on derivatives capable of describing the power-law mechanism. Firstly, the more complex fractional-order derivatives which require many parameters and secondly the less complex fractal-order derivatives that involve relatively fewer parameters. The fractional-order derivative-based constitutive equations are incorporated with the overstress and gamma functions. To build an improved time variation viscoelastic viscoplastic constitutive model for the 3-phase creep description. Even though the model can successfully describe the 3-phase

creep behaviour, it needed improvement to address certain limitations such as the number of parameters required and most importantly the explicit description of the accelerated creep phase associated with damage evolution. Hence, the second improved constitutive equations based on the fractal-order derivatives are derived to consider these aspects.

In this improvement the fractal-order derivative, overstress function, and damage factor are applied to build a damage constitutive function. This represents a nonlinear creep damage model with time-varying viscoelasticity viscoplasticity for 3-phase creep behaviour estimation. This power-law and damage functions integrated constitutive model is efficient, easy to implement, and requires less computational time as compared to one which incorporates the gamma and overstress law. Finally, it shows good agreement with the 3-phase creep experimental data and requires few creep parameters to explicitly depict the 3-phase behaviour as compared to the viscoelastic viscoplastic constitutive model.

These constitutive equations are realized by implementing in FLAC^{3D} as user-defined constitutive models and efficiently employed to simulate mechanical responses associated with creep. Which includes long-term time-dependent deformation and damage evolution exhibited by squeezing ground. The models can successfully be employed to conduct the time-dependent stability and failure analysis of tunnels excavated in squeezing rock mass.

8.2 Recommendation for future research

This study face limitation that remains unaddressed involving the implemented constitutive model's applicability on the time-dependent tunnel response in squeezing ground and its verification. Hence, this section outlines the limitation and makes the recommendation to address them as follows:

- The numerically implemented constitutive model does not consider other factors that influence squeezing mechanisms. This includes (1) the heterogeneity influence on damage evolution characterized by the viscoplastic behaviour of the rock mass discontinuities. That plays a major role in the extension of delayed deformations responsible for squeezing. Even though heterogeneity was partly considered by the creep parameter scaling, partial verification was attained because the fractured rock mass complete material properties are unknown. (2) The dynamic response as a result of ground vibration, blasting, and seismicity. (3) The civil application assumption adopted which does not consider cases of temperature effects. However, in cases of squeezing ground in deep underground mining, the temperature effect attributed to the geothermal gradient should be considered in tunnel stability analysis. Therefore, further work on the constitutive equations should consider the heterogeneity, dynamic, and temperature effects on squeezing.

- This implemented model is used to perform a numerical stability analysis with the intent to estimate the actual time-dependent tunnel convergence associated with creep and its implications. However, the analysis can be extended further if there is access to a large monitored convergence dataset attained from squeezing prone tunnels. Attempts to attain this large dataset were unsuccessful and the available employed in the numerical back analysis proved incomplete and captured over a short period. In that monitored time-dependent convergence dataset associated with squeezing requires a significant period of acquisition. Hence, the acquisition of dataset measured over time (years) is cardinal for the reliable tunnel response depiction in squeezing ground.

- The results attained from numerical simulations are usually influenced by the numerical code (continuum or discontinuum), the mesh concentration, the constitutive model employed, among others. The choice of the continuum or discontinuum numerical simulation is mainly dependent on the problem scale and fracture system geometry. Needless, to say the employment of a wide range of numerical simulations requires different types of rock property characterization. As such the rock mass behaviour's realistic capture correlates with the numerical simulation type and rock mass properties. In this study, the simulation is performed in a continuum finite volume code that considers an equivalent continuous rock mass material. However, it is necessary to explicitly depict the heterogeneity attributed to the ground material fracture growth and block rotation. Additionally, the ability of the presented constitutive model to account for the rock mass and support structure interaction need also be studied through explicit discontinuum numerical simulation. More importantly the evaluation of tunnel stability and support installation at the right location and right time.